

**In-situ analysis of phase transformations in a supermartensitic stainless steel  
A magnetic approach**

Bojack, Andrea

**DOI**

[10.4233/uuid:f85b8393-6071-4af6-9507-f713610c0f06](https://doi.org/10.4233/uuid:f85b8393-6071-4af6-9507-f713610c0f06)

**Publication date**

2018

**Document Version**

Final published version

**Citation (APA)**

Bojack, A. (2018). *In-situ analysis of phase transformations in a supermartensitic stainless steel: A magnetic approach*. [Dissertation (TU Delft), Delft University of Technology]. <https://doi.org/10.4233/uuid:f85b8393-6071-4af6-9507-f713610c0f06>

**Important note**

To cite this publication, please use the final published version (if applicable).  
Please check the document version above.

**Copyright**

Other than for strictly personal use, it is not permitted to download, forward or distribute the text or part of it, without the consent of the author(s) and/or copyright holder(s), unless the work is under an open content license such as Creative Commons.

**Takedown policy**

Please contact us and provide details if you believe this document breaches copyrights.  
We will remove access to the work immediately and investigate your claim.

# **In-Situ Analysis of Phase Transformations in a Supermartensitic Stainless Steel**

## **A magnetic approach**

Proefschrift

ter verkrijging van de graad van doctor  
aan de Technische Universiteit Delft,  
op gezag van de Rector Magnificus Prof.dr.ir. T.H.J.J. van der Hagen  
voorzitter van het College voor Promoties,  
in het openbaar te verdedigen  
op dinsdag 30 januari 2018 om 10:00 uur

door

**Andrea BOJACK**

Diplom-Ingenieurin in Werkstoffwissenschaft und Werkstofftechnologie,  
Technische Universität Bergakademie Freiberg,  
Freiberg, Germany,  
geboren te Freiberg, Germany.

*Dit proefschrift is goedgekeurd door de promotor:*

Prof. dr. ir. J. Sietsma

*Samenstelling promotiecommissie:*

Rector Magnificus	Voorzitter
Prof. dr.ir. J. Sietsma	Technische Universiteit Delft, The Netherlands, promotor

*Onafhankelijke leden:*

Prof.dr.ir. L.A.I. Kestens	Technische Universiteit Delft, The Netherlands
Prof.dr.-ing. U. Prah	Technische Universität Bergakademie Freiberg, Germany
Dr. D. San Martin	National Centre for Metallurgical Research (CENIM), Spain
Em.prof.dr. A. Howe	The University of Sheffield, Great Britain

*Other members:*

Dr. L. Zhao	VDL Weweler, The Netherlands
Dr. P.F. Morris	TATA Steel, Great Britain

*Reservelid:*

Prof.dr. J. Dik	Technische Universiteit Delft, The Netherlands
-----------------	--

Dr. L. Zhao heeft als begeleider in belangrijke mate aan de totstandkoming van het proefschrift bijgedragen.

This research was carried out under the project number M41.5.10392 in the framework of the Research Program of the Materials innovation institute (M2i) in The Netherlands ([www.m2i.nl](http://www.m2i.nl)).

ISBN: 978-94-91909-48-1

Copyright © 2018 by A. Bojack

All rights reserved. No part of the material protected by this copyright notice may be reproduced or utilized in any form or by any means, electronically, including photocopying, recording or by any information storage and retrieval system, without written permission from the author.

Printed by: ProefschriftMaken | [www.proefschriftmaken.nl](http://www.proefschriftmaken.nl)  
Cover art: [iStock.com/gmutlu](https://www.istock.com/gmutlu)

# Table of Content

<b>Symbols and abbreviations</b> .....	<b>vii</b>
<b>1. Introduction</b> .....	<b>1</b>
1.1 Research objectives .....	2
1.2 Thesis outline .....	2
REFERENCES .....	4
<b>2. Background</b> .....	<b>5</b>
2.1 Supermartensitic stainless steels .....	5
2.1.1 Chemical composition of SMSS .....	6
2.1.2 Heat treatment and microstructure of SMSS .....	7
2.1.3 Properties of SMSS depending on the retained austenite fraction .....	12
2.2 Magnetism in metallurgy .....	14
2.2.1 Introduction .....	14
2.2.2 Magnetic measurements for determination of austenite fraction .....	16
2.2.3 Saturation magnetization for steels depending on chemical composition .....	19
REFERENCES .....	21
<b>3. Materials and experimental techniques</b> .....	<b>27</b>
3.1 Materials .....	27
3.1.1 Supermartensitic stainless steel .....	27
3.1.2 Fe-C-Mn-Si steels .....	28
3.2 Thermo-magnetic measurements .....	29
3.2.1 Vibrating sample magnetometer .....	29
3.2.2 Magnetic measurements .....	31
3.2.3 Correction of systematic errors of the Vibrating Sample Magnetometer .....	32
3.3 Dilatometry .....	37
3.4 X-ray diffraction analysis .....	38
3.5 Optical and scanning electron microscopy .....	39
3.6 Thermodynamic calculations .....	39
REFERENCES .....	40

<b>4. Thermodynamic analysis of compositional variations in SMSS</b>	<b>41</b>
4.1 Introduction	41
4.2 Temperature dependence of equilibrium phase fractions	42
4.3 Effect of compositional variations on austenite fraction	45
4.4 Pseudo-binary phase diagrams of the 13Cr6Ni2Mo SMSS	48
4.5 Conclusions	51
REFERENCES	51
<b>5. In-situ determination of austenite and martensite in SMSS</b>	<b>53</b>
5.1 Introduction	53
5.2 Experimental	55
5.2.1 Magnetic measurements	55
5.2.2 Dilatometry	57
5.2.3 High-temperature X-ray diffraction (HT-XRD)	58
5.3 Results	59
5.3.1 Magnetic measurements	59
5.3.2 Dilatometer experiment	62
5.3.3 High-temperature XRD experiment	63
5.4 Discussion	65
5.4.1 Austenite formation	66
5.4.2 Martensite formation	67
5.4.3 Comparison of the in-situ techniques	68
5.5 Conclusions	70
REFERENCES	70
<b>6. In-situ thermo-magnetic investigation of the austenitic phase during tempering of an SMSS</b>	<b>73</b>
6.1 Introduction	73
6.2 Experimental	74
6.2.1 Magnetic measurements	75
6.2.2 Optical and scanning electron microscopy	76
6.2.3 Thermodynamic calculations	76
6.3 Results	77
6.3.1 Magnetization of martensite for calculating the austenite fraction at elevated temperatures	77
6.3.2 Microstructural analysis during first tempering step	79
6.3.3 Microstructural analysis during second tempering step	84
6.3.4 Microstructures after tempering	86

6.4	Discussion	91
6.4.1	Austenite formation and growth during first tempering step	91
6.4.2	Austenite stability	95
6.4.3	Austenite formation during the second tempering step	99
6.4.4	Austenite fraction from calculations of phase composition	99
6.5	Conclusions and recommendations	101
6.5.1	Conclusions	101
6.5.2	Recommendations for future work	102
	REFERENCES	103

## 7. Influence of austenitization treatment on the austenite fraction during

	<b>subsequent heat treatment of an SMSS</b>	<b>107</b>
7.1	Introduction	107
7.2	Experimental	108
7.2.1	Material	108
7.2.2	Heat treatments	109
7.2.3	Microscopy	111
7.3	Results	111
7.3.1	Influence of previous austenitization treatment and the heating rate on austenite formation upon reheating	111
7.3.2	Influence of previous austenitization treatment on retained austenite fraction after tempering	121
7.3.3	Microstructures after tempering	121
7.4	Discussion	122
7.4.1	Austenite formation in two stages	122
7.4.2	Influence of previous austenitization treatment on the austenite formation	125
7.5	Conclusions and recommendations	127
7.5.1	Conclusions	127
7.5.2	Recommendations for future work	128
	REFERENCES	128

## 8. In-situ thermo-magnetic and dilatometry investigation of phase

	<b>transformations in multi-phase steels</b>	<b>131</b>
8.1	Introduction	131
8.2	Experimental	132
8.2.1	Material	132
8.2.2	Equilibrium phase analysis	132

8.2.3	Heat treatment experiments in the magnetometer	133
8.2.4	Heat treatment experiments in the dilatometer	136
8.2.5	X-ray diffraction	137
8.2.6	Optical and scanning electron microscopy	138
8.3	Results	139
8.3.1	Microstructure of as-received materials	139
8.3.2	Equilibrium phase analysis	139
8.3.3	Magnetization and dilatometry measurements	141
8.3.4	Determination of the austenite fraction from saturation magnetization	150
8.4	Discussion	157
8.4.1	Phase transformations during tempering	157
8.4.2	Phase transformations during cooling	159
8.4.3	Application of in-situ thermo-magnetic analysis to quenching and partitioning treatment	162
8.5	Conclusions and recommendations	163
8.5.1	Conclusions	163
8.5.2	Recommendations for future work	164
	REFERENCES	164
	<b>Summary</b>	<b>167</b>
	<b>Samenvatting</b>	<b>171</b>
	<b>Acknowledgements</b>	<b>175</b>
	<b>List of publications</b>	<b>177</b>
	<b>About the author</b>	<b>179</b>

# Symbols and abbreviations

Symbol	Description	Unit
$a$	Constant	-
$a_0$	Initial lattice parameter	Å
$a_\alpha$	Lattice parameter of ferrite	Å
$a_{\alpha'}$	Lattice parameter of martensite	Å
$a_\theta, b_\theta, c_\theta$	Lattice parameters of cementite	Å
$a_\gamma$	Lattice parameter of austenite	Å
$A$	Material dependent constant in magnetic calculations	-
$\bar{A}_m$	Mean atomic weight	g mol <sup>-1</sup>
<b>A</b>	Austenite	-
$A_0$	Extrapolated temperature to a zero heating rate	°C
$A_0^{f1}$	Extrapolated temperature to a zero heating rate for end temperature of austenite formation in first stage	°C
$A_0^{s1}$	Extrapolated temperature to a zero heating rate for start temperature of austenite formation in first stage	°C
$A_0^{s2}$	Extrapolated temperature to a zero heating rate for start temperature of austenite formation in second stage	°C
$A_{c1}$	Start temperature for austenite formation during heating	°C
$A_{c3}$	Temperature at which material is fully austenitic during heating	°C
$A_{e1}$	Start temperature for austenite formation under equilibrium condition	°C
$A_{e3}$	Temperature above which material is austenitic under equilibrium condition	°C
$A_{e4}$	Maximum temperature at which material is austenitic under equilibrium condition	°C
$A_{f1}$	Temperature at which austenite formation during first stage ends	°C
$A_{r3}$	Temperature at which ferrite starts to form during cooling	°C
$A_{s1}$	Start temperature for austenite formation in first stage during heating	°C
$A_{s2}$	Start temperature for austenite formation in second stage during heating	°C
$A_{s,f}$	Start and finish transformation temperature	°C
$A_\theta$	Maximum temperature at which cementite is stable in equilibrium	°C
$b$	Constant	-
<b>B</b>	Bainite	-

$B$	Magnetic induction	$\text{Wb m}^{-2}$
$B_r$	Remanence	$\text{Wb m}^{-2}$
$B_s$	Temperature at which bainite formation ends	$^{\circ}\text{C}$
bcc	Body-centred cubic	-
bct	Body-centred tetragonal	-
<b>C</b>	Carbides	-
$C$	Material dependent constant in magnetic calculations	-
$d$	Diffusion distance	mm
$D$	Diffusion coefficient	$\text{m}^2 \text{s}^{-1}$
$D_0$	Pre-exponential factor	$\text{m}^2 \text{s}^{-1}$
$E$	Effective activation energy	$\text{J mol}^{-1}$
<b>F</b>	Ferrite	-
fcc	Face-centred cubic	-
$f$	Phase fraction	-
$f_B$	Bainite fraction	-
$f_i$	Phase fraction of phase $i$	-
$f_i$	Phase fraction at maximum transformation rate	-
$f_{ini}$	Maximum fraction of austenite stable after tempering	-
$f_{end}$	Equilibrium austenite fraction at $T_{1t}$	-
$f_P$	Pearlite fraction	-
$f_{\alpha'}$	Martensite fraction	-
$f_{\alpha',i}$	Initial martensite fraction	-
$f_{\alpha',f}$	Final fraction of martensite	-
$f_{\gamma}$	Austenite fraction	-
$f_{RT}^{\gamma}$	Austenite fraction after holding at room temperature	-
$f_{\gamma,i}$	Initial austenite fraction	-
$f_{\theta}$	Cementite fraction	-
<b>H</b>	Magnetic field strength	$\text{A m}^{-1}$
$H_c$	Coercivity	$\text{A m}^{-1}$
hkl	Miller indices	-
$I_{hkl}^j$	Net integral intensity of phase $j$	counts
<b>L</b>	Laves-phase	-
$L_0$	Initial sample length	mm
$k$	Rate constant	$\text{s}^{-1}$
$k_0$	Pre-exponential factor	$\text{s}^{-1}$
$m$	Constant	$^{\circ}\text{C}$
$M$	Mass magnetization	$\text{A m}^2 \text{kg}^{-1}$
$M$	Volume magnetization	$\text{A/m}$

M	Martensite	-
$M_P$	Magnetization at point P	$A\ m^2\ kg^{-1}$
$M_{ref}(T)$	Temperature dependent saturation magnetization of austenite-free reference sample	$A\ m^2\ kg^{-1}$
$M_{sat}(c)$	Saturation magnetization of austenite containing sample, or measured magnetization	$A\ m^2\ kg^{-1}$
$M_{sat}(ref)$	Saturation magnetization of reference sample	$A\ m^2\ kg^{-1}$
$M_s$	Start temperature for martensite formation	$^{\circ}C$
$M_{sat}$	Saturation magnetization	$A\ m^2\ kg^{-1}$
$M_{sat,i}$	Saturation magnetization of phase $i$	$A\ m^2\ kg^{-1}$
$M_{sat,Fe}$	Saturation magnetization of pure iron	$A\ m^2\ kg^{-1}$
$M_{sat0}$	Saturation magnetization at 0 K	$A\ m^2\ kg^{-1}$
$n$	Time exponent, or number of atoms in a unit cell	-
$n_{\alpha}, n_{\gamma}$	Numbers of diffraction peaks	-
$N_A$	Avogadro number	$mol^{-1}$
P	Pearlite	-
$P_s$	Temperature at which pearlite formation starts	$^{\circ}C$
$P_f$	Temperature at which pearlite formation ends	$^{\circ}C$
$Q$	Activation energy	$J\ mol^{-1}$
$r$	Constant	$K\ min^{-1}$
$R$	Gas constant	$J\ mol^{-1}\ K^{-1}$
$R_{hkl}^j$	Theoretical diffraction line intensity of phase $j$	counts
$R_{13Cr6Ni2Mo}$	Theoretical diffraction line intensity for steel 13Cr6Ni2Mo SMSS	counts
$s$	$T/T_C$	-
$t$	Time	s, min
$t_0$	Initial time of cooling	min
$t_1, t_2, t_3$	Times during heating, holding and cooling in magnetometer experiments	h, min
$t_{1t}$	Time of first tempering step	h, min
$t_{2t}$	Time of second tempering step	h, min
$t_A$	Austenitization time	h, min
$t_b$	Time parameter accounting for previous austenite formation	s
$t_h$	Time of isothermal holding	min
$t_P$	Time at point P	min
$t_r$	Holding time at temperature of reheating step	h
$t_t$	Tempering time	min

**Symbols and abbreviations**

---

$T$	Temperature	°C, K
$T_0$	Temperature before cooling	°C
$T_{1t}$	Temperature of first tempering step	°C
$T_{2t}$	Temperature of second tempering step	°C
$T_A$	Austenitization temperature	°C
$T_C$	Curie temperature	°C, K
$T_f$	Temperature for fixed phase fraction transformed for various heating rates	K
$T_{f1}, T_{f2}$	Temperature where an observed contraction ends during heating	°C
$T_F$	Heater or furnace temperature in the magnetometer	°C
$T_h$	Isothermal holding temperature	°C
$T_i$	Temperature at maximum transformation rate	K
$T_{KM}$	Theoretical martensite start temperature in Koistinen-Marburger relation	°C, K
TM	Tempered martensite	-
$T_{peak}$	Temperature of peak in austenite fraction at room temperature	°C
$T_E$	Temperature after cooling from tempering temperature	°C
$T_r$	Temperature of holding at reheating step	°C
$T_{RT}$	Room temperature	°C
$T_S$	Sample temperature	°C
$T_{s1}, T_{s2}$	Temperatures where a contraction is observed during heating	°C
$T_t$	Tempering temperature	°C
$\Delta V$	Average atomic volume change	m <sup>3</sup>
$V$	Volume of unit cell	m <sup>3</sup>
$V_0$	Initial atomic volume	m <sup>3</sup>
$\emptyset$	Diameter	mm
$x_i$	Concentration of alloying element $i$	wt.%
$y_i$	Concentration of alloying element $i$	at.%
$\alpha$	Factor (=1/(Ks))	K <sup>-1</sup> s <sup>-1</sup>
$\alpha$	$\alpha$ -ferrite	-
$\alpha'$	Martensite	-
$\alpha'_{1T}$	Single tempered martensite	-
$\alpha'_{2T}$	Double tempered martensite	-
$\alpha'_F$	Fresh martensite	-
$\alpha'_T$	Tempered martensite	-

$\alpha_{KM}$	Koistinen-Marburger rate parameter	$K^{-1}$
$\alpha_{th}$	Linear coefficient of thermal expansion	$K^{-1}$
$\alpha_{th}(\alpha')$	Linear coefficient of thermal expansion of martensite	$K^{-1}$
$\alpha_{th}(\gamma)$	Linear coefficient of thermal expansion of austenite	$K^{-1}$
$\beta$	Material dependent constant in magnetic calculations	-
$\beta, \beta_f$	State variables determining transformed phase fraction	-
$\gamma$	Austenite	-
$\delta$	$\delta$ -ferrite	-
$\Delta a$	Change in lattice parameter	Å
$\Delta L/L_0$	Dilatation (length change normalized by initial sample length)	%
$\Delta L_A$	Fitting parameter	mm
$\Delta L_B$	Fitting parameter	mm
$\Delta L_H/L_0$	Relative length change during holding	%
$\Delta L_{ini}/L_0$	Initial relative length change during holding	%
$\Delta L_{inf}/L_0$	Relative length change after infinite holding	%
$\Delta L_1, \Delta L_2$	Difference between measured and extrapolated length change	mm
$\Delta L_{tot}$	Differences between extrapolated length changes	mm
$\Delta_1$	Difference in magnetization between start and end of the cooling	$A m^2 kg^{-1}$
$\Delta_2$	Difference in magnetization between start and end of the holding	$A m^2 kg^{-1}$
$\varepsilon$	$\varepsilon$ -carbide	-
$\eta$	$\eta$ -carbide	-
$\theta$	Diffraction angle	degrees
$\theta$	Cementite	-
$\lambda$	Wavelength of X-ray beam	Å
$\mu$	Permeability of a material	$H m^{-1}$
$\mu_0$	Permeability of vacuum ( $= 4\pi \times 10^{-7} H m^{-1}$ )	$H m^{-1}$
$\rho$	Density	$kg m^{-3}$
$\tau$	Time constant of cooling	min
$\tau_A, \tau_B$	Mean rate parameters	$min^{-1}$
$\tau_{DIL}$	Time constant of cooling in dilatometer	min
$\tau_{VSM}$	Time constant of cooling in magnetometer furnace	min
$\phi$	Heating rate	$K min^{-1}, K s^{-1}$
$\chi$	Chi-phase	-
$\omega$	Effect of cementite on magnetization	$A m^2 kg^{-1}$

<b>Abbreviation</b>	<b>Meaning</b>
AF	Air furnace
as-rec.	as-received
DIL	Dilatometer
EDM	Electro-discharge machine
GB	Grain boundaries
hq	Helium gas quenching
KM	Koistinen-Marburger
L-B	Lichtenegger-Blöch etchant
PID	Proportional-integral-derivative
PSD	Position sensitive detector
QP	Quenching and partitioning
RA	Retained austenite
RT	Room temperature
SEM	Scanning electron microscope
SMSS	Supermartensitic stainless steel
SSC	Sulphide stress cracking
VSM	Vibrating sample magnetometer
wq	Water quenching
XRD	X-ray diffraction

# 1

## Introduction

Since the beginning of the industrialization in the 18th century steel has been the main material for the transportation, production and construction industry. Over the years, the pressure of cost and weight reduction has led to the development and application of alternative materials such as aluminium alloys, magnesium alloys and composites. Owing to the constant research and development of steels and the thus obtained variety of property combinations, steel is still irreplaceable in a wide range of applications. The knowledge of the influence of composition and heat treatment as well as thermo-mechanical treatment on the microstructure evolution are key factors in tailoring the properties of steels. Amongst others, controlling the retention of austenite during the thermal processing of advanced multiphase steels has become a major issue in their production, since retained austenite can influence the steel properties to a large extent. Austenite is a face-centred cubic phase of steels that is in equilibrium only present at elevated temperatures, i.e. above the  $A_{e1}$ -temperature, but can be stabilized to lower temperatures as a result of alloy design and heat treatment.

Retained austenite exists widely in steels, possibly as an inevitable product of thermal processing but often introduced by a deliberately designed thermal processing. The latter takes advantage of retained austenite with respect to its beneficial contribution to various properties, for instance the formability of steel sheets via the transformation-induced plasticity effect or hydrogen-induced stress corrosion cracking due to its affinity to hydrogen. It is therefore important to understand the retention mechanism of austenite in order to extend the range and to have a better control of materials properties. This understanding can be enhanced via *in-situ* monitoring the evolution of austenite during thermal processing.

The development of the austenite fraction can in principle be monitored on the basis of its difference with ferrite in terms of density or crystal structure. The density difference, however, is not much more than 1 % and the crystal structure can only be monitored *in-situ* by means of X-ray diffraction at synchrotron sources. A promising alternative is using the distinct difference in magnetic properties: ferrite is ferromagnetic below the Curie temperature (for pure iron around 770 °C), the same as martensite or bainite. Austenite, on the other hand, is paramagnetic at all investigated temperatures in this project. Therefore, magnetic techniques are of increasing interest in the steel industry as understanding of magnetic phenomena has recently led to the development of various *in-situ* and *ex-situ*

detection techniques. Using these techniques, one can for example monitor online the fraction of existing phases during thermal processing [1], create interesting microstructures under high magnetic fields [2], perform non-destructive examination of steel products [3, 4], and determine accurately the fraction of retained austenite [5] and its thermal stability [6]. The calculation of the fraction of austenite from the saturation magnetization is based on physical concepts, but can be complicated by the effects of alloying elements and the formation or dissolution of carbides. In view of the industrial demand for *in-situ* monitoring of austenite fractions, there is an increasing need to improve the application range and accuracy of magnetic methods.

In this project *in-situ* and *ex-situ* magnetic investigation using the Vibrating Sample Magnetometer as a primary experimental technique, combined with other techniques such as X-ray diffraction, dilatometry, microscopy and thermodynamic calculations, are applied to two types of advanced steels: a supermartensitic stainless steel (SMSS), on which the main focus of the thesis is, and multi-phase Fe-C-Mn-Si steels. Both steel types undergo a range of microstructural processes during heat treatment, including austenite formation, ferrite formation, bainite formation and martensite formation. The mechanical properties of SMSS are strongly dependent on the fraction and stability of retained austenite, which can be controlled by the heat treatment. It is therefore important to accurately monitor the formation of austenite during heat treatment in order to improve the consistency of the retained austenite fraction at a given tempering temperature. For the multi-phase Fe-C-Mn-Si steels, this project can contribute to the development of these advanced steels and a more accurate control over the microstructure development in order to have a better predictive capability.

### 1.1 Research objectives

This project aims at an improvement of the basic understanding of the phase transformations during thermal processing of supermartensitic stainless steels and also multiphase Fe-C-Mn-Si steels. The scientific aim of the project is twofold: (i) to study the microstructural evolution involved in thermal processing of advanced steels based on optimising retained austenite and (ii) to optimise and extend the application of magnetic methods for these steels.

### 1.2 Thesis outline

This thesis is structured as follows:

**Chapter 2 “Background”** presents an introduction on supermartensitic stainless steels, whose analysis is the main focus of this thesis. Furthermore, an account is given on fundamentals of magnetism, relevant for this work, and its application in metallurgy,

especially for the detection of austenite by saturation magnetization measurements. Based on literature information, an improved equation to calculate the theoretical saturation magnetization of SMSS is proposed.

**Chapter 3 “Materials and experimental techniques”** introduces the materials and experimental techniques used in this thesis. The determination of austenite from the different in-situ techniques is briefly described.

In **Chapter 4 “Thermodynamic analysis of compositional variations in SMSS”** the influence of compositional variations on the equilibrium austenite phase fraction and equilibrium transformation temperatures of 13Cr6Ni2Mo SMSS are analysed using the Thermo-Calc software package [7]. Furthermore, pseudo binary Fe-Ni phase diagrams of the 13Cr6Ni2Mo SMSS are calculated to discuss the influence of Ni on the phases being present in equilibrium.

In **Chapter 5 “In-situ determination of austenite and martensite in SMSS”** the phase transformations in a 13Cr6Ni2Mo SMSS are analysed in-situ during austenitization treatment using thermo-magnetic measurement, dilatometry and high temperature X-ray diffractometry. An approach for in-situ determination of the austenite fraction from thermo-magnetic measurements below the  $A_{c1}$ -temperature is presented. The evolution of the austenite fraction is monitored and the results obtained by the different techniques are compared.

**Chapter 6 “In-situ thermo-magnetic investigation of the austenitic phase during tempering of a SMSS”** studies the austenite formation during different tempering treatments of 13Cr6Ni2Mo SMSS samples by in-situ thermo-magnetic measurements. An approach to determine the austenite fraction from in-situ thermo-magnetic measurements is presented for temperatures above  $A_{c1}$ . The activation energy for isothermal martensite-to-austenite transformation is determined and the role of Ni and Mn on the austenite stabilization is discussed. Moreover, austenite decomposition at room temperature is observed and analysed. Furthermore, the magnetization, and hence the austenite fraction, is related to the compositions and fractions of equilibrium phases.

In **Chapter 7 “Influence of austenitization treatment on the austenite fraction during subsequent heat treatment of an SMSS”** the influence of different austenitization treatments of a 13Cr6Ni2Mo SMSS on austenite formation during reheating (dilatometry) and on the fraction of austenite retained after tempering treatment (magnetic technique) is measured and analysed. Furthermore, the influence of the heating rate on the austenite formation and the activation energy of the martensite-to-austenite transformation during continuous heating is studied by means of dilatometry.

**Chapter 8 “In-situ thermo-magnetic and dilatometry investigation of phase transformations in multi-phase steels”** examines in-situ phase formations in two multi-phase Fe-C-Mn-Si steels with different carbon contents during austenitization treatment by thermo-magnetic measurements, dilatometry and room-temperature X-ray diffractometry.

This chapter presents the *in-situ* thermo-magnetic phase formation analysis of steels with more than two phases, which makes the calculation of the austenite fraction less straightforward than for the SMSS analysed by thermo-magnetic measurements in *chapter 5* and *6*. An approach to determine the austenite fraction is presented and the phase formations are discussed.

## **REFERENCES**

- [1] X.J. Hao, W. Yin, M. Strangwood, A.J. Peyton, P.F. Morris and C.L. Davis: *Metall. Mater. Trans. A*, 2009, vol. 40A, no. 4, pp. 745-56.
- [2] Y.D. Zhang, C. Esling, M.L. Gong, G. Vincent, X. Zhao and L. Zuo: *Scripta Mater.*, 2006, vol. 54, no. 11, pp. 1897-1900.
- [3] A. Mitra, J.N. Mohapatra, J. Swaminathan, M. Gosh, A.K. Panda and R.N. Gosh: *Scripta Mater.*, 2007, vol. 57, no. 9, pp. 813-6.
- [4] V. Moorthy, B.A. Shaw, P. Mountford and P. Hopkins: *Acta Mater.*, 2005, vol. 53, no. 19, pp. 4997-5006.
- [5] L. Zhao, N.H. van Dijk, E. Brück, J. Sietsma and S. van der Zwaag: *Mater. Sci. Eng. A*, 2001, vol. 313, no. 1-2, pp. 145-52.
- [6] N. Luzginova, L. Zhao and J. Sietsma: *Mater. Sci. Eng. A*, 2007, vol. 448, no. 1-2, pp. 104-10.
- [7] Thermo-Calc Software package, Version S, Database TCFeV6.2, Stockholm, Sweden, 2011.

# 2

## Background

The first part of this chapter presents an introduction on supermartensitic stainless steels. The desired microstructure and properties of supermartensitic stainless steels are obtained by the combination of alloying elements used and applied heat treatment, which are described in detail. In the second part of this chapter an account is given on fundamentals of magnetism, relevant for this work, and its application in metallurgy, especially for the detection of austenite by saturation magnetization measurements.

### 2.1 Supermartensitic stainless steels

Stainless steels are primarily developed to withstand corrosive environments, where for instance plain carbon steels are susceptible to corrosion. This is primarily owed to the addition of Cr, usually between 11 and 30 wt.%, which has the ability to form a protective, stable chromium oxide layer on the steel surface. Stainless steels may be divided into several classes and sub-groups according to their chemical composition and properties. Typical classes are: austenitic stainless steels, ferritic stainless steels, martensitic stainless steels, duplex stainless steels, precipitation hardening stainless steels and Mn-N substituted austenitic stainless steels. [1-3]

Supermartensitic stainless steels (SMSS) have been developed from soft martensitic stainless steels with much lower levels of interstitials like C and N [4]. They possess an outstanding combination of properties, i.e. high strength, good toughness, good corrosion resistance, and reasonable weldability [4-7]. Due to the increasing need for a more cost effective use of materials, SMSS have been further developed in the past 20 years and are for instance increasingly being applied in the offshore oil and gas industry to replace highly alloyed alternatives [5, 6]. The steels utilized in the offshore oil and gas industry need to be robust, consistent and reliable. They need a high tensile strength in combination with good toughness, the latter is often required at sub-zero temperatures. They need to be wear and corrosion resistant, for instance against sulphide stress cracking (SSC), which requires certain hardness limitations. A careful selection of the alloy composition provides a cost effective solution [8]. The properties of SMSS, particularly the yield stress, are strongly dependent on the fraction of retained austenite [9], which can be controlled by the heat treatment. The following sections provide an introduction to the SMSS, the influence of the alloy design and the heat treatment procedure on the fraction of retained austenite and the properties of SMSS.

### 2.1.1 Chemical composition of SMSS

In order to limit the alloy cost while maintaining good mechanical properties in combination with good corrosion resistance, the alloy design of SMSS is by a careful selection of alloying elements [9]. SMSS typically contains <0.03 wt.% C, 11.5~13 wt.% Cr, 2~6.5 wt.% Ni, 0~2.5 wt.% Mo, 0~2 wt.% Mn, <0.4 wt.% Si, <1.5 wt.% Cu, <0.05 wt.% N and small fractions (<0.3 wt.%) of V, Ti or Nb [4, 5, 9, 10]. Depending on the application, certain alloying combinations are produced in order to offer a wide range of properties. According to the fractions of the major alloying elements, SMSS may be roughly grouped in three grades: lean, medium and high [4]. Typical compositions ranges for these grades are listed in Table 2.1. Research and development is continuing, for instance the testing of new alloying combinations with 15 wt.% Cr, 1 wt.% W and up to 3 wt.% Cu [11-13].

Table 2.1 Typical compositions of SMSS grades (in wt.%), balance Fe [4].

	C	Cr	Ni	Mo	Mn	Si	N	S	P
Lean	0.01	11	2	-	1.5	0.2	<0.01	<0.01	<0.02
Medium	0.01	12	4.5	1.5	1	0.2	<0.01	<0.01	<0.02
High	0.01	12	6	2.5	1	0.2	<0.01	<0.01	<0.02

The effective alloy design for SMSS can be summarized as follows:

- Reduced C-content, which increases the effective Cr-content that is available for corrosion resistance, due to reduced carbide formation [7].
- Addition of Ni, as the most effective addition to stabilize the austenite and to maintain the martensitic phase without formation of  $\delta$ -ferrite [7].
- Low contents of C and N in SMSS result in improved weldability [14].
- The low C-content lowers the hardness, improves toughness and is beneficial to the resistance against SSC [7].
- Mo in SMSS improves the resistance to both SSC and localized pitting corrosion [7].
- Good low temperature toughness is obtained by ensuring cleanliness of the steels by low S and P concentrations [6, 14].
- V, Ti and Nb form carbides, nitrides or carbo-nitrides and cause microstructure refinement and improved mechanical properties [7, 9, 15, 16]. They produce secondary hardening, but a small addition of Ti was reported to reduce secondary hardening [7].

The influence of the elements Cr, Ni and Mo on the presence of martensite in 0.1wt.%C-Fe-Cr-Mo steels, verified by microstructure observations after cooling from austenitization at 1050 °C [7], is shown in Figure 2.1. The addition of Mo narrows the martensite single phase region, which is balanced by the addition of Ni. However, addition of Ni stabilizes the austenite phase, so retained austenite will remain after cooling since the  $M_f$ -temperature, defined as the temperature at which 100 % martensite has formed, falls below room temperature. Addition of Cr will promote  $\delta$ -ferrite formation, thus the martensite single phase will be narrowed [6, 7].  $\delta$ -ferrite has a negative effect on low-temperature toughness and needs to be avoided [5]. Hence, the design of SMSS is a chemical balance to avoid ferrite

in the structure, but also expensive over-alloying in austenite stabilizing elements needs to be avoided [6].

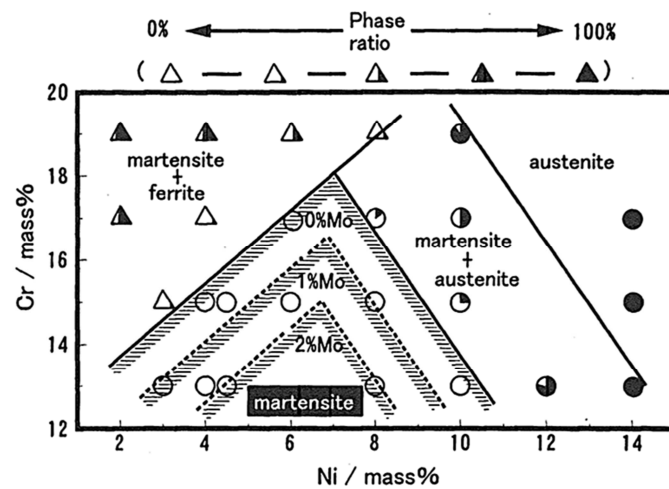


Figure 2.1 Effect of Cr, Ni and Mo on the presence of martensite of 0.01wt.%C-Fe-Cr-Mo system after austenitization at 1050 °C and cooling [7].

### 2.1.2 Heat treatment and microstructure of SMSS

The fraction of retained austenite is very sensitive to the heat treatment, where small changes in the tempering temperature can have a significant effect on the mechanical properties like yield strength and hardness. In offshore applications these steels have to meet strict requirements [9] such as a high yield strength in combination with good toughness, even at sub-zero temperatures, and good stress-corrosion resistance. To meet the required properties of the material, the heat treatment has to be accurately controlled.

The heat treatment of SMSS is usually carried out in three steps: austenitizing and two tempering steps (see Figure 2.2). The heat treatment is called single tempering if only the first tempering step after the austenitizing is carried out. If two tempering steps are carried out, the heat treatment is designated as double tempering. After the heat treatment, the microstructure usually consists of finely dispersed retained austenite in a martensitic matrix, as shown in Figure 2.3. The following paragraphs focus on the heat treatment steps, which are important in achieving the outstanding combination of mechanical properties and corrosion resistance, and the accompanying changes in the microstructure.

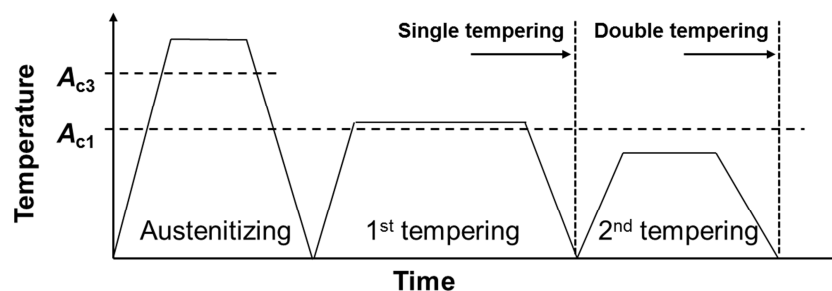


Figure 2.2 Heat treatment cycle for SMSS.

### Austenitization treatment

The austenitizing is carried out above the  $A_{c3}$ -temperature to obtain a completely austenitic microstructure, where all components are dissolved to a large extent [17] (see chapter 4). The austenitization of SMSS is usually carried out between 950 and 1100 °C [7, 15, 18-23]. Carbides, nitrides and carbo-nitrides should be dissolved during the holding above the  $A_{c3}$ -temperature. The grain size of the austenite can change during austenitizing. The state of austenitizing is not only influenced by the austenitizing temperature and time, but also influenced by the heating rate, the chemical composition and the microstructure of the as-received material. The influence of the heating rate on the transformation temperatures on the beginning of the austenite formation is shown in Figure 2.4. It can be seen that with increasing heating rate the transformation lines are shifted to higher temperatures. By the subsequent cooling, the components are redistributed and so a change of properties can be obtained. [17]

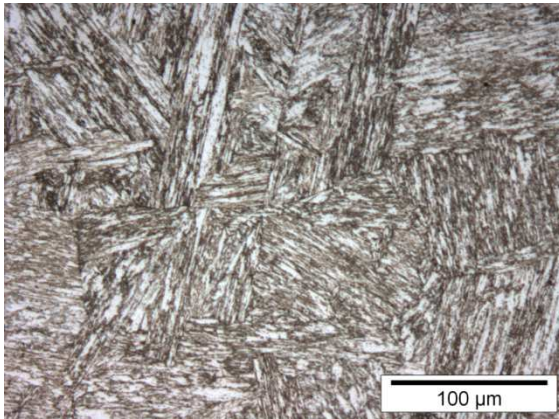


Figure 2.3 Microstructure of a 13Cr6Ni2Mo SMSS double tempered at 635 °C for 4 h and 550 °C for 2 h. (Light: martensite, dark: austenite)

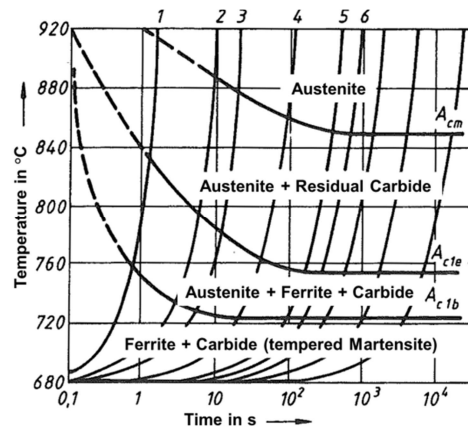


Figure 2.4 Continuous time-temperature-austenitization-diagram of an eutectoid steel [17].

By cooling from the austenitizing temperature to ambient temperature an essentially martensitic microstructure can be obtained for SMSS. This depends greatly on the concentration of austenite-stabilizing elements in the steel, since these elements decrease the martensite start temperature [24]. Hence, more austenite is expected to be stable at room temperature with increasing content of austenite-stabilizing elements and the microstructure after cooling from austenitizing temperature will not be completely martensitic, since a small fraction of retained austenite can be present. For SMSS air cooling is sufficient to reach an almost fully martensitic microstructure [6] of highly dislocated laths [22]. In Figure 2.5 continuous cooling curves with approximate martensite start and finishing temperatures of the different SMSS alloy grades are given, showing the influence of the alloying and the plate thickness on the microstructure after cooling from austenitization temperature.

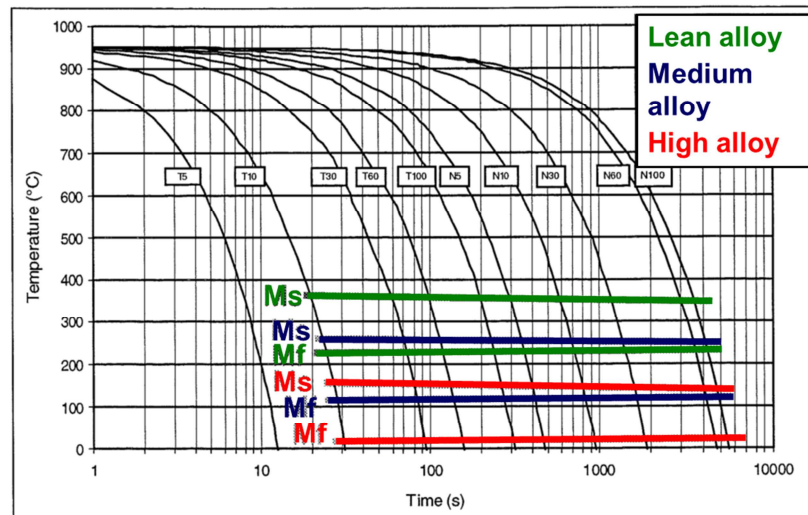


Figure 2.5 Continuous cooling curves of different SMSS grades showing martensitic transformation ranges from water quenching of a 5 mm plate (curve T5) to still air cooling of a 100 mm plate (curve N100) (modified from [6]).

During cooling from austenitizing temperature the martensitic microstructure, supersaturated with C, is formed. The martensitic formation is a diffusionless shear mechanism which leads to a characteristic microstructure. For low alloy steels up to 0.5 wt.% C the morphology of martensite is lath- or plate-like, referred to as lath martensite. For increasing C-content the crystal structure of martensite gradually changes from body-centred cubic (bcc) to body-centred tetragonal (bct). The tetragonality of martensite arises as a direct result of interstitial solution of C atoms with the preference of octahedral sites due to the diffusionless character of the reaction [24]. In Figure 2.6 the effect of C on the lattice parameters of martensite is shown. It is well known that the bct martensite causes distortions of the lattice and hence an increase in hardness. Since for SMSS the C-content is very low the  $c/a$ -ratio is close to 1 and a bcc structure can be assumed.

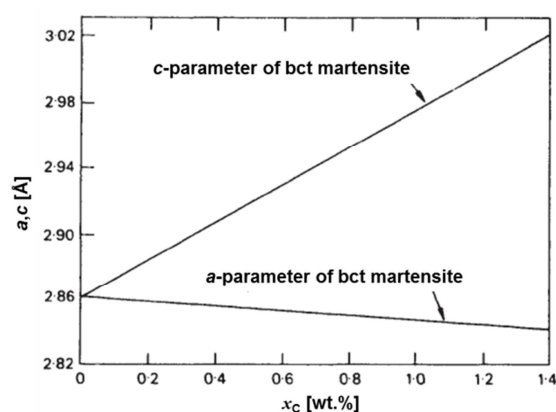


Figure 2.6 Effect of carbon on lattice parameters of martensite (modified from [24]).

**Tempering treatment**

Usually, SMSS are double tempered after the solution treatment (see Figure 2.2). The first tempering step is carried out above  $A_{c1}$  to obtain low-carbon tempered martensite and to form a controlled fraction of austenite that should be stable during cooling to room temperature. If  $A_{c1}$  is exceeded by too much, fresh martensite will form during cooling, having a detrimental effect on the ductility [9, 25]. The reason for the fresh-martensite formation lies in the increase of the volume fraction of austenite with increasing temperature, containing lower concentrations of austenite-stabilizing elements, which makes these areas less stable against transformation to martensite during cooling. Therefore, the tempering temperature should be chosen carefully. During a second tempering step fresh martensite will be tempered and partly transforms to austenite that is stable during cooling to room temperature [9, 18, 19, 26, 27], provided the tempering temperature is above the  $A_{c1}$  of the fresh martensite. Furthermore, the second tempering step also serves as a stress relief treatment.

A scheme of the phase fractions at room temperature, depending on the tempering temperature, is shown in Figure 2.7 for a modified 13%Cr steel (in wt.%: 0.023C, 13Cr, 5.1Ni, 2.01Mo, 0.22Si, 0.36Mn, 0.018P, 0.001S, 0.019Al). The initial microstructure after austenitization is fully martensitic. With increasing tempering temperature the microstructure consists of tempered martensite and an increasing fraction of retained austenite. A peak in retained austenite fraction is observed and with further increase in tempering temperature fresh martensite is obtained at room temperature. The evolution of the retained austenite fraction as a function of the first tempering temperature of a 13Cr6Ni2Mo SMSS is shown in Figure 2.8. A peak in austenite fraction is obtained at a temperature around 635 °C. Above this peak temperature ( $T_{peak}$ ), fresh martensite forms from austenite during cooling. The second tempering can result in grain refinement and was found to be beneficial to the properties of SMSS [9, 18, 26]. In addition, depending on the tempering temperature, it causes an increase in retained austenite fraction if the first tempering temperature was higher than  $T_{peak}$ , as can be seen in Figure 2.8. It is apparent from Figure 2.7 and Figure 2.8 that variation by just 5 °C of the first tempering temperature can cause a significant change in the microstructure, especially in the region of the peak in austenite fraction, and hence in the mechanical properties. Furthermore, the fraction of retained austenite not only depends on the tempering temperature, but also on the holding time at this temperature [9, 28, 29].

The stabilization of austenite at room temperature is obtained by austenite stabilizing elements like Ni, Mn and C, that enrich austenite during tempering [9, 18, 26, 27]. Since the C-content in SMSS is very small (less than 0.03 wt.%), mainly Ni [29, 30] and Mn [21] are responsible for the austenite stabilization, leading to a martensite start temperature below room temperature. It was also reported that the stability of austenite may have substructural origins, like an increased barrier against the shear of the martensitic transformation caused by a high dislocation density within the austenite particles [26] and the concentration of quenched-in vacancies, which is increasing with increasing tempering temperature [31]. The tempering of martensitic steels may also result in precipitation of minor phases like carbides and/or nitrides [20], which are known to cause secondary hardening with an increase in strength. Complex carbo-nitrides may also form. Carbon can

only be dissolved in very small concentrations in the nitride and almost all nitrogen forms nitrides, due to their high stability and the low solubility of nitrogen [32].

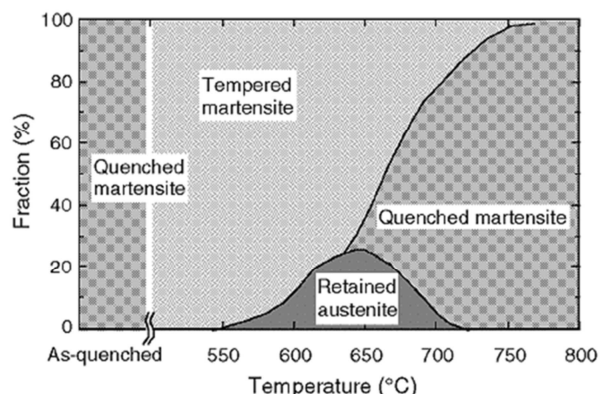


Figure 2.7 Schematic illustration of the microstructure for a modified 13% Cr steel after heat treatment as a function of tempering temperature [33].

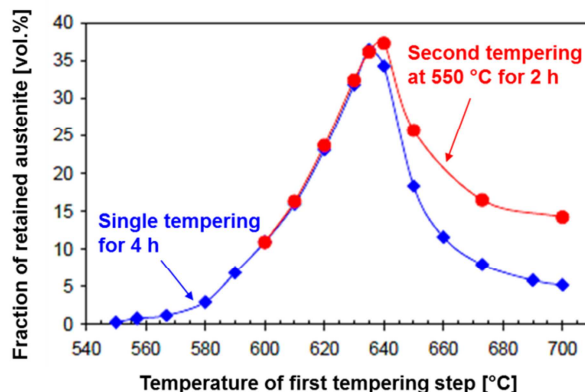


Figure 2.8 Effect of first tempering temperature on retained austenite fraction of a 13Cr6Ni2Mo SMSS after single and double tempering (modified from [9]).

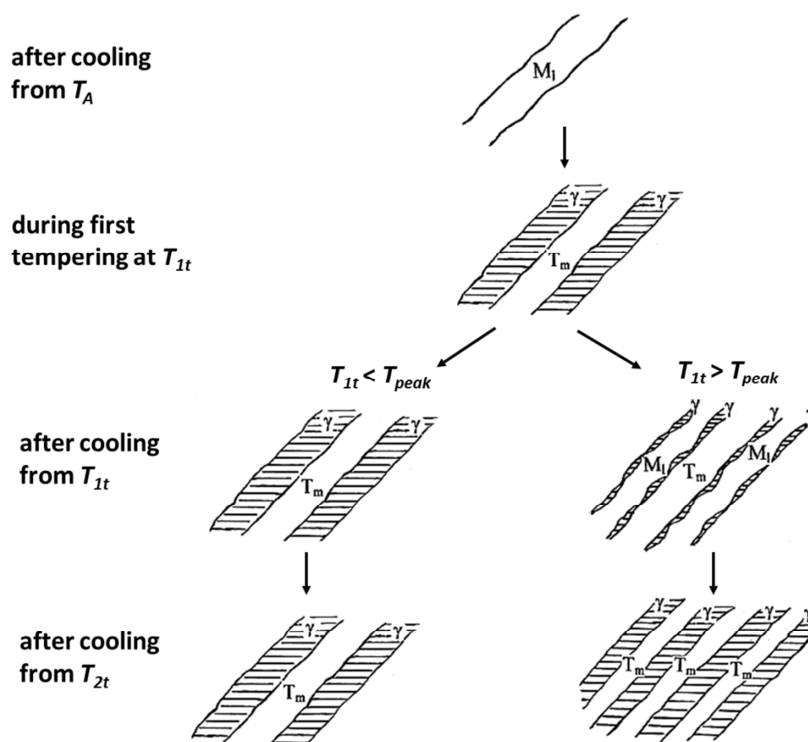


Figure 2.9 Scheme of structural refinement due to double tempering (modified from [26] and after [9, 18]).  $T_A$ : austenitization temperature,  $M_f$ : fresh martensite,  $T_m$ : tempered martensite,  $\gamma$ : austenite,  $T_{1t}$ ,  $T_{2t}$ : first and second tempering temperature,  $T_{peak}$ : temperature where the maximum fraction of retained austenite was formed after single tempering at  $T_{1t}$ .

Due to the formation of martensite and retained austenite, the tempering treatment of SMSS leads to a structural refinement, which is schematically described by several authors [18, 26, 28]. This is summarized in Figure 2.9, where the influence of the tempering temperature is shown. If the first tempering temperature is above  $T_{peak}$ , retained austenite is more dispersed after the second tempering due to the formation of fresh martensite during cooling from the first tempering temperature.

The nucleation of austenite is reported to mainly occur on martensite laths [21, 22, 30], but also on prior austenite grain boundaries [18, 34], since they act as preferred nucleation sites. Nakada et al. [35] reported a temperature dependence of the austenite nucleation sites and the shape of retained austenite for a Fe-13Cr-6Ni-0.012C-0.012N-2.1Mo (in wt.%), where at lower temperatures preferentially needle-like austenite forms at the martensite lath boundaries and at higher temperatures granular austenite forms at prior austenite grain boundaries. Lee et al. [31] observed for a Fe-3Si-13Cr-7Ni martensitic stainless steel film-like austenite at the interface of martensite laths and granular austenite inside the martensite laths, which also depends on the tempering temperature. Dislocations within the martensite laths and carbides may act as nucleation sites for austenite [18, 30, 34, 36, 37], since they could be rapid diffusion paths for solute atoms [24] such as Ni or Mn.

### 2.1.3 Properties of SMSS depending on the retained austenite fraction

As mentioned before, the mechanical properties of SMSS are strongly dependent on the fraction of retained austenite [9, 25, 38, 39]. Thus, selected properties of SMSS are discussed in relation to their austenite fraction. A controlled fraction of retained austenite in SMSS may offer an improved corrosion resistance [33] and contributes to a high impact toughness at low temperatures [21]. The impact energy versus the temperature for three SMSS alloy grades is shown in Figure 2.10, showing at low temperatures an improved impact toughness with an increase in Ni and Mo concentrations in the material, which also depends on the applied heat treatment and hence the retained austenite fraction [39]. Furthermore, the formability of SMSS was reported to increase with increasing austenite fraction [9, 25, 38, 39].

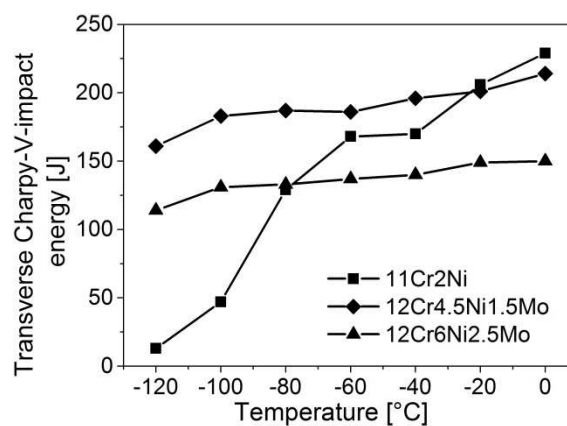


Figure 2.10 Transverse Charpy-V-impact energy of three SMSS alloy grades versus temperature (after Dufrane [5]).

Typical strength values of SMSS are 550-850 MPa for the 0.2% yield strength and 780-1000 MPa for the tensile strength [10]. In Figure 2.11 the effect of the austenite fraction on the 0.2% yield strength is shown for a 13Cr6Ni2Mo SMSS for different tempering procedures. It is shown that the yield strength is almost linearly decreasing with increasing fraction of retained austenite. Due to the reversed transformation of fresh martensite to retained austenite, double tempering leads to an increase in the proof strength if the first tempering step is above  $T_{peak}$ . This is due to the relieve of internal stresses, high dislocation density and a fine grain size [9]. Figure 2.12 shows the effect of the austenite fraction on the hardness for the same 13Cr6Ni2Mo SMSS. There it can be seen that the hardness is also linearly decreasing with increasing austenite fraction and that double tempering leads to an increase in hardness if the first tempering step is above  $T_{peak}$ . Tempering below  $T_{peak}$  results in lower hardness values with respect to the austenite fraction. As mentioned in section 2.1.1, a low hardness is required for improved resistance against SSC, in combination with an adequately high strength to meet the required specifications. From Figure 2.11 and Figure 2.12 it is apparent that a minimum strength and maximum hardness needs to be optimised, since both the strength and hardness decrease with increasing fraction of retained austenite. This might result in just a small window for the heat treatment parameters, since already a change in 5 °C of the first tempering temperature changes the austenite fraction, especially in the region of  $T_{peak}$  (see Figure 2.8) [9].

The tempering treatment also has an effect on the corrosion resistance of SMSS [33, 40, 41]. For instance, Kimura et al. [33] investigated the effect of the austenite fraction on the corrosion performance of a modified 13% Cr-steel (wt%-0.023C-5.1Ni-2.01Mo-0.36Mn-0.22Si) subjected to different heat treatments. They measured a decrease of the maximum H-permeation rate in the steel with increasing fraction of retained austenite, which is beneficial for the SSC resistance [33]. Solheim et al. [40] measured a decrease in ductility with increasing fraction of retained austenite during hydrogen charging due to the higher hydrogen solubility in austenite compared to martensite. They concluded that the retained austenite may affect the hydrogen embrittlement.

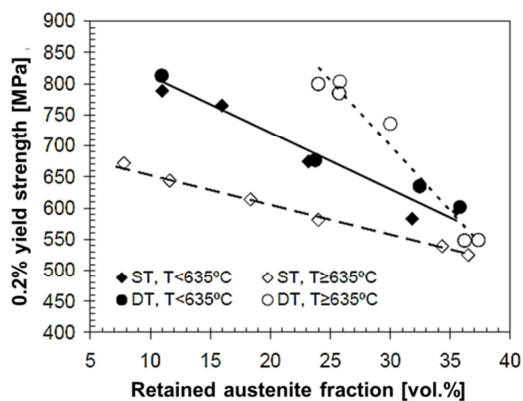


Figure 2.11 Effect of retained austenite fraction on 0.2% proof strength after single tempering (ST) and double tempering (DT) for a 13Cr6Ni2Mo SMSS (modified from [9]). ST for 4 h, DT at 550 °C for 2 h.  $T_{peak} = 635$  °C.

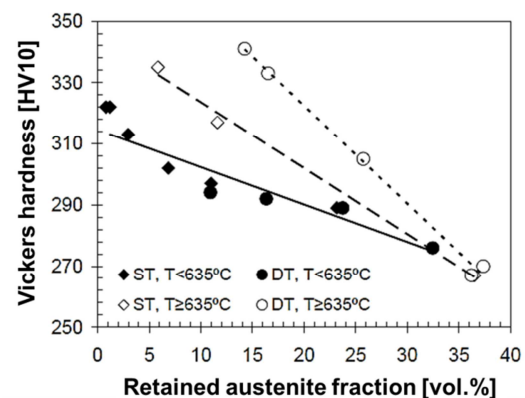


Figure 2.12 Effect of retained austenite fraction on hardness of a 13Cr6Ni2Mo SMSS after single tempering (ST) and double tempering (DT) (modified from [9]). ST for 4 h, DT at 550 °C for 2 h.  $T_{peak} = 635$  °C.

## 2.2 Magnetism in metallurgy

Magnetic techniques have been used for more than a century to study the microstructure of steels and their changes during the heat treatment by analysing their magnetic properties, which are a consequence of magnetic moments of electrons [42]. In the following, a brief introduction to the magnetic properties and magnetic phenomena as well as equations describing them, relevant for this thesis, are discussed.

### 2.2.1 Introduction

#### *Magnetic properties*

When a material is subjected to a magnetic field  $H$ , the response of the material is called magnetization  $M$ , which is described as the magnetic moment per unit volume of a solid [43]. The magnetic induction  $B$  is the sum of  $H$  and  $M$  via  $B = \mu_0 (H + M)$ , where  $\mu_0$  is the permeability in vacuum [43]. The effect of an applied magnetic field on the magnetic induction is shown in Figure 2.13. With applying a magnetic field  $H$  to a ferromagnetic material, initially un-magnetized, the magnetic induction  $B$  is increasing until above a certain field, where the magnetization is levelling off and becoming independent of  $H$  [42]. This is called saturation magnetization. If in the following  $H$  is decreased to zero, the magnetic induction does not reduce to zero, but to  $B_r$ , which is called remanence. The field that is required to reduce the magnetic induction to zero is called coercivity  $H_c$ . A further decrease of  $H$  leads to saturation in the reverse direction. A subsequent increase of  $H$  to zero causes a negative remanence in the material and with a further increase of  $H$  the magnetic induction will reach zero at a positive coercivity value, and furthermore  $M$  saturates again. This curve is called magnetic hysteresis loop. The phenomenon of a hysteresis curve describes that the material can retain its magnetization in absence of the magnetic field and is very important for technological applications such as permanent magnets. The permeability  $\mu$  of the material, which is a measure of the degree of magnetizability of a material, is equal to the slope of the initial magnetization curve. [42-45]

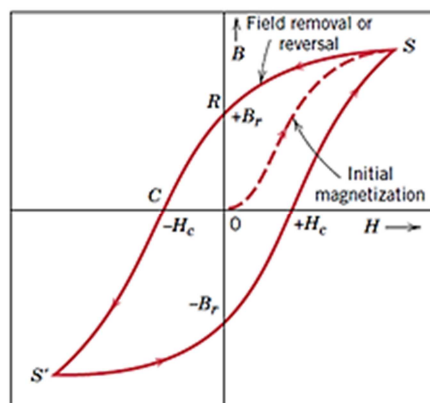


Figure 2.13 Magnetic induction  $B$  versus magnetic field strength  $H$  [42]. Coercivity  $H_c$  and remanence  $B_r$  are indicated.

Magnetic properties of materials can be divided into structure-sensitive and structure-insensitive [46]. Structure-sensitive properties are controlled through the materials processing, such as heat treatment or deformation, and are affected for instance by impurities, dislocations, texture and strain. The structure-sensitive magnetic properties are for instance the permeability, coercivity and remanence [46]. Structure-insensitive properties are for instance the saturation magnetization and the Curie temperature [44, 46, 47], which are largely dependent on the composition of the alloy [46, 47], but not on the structure.

### ***Ferromagnetism and paramagnetism***

Depending on their magnetic properties and behaviour, materials can be divided in several groups: ferromagnetic, ferrimagnetic, paramagnetic, antiferromagnetic, and diamagnetic [48]. Most important for this thesis are ferromagnetism and paramagnetism, which will be briefly described in the following.

*Ferromagnetic* materials can have a permanent magnetic moment in the absence of an external magnetic field and can possess very large and permanent magnetizations [42]. They have high relative permeabilities, which are not constant as a function of magnetic field [43]. The magnetization curve in Figure 2.13 is characteristic for ferromagnetic materials. Examples of ferromagnets are bcc-iron, cobalt and nickel [42], but also martensite is ferromagnetic. In Figure 2.14a a schematic illustration of magnetic dipoles alignment for a ferromagnetic material within one domain is shown [42]. A *domain* is a microscopic area of the material with the same orientation of the magnetic moments [49]. Domains are independent on the microstructure of the magnetized material. This means that adjacent domains only vary in the orientation of their magnetic moments [49]. In Figure 2.15 the initial magnetization curve of a ferromagnet is shown, indicating the different domain configurations. At a zero field the net-induction is zero and the material is non-magnetic, since the vector sum of the magnetic moments is zero [49]. With increasing magnetic field the magnetic moments of a domain align in the direction of the external field and cause an increase of the induction in the direction of the applied field. Domains with the same magnetic orientation as the external field expand at the expense of the non-favourably aligned domains. When the saturation magnetization is reached the magnetic structure has evolved into a single domain with the same orientation as the external field. This process is reversible when cycling through a hysteresis loop [49].

Ferromagnetic materials can be classified on the basis of their coercivity [43]. They are usually divided into soft-magnetic materials (easy to magnetize and demagnetize) and hard-magnetic materials (hard to magnetize and demagnetize) [44], where the hard-magnetic materials can store more magnetic energy, which is related to the second quadrant of the  $B$ - $H$ -curve [50]. A scheme of the hysteresis curves of soft- and hard-magnetic materials are shown in Figure 2.16.

Above a critical temperature, the Curie temperature  $T_C$  (770 °C for iron [45]), all ferromagnetic materials become *paramagnetic* due to the thermal energy annihilating the magnetic order of ferromagnetic materials [42]. Atoms in paramagnetic materials have net magnetic moments, which are only weakly coupled to each other and are randomly aligned (see Figure 2.14b). In the presence of an external magnetic field these moments align to a

very low degree for all practical field strengths [51]. The permeabilities of paramagnetic materials are independent on magnetic field strength and very low compared to ferromagnetic materials [45]. Since they only exhibit a very small magnetization in the presence of an external field, paramagnetic materials are considered to be non-magnetic [42]. Examples of paramagnetic materials are aluminium, oxygen and platinum [43]. Fcc-austenite is paramagnetic [44] above room temperature.

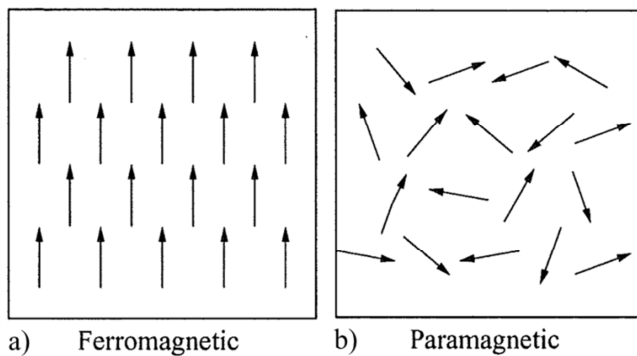


Figure 2.14 Scheme of the ordering of magnetic moments (schematically shown by the arrows) of ferro- and paramagnetic materials [51].

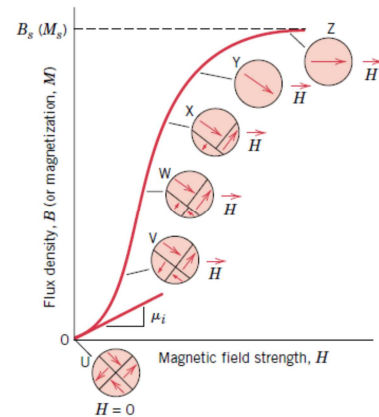


Figure 2.15 Initial magnetization curve of a ferromagnetic material with indicated domain configurations [42].

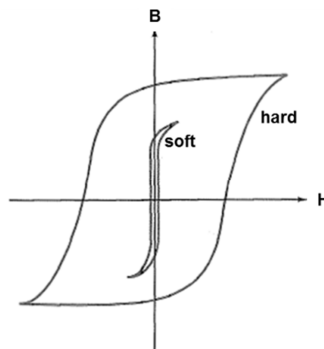


Figure 2.16 Comparison of characteristic magnetization curves of “soft-” and “hard-magnetic” materials [49].

### 2.2.2 Magnetic measurements for determination of austenite fraction

Magnetic techniques have been widely used for phase-transformation measurements on different stainless steels [52-54]; particularly saturation magnetization measurements have been widely used for *ex-situ* studies [55-58] and also sometimes for *in-situ* monitoring of the phase transformation [59-65]. In the present thesis, the saturation magnetization is the main parameter for *in-situ* analysing the formation and transformation of austenite. Therefore, the following sections discuss the saturation magnetization for analysing phase transformations.

### Saturation magnetization and microstructural analysis

The saturation magnetization,  $M_{sat}$ , is a structure-insensitive magnetic property. Hence, if a ferromagnet is magnetized in a high magnetic field to saturation, the influence of mechanical and magneto-mechanical properties on the magnetization, for instance internal stresses, is decreasing and  $M_{sat}$  depends only on the temperature, the chemical composition of the material [66] and the phases present [48]. In practice, a ferromagnet cannot be completely magnetized to saturation with experimental techniques [43, 66]. Nevertheless, the approach to saturation  $M_{sat}$  with increasing field can be described by [43, 44, 55]:

$$M = M_{sat} \left( 1 - \frac{a}{H} - \frac{b}{H^2} \right), \quad (2.1)$$

where  $a$  and  $b$  are constants, depending on different physical origins.  $a$  arises from nano-scale microstructural effects such as inclusions, voids, point defects and/or micro-stresses, and  $b$  from the crystal anisotropy [44, 55].

The magnetization is temperature dependent, as it turns from ferromagnetic to paramagnetic state when heating to the Curie temperature  $T_C$ . Above 0 K the thermal energy will cause the individual magnetic moments to precess about the field direction in low-level excited states [43]. This will lead to a saturation magnetization which is less than it would be at 0 K, where all the magnetic moments are completely aligned with the field, since there is no thermal energy for precession [43]. With increasing temperature the precession becomes greater, which causes the spontaneous magnetization to be smaller [43]. With reaching  $T_C$ , the spin coupling is overruled by the thermal energy [42], which causes the random alignment of the magnetic moments [43].

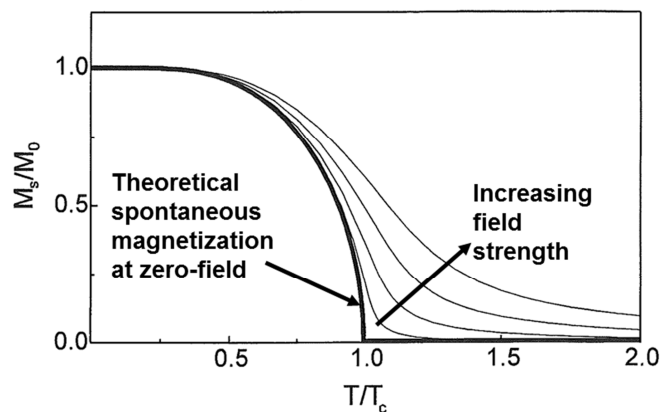


Figure 2.17 Dependence of magnetization from magnetic field (modified from [67]) of a material with a single ferromagnetic phase.  $M_s$  denotes the saturation magnetization and  $M_0$  the saturation magnetization at 0 K.

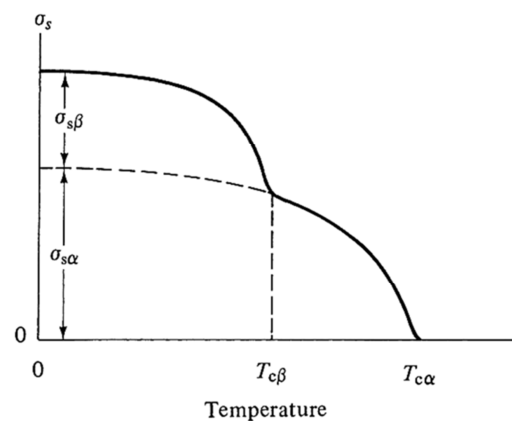


Figure 2.18 Saturation magnetization ( $= \sigma_s$ ) versus temperature in a material with two ferromagnetic phases  $\alpha$  and  $\beta$  [44].

The temperature dependence of the saturation magnetization of a material with a single ferromagnetic phase is shown in Figure 2.17. If no or a very low magnetic field is applied, the

determination of  $T_C$  is straightforward [48]. However, it can be seen that the curves become less steep in the transition area to  $T_C$  with increasing magnetic field, forming a so-called tail [45, 48]. A tail may also arise from local composition variations in the single-phase [48]. An approximate value of  $T_C$  can be obtained from the minimum of the first derivative  $dM/dT$  of the magnetization curve [48, 61].

The temperature dependence of the total saturation magnetization of a material is a linear superposition of the saturation magnetization of the single phases [48, 68], as can be seen in Figure 2.18. However, to differentiate between the single ferromagnetic phases either their Curie temperatures must be well below the temperature of rapid diffusion, or the solubility limits of each phase must not change with temperature [44]. Hence, if the composition of these phases change, the quantitative analysis of the magnetization curve should include these composition changes.

The temperature-dependent saturation magnetization of a ferromagnetic phase can be fitted for temperatures well below  $T_C$  by [45, 69, 70]:

$$M_{sat}(T) = M_{sat0} \left(1 - kT^{3/2}\right), \quad (2.2)$$

where  $M_{sat0}$  is the magnetization at 0 K (-273 °C) and  $k$  [in  $K^{-3/2}$ ] is a constant.

Arrott and Heinrich [69] described the saturation magnetization of pure iron in a 'zero'-field including the effect of  $T_C$  by the following equation:

$$M_{sat}(T) = M_{sat0} \frac{(1-s)^\beta}{1 - \beta s + As^{3/2} - Cs^{7/2}}, \quad (2.3)$$

with  $\beta$ ,  $A$  and  $C$  material dependent constants, and  $s = T/T_C$ .

In high magnetic fields, the magnetization as a function of the temperature can be described by the Weiss-theory [45]:

$$\frac{M_{sat}}{M_{sat0}} = \tanh \frac{(M_{sat}/M_{sat0}) + H/(NM_{sat0})}{T/T_C}, \quad (2.4)$$

where  $N$  is the molecular field constant [45].

### **Calculation of austenite fraction from saturation magnetization**

Since austenite is paramagnetic, the volume fraction of austenite,  $f_\gamma$ , measured by magnetization techniques, can be obtained by comparing the saturation magnetization of an austenite-containing sample,  $M_{sat(c)}$ , to the saturation magnetization of an austenite-free, entirely ferromagnetic, reference sample,  $M_{sat(ref)}$ , of the same composition. The fraction can then be calculated by [55, 68]

$$f_{\gamma} = 1 - \frac{M_{sat}(c)}{M_{sat}(ref)}. \quad (2.5)$$

However, this equation is only valid if the ferromagnetic phases have the same magnetization. As discussed before, if more phases are present in the material, the overall saturation magnetization can be described by the linear relation [48, 68]

$$M_{sat} = \sum_i f_i M_{sat,i}, \quad (2.6)$$

where  $f_i$  denotes the fraction of the individual phases  $i$  and  $M_{sat,i}$  denotes the saturation magnetization of the individual phases  $i$ .

Note that, since the saturation magnetization is temperature dependent, equations (2.5) and (2.6) are also dependent on temperature.

### 2.2.3 Saturation magnetization for steels depending on chemical composition

As already discussed in the previous sections the saturation magnetization  $M_{sat}$  is sensitive to the chemical composition of the ferromagnetic phases. Alloying elements may partition during thermal processing, which could not only influence the total  $M_{sat}$  of the sample, but also the intrinsic  $M_{sat}$  of the ferromagnetic phases. It is therefore important to know the intrinsic  $M_{sat}$  of each ferromagnetic phase, which can be obtained in the best case from the measurement of the magnetization of the steel in completely ferritic or martensitic state. However, this is not always possible and it is therefore desirable to be able to calculate  $M_{sat}$  for a ferromagnetic phase on the basis of its composition. The influence of certain elements on the total  $M_{sat}$  of iron alloys and steels was investigated [47, 71-75] and the most recent equation to calculate the saturation magnetization was proposed by Merinov et al. for ferrite ( $\delta$ ) [47, 74, 75]:

$$M_{sat} = \left[ \begin{array}{l} 2.16 - 0.0275x_{Cr} - 0.033x_{Ni} - 0.026x_{Mo} - 0.067x_{Ti} - 0.061x_{Si} \\ -0.063x_{Al} - 0.06x_V - 0.028x_{Mn} - 0.05x_{Nb} - 0.022x_W - 0.01x_{Cu} \\ -0.05x_P - 0.01(x_C + x_N) \end{array} \right] \times \frac{10^7}{4\pi} \times \frac{1}{\rho} \quad (2.7)$$

$$\pm \left( 0.03 \times \frac{10^7}{4\pi} \times \frac{1}{\rho} \right)$$

where  $x_i$  denotes the weight fraction of element  $i$  in wt.% and  $M_{sat}$  is in Am<sup>2</sup>/kg (magnetization per unit mass).  $\rho$  denotes the density of the material in kg/m<sup>3</sup>.

Equation (2.7) was obtained by multiple regressive analysis of a large data set using the design of experiment (DoE) method, where the effects of the elements are assumed to be additive and the magnetization of the ferrite phase decreases with the decrease of iron content [76]. However, the influence of the single elements on the saturation magnetization in equation (2.7) is assumed to be linear, which is regarded to be not true for the alloying elements Ni and Si [45]. Therefore, for the calculation of the saturation magnetization for

the composition of the 13Cr6Ni2Mo SMSS, analysed in this work, a different, rather simple, approach was used. From the influence of each single element X on the magnetization of pure iron, obtained by fitting curves of the saturation induction versus the composition of Fe-X alloys given in [45], an empirical equation for the room temperature magnetization as a function of chemical composition was obtained, where the non-linear influence of Ni and Si was considered. This equation reads:

$$M_{sat} = \left[ \begin{array}{c} 172 - 2.40x_{Cr} - 5.25x_{Mo} - 4.26x_{Al} - 1.49x_{Mn} \\ - 21.58x_C + z_{Ni} + z_{Si} + z_{Cu} \end{array} \right] \times \frac{10^4}{\rho} \pm \left( 2.4 \times \frac{10^4}{\rho} \right), \quad (2.8)$$

with:

$$z_{Ni} = -7 \times 10^{-5} (x_{Ni})^4 + 3 \times 10^{-3} (x_{Ni})^3 - 0.07 (x_{Ni})^2 + 0.53 x_{Ni}, \quad (2.9)$$

$$z_{Si} = -0.17 (x_{Si})^2 - 3.30 x_{Si}, \quad (2.10)$$

$$z_{Cu} = -5.27 x_{Cu} \text{ for } 0 \leq x_{Cu} \leq 1.6, \quad (2.11)$$

$$z_{Cu} = -1.53 x_{Cu} \text{ for } 1.6 \leq x_{Cu} \leq 39. \quad (2.12)$$

$x_i$  is in wt.%,  $M_{sat}$  in Am<sup>2</sup>/kg and  $\rho$  in kg/m<sup>3</sup>.

The density  $\rho$  of the material is obtained from the atomic weight and the volume of the bcc-unit cell as a function of the bulk composition of the material.  $\rho$  (in kg/m<sup>3</sup>) is calculated by [42]:

$$\rho = \frac{n \overline{A}_m}{V N_A} \times 10^{-3}, \quad (2.13)$$

with  $n$  the number of atoms contained in the unit cell,  $\overline{A}_m$  the mean atomic weight in g/mol,  $V$  the volume of the unit cell in m<sup>3</sup> and  $N_A$  the Avogadro number ( $6.022045 \times 10^{23}$  mol<sup>-1</sup> [77]).  $\overline{A}_m$  is obtained by:

$$\overline{A}_m = \sum_i A_{m,i} y_i, \quad (2.14)$$

with  $A_{m,i}$  the atomic weight of element  $i$  and  $y_i$  the atomic fraction of element  $i$ .

The volume of the bcc unit cell was obtained by  $V = a_{0\alpha}^3$ . For this, the room temperature lattice parameter of bcc-ferrite  $a_{0\alpha}$  (in Å) was calculated by [78]:

$$a_{0\alpha} = 2.8664 + (3a_{Fe}^2)^{-1} \times \left[ (a_{Fe} - 0.279y_C)^2 (a_{Fe} + 2.496y_C) - a_{Fe}^3 \right] - 0.03y_{Si} + 0.06y_{Mn} + 0.07y_{Ni} + 0.31y_{Mo} + 0.05y_{Cr} + 0.096y_V, \quad (2.15)$$

with  $y_i$  the atomic fraction of element  $i$  in ferrite and  $a_{Fe} = 2.8664$  Å [78].

Note that equation (2.8) does not take into account the interaction of different elements and should thus merely be understood as an approximation of the magnetization. Equation

(2.8) was obtained for the composition ranges (in wt.%): 0-22 Ni, 0-32 Cr, 0-5 Mo, 0-10 Si, 0-6 Mn, 0-39 Cu, 0-0.2 C, and 0-11 Al.

Table 2.2 lists the room temperature saturation magnetization of the ferritic or martensitic phase of different selected steels. The values are compared to the ones calculated by equations (2.7) and (2.8). As can be seen, the values from both the equations agree with the measured values within a reasonable range. Especially for the SMSS, the  $M_{sat}$ -values obtained by equation (2.8) agree well with the measured values.

Table 2.2 Room temperature  $M_{sat}$  values of fully ferromagnetic samples (in  $Am^2/kg$ ) of different steels from literature compared with values obtained by equations (2.7) and (2.8).

Material	$M_{sat}$ / Ref.	$M_{sat}$ -Merinov, eq. (2.7)	$M_{sat}$ eq. (2.8)
UNS S39205 duplex stainless steel	133.0 [79]	$135 \pm 3$	$138 \pm 3$
UNS S32750 super duplex stainless steel	128.0 [58]	$117 \pm 3$	$120 \pm 3$
AISI 301LN	157.1 [80]	$143 \pm 3$	$163 \pm 3$
12Cr6Ni2Mo SMSS +0.28Ti	171.3 [56]	$159 \pm 3$	$170 \pm 3$
13Cr6Ni2Mo SMSS	170.8 this work	$159 \pm 3$	$169 \pm 3$

## REFERENCES

- [1] G. Krauss: *Steels: Heat Treatment and Processing Principles*, pp. 351-99, ASM International, Materials Park, Ohio, 1990.
- [2] R.A. Lula: *Stainless Steel*, pp. 1-5, The American Society for Metals, Metals Park, Ohio, 1986.
- [3] K.H. Lo, C.H. Shek and J.K.L. Lai: *Mater. Sci. Eng. R*, 2009, vol. 65, no. 4-6, pp. 39-104.
- [4] J.C.M. Farrar: *The alloy tree: A guide to low-alloy steels, stainless steels and nickel-base alloys*, pp. 48-49, Woodhead Publishing Ltd., Cambridge, 2004.
- [5] J.J. Dufrane: in *Supermartensitic Stainless Steel '99*, KCI Publishing BV, Brussels, 1999, pp. 19-24.
- [6] P. Toussaint and J.J. Dufrane: in *Supermartensitic Stainless Steel 2002*, KCI Publishing BV, Brussels, 2002, pp. 23-8.
- [7] K. Kondo, M. Ueda, K. Ogawa, H. Amaya, H. Hirata, H. Takabe and Y. Miyazaki: in *Supermartensitic Stainless Steel '99*, KCI Publishing BV, Brussels, 1999, pp. 11-18.
- [8] C. Bell, *Private Communication*, 2010.
- [9] Y. Wei: *Microstructural Characterization and Mechanical Properties of Super 13% Cr Steel*, PhD Thesis, The University of Sheffield, England, 2005.

- [10] [http://www.stainless-steel-world.net/pdf/sswxx\\_supermartensitic\\_grades.pdf?resourceId=397](http://www.stainless-steel-world.net/pdf/sswxx_supermartensitic_grades.pdf?resourceId=397), 2015.
- [11] D. Ye, J. Li, Q.-L. Yong, J. Su, J.-M. Tao and K.-Y. Zhao: *Mater. Technol.*, 2012, vol. 27, no. 1, pp. 88-91.
- [12] D. Ye, J. Li, W. Jiang, J. Su and K. Zhao: *Mater. Des.*, 2012, vol. 41, pp. 16-22.
- [13] W. Jiang, D. Ye, J. Li, J. Su and K. Zhao: *Steel Res. Int.*, 2014, vol. 85, no. 7, pp. 1150-7.
- [14] H. van der Winden, P. Toussaint and L. Coudreuse: in *Supermartensitic Stainless Steel 2002*, KCI Publishing BV, Brussels, 2002, pp. 9-13.
- [15] C.A.D. Rodrigues, P.L.D. Lorenzo, A. Sokolowski, C.A. Barbosa and J.M.D.A. Rollo: *Mater. Sci. Eng. A*, 2007, vol. 460, pp. 149-52.
- [16] C.A.D. Rodrigues, P.L.D. Lorenzo, A. Sokolowski, C.A. Barbosa and J.M.D.A. Rollo: *J. ASTM Int.*, 2006, vol. 3, No. 5, pp. 1-5.
- [17] W. Seidel: *Werkstofftechnik: Werkstoffe - Eigenschaften - Prüfung - Anwendung*, 5th ed., pp. 106-8, Carl Hanser Verlag, München, 2001.
- [18] J. Hubackova, V. Cihal and K. Mazanec: *Z. Werkstofftech.*, 1984, vol. 15, pp. 411-5.
- [19] C. Gesnouin, A. Hazarabedian, P. Bruzzoni, J. Ovejero-García, P. Bilmes and C. Llorente: *Corros. Sci.*, 2004, vol. 46, no. 7, pp. 1633-47.
- [20] G. Rožnovská et al.: *The Effect of Heat Treatment on Microstructure and Properties of a 13Cr6Ni2.5Mo Supermartensitic Steel*, Sborník vědeckých Vysoké školy báňské – TU Ostrava, číslo 1, rok 2005, ročník XLVIII, řada hutnická článek č. 1241, pp. 225-31; from: <http://www.fmmi.vsb.cz/shared/uploadedfiles/fmmi/35Roz41-225.pdf>
- [21] Y.Y. Song, D.H. Ping, F.X. Yin, X.Y. Li and Y.Y. Li: *Mater. Sci. Eng. A*, 2010, vol. 527, no. 3, pp. 614-8.
- [22] X.P. Ma, L.J. Wang, C.M. Liu and S.V. Subramanian: *Mater. Sci. Eng. A*, 2012, vol. 539, pp. 271-9.
- [23] P. Wang, S. Lu, D. Li, X. Kang and Y. Li: *Acta Metall. Sinica*, 2008, vol. 44, no. 6, pp. 681-5.
- [24] R.W.K. Honeycombe and H.K.D.H. Bhadeshia: *Steels: Microstructure and Properties*, 3rd ed., pp. 95-128, Elsevier Ltd., Amsterdam, 2006.
- [25] D.N. Zou, Y. Han, W. Zhang and X.D. Fang: *J. Iron Steel Res. Int.*, 2010, vol. 17, no. 8, pp. 50-4.
- [26] P.D. Bilmes, M. Solari and C.L. Llorente: *Mater. Charact.*, 2001, vol. 46, no. 4, pp. 285-96.
- [27] T.G. Gooch, P. Woollin and A.G. Haynes: in *Supermartensitic Stainless Steel '99*, KCI Publishing BV, Brussels, 1999, pp. 188-95.
- [28] D.K. Xu, Y.C. Liu, Z.Q. Ma, H.J. Li and Z.S. Yan: *Int. J. Minerals, Metallurgy, Mater.*, 2014, vol. 21, no. 3, pp. 279-88.
- [29] Y. Song, X. Li, L. Rong and Y. Li: *Mater. Sci. Eng. A*, 2011, vol. 528, no. 12, pp. 4075-9.
- [30] Y.Y. Song, X.Y. Li, L.J. Rong, D.H. Ping, F.X. Yin and Y.Y. Li: *Mater. Lett.*, 2010, vol. 64, no. 13, pp. 1411-4.
- [31] Y.K. Lee, H.C. Shin, D.S. Leem, J.Y. Choi, W. Jin and C.S. Choi: *Mater. Sci. Technol.*, 2003, vol. 19, no. 3, pp. 393-8.

- [32] A.F. Padilha and P.R. Rios: *ISIJ Int.*, 2002, vol. 42, no. 4, pp. 325-37.
- [33] M. Kimura, Y. Miyata, T. Toyooka and Y. Kitahaba: *Corros.*, 2001, vol. 57, no. 5, pp. 433-9.
- [34] Y.R. Liu, D. Ye, Q.L. Yong, J. Su, K.Y. Zhao and W. Jiang: *J. Iron Steel Res. Int.*, 2011, vol. 18, no. 11, pp. 60-6.
- [35] N. Nakada, T. Tsuchiyama, S. Takaki and N. Miyano, *ISIJ Int.*, 2011, vol. 51, no. 2, pp. 299-304.
- [36] Y. He, K. Yang and W. Sha: *Metall. Mater. Trans. A*, 2005, vol. 36A, no. 9, pp. 2273-87.
- [37] R. Schnitzer, R. Radis, M. Nöhrer, M. Schober, R. Hochfellner, S. Zinner, E. Povoden-Karadeniz, E. Kozeschnik and H. Leitner: *Mater. Chem. Phys.*, 2010, vol. 122, no. 1, pp. 138-45.
- [38] B. Qin, Z.Y. Wang and Q.S. Sun: *Mater. Charact.*, 2008, vol. 59, no. 8, pp. 1096-100.
- [39] X.P. Ma, L.J. Wang, C.M. Liu and S.V. Subramanian: *Mater. Sci. Eng. A*, 2011, vol. 528, no. 22-23, pp. 6812-8.
- [40] K.G. Solheim, J.K. Solberg, J. Walmsley, F. Rosenqvist and T.H. Bjørnå: *Eng. Fail. Anal.*, 2013, vol. 34, pp. 140-9.
- [41] T. J. Mesquita, E. Chauveau, M. Mantel, N. Bouvier and D. Koschel: *Corros. Sci.*, 2014, vol. 81, pp. 152-61.
- [42] W.D. Callister, Jr.: *Fundamentals of Materials Science and Engineering: An integrated approach*, 2<sup>nd</sup> ed., p. 39, pp. 730-64, John Wiley & Sons, Inc., 2005.
- [43] D. Jiles: *Introduction to Magnetism and Magnetic Materials*, 2nd ed., pp. 44-6, p. 90, pp. 94-5, p. 119, Taylor & Francis Group, Boca Raton, 1998.
- [44] B.D. Cullity and C.D. Graham: *Introduction to Magnetic Materials*, 2nd ed., pp. 1-21, p. 115, p. 147, p. 149, pp. 325-6, p. 439, John Wiley & Sons, Inc., Hoboken, New Jersey, 2009.
- [45] R. M. Bozorth: *Ferromagnetism*, pp. 1-13, pp. 30-6, p. 54, p. 109, pp. 216-35, p. 368, pp. 716-9, John Wiley & Sons, Inc., Hoboken, NJ, 2003.
- [46] D.C. Jiles: *Acta Mater.*, 2003, vol. 51, no. 19, pp. 5907-39.
- [47] P.E. Merinov and A.G. Mazepa: *Industrial Laboratory (Diagn. Mater.)*, 1997, vol. 63, no. 3, pp. 149-53.
- [48] A.E. Berkowitz and E. Kneller (Eds.): *Magnetism and Metallurgy*, vol. 1, pp. 331-347, p. 415, Academic Press, Inc., New York, 1969.
- [49] J.F. Shackelford: *Werkstofftechnologie für Ingenieure: Grundlagen-Prozesse-Anwendungen*, 6th ed., p. 795, p. 802, p. 983, Pearson Studium, München, 2005.
- [50] R.C. O'Handley: *Modern Magnetic Materials: Principles and Application*, pp. 20-2, John Wiley & Sons, Inc., New York, 2000.
- [51] N.A. Spaldin: *Magnetic Materials: Fundamentals and Device Applications*, pp. 11-6, Cambridge University Press, Cambridge, 2003.
- [52] C. Lemoine, A. Fnidiki, J. Teillet, M. Hédin and F. Danoix: *Scr. Mater.*, 1998, vol. 39, no. 1, pp. 61-6.
- [53] K.H. Lo, J.K.L. Lai, C.H. Shek and D.J. Li: *Mater. Sci. Eng. A*, 2007, vol. 452-453, pp. 149-60.

- [54] A.M. Beese and D. Mohr: *Exp. Mech.*, 2011, vol. 51, no. 5, pp. 667-76.
- [55] L. Zhao, N.H. van Dijk, E. Brück, J. Sietsma and S. van der Zwaag: *Mater. Sci. Eng. A*, 2001, vol. 313, no. 1-2, pp. 145-52.
- [56] G.F. da Silva, S.S.M. Tavares, J.M. Pardal, M.R. Silva and H.F.G. Abreu: *J. Mater. Sci.*, 2011, vol. 46, no. 24, pp. 7737-44.
- [57] K. Mumtaz, S. Takahashi, J. Echigoya, Y. Kamada, L.F. Zhang, H. Kikuchi, K. Ara and M. Sato: *J. Mater. Sci.*, 2004, vol. 39, no. 6, pp. 1997-2010.
- [58] S.S.M. Tavares, J.M. Pardal, J.A. de Souza, J.M. Neto and M.R. da Silva: *J. Alloys Compd.*, 2006, vol. 416, no. 1-2, pp. 179-82.
- [59] S.S.M. Tavares, J.M. Neto and J.R. Teodosio: *J. Magn. Magn. Mater.*, 1998, vol. 182, no. 1-2, pp. 193-8.
- [60] S.S.M. Tavares, D. Fruchart and S. Miraglia: *J. Alloys Compd.*, 2000, vol. 307, pp. 311-7.
- [61] S.S.M. Tavares, R.F. de Noronha, M. R. da Silva, J.M. Neto and S. Pairis: *Mater. Res.*, 2001, vol. 4, no. 4, pp. 237-40.
- [62] N. Luzginova, L. Zhao and J. Sietsma: *Mater. Sci. Eng. A*, 2007, vol. 448, no. 1-2, pp. 104-10.
- [63] S.S.M. Tavares, S.R. Mello, A.M. Gomes, J.M. Neto, M.R. da Silva and J. M. Pardal: *J. Mater. Sci.*, 2006, vol. 41, no. 15, pp. 4732-6.
- [64] M. Amirthalingam, M.J.M. Hermans, L. Zhao and I.M. Richardson: *Metall. Mater. Trans. A*, 2010, vol. 41A, no. 2, pp. 431-9.
- [65] D. San Martin, N.H. van Dijk, E. Jiménez-Melero, E. Kampert, U. Zeitler and S. van der Zwaag: *Mater. Sci. Eng. A*, vol. 527, no. 20, pp. 5241-5.
- [66] A.E. Berkowitz and E. Kneller (Eds.): *Magnetism and Metallurgy*, vol. 2, pp. 689-90, Academic Press, Inc., New York, 1969.
- [67] G. Bertotti: *Hysteresis in Magnetism: For physicists, Materials Scientists, and Engineers*, p. 137, Academic Press, Inc., San Diego, California, 1998.
- [68] J. Crangle and W. Sucksmith: *J. Iron Steel Inst.*, 1951, vol. 168, pp. 141-51.
- [69] A.S. Arrott and B. Heinrich: *J. Appl. Phys.*, 1981, vol. 52, no. 3, pp. 2113-5.
- [70] L. Zhao, F.J. Vermolen, J. Sietsma and S. van der Zwaag: *J. Mater. Sci. Technol.*, 2003, vol. 19, pp. 105-8.
- [71] W. Steinhaus, A. Kußmann and E. Schoen: *Physikalische Zeitschrift*, 1937, vol. 38, no. 20, pp. 777-85.
- [72] J.W. Elmer and T.W. Eagar: *Weld. J.*, 1990, vol. 69, no. 4, pp. 141-50.
- [73] G.C. Curtis and J. Sherwin: *Br. J. Appl. Phys.*, 1961, vol. 12, pp. 344-5.
- [74] P. E. Merinov, et al.: *Weld. Prod.*, 1977, vol. 24, no. 3, pp. 49-51.
- [75] P. Merinov, S. Entin, B. Beketov and A. Runov: *NDT Int.*, vol. 11, no. 1, pp. 9-14, 1978.
- [76] P.E. Merinov, A.E. Korneev and N.S. Tsikunov: *Metal Sci. Heat Treatment*, 2006, vol. 48, no. 7-8, pp. 328-34.
- [77] *Smithells Metals Reference Book*, W.F. Gale and T.C. Totemeier (Eds.), 8 ed., chapter 3, Elsevier Butterworth-Heinemann, Amsterdam, 2004.

- [78] H.K.D.H. Bhadeshia, S.A. David, J.M. Vitek and R.W. Reed: *Mater. Sci. Technol.*, 1991, vol. 7, no. 8, pp. 686-98.
- [79] S.S.M. Tavares, P.D.S. Pedrosa, J.R. Teodósio, M.R. da Silva, J.M. Neto and S. Pairis: *J. Alloys Compd.*, 2003, vol. 351, no. 1-2, pp. 283-8.
- [80] S.S.M. Tavares, J.M. Neto, M.R. da Silva, I.F. Vasconcelos and H.F.G. de Abreu: *Mater. Charact.*, 2008, vol. 59, no. 7, pp. 901-4.



# 3

## Materials and experimental techniques

Throughout the thesis, various experimental techniques to study the formation and stability of retained austenite were applied. Two steel grades were investigated in this thesis, a supermartensitic stainless steel (chapters 4 to 7) and two Fe-C-Mn-Si steels (chapter 8). The experimental techniques applied include thermo-magnetic measurements as the main analysing tool, dilatometry, X-ray diffraction analysis, optical as well as scanning electron microscopy. Equilibrium phase analysis was performed with a software for thermodynamic calculations. In this chapter, the materials and the experimental techniques used are described. Furthermore, a brief description of the calculation of the austenite fraction from magnetic, dilatometry and X-ray diffraction measurements are given.

### 3.1 Materials

#### 3.1.1 Supermartensitic stainless steel

In this thesis a 13Cr6Ni2Mo supermartensitic stainless steel (SMSS) (X2CrNiMoV13-5-2), provided by Tata Steel Speciality Steels, was investigated. Samples were taken from two casts with minor differences in composition, which are given in Table 3.1. Steelmaking is carried out by the electric arc furnace and the secondary steelmaking method, followed by casting into ingots. The ingots were hot rolled followed by slow cooling to prevent cracking. The as-received material was supplied in the hardened, tempered and stress relieved condition. A typical heat treatment is 2 h at 950 °C, 4 h at 635 °C and 2 h at 550 °C. The microstructure of an as-received sample is shown in Figure 3.1, consisting of martensite, finely dispersed retained austenite and a very small fraction of carbides, nitrides and carbonitrides [1].

*Table 3.1 Chemical composition of the 13Cr6Ni2Mo SMSS (in wt.%), balance Fe.*

Cast	Cast no.	C	Cr	Ni	Mo	Mn	Si	V	Ti	N
# 1	A4319	0.015	12.34	5.66	2.02	0.42	0.22	0.18	0.01	0.013
# 2	A4508	0.020	12.27	5.62	2.01	0.42	0.21	0.18	0.01	0.016

P is 0.015 max., S is 0.003 max., Cu is 0.20 max.

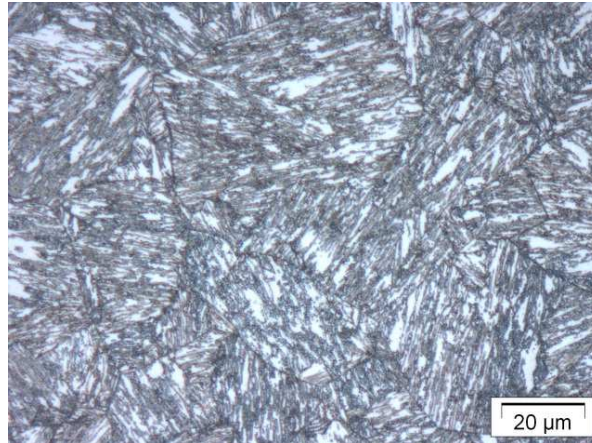


*Figure 3.1 Optical micrograph of the as-received 13Cr6Ni2Mo SMSS. Martensitic microstructure with finely dispersed retained austenite (etchant: Lichtenegger-Blöch).*

### 3.1.2 Fe-C-Mn-Si steels

Two Fe-C-Mn-Si steels, provided by Tata Steel RD&T IJmuiden, with main differences in C-concentrations, were investigated in this thesis. The as-received materials were produced using a laboratory vacuum induction furnace and were hot rolled after casting to a final thickness of 4.5 mm [2]. The chemical compositions of these steels are listed in Table 3.2 and the microstructures of the as-received materials are shown in Figure 3.2. Both as-received materials consist of a mixture of austenite, martensite, (ferritic-)bainite and carbides.

*Table 3.2 Chemical composition of the analysed Fe-C-Mn-Si steels (in wt.%), balance Fe.*

Steel name	C	Mn	Si	Mo	Al	P
0.6C <sup>1</sup>	0.57	3.54	1.480	-	0.030	-
0.2C <sup>2</sup>	0.20	3.51	1.523	0.247	0.040	0.005

<sup>1</sup> Internal code: QP1

<sup>2</sup> Internal code: QPF

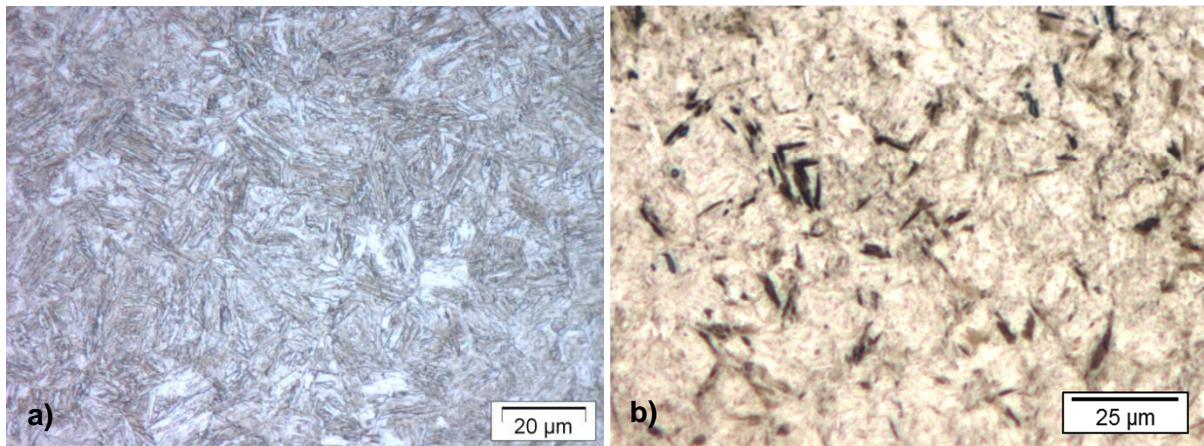


Figure 3.2 Optical micrographs of the as-received Fe-C-Mn-Si steels. a) 0.2C-steel, b) 0.6C-steel (etchant: 2 % nital).

## 3.2 Thermo-magnetic measurements

### 3.2.1 Vibrating sample magnetometer

Magnetic measurements at room temperature and thermo-magnetic measurements were performed in a Lake Shore 7307 Vibrating Sample Magnetometer (VSM) equipped with a high temperature furnace (model 73034) and a 340 Temperature Controller (see Figure 3.3).

A schematic drawing of a VSM is shown in Figure 3.4. The sample is placed in a constant magnetic field between the two electromagnets (field coils) and is then sinusoidally vibrated perpendicular to the magnetic field. This will induce a voltage in the detection coils (pick-up coils). The vibration route is indicated by the red arrow and the magnetic field direction by the blue arrow in Figure 3.4. The magnetization of the sample can be deduced from the measured signal. Synchronously, a stationary reference (permanent magnet) is driven with the sample, inducing a voltage in the reference coils, which is proportional to the magnetic moment of the analysed sample. Phase and amplitude of both measured voltages are directly related. This enables the measurements to be made insensitive to the amplitude and frequency of the vibration, small magnetic field instabilities, non-uniformities of the magnetic field, amplifier gain or amplifier linearity [3, 4]. More details about the VSM can be found in the literature [3-5].

Figure 3.5 shows a schematic drawing of the sample assembly in the furnace. For the in-situ heat treatments helium gas is used to establish an inert environment in the furnace chamber in order to avoid oxidation at higher temperatures. Between the furnace walls, a vacuum of about  $2 \times 10^{-4}$  mPa is realized to prevent heat losses to the surrounding environment. The temperature of the sample is not measured directly on the sample, but at the heating coils (further referred to as heater or furnace temperature,  $T_F$ ). The approximate position of the thermocouple is indicated in Figure 3.5. It is therefore expected that the sample temperature ( $T_S$ ) will lag the heater temperature when heating or cooling at high rates [6]. A correction method to obtain the sample temperature was applied, which is described in section 3.2.3. In this study, all the temperatures corresponding to the thermo-magnetic

measurements are the corrected temperature values, i.e. only the sample temperatures are given without further notice.



Figure 3.3 Lake Shore 7307 Vibrating Sample Magnetometer with room temperature set-up.

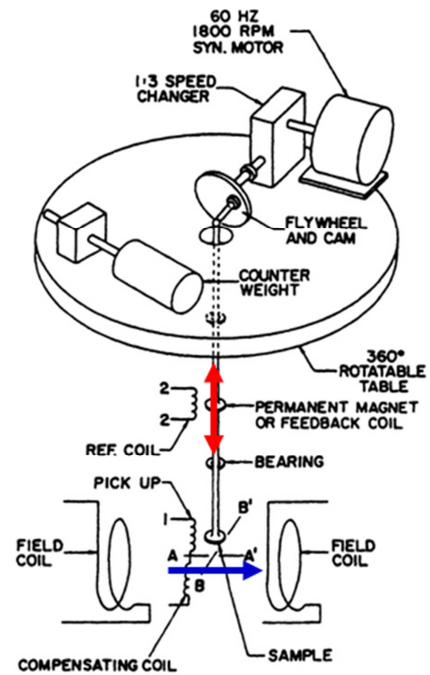


Figure 3.4 Schematic drawing of a VSM, modified from [5]. The red arrow indicates the direction of vibration and the blue arrow the direction of the magnetic field.

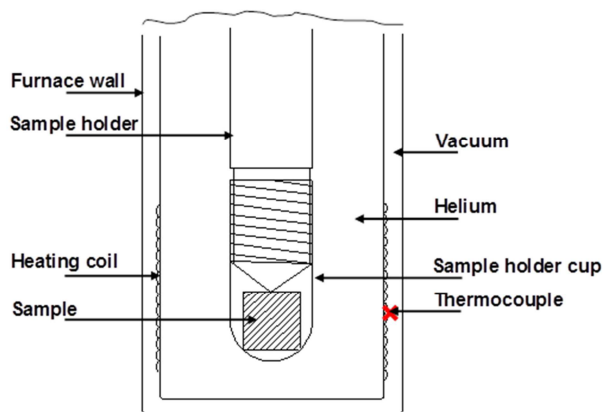


Figure 3.5 Schematic drawing (not true to scale) of the sample assembly in the VSM furnace. The approximate position of the thermocouple is indicated.

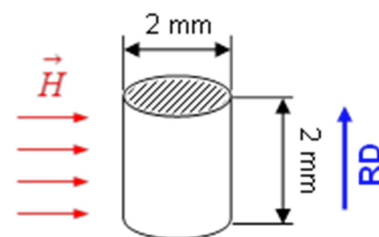


Figure 3.6 Drawing of the specimen for VSM tests with indication of positioning in the magnetic field,  $H$ . The hashed area denotes the area analysed by microscopy (perpendicular to rolling direction RD).

For the magnetic experiments, cylindrical samples were prepared by electro-discharging machine (EDM) cutting and finally ground with a grit size of 500  $\mu\text{m}$  to minimize the influence of an oxide layer, which forms during EDM-cutting. The sample dimension was 2 mm in length, with a diameter of 2 mm. A drawing of the sample is given in Figure 3.6. When the samples were placed in the sample holder of the VSM, care was taken that the longitudinal axis (parallel to rolling direction) of the samples was later placed perpendicular to the magnetic field, as indicated in Figure 3.6.

Prior to experiments, the VSM is calibrated with a standard Nickel specimen (SRM<sup>®</sup> 772a from NIST) for the moment gain and moment offset according to the procedures described in the VSM software manual by Lake Shore Cryotronics, Inc. [7]. During the moment gain calibration, the saddle points for the standard sample in the constant magnetic field are determined in the  $x$ -,  $y$ - and  $z$ -directions at a field of 0.5 T and a moment gain calibration constant is obtained. With this constant the measured voltage is converted into the magnetization value. The moment offset calibration is done with the empty sample holder vibrating in a zero field, where a zero calibration algorithm is carried out and the offsets for all moment ranges are measured and stored [6, 7].

The accuracy of the magnetization measurement does not only depend on the calibration of the system, but also on the geometry of the analysed sample and its relative position in the magnetic field. Any influence of the sample shape is minimized in the present work by using cylindrical samples, which are always placed alike in the magnetic field (see Figure 3.6). The uncertainty of the magnetization measurement at room temperature was estimated to be  $\pm 0.6 \text{ Am}^2/\text{kg}$ . With increasing temperature sample expansion can influence the measured magnetization. However, since the size of the sample is small, the effect of the sample expansion can be neglected compared to the influence of the moment offset drift, which was observed during a series of room temperature measurements and during the thermo-magnetic measurements. The moment offset drift and its correction is addressed in section 3.2.3. All magnetization values given in this study are the corrected values, unless indicated otherwise.

### 3.2.2 Magnetic measurements

Room temperature magnetization curves were measured by stepwise changing the applied magnetic field from 1.6 T to -1.6 T with a step size of 0.1 T. In the present work, the measured magnetization is expressed as the mass magnetization. An example of a room temperature magnetization curve is shown in Figure 3.7 for the as-received 13Cr6Ni2Mo SMSS.

Throughout the thermo-magnetic experiments, the magnetization of the samples was measured in a constant magnetic field of 1.5 T, where the magnetization is close to its saturation value, as indicated in Figure 3.7.

To ensure a homogeneous heating of the samples in the VSM furnace the thermo-magnetic experiments were performed with a low nominal heating rate of 3 or 5 K/min. The cooling was performed in the furnace of the magnetometer, by switching off the heating, where the temperature approximately follows an exponential relation:

$$T = (T_0 - T_E) \cdot \exp\left[-(t - t_0)/\tau\right] + T_E. \quad (3.1)$$

$T_0$  denotes the temperature before cooling,  $T_E$  the temperature after cooling and  $\tau$  a time constant.  $t$  and  $t_0$  denote the time and the initial time for the cooling step, respectively.

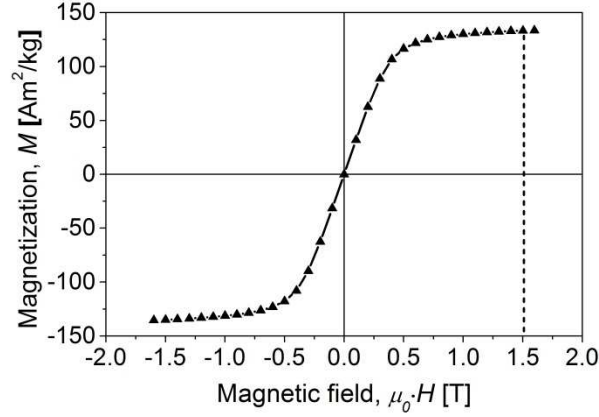


Figure 3.7 Room temperature curve of magnetization  $M$  versus the magnetic field ( $\mu_0 \cdot H$ ) for the as-received 13Cr6Ni2Mo SMSS. The dashed line indicates the magnetic field of 1.5 T at which the magnetization was measured during the thermo-magnetic experiments.

If austenite is the only paramagnetic phase present in the microstructure, the temperature dependent volume fraction of austenite,  $f_\gamma$ , was determined using [8, 9]:

$$f_\gamma = 1 - \frac{M_{sat}(c)}{M_{sat}(ref)}, \quad (3.2)$$

where  $M_{sat}(c)$  denotes the measured saturation magnetization of the austenite containing sample and  $M_{sat}(ref)$  the saturation magnetization of an austenite-free reference sample of the same composition, both measured at a magnetic field of 1.5 T.

For consistency, the magnetization from the room temperature curve measured at 1.5 T was used for the calculation of the austenite fraction at room temperature.

### 3.2.3 Correction of systematic errors of the Vibrating Sample Magnetometer

Errors are inherent to any experimental setup and can be classified as random and systematic errors. Random errors will always exist and may be established by repeating the experiments. Systematic errors are, in the simplest case, constant throughout an experiment series. They can be caused by an inaccurate apparatus or operational inconsistency. Since they are mostly concealed, systematic errors bear the highest risk of being missed. Therefore, they need to be discovered and eliminated. However, there is no general rule for the correction of systematic errors and an individual solution needs to be established. [10]

For the VSM 7300 system, used for the magnetic experiments in the present work, systematic errors were observed in the moment offset and the temperature measurement. In the following section these errors are described together with the applied correction method.

### Moment offset drift and correction

As mentioned in section 3.2.1, a moment gain and offset calibration is carried out before the magnetic experiments. However, a drift of the offset was observed during a set of experiments carried out at room temperature and also during the high temperature experiments. In general, this offset drift could be to the positive or negative direction of the magnetic moment, but was in this study only observed to be negative. In Figure 3.8 an enlargement of a room temperature magnetization curve, measured from +1.6 T to -1.6 T, versus the applied magnetic field with an offset in the magnetic moment is shown. The offset implies a shift of the values on the y-axis. Therefore, a correction can be done by simply adding the value of the offset to each point of the curve, without losing accuracy of the measurement itself.

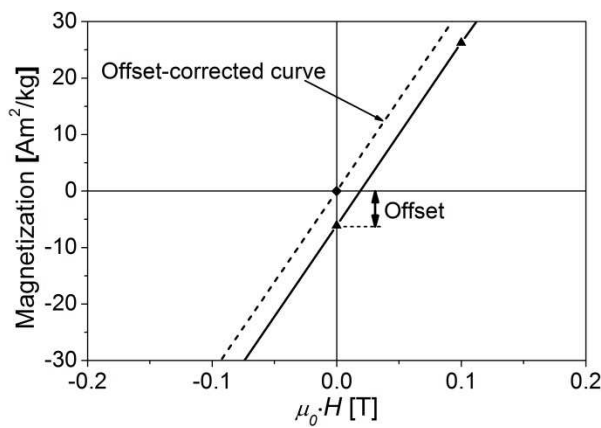


Figure 3.8 Room temperature magnetization versus applied magnetic field, showing an offset in the moment together with the respective offset-corrected curve.

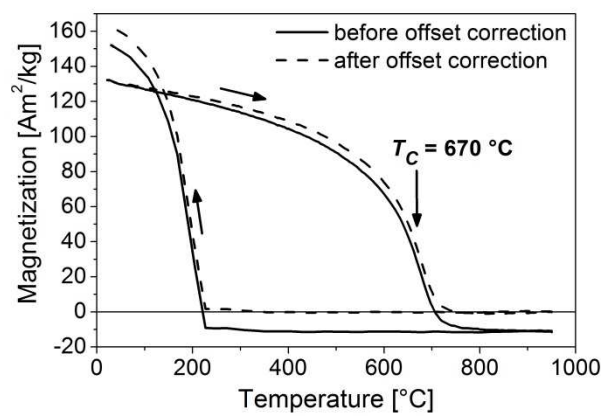


Figure 3.9 Magnetization versus temperature of an as-received 13Cr6Ni2Mo SMSS sample during heating to 950 °C and cooling. Heating and cooling are indicated by arrows. The Curie temperature,  $T_C$ , is indicated.

It was observed that the negative offset is increasing with experiment duration and increasing temperature of the furnace. The reason for this shift is not fully understood, but it could be due to friction in the system and hence a temperature rise in the system. Figure 3.9 shows the magnetization curve, measured at 1.5 T, of a 13Cr6Ni2Mo SMSS as-received sample heated to 950 °C at a rate of 5 K/min, followed by 30 min holding and subsequent cooling in the furnace. The Curie temperature ( $T_C$ ) for this material, obtained from the minimum of the first derivative  $dM/dT$  of the measured magnetization curve during heating [11, 12], was determined to be 670 °C and the magnetization should thus level off to zero with increasing temperature. Instead, the magnetization is levelling off at -10 Am<sup>2</sup>/kg.

While the maximum negative offset is observable from the experiments carried out above the  $T_C$ -temperature, it is, however, not obvious from experiments carried out at lower temperatures. For analysing how the offset is changing with temperature and for later correction of this systematic error, various experiments without a sample were performed with the same temperature profile as carried out with the samples. Since these experiments

were carried out without a sample, the measured magnetization unit was  $\text{Am}^2$ . To obtain the magnetization in  $\text{Am}^2/\text{kg}$ , the magnetization measured without a sample (in  $\text{Am}^2$ ) was normalized by an assumed weight of  $4.9 \times 10^{-5} \text{ kg}$ , a value in the weight range of the analysed samples. Figure 3.10 shows the results for three empty sample holder experiments during tempering at  $640^\circ\text{C}$ , carried out for the 13Cr6Ni2Mo SMSS. With increasing temperature during heating the apparent magnetization of the empty sample holder is decreasing as well as during the 4 h of holding at  $640^\circ\text{C}$ . During cooling the magnetization slightly increases, resulting in a lower offset than at the end of the holding step. While the progress of the magnetization during holding and cooling are similar for the three experiments, it is not the same during heating and hence the magnitude of the magnetization change is different. However, the offset obtained after the cooling at around  $30^\circ\text{C}$  was always similar to the magnitude of the offset obtained by a room temperature curve, which was performed immediately after the cooling step. Furthermore, a relation of the offset obtained from the room temperature curve after the cooling and the progress of the offset was obtained and is described in the following.

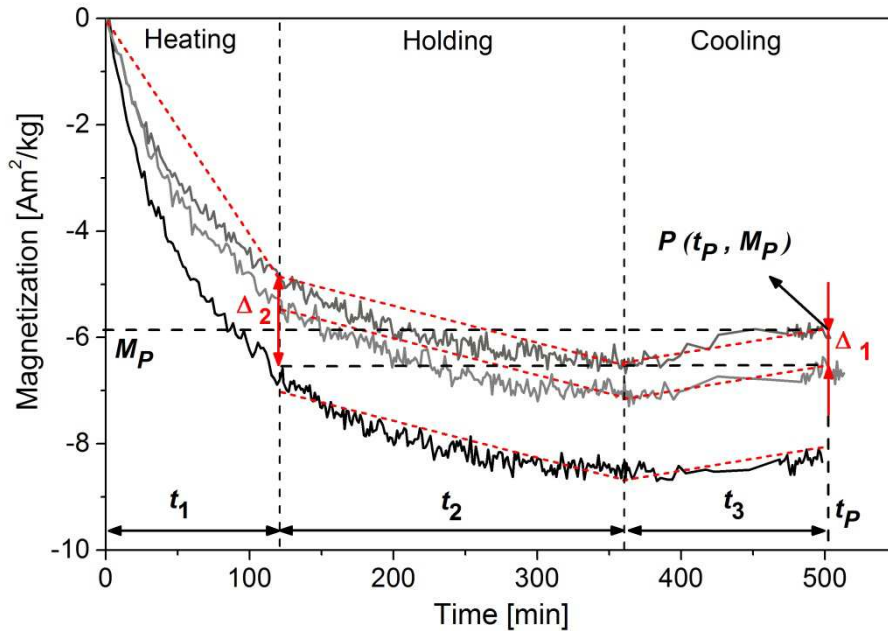


Figure 3.10 Magnetization of the empty sample holder versus temperature for three experiments when tempering at  $640^\circ\text{C}$ .  $t$  denotes time,  $M_P$  and  $t_P$  are magnetization and time at point  $P$ .  $\Delta_1$  and  $\Delta_2$  indicate differences in magnetization.

For correcting the systematic error caused by the offset change, the curves with the empty sample holder are divided into three sections: heating, holding and cooling (see Figure 3.10). The three sections can be fitted using the following linear equations, which are based on the knowledge of the offset right after the cooling (point  $P(t_P, M_P)$  in Figure 3.10), the difference of the magnetization  $M$  between start and end of the cooling,  $\Delta_1$ , and between start and end of the holding,  $\Delta_2$ :

$$\text{Heating: } M = \frac{M_P + \Delta_2 - \Delta_1}{t_1} \cdot t \quad (3.3)$$

$$\text{Holding: } M = -\frac{\Delta_2}{t_2} \cdot t + M_P - \Delta_1 + \frac{\Delta_2}{t_2} \cdot (t_P - t_3) \quad (3.4)$$

$$\text{Cooling: } M = \frac{\Delta_1}{t_3} \cdot t + M_P - \frac{\Delta_1}{t_3} \cdot t_P \quad (3.5)$$

$t$  denotes time and  $t_1, t_2, t_3$  are the durations of the heating, holding and cooling respectively. Table 3.3 gives the values of the parameters  $\Delta_1$  and  $\Delta_2$  for the different tempering treatments carried out with the 13Cr6Ni2Mo SMSS in the furnace of the VSM (details of the tempering experiments are given in chapter 6). The values of both  $\Delta_1$  and  $\Delta_2$  are an approximation from several tempering treatments.  $\Delta_1$  and  $\Delta_2$  for the offset correction of experiments heated to temperatures well above  $T_C$  were obtained from the measured magnetization values, since the maximum offset could be directly obtained from the results, as can be seen in Figure 3.9. By applying this approach, the systematic error, caused by the offset drift, can be corrected by adding  $M$ , obtained through equations (3.3) to (3.5), to the measured magnetization as shown for the example in Figure 3.9 by the dashed curves. The uncertainty of the magnetization obtained through this correction method is estimated to be  $\pm 0.6 \text{ Am}^2/\text{kg}$  for the heating,  $\pm 0.3 \text{ Am}^2/\text{kg}$  for the holding and  $\pm 0.2 \text{ Am}^2/\text{kg}$  for the cooling. Repeated measurements of samples at room temperature indicate an uncertainty of  $\pm 0.6 \text{ Am}^2/\text{kg}$  and at high temperatures  $\pm 1.2 \text{ Am}^2/\text{kg}$ , where the temperature-dependent systematic errors of the instrument were taken into account.

Table 3.3 Parameters  $\Delta_1$  and  $\Delta_2$  (in  $\text{Am}^2/\text{kg}$ ) used in equations (3.3) to (3.5) for correction of the moment offset for the tempering experiments with the 13Cr6Ni2Mo SMSS below  $T_C$ .

	1 <sup>st</sup> temper	2 <sup>nd</sup> temper
$\Delta_1$	0.4	0.4
$\Delta_2$	1.9	1.1

From equation (3.2) it becomes apparent that the accuracy of the austenite fraction not only depends on the accuracy of the magnetization measurement, but also on the reference sample. The estimated uncertainty of the calculated austenite fraction from the measured magnetization of the 13Cr6Ni2Mo SMSS, including the influence of the reference sample and variations in calibration, is  $\pm 0.5 \text{ vol.}\%$  at room temperature. At high temperatures the estimated uncertainty can be up to  $\pm 1.5 \text{ vol.}\%$ , taking the influence of the moment offset correction into account.

### Temperature lag and correction

As mentioned in section 3.2.1 the internal thermocouple only monitors the heater (furnace) temperature ( $T_F$ ) and changes in the sample temperature ( $T_S$ ) might lag the heater temperature. This lag depends on the heating rate and it is therefore recommended by the manufacturer to heat up slowly [6]. The heater temperature also depends on the settings of the proportional-integral-derivative (PID) controller. However, all the experiments carried out in the furnace of the magnetometer were performed with the default PID-settings. To get information about  $T_S$  during the performed experiments the temperature was measured at the position where the samples are placed in the furnace. For this purpose, a K-type thermocouple was fixed between small austenitic stainless steel (316L) samples, placed in the sample holder cup, to assure that the thermocouple was placed in the centre of the sample holder cup. Austenitic stainless steel was chosen to avoid any transformation heat influencing the temperature measurements. The total volume of these samples were approximately the same as the analysed samples for the magnetic experiments. A series of heating experiments were performed at different heating rates (between 3 and 7 K/min) and different target temperatures. Figure 3.11 shows the evolution of the measured sample temperature versus the heater temperature, where the temperature lag measured for the different heating rates were similar. It can be seen that the temperature difference is biggest in the beginning and decreases with reaching the target temperature. However, when reaching the target temperature,  $T_S$  still lags  $T_F$  for temperatures below 800 °C, independent from the holding time. The evolution of the temperature lag of the sample versus  $T_F$  during cooling is shown in Figure 3.12 for start temperatures between 600 and 950 °C. From these measurements a temperature correction fit was obtained for heating rates from 3 to 7 K/min and for the cooling, with which the data of  $T_F$  were corrected to obtain  $T_S$ . Without further notice, all temperature data given for the thermo-magnetic experiments in this work are the corrected sample temperature data,  $T_S$ . The uncertainty of the temperature measurement for the thermo-magnetic experiments lies within  $\pm 2.5$  °C, the precision of the thermo-couple used for the measurement of  $T_S$ .

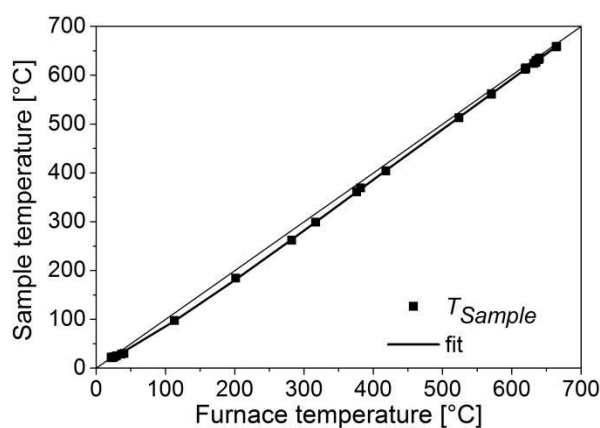


Figure 3.11 Temperature, measured at the position of the samples in the VSM furnace, versus furnace temperature during heating at rates between 3 to 7 K/min.

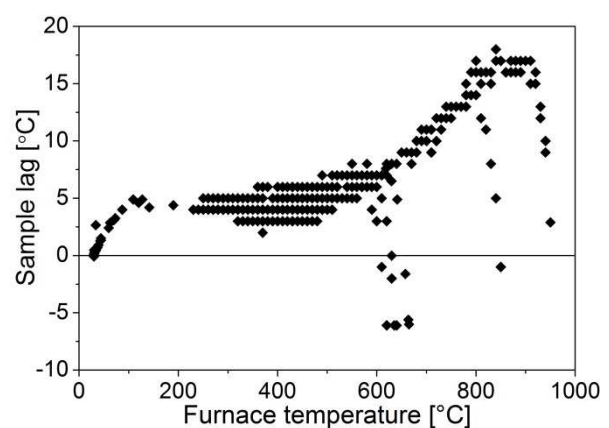


Figure 3.12 Lag of the temperature, measured at the position of the samples in the furnace of the VSM, versus furnace temperature during cooling from different temperatures.

### 3.3 Dilatometry

A Bähr 805 A/D dilatometer was used to perform several heat treatment experiments where the change in length of cylindrical specimens was measured. During phase transformations, the lattice structure of the material is changing, which is accompanied by a change in specific volume [13]. Changes in the phase fractions can then be obtained from the measured length changes. Cylindrical samples were prepared by EDM with a dimension of  $\varnothing$  5 mm x 10 mm for the SMSS and  $\varnothing$  4 mm x 10 mm for the Fe-C-Mn-Si steels, with the longitudinal axis parallel to the rolling direction. The samples were placed in the dilatometer between two quartz rods. The sample temperature was measured with an S-type thermocouple ( $\pm 2.5$  °C precision) spot-welded on to the centre of the sample surface. The samples were heated by induction and protected against oxidation by a vacuum of about  $2 \times 10^{-4}$  mPa. The austenite fraction was calculated from the length change measurements using the lever rule [13]:

$$f_{\gamma} = \frac{\Delta L_1}{\Delta L_{tot}}, \quad (3.6)$$

where  $\Delta L_1$  is the difference between the measured length change of the sample and the extrapolated length change of the transformed phase at a certain temperature.  $\Delta L_{tot}$  is the total length change between the extrapolated length changes of the phase transformed and that of austenite for the same temperature, as shown in Figure 3.13 for an as-received SMSS sample during heating.

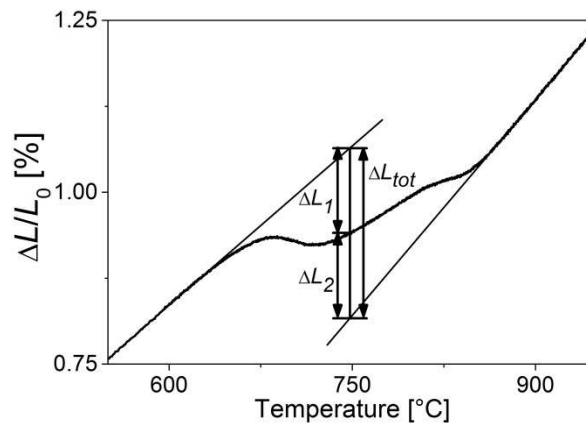


Figure 3.13 Example of a dilatation curve of an as-received 13Cr6Ni2Mo SMSS sample during heating. The parameters for determining the transformed fraction from the dilatation by the lever rule are indicated.  $\Delta L/\Delta L_0$  is the length change normalized by the initial sample length.  $\Delta L_1$  denotes the difference between the measured length change and the extrapolated length change of the transformed phases,  $\Delta L_2$  the difference between the measured length change and the extrapolated length change of austenite and  $\Delta L_{tot}$  the total length change, all at a specific temperature.

Lever rule analysis relies on the assumption that lattice spacing depends on temperature only. The influence of the specific volume of different phases is neglected in the lever rule, which can cause errors in the obtained phase fraction if more than one phase is present in

the material [13]. Furthermore, possible errors of the transformed phase fraction obtained by the lever rule can arise from the microstructure of the sample, since the lever rule does not account for the carbon enrichment in austenite, which has a strong influence on the lattice parameter and hence on its specific volume [13]. Moreover, uncertainties in the obtained phase fraction using the dilatometer can arise from the influence of the texture in the material, where a banded structure can show distinct differences in the dilatation depending on the rolling direction [13].

The accuracy of the dilatation measurement was about  $\pm 0.3 \mu\text{m}$ . In the present study, phase fractions were calculated by the lever rule for the SMSS samples, where the estimated uncertainty is  $\pm 3 \text{ vol.}\%$ . The redistribution of alloying elements during heat treatment could increase the uncertainty of the austenite fraction in this study to approximately  $\pm 6 \text{ vol.}\%$ .

### 3.4 X-ray diffraction analysis

X-ray diffraction (XRD) measurements were carried out at room temperature and in-situ at high temperatures. The surface of the samples was metallographically prepared with a final polishing step using  $1 \mu\text{m}$  diamond paste.

For XRD measurements at room temperature, a Bruker-AXS D8 Advanced  $\theta$ - $2\theta$  diffractometer equipped with a Bruker-AXS Vantec1 position sensitive detector (PSD) was used with  $\text{CoK}\alpha$ -radiation.

In-situ high temperature XRD (HT-XRD) measurements were carried out in a Bruker-AXS D5005  $\theta$ - $\theta$  diffractometer with a Bruker-AXS MRI high-temperature chamber with  $\text{CuK}\alpha$ -radiation. A diffracted-beam graphite monochromator was positioned in front of the scintillation counter. The sample with a size of  $10 \text{ mm} \times 5 \text{ mm}$  and  $1 \text{ mm}$  thickness was directly heated by a heater strip in a helium gas atmosphere to prevent oxidation. The actual surface temperature depends on the thermal conductivity of the sample and the heat loss to the ambience. Since the sample is positioned on a heater strip, the temperature of the sample surface strongly depends on the sample thickness. Temperature measurements on the surface of different samples have shown to be up to  $10 \text{ }^\circ\text{C}$  below the measured temperature of the heater strip [14].

The volume fraction of austenite was calculated from the net integral intensities,  $I_{hkl}^j$ , with  $j$  indicating the phase, of the austenite and bcc-martensite/ferrite peaks using the following equation [15]:

$$f_{\gamma} = \frac{\frac{1}{n_{\gamma}} \sum \frac{I_{hkl}^{\gamma}}{R_{hkl}^{\gamma}}}{\frac{1}{n_{\alpha}} \sum \frac{I_{hkl}^{\alpha}}{R_{hkl}^{\alpha}} + \frac{1}{n_{\gamma}} \sum \frac{I_{hkl}^{\gamma}}{R_{hkl}^{\gamma}}} \quad (3.7)$$

where  $hkl$  represents the Miller indices of the diffraction plane,  $n_{\alpha}$  and  $n_{\gamma}$  are the numbers of  $\{hkl\}$  peaks for which the integrated intensities have been measured, and  $R_{hkl}^j$  denotes the

theoretical intensity of phase  $j$  [15]. For analysing the diffraction peaks the EVA software from Bruker-AXS (version 17.0.0.2, 2011) was used.

The accuracy of the austenite fraction by means of XRD measurements is influenced by the sample conditions such as micro-stress at the sample surface, texture and grain size, by the instrument and experimental parameter such as step size and counting time of the scan, by the background and by the analysis method [8]. These factors make it hard to quantify the total error of the XRD-measurements [8] and lower the detection limit of phase fractions [15]. Measurements on a standard reference sample (NBS #488), containing 2 vol.% austenite, using the above described XRD devices successfully detected 2 vol.% austenite [14]. Hence, the detection limit of austenite by XRD for the present study is below 2 vol.%.

### 3.5 Optical and scanning electron microscopy

Microstructural analysis of the samples was carried out using optical microscopy (OM) and a JEOL JSM 6500 field emission gun scanning electron microscope (FEG-SEM) operated at 15 kV. For both steel grades the surface perpendicular to the rolling direction was analysed.

The 13Cr6Ni2Mo SMSS samples were metallographically prepared with a final polishing step of 1  $\mu\text{m}$  diamond paste and subsequently etched. For OM analysis the SMSS samples were etched using Lichtenegger-Blöch (L-B) or Kalling's no. 2 etchant. For an increased etching effect, the L-B etchant (20 g  $\text{NH}_4\text{F}\cdot\text{HF}$  (ammonium difluoride) + 0.5 g  $\text{K}_2\text{S}_2\text{O}_5$  (potassium metabisulfite) + 100 ml of distilled water) [16], where  $\text{Na}_2\text{S}_2\text{O}_5$  (sodium metabisulfite) was used instead of the  $\text{K}_2\text{S}_2\text{O}_5$ , was heated up to 60 °C [17] with an etching time of 30 to 60 s. Samples etched in Kalling's no.2 etchant (5 g  $\text{CuCl}_2$ , 100 ml HCl, 100 ml ethanol) [18] were etched for 10 to 120 s. For SEM analysis the SMSS samples were etched for 15 to 30 s in a modified Vilella's reagent (1 g picric acid, 10 ml HCl, 100 ml ethanol), in which the HCl addition was increased from 5 ml [18] to 10 ml to compensate for the high corrosion resistance of the alloy being studied.

Samples of the Fe-C-Mn-Si steels were metallographically prepared for both, OM and SEM analysis, with a final polishing step of 1  $\mu\text{m}$  diamond paste and subsequently etched in 2 % nital solution for 10 to 15 s.

### 3.6 Thermodynamic calculations

For predicting possible phases and their composition present in equilibrium, thermodynamic calculations for the different materials throughout the thesis were carried out using the Thermo-Calc Software package (Thermo-Calc<sup>®</sup>:TCC™ version S, Database: TCFE v6.2) [19]. Details on the choice of phases are given in the respective chapters.

## REFERENCES

- [1] Y. Wei: *Microstructural Characterization and Mechanical Properties of Super 13% Cr Steel*, PhD Thesis, The University of Sheffield, England, 2005.
- [2] M. J. Santofimia, T. Nguyen-Minh, L. Zhao, R. Petrov, I. Sabirov and J. Sietsma: *Mater. Sci. Eng. A*, 2010, vol. 527, pp. 6429-39.
- [3] S. Foner: *Rev. Scientific Instrum.*, 1959, vol. 30, no. 7, pp. 548-57.
- [4] S. Foner: *J. Appl. Phys.*, 1996, vol. 79, no. 8, pp. 4740-5.
- [5] D. Jiles: *Introduction to Magnetism and Magnetic Materials*, 2nd ed., pp. 68-70, Taylor & Francis Group, Boca Raton, 1998.
- [6] Lake Shore Cryotronics, Inc.: *User's Manual: 7300 Series, VSM System*, 2001.
- [7] Lake Shore Cryotronics, Inc.: *Help Files: 7400 Series, VSM System Software*.
- [8] L. Zhao, N.H. van Dijk, E. Brück, J. Sietsma and S. van der Zwaag: *Mater. Sci. Eng. A*, 2001, vol. 313, pp. 145-52.
- [9] J. Crangle and W. Sucksmith: *J. Iron Steel Inst.*, 1951, vol. 168, pp. 141-51.
- [10] G.L. Squires: *Practical Physics*, 4<sup>th</sup> ed., pp. 6-8, Cambridge University Press, Cambridge, 2001.
- [11] S.S.M. Tavares, R.F. de Noronha, M.R. da Silva, J.M. Neto and S. Pairis: *Mater. Res.*, 2001, vol. 4, no. 4, pp. 237-40.
- [12] A.E. Berkowitz: Constitution of Multiphase Alloys, in: A.E. Berkowitz and E. Kneller (Eds.): *Magnetism and Metallurgy*, vol. 1, p. 344, Academic Press, Inc., New York, 1969.
- [13] T.A. Kop: *A dilatometric study of the austenite/ferrite interface mobility*, PhD Thesis, Technische Universiteit Delft, The Netherlands, 2000.
- [14] R.W.A. Hendrikx, *Private communication*, 2015.
- [15] C.F. Jatczak, J.A. Larson and S.W. Shin: *Retained austenite and its measurements by X-ray diffraction*, Society of Automotive Engineers, Inc., Warrendale, 1980.
- [16] P. Lichtenegger and R. Blösch: *Prakt. Metallographie*, 1975, vol. 12, pp. 567-73.
- [17] D. San Martin, P.E.J. Rivera Diaz del Castillo, E. Peekstok and S. van der Zwaag: *Mater. Charact.*, 2007, vol. 58, no. 5, pp. 455-60.
- [18] G.F. Vander Voort: *Metallography, principles and practice*, p. 647, McGraw-Hill, Inc., New York, 1984.
- [19] Thermo-Calc Software package, Version S, Database TCFE6.2, Stockholm, Sweden, 2011.

# 4

## Thermodynamic analysis of compositional variations in SMSS<sup>1</sup>

In this chapter the phases present in equilibrium and the influence of compositional variations on phase stabilities in the 13Cr6Ni2Mo supermartensitic stainless steel (SMSS) are thermodynamically analysed using the Thermo-Calc<sup>®</sup> software package. It was found for the bulk composition that in equilibrium austenite is still present at room temperature and therefore an  $A_{e1}$ -temperature could not be identified. The influence of the alloying elements on the equilibrium fraction of austenite and on the  $A_{e3}$ - and  $A_{e4}$ -temperatures, the minimum and maximum temperatures at which the equilibrium structure is austenitic, is analysed. Moreover, pseudo-binary phase diagrams are calculated as a function of the concentration of Ni, the most important austenite stabilizer in the SMSS.

### 4.1 Introduction

As mentioned in chapter 2, it is well known that the mechanical properties of SMSS are strongly dependent on the fraction of retained austenite, which is controlled by the heat treatment. Because the products manufactured out of these steels are often in large sections, temperature gradients and corresponding compositional inhomogeneities are inevitable. Also during heat treatment, partitioning of elements between the phases will give local concentrations removed from the bulk levels.

The following phases were experimentally identified for the investigated 13Cr6Ni2Mo SMSS by Wei [1] after austenitization and single and double tempering, where the tempering temperatures of the first step varied between 550 and 700 °C: austenite, martensite, Cr-rich  $M_{23}C_6$ , Mo-rich  $M_6C$ , V(C,N) and small fractions of  $\delta$ -ferrite. Rožnovská et al. [2] reported  $Fe_2Mo$  Laves-phase to be present in a 13Cr6Ni2.5Mo SMSS after 6 h of tempering at temperatures above 590 °C. However, as mentioned above, Laves-phase was not found during the applied tempering process for the 13Cr6Ni2Mo SMSS [1]. The reason could be the shorter tempering time and also the lower content of Mo in the SMSS analysed in this thesis, which might be rather bound in Mo-rich carbides. Another possible intermetallic phase, that

---

<sup>1</sup> This chapter is based on: A. Bojack, L. Zhao and J. Sietsma: Thermodynamic analysis of the effect of compositional inhomogeneity on phase transformations in a 13Cr6Ni2Mo supermartensitic stainless steel, *Solid State Phenom.*, 2011, vols. 172-174, pp. 899-904.

can be present in the 13Cr6Ni2Mo SMSS is Chi-phase ( $\chi$ ), denoted as  $(\text{Fe,Ni})_{36}\text{Cr}_{12}\text{Mo}_{10}$  for austenitic stainless steels, which is considered to have a detrimental effect on the steel properties [3]. Xu et al. [4] reported that the intermetallic  $\chi$ -phase was present in a high molybdenum stainless steel (12Cr-9Ni-4Mo-2Cu-0.9Ti-0.3Al-0.3Si-C,N<0.01 in wt.%) with a composition close to the one of 13Cr6Ni2Mo SMSS, but with higher Mo and Ni contents. A different heat treatment was applied, but their thermodynamic calculations showed  $\chi$ -phase to be stable in equilibrium up to around 920 °C.

Besides the effects of the applied heat treatment, the retention of austenite in these steels is, for thermodynamic reasons, dependent on the chemical composition and fluctuations therein. This chapter aims to understand the influence of compositional changes on the equilibrium phase fractions and transformation temperatures of the 13Cr6Ni2Mo SMSS by means of thermodynamic analysis using the Thermo-Calc Software package [5]. To show the influence of the presence of  $\chi$ - and Laves-phases in the microstructure on the equilibrium phase fractions of the other phases, thermodynamic calculations have been carried out allowing  $\chi$ - and Laves-phases to be present. As discussed above, these phases can exist in equilibrium, but due to kinetic constraints like tempering time and temperature, in relation to activation energy for nucleation and the critical nucleation radius, in practice they may not form. Therefore, further equilibrium calculations are carried out in absence of  $\chi$ - and Laves-phases.

## 4.2 Temperature dependence of equilibrium phase fractions

The elements and compositions, considered for the equilibrium calculations, of the two casts that were used for the experimental research in this thesis are given in Table 4.1. The following phases were allowed to be present for the calculations: liquid, fcc, bcc, cementite,  $\text{M}_6\text{C}$ ,  $\text{M}_{23}\text{C}_6$  and  $\text{M}_7\text{C}_3$ ,  $\chi$ -phase and Laves-phase. The temperature range for the calculations was 300 to 1200 °C at fixed intervals of 2.5 °C. The  $A_{e3-}$  and  $A_{e4-}$  temperature were defined as the minimum and maximum temperature at which the equilibrium structure of the matrix is completely austenitic, with the possible presence of carbides, nitrides,  $\chi$ - and Laves-phases. Also the differences between the composition of both casts are compared in the following.

*Table 4.1 Bulk compositions of 13Cr6Ni2Mo SMSS used for the thermodynamic calculations (in wt.%), balance Fe.*

cast	C	Cr	Ni	Mo	Mn	Si	V	Ti	N
#1	0.015	12.34	5.66	2.02	0.42	0.22	0.18	0.01	0.013
#2	0.020	12.27	5.62	2.01	0.42	0.21	0.18	0.01	0.016

The evolution of the equilibrium phase fractions as a function of temperature for the composition of cast #1 is given in Figure 4.1a-c. For the temperature range considered no cementite and  $\text{M}_7\text{C}_3$ -carbide was found to be present in equilibrium. In Figure 4.1a the intermetallic  $\chi$ - and Laves-phases were allowed to be present to show the influence of their presence on the evolution of the other phases. In Figure 4.1b the calculations were

performed excluding  $\chi$ - and Laves-phases. Both calculations show that austenite is stable even down to 300 °C and it is not possible to derive the  $A_{e1}$ -temperature for this steel from the calculations for temperatures above 300 °C. Additional calculations with Thermo-Calc have shown the austenite to even be stable at a mass fraction of about 9 % at room temperature. The  $A_{e3}$ -temperature was found to be 721 °C when  $\chi$ - and Laves-phases are present and 741 °C when they are absent. The underlying reason is that without the presence of  $\chi$ - and Laves-phases more Cr and Mo is dissolved in the matrix, restricting the austenite field. This can be seen in the differences of the austenite fraction shown in Figure 4.1c, where due to the presence of  $\chi$ -phase the austenite fraction at  $A_{e3}$  is lower than when  $\chi$ -phase is excluded. If  $\chi$ - and Laves-phases are allowed for the equilibrium calculations,  $\chi$ -phase will be present between 518 and 806 °C and Laves-phase at temperatures below 548 °C, replacing the  $M_6C$  above 300 °C and limiting the stability of  $M_{23}C_6$ .

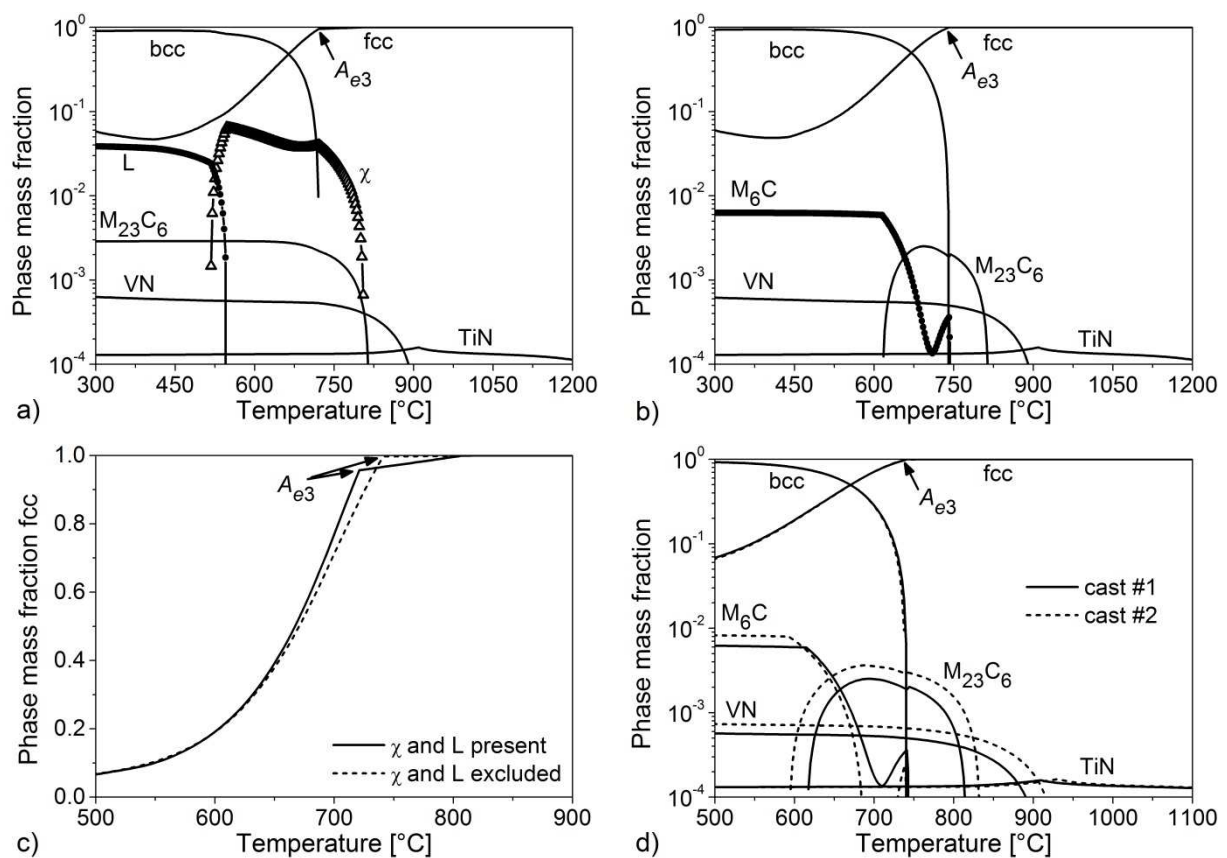


Figure 4.1 Temperature dependence of the equilibrium mass fractions of the phases. a) including Chi ( $\chi$ )- and Laves (L)-phases, b) excluding  $\chi$ - and Laves-phases, c) influence of  $\chi$ - and Laves-phases on the austenite fraction and d) comparison of cast #1 and #2 excluding  $\chi$ - and Laves-phases.

Figure 4.1 also indicates that VN is present at temperatures below 900 °C. TiN is even more stable and will not be dissolved during austenitization treatment. The fractions of both VN and TiN are not significantly affected by the presence of  $\chi$ - and Laves-phases. When  $\chi$ - and Laves-phases are allowed for the calculations, no  $M_6C$ -carbide is present in the equilibrium

condition above 300 °C since Mo is then dissolved in the intermetallic phases. Table 4.2 gives the average composition of the precipitates and intermetallic compounds of cast #1. The compositions of  $M_6C$ ,  $M_{23}C_6$ , VN, TiN, and  $\chi$ -phase were calculated as an average of the equilibrium compositions obtained between 600 and 750 °C, a range where most phases are present. The composition of the Laves-phase was obtained as an average of the equilibrium compositions at 300 and 450 °C. Table 4.2 also shows that the compositions of  $M_{23}C_6$ , VN and TiN do not change significantly with the presence of  $\chi$ - and Laves-phases. According to the calculations,  $\chi$ -phase mainly consists of Fe, Cr and Mo, and a small concentration of Ni. The composition of Laves-phase, obtained by the equilibrium calculations, does not contain Fe as denoted by Rožnovská et al. [2] for a 13Cr6Ni2.5Mo SMSS. Without  $\chi$ - and Laves-phases  $M_6C$ -carbide will be stable until 745 °C at the expense of  $M_{23}C_6$ -carbide, which is then only stable between 617 and 816 °C. Since  $\chi$ - and Laves-phases were not identified after tempering of 13Cr6Ni2Mo SMSS using similar heat treatment parameters as in the present work [1], the calculations presented in the following were performed excluding them. However, the result of Figure 4.1a shows  $\chi$ - and Laves-phases to be thermodynamically more favourable than  $M_6C$ . Higher tempering temperature and/or longer time can therefore lead to  $\chi$ - and/or Laves-phase formation.

*Table 4.2 Average compositions of precipitates,  $\chi$ - and Laves (L)-phases from thermo-dynamic calculations for cast #1 (see Figure 4.1). The temperatures from which the compositions were obtained and averaged are also listed.*

Phases	Temperatures [°C]	L and $\chi$ present	L and $\chi$ excluded	Comments
L	300, 450	$(Cr_xSi_{(1-x)})_2Mo$	-	$x \approx 0.85$
$\chi$	675, 750	$Fe_xCr_{12}Mo_yNi$	-	$x \approx 33$ $y \approx 6$
$M_{23}C_6$	675, 750	$(Cr_wMo_xFe_yV_z)_{23}C_6$	$(Cr_wMo_xFe_yV_z)_{23}C_6$	$w \approx 0.74$ $x \approx 0.12$ $y \approx 0.10$ $z \approx 0.03$
$M_6C$	600, 675	-	$(Mo_wFe_xCr_yV_z)_6C$	$w \approx 0.55$ $x \approx 0.34$ $y \approx 0.08$ $z \approx 0.02$
VN	600, 675, 750	$V_{(1+x)}N$	$V_{(1+x)}N$	$x \approx 0.21$
TiN	600, 675, 750	$Ti_{(1+x)}N$	$Ti_{(1+y)}N$	$x \approx -0.01$ $y \approx -0.02$

It is worth to mention that the fcc and bcc phases were found to split up in several phases below 300 and 500 °C, respectively, which is not shown in the presented results. The fcc phases were added up to one phase since the different compositions are not significant. The bcc phases showed greater differences in mainly Fe, Cr and Mo concentrations. However,

due to kinetic reasons partitioning of Cr and Mo will be too slow at this temperature range and hence the bcc phases were also added up to one phase.

Figure 4.1d shows a comparison of cast #1 and #2. The differences in the equilibrium phase fractions are minor, which are for instance a maximum difference in austenite fraction of 0.003 below 700 °C and 0.012 above 700 °C. However, due to the slightly higher content of C and N in cast #2 the  $M_{23}C_6$  and VN are more stable with a difference in transformation temperatures of around 20 °C. The difference in the fractions of both carbides and nitrides are minor. The most important equilibrium transformation temperatures and phase stability ranges of both casts with and without the presence of  $\chi$ - and Laves-phases are listed in Table 4.3. Since both casts show only minor differences, the results in the following sections are presented for cast #1 only.

Table 4.3 Overview of most important equilibrium transformation temperatures and phase stability ranges (in °C) for cast #1 and #2. L and  $\chi$  denote Laves- and  $\chi$ -phases.

cast	L and $\chi$ present				L and $\chi$ excluded			
	$A_{e3}$	$\chi$	$M_{23}C_6$	VN	$A_{e3}$	$M_6C$	$M_{23}C_6$	VN
#1	721	517-806	< 817	< 910	741	< 745	617-816	< 910
#2	721	515-803	< 834	< 933	739	< 741	595-835	< 933

### 4.3 Effect of compositional variations on austenite fraction

Diffusion and partitioning between the phases can give local concentrations far removed from the bulk levels, which will influence the formation and fraction of austenite. If the composition of the 13Cr6Ni2Mo SMSS is varied, the relevance of the different elements on the equilibrium austenite fraction becomes obvious. As mentioned in Chapter 2, the stabilization of austenite at room temperature is obtained by austenite-stabilizing elements like Ni, Mn, and C, that enrich austenite [1, 6-8]. Since the C-content in SMSS is very small (<0.03 wt pct), it is mainly Ni [9, 10] and Mn [11] that are responsible for the austenite stabilization. Wei [1] measured the concentration of different elements in retained austenite and tempered martensite in the 13Cr6Ni2Mo SMSS after different single and double tempering treatments by energy dispersive X-ray (EDX) technique. An overview of approximate minimum and maximum concentrations of Cr, Ni, Mo and Si are listed in Table 4.4. Furthermore, EDX analysis of not distinct austenite/martensite areas, precipitates or  $\delta$ -ferrite have shown variations from the values listed in Table 4.4 [1]. Therefore, levels for the alloying elements well beyond those permitted in the material specification (see [12]) have been examined in the following.

The influence of the alloying elements Cr, Ni, Mo and Mn on the equilibrium fraction of austenite is shown in Figure 4.2, where only the respective element of the base composition of the 13Cr6Ni2Mo SMSS (cast #1) was varied and balanced with Fe. Cr and Mo are known to stabilize the ferrite and with increasing their content, the temperature range of the austenite phase decreases. This would also decrease the possible temperature range for the

austenitization treatment. Ni and Mn stabilize the austenite and thus increase the temperature range and decrease the minimum temperature at which the material remains basically austenitic. These elements also decrease the martensite start temperature [13] and hence more austenite is expected to be retained at room temperature with increasing Ni and Mn contents.

Table 4.4 Overview of approximate minimum and maximum alloy concentration (in wt.%) in retained austenite and tempered martensite of differently tempered 13Cr6Ni2Mo SMSS by Wei [1].

	Tempered martensite				Retained austenite			
	Cr	Ni	Mo	Si	Cr	Ni	Mo	Si
min.	12	4	1.7	0.5	12	8	1.9	0.5
max.	13	6	2.6	0.6	13	12	2	0.5

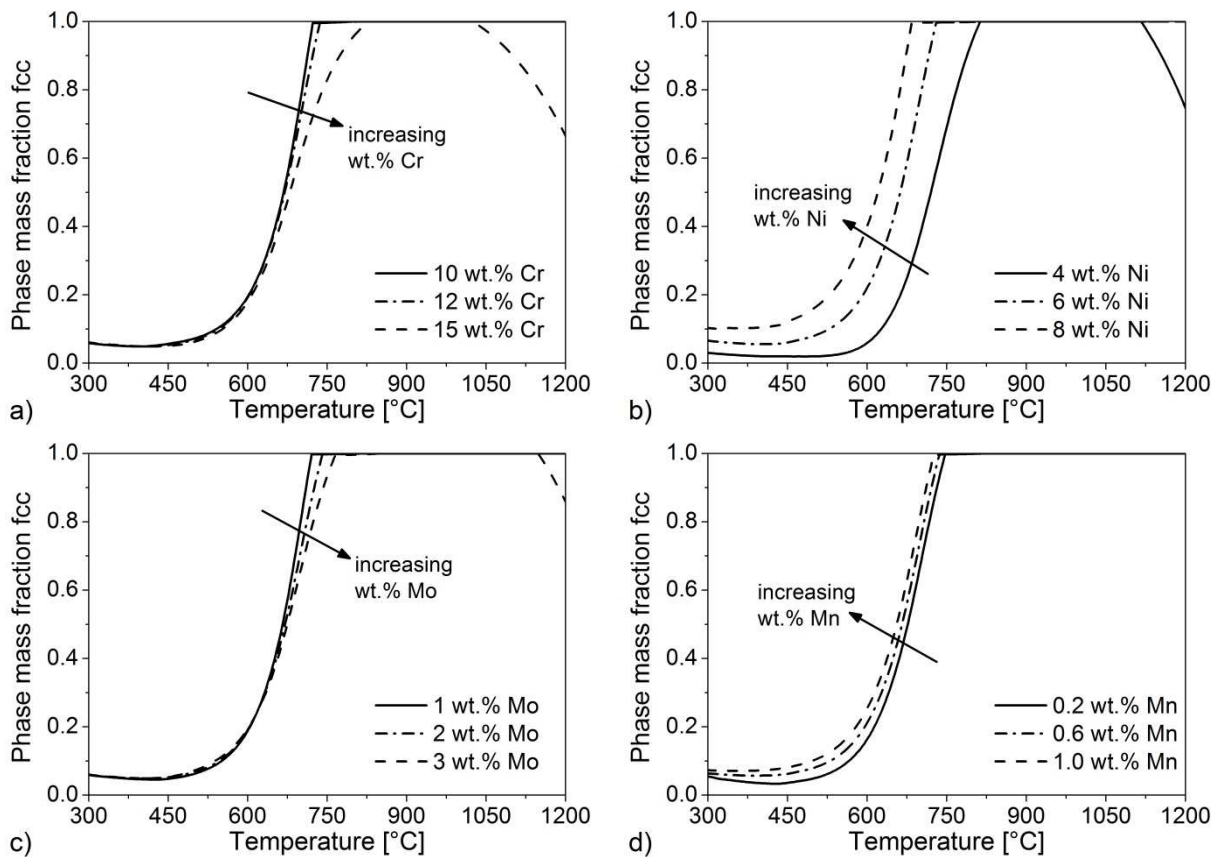


Figure 4.2 Influence of a) Cr, b) Ni, c) Mo and d) Mn on the phase fraction of fcc-austenite in the 13Cr6Ni2Mo SMSS.

An overview of the influence of compositional changes on the  $A_{e3}$ -temperature is given in Figure 4.3, where the base composition (cast #1) was again balanced with Fe. From the elements analysed, the main alloying elements Cr, Ni and Mo and also Mn show a strong influence between the compositional range considered. This is indicated by the slopes of the curves in Figure 4.3. Within the concentration range analysed, the  $A_{e3}$ -temperature increases with an approximate average slope of +20 °C/wt.% for increasing Cr-concentration and with an approximate average slope of +32 °C/wt.% for increasing Mo-concentration. With increasing concentration of Ni and Mn the  $A_{e3}$ -temperature is decreasing with an approximate slope of -42 °C/wt.% and -27 °C/wt.%, respectively. Within the concentration range analysed, Ni showed the greatest influence on the absolute values of the  $A_{e3}$ -temperature. The smallest influences on the absolute value of the  $A_{e3}$ -temperature were obtained for C and Si within the considered compositional ranges. However, for C the range studied of 0 to 0.05 wt.% was very narrow. The effect of C on the  $A_{e3}$ -temperature was, with an approximate slope of -265 °C/wt.%, the highest of all the examined elements.

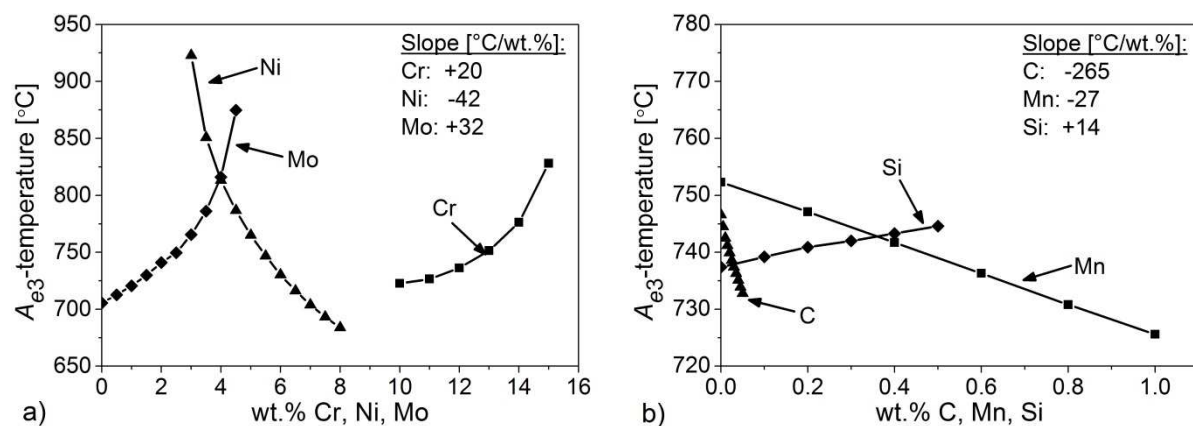


Figure 4.3 Influence of the variation of the main alloying elements on the  $A_{e3}$ -temperature of the 13Cr6Ni2Mo SMSS balanced with Fe. The average slopes of the curves are indicated.

The influence of the elements Cr, Ni and Mo on the temperature range of the austenite phase, which is important for the definition of the austenitization temperature, can be found in Figure 4.4. The diagrams show the  $A_{e3}$ - and  $A_{e4}$ -temperatures, between which no ferrite is present, depending on the concentration of the elements. It is shown that with increasing Cr and Mo content the austenite field narrows and with increasing Ni content it widens.

The compositional variations analysed show the sensitivity of the transformation temperatures and the austenite fraction on changes particularly for the Ni-concentration. This is important to note, since the Ni-concentration shows the greatest variation within retained austenite and tempered martensite (see Table 4.4).

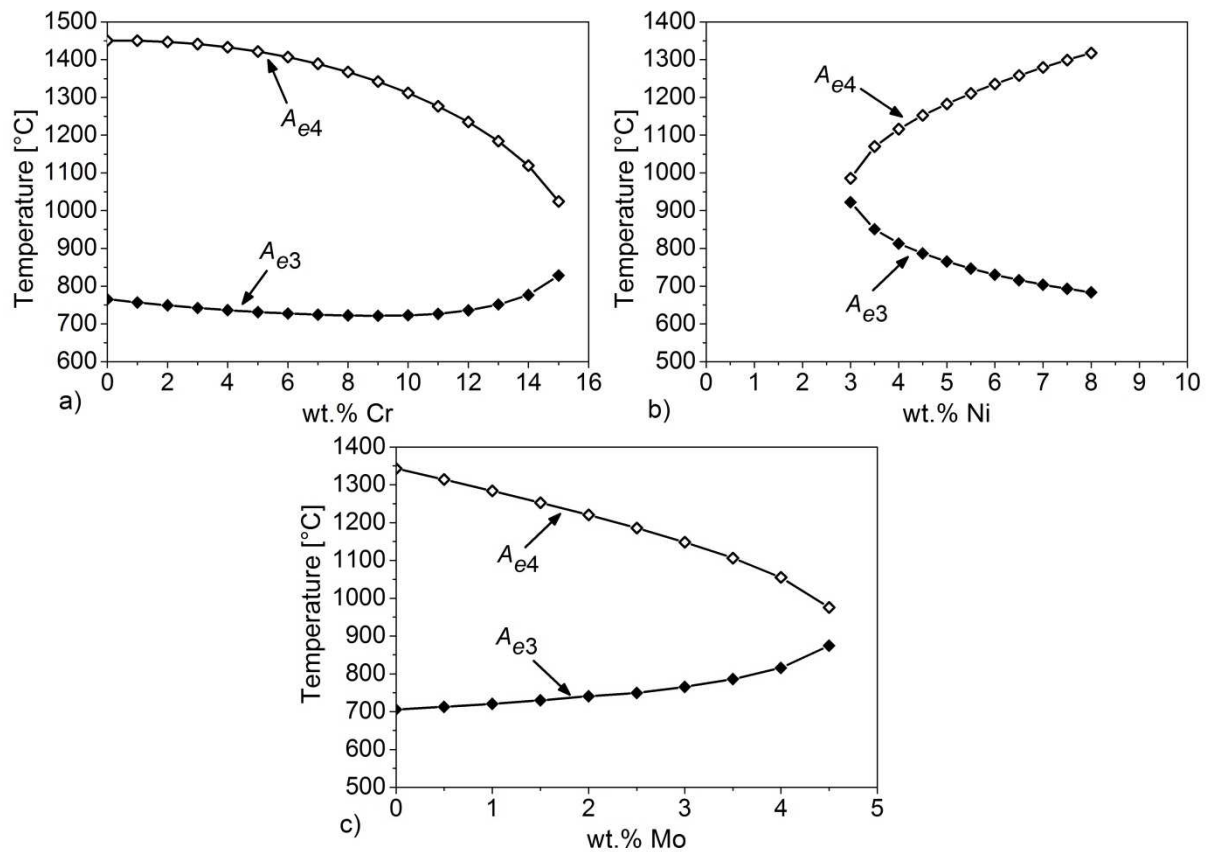


Figure 4.4 Influence of a) Cr, b) Ni and c) Mo on the austenite temperature range in the 13Cr6Ni2Mo SMSS.

#### 4.4 Pseudo-binary phase diagrams of the 13Cr6Ni2Mo SMSS

Since Ni is discussed to have crucial influence on the stability of retained austenite in SMSS [9, 10], pseudo-binary phase diagrams for the 13Cr6Ni2Mo SMSS were calculated between 500 and 1400 °C as a function of Ni-content to show the effect of Ni on the phase stabilities in equilibrium. The following phases were allowed to be present for the calculations: liquid, fcc, bcc, cementite,  $M_6C$ ,  $M_{23}C_6$  and  $M_7C_3$ ,  $\chi$ - and Laves-phases. In Figure 4.5 the pseudo-binary phase diagrams for the composition of cast #1 are shown for  $\chi$ - and Laves-phases being present (Figure 4.5a) or absent (Figure 4.5b). For the compositional and temperature range considered, no cementite and  $M_7C_3$ -carbide were found to be present in equilibrium. It is shown that with increasing Ni-concentration the austenite single-phase field widens. Hence, the austenitization treatment can be carried out at higher temperatures without the risk of  $\delta$ -ferrite formation. With decreasing Ni-concentration, below 3 wt.%, ferrite always exists. This implies that after cooling from austenitization treatment, martensite, formed during quenching, retained austenite and also ferrite will be present in the material, together with nitrides. With increasing Ni-concentration from 4 to 20 wt.% and decreasing concentration between 4 and 0 wt.% the presence of  $\chi$ -phase is shifted to lower temperatures, when both  $\chi$ - and Laves-phases are allowed to be present (Figure 4.5a).

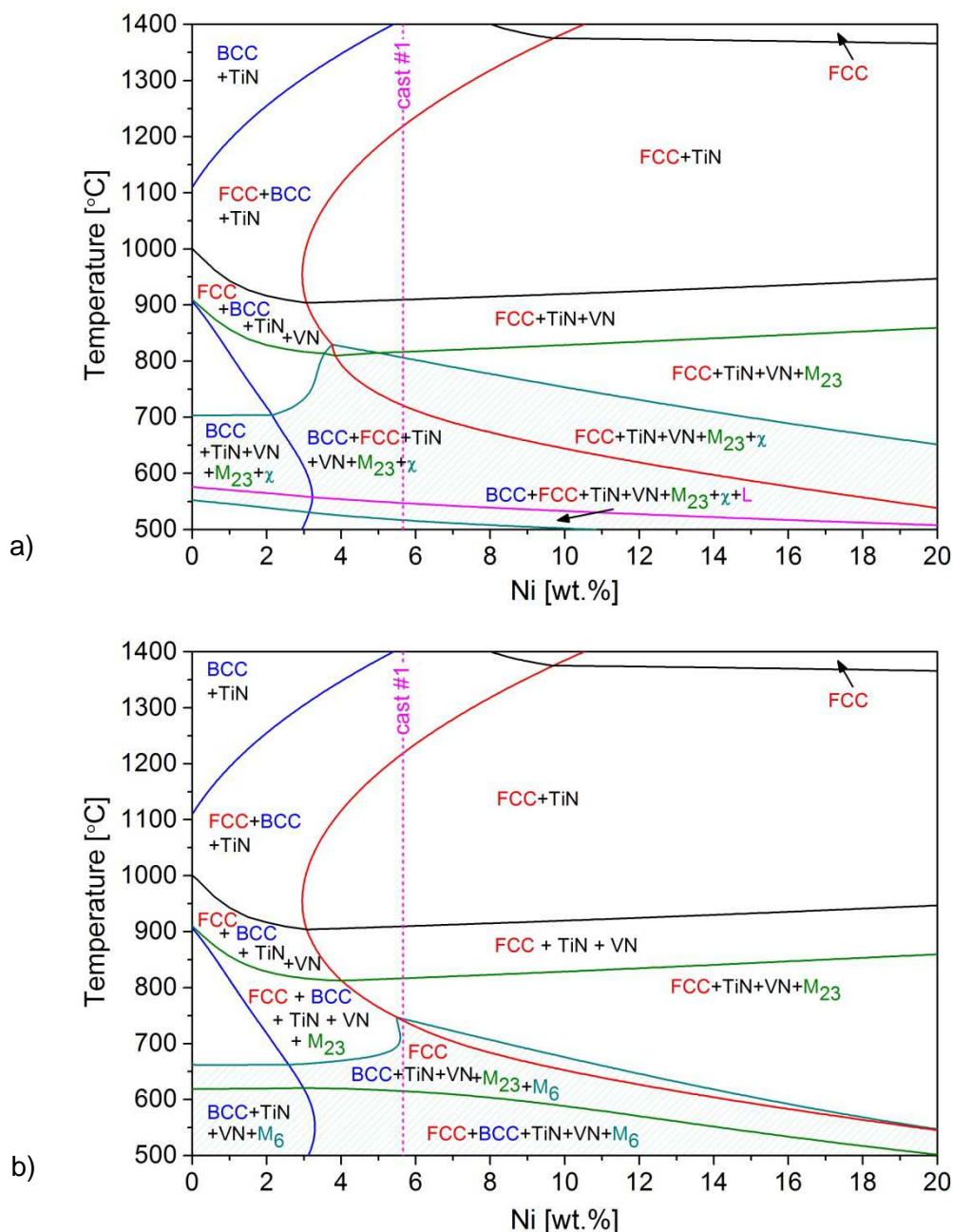


Figure 4.5 Pseudo-binary phase diagrams for 13Cr6Ni2Mo SMSS, cast #1. a)  $\chi$ - and Laves ( $L$ )-phases present. b)  $\chi$ - and Laves-phases absent. The blue line indicates the presence of bcc-ferrite and the red line the presence of the fcc-austenite single phase field, without consideration of carbides and nitrides,  $\chi$ - and Laves-phases. The dotted magenta line indicates the bulk Ni-content of cast #1.  $M_{23}$  and  $M_6$  represent  $M_{23}C_6$  and  $M_6C$ . The hashed area indicates the presence of  $\chi$ -phase and  $M_6C$ , respectively.

Figure 4.5a shows that Laves-phase is stable below 580 °C and is suppressed to lower temperatures by about 70 °C with the Ni-concentration increasing to 20 wt.%. Within the range analysed  $M_{23}C_6$  is present below approximately 900 °C. VN is stable below 900 °C and TiN is stable within the calculated temperature range up to 8 wt.% of Ni. Above 8 wt.% until

the calculated maximum Ni-concentration of 20 wt.% TiN is stable only until around 1350 °C. When  $\chi$ - and Laves-phases are excluded in equilibrium (Figure 4.5b)  $M_6C$  is present below 750 °C instead, as discussed earlier in this chapter. Compared to Figure 4.5a the stability of TiN and VN is not influenced by the presence of  $\chi$ - and Laves-phases, which is also seen for the upper phase boundary of  $M_{23}C_6$ . The stability of both carbides shows a dependence on the Ni-concentration, i.e. the presence of  $M_{23}C_6$  is shifted to lower temperatures with increasing Ni-concentration from 5.5 to 20 wt.%, while the stability of  $M_6C$  at higher temperatures is decreasing.

Due to kinetic constraints, for instance due to high heating rates, it is useful to examine the effect of C and N on fcc- and bcc-phases, as well as the effect of  $\chi$ - and Laves-phases, which is shown in Figure 4.6. In Figure 4.6a pseudo-binary phase diagrams of cast #1 are shown comparing fcc and bcc phase fields when  $\chi$ - and Laves-phases are excluded and when fcc and bcc are the only phases present. It is seen that the presence of  $\chi$ - and Laves-phases is only significant for the presence of austenite below 3 wt.% Ni-concentration and between 650 and 900 °C. The influence of 0.015 wt.% C and 0.013 wt.% N (cast #1) on the stability of fcc and bcc is shown in Figure 4.6b, when fcc and bcc are the only phases present. If no C and N would be in the material, no fcc-phase would form below 0.65 wt.% Ni. Moreover, the small additions of C and N widen the single fcc phase field above 700 °C. Below 700 °C, N and C show no significant influence on the fcc and bcc phase fields. This is important to note, since the tempering treatment of the 13Cr6Ni2Mo SMSS is carried out below 700 °C.

The influence of C and N content on the  $A_{e3}$ -temperatures in the ranges discussed might be not significant, but an increased stability and fraction of carbides and nitrides, as shown for cast #2 in Figure 4.1d, might influence the formation of austenite. They can act as heterogeneous nucleation sites for austenite, thus influencing the activation energy for austenite formation. The dependence of austenite stability on alloying elements will be further discussed in chapter 6.

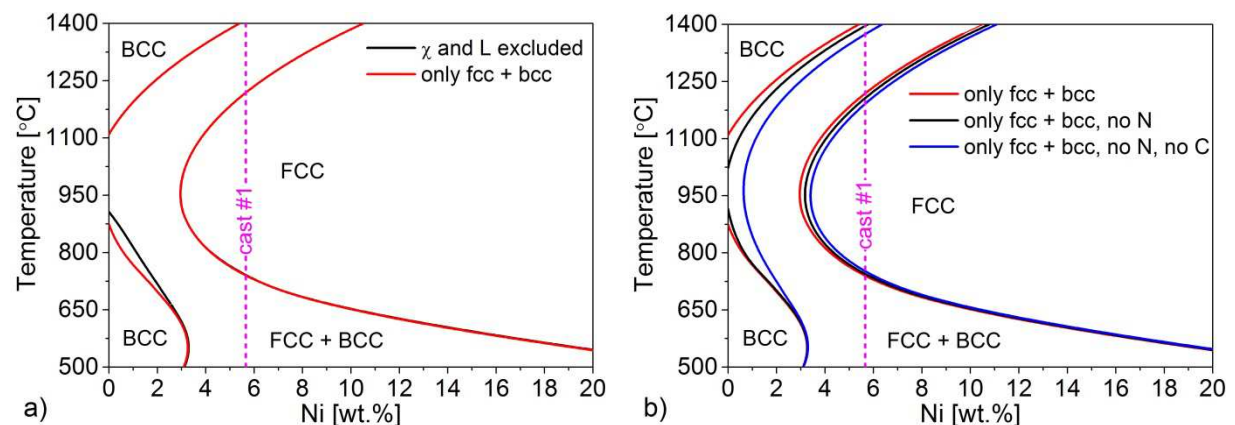


Figure 4.6 Pseudo-binary phase diagrams showing only fcc and bcc phases for the base composition of cast #1. a) Comparison of fcc and bcc when  $\chi$ - and Laves (L)-phases are excluded and when fcc and bcc are the only phases allowed to be present. b) Comparison of the effect of the interstitials C and N (cast #1) on fcc and bcc when fcc and bcc are the only phases present in the material. The dotted magenta lines indicate the bulk Ni-content of cast #1.

## 4.5 Conclusions

The thermodynamic calculations carried out for the 13Cr6Ni2Mo SMSS show the influence of the alloying elements on the equilibrium phases, the phase fraction of austenite and corresponding changes in the transformation temperatures  $A_{e3}$  and  $A_{e4}$ . The main conclusions are:

- 1) The results have shown that, even though C is a strong austenite stabilizer, its influence on the absolute value of the  $A_{e3}$ -temperature is, within the compositional range considered (0-0.05 et.%), small, because C is only present in small concentrations in the 13Cr6Ni2Mo SMSS, i.e. max. 0.03 wt.% [12].
- 2) Within the compositional range considered, the  $A_{e3}$ -temperature is sensitive to changes of Cr, Ni and Mo. Most sensitivity of the  $A_{e3}$ -temperature and the austenite fraction is found for changes in Ni-concentration within the compositional range considered.
- 3) The calculations have shown that Ni and Mn stabilize the austenite and thus increase the temperature range and decrease the minimum temperature at which the material remains completely austenitic. Hence a higher concentration of Ni and Mn in austenite at room temperature would increase its stability.
- 4)  $\chi$ - and Laves-phases are thermodynamically more favourable than  $M_6C$ . This implies that deviations from the original heat treatment (higher tempering temperature and longer holding times) could lead to  $\chi$ - and/or Laves-phase formation.
- 5) A comparison of pseudo-binary phase diagrams, with different phases allowed to be present in equilibrium, shows the presence of  $\chi$ - and Laves-phases to be dependent on the Ni-content of the material.
- 6) Although C and N are primarily bound in carbides and nitrides, the presence of carbides and nitrides could influence the nucleation of austenite, since they can act as heterogeneous nucleation sites for austenite.
- 7) Only minor differences were observed in the equilibrium fraction of fcc between the two casts used in this work.

## REFERENCES

- [1] Y. Wei: *Microstructural Characterization and Mechanical Properties of Super 13% Cr Steel*, PhD Thesis, The University of Sheffield, England, 2005.
- [2] G. Rožnovská et al.: *The Effect of Heat Treatment on Microstructure and Properties of a 13Cr6Ni2.5Mo Supermartensitic Steel*, Sborník vědeckých Vysoké školy báňské – TU Ostrava, číslo 1, rok 2005, ročník XLVIII, řada hutnická článek č. 1241, pp. 225-31; from: <http://www.fmfi.vsb.cz/shared/uploadedfiles/fmfi/35Roz41-225.pdf>
- [3] A. F. Padilha and P. R. Rios, "Decomposition of austenite in austenitic stainless steels," *ISIJ International*, vol. 42, no. 4, pp. 325-37, 2002.
- [4] W. Xu, D. San Martin, P.E.J. Rivera Diaz del Castillo and S. van der Zwaag: *Adv. Mater. Res.*, 2007, vols. 15-17, pp. 531-6.
- [5] Thermo-Calc Software package, Version S, Database TCFE6.2, Stockholm, Sweden, 2011.
- [6] J. Hubackova, V. Cihal and K. Mazanec: *Z. Werkstofftech.*, 1984, vol. 15, pp. 411-5.

- [7] P.D. Bilmes, M. Solari and C.L. Llorente: *Mater. Charact.*, 2001, vol. 46, no. 4, pp. 285-96.
- [8] T.G. Gooch, P. Woollin and A.G. Haynes: in *Supermartensitic Stainless Steel '99*, KCI Publishing BV, Brussels, 1999, pp. 188-95.
- [9] Y. Song, X. Li, L. Rong and Y. Li: *Mater. Sci. Eng. A*, 2011, vol. 528, no. 12, pp. 4075-9.
- [10] Y.Y. Song, X.Y. Li, L.J. Rong, D.H. Ping, F.X. Yin and Y.Y. Li: *Mater. Lett.*, 2010, vol. 64, no. 13, pp. 1411-4.
- [11] Y.Y. Song, D.H. Ping, F.X. Yin, X.Y. Li and Y.Y. Li: *Mater. Sci. Eng. A*, 2010, vol. 527, no. 3, pp. 614-8.
- [12] [http://www.tatasteeleurope.com/file\\_source/StaticFiles/Business%20Units/Engineering%20steels/SF1325.PDF](http://www.tatasteeleurope.com/file_source/StaticFiles/Business%20Units/Engineering%20steels/SF1325.PDF), " 2013.
- [13] R.W.K. Honeycombe and H.K.D.H. Bhadeshia: *Steels: Microstructure and Properties*, 3rd ed., p. 117, Elsevier Ltd., Amsterdam, 2006.

# 5

## In-situ determination of austenite and martensite in SMSS<sup>1</sup>

In-situ analysis of the phase transformations in the 13Cr6Ni2Mo SMSS was carried out using the thermo-magnetic technique (VSM), dilatometry and high temperature X-ray diffractometry (HT-XRD). A combination of the results obtained by the three applied techniques gives a valuable insight in the phase transformations during the austenitization treatment, including subsequent cooling, of the 13Cr6Ni2Mo SMSS, where the magnetic technique offers a high accuracy in in-situ monitoring the austenite fraction. It was found by dilatometry that the austenite formation during heating takes place in two stages, most likely caused by partitioning of Ni into austenite. The in-situ evolution of the austenite fraction is monitored by high-temperature XRD and dilatometry. The progress of martensite formation during cooling was described with a modified Koistinen-Marburger relation for the results obtained from the magnetic and dilatometer experiments. Enhanced martensite formation at the sample surface was detected by X-ray diffraction, which is assumed to be due to relaxation of transformation stresses at the sample surface. Due to the high alloy content and thermodynamic stability of austenite at room temperature, about 5 vol.% of austenite was found to be retained at room temperature after the austenitization treatment.

### 5.1 Introduction

During the past 20 years much work has been done to characterize and optimize the microstructure and thus the mechanical behaviour of low carbon martensitic stainless steels and SMSS [1-6]. To analyse the evolution of phase fractions, most of these studies used ex-situ techniques [1, 4], besides dilatometry [2, 3, 5, 6] or high temperature X-ray diffraction [2] for in-situ analysis. Dilatometry is a well-known and convenient technique, where phase fractions and transformation temperatures can be obtained from the dilatation of the sample [7]. However, this technique has its limits in accuracy since only the length change of the sample is measured, i.e. the phases are not directly observed as with XRD techniques.

---

<sup>1</sup> This Chapter is based on: A. Bojack, L. Zhao, P.F. Morris and J. Sietsma: In-Situ Determination of Austenite and Martensite Formation in 13Cr6Ni2Mo Supermartensitic Stainless Steel, *Mater. Charact.*, 2012, vol. 71, pp. 77-86.

The latter are widely used to measure the fraction of retained austenite of low-carbon martensitic stainless steels and SMSS [1, 2, 4], but also have limitations due to the influence of the sample condition, such as stress at the sample surface, texture and grain size, or instrumental limitations and the analysis methods [8]. Furthermore, the penetration depth in XRD analysis is limited to several microns and hence the information obtained is restricted to the surface region. Magnetic techniques have been widely used for phase-transformation measurements on different stainless steels [9-11]; particularly saturation magnetization measurements have been widely used for ex-situ studies [8, 12-14] and also sometimes for in-situ monitoring of the phase-transformation [15-21]. Especially in determining the austenite fraction by analysing the saturation magnetization, the magnetic techniques are more accurate than XRD or metallography [8], as the saturation magnetization is a property, which depends on the chemical composition and the phases present in the material, but not on other microstructural features like texture or defects [22, 23]. Since austenite is paramagnetic, the austenite fraction can be derived from the ratio of the saturation magnetization of the austenite-containing sample and the saturation magnetization of a sample of the same composition containing only ferromagnetic phases like ferrite or martensite [8, 23]. In addition, unlike XRD and metallographic analysis, a direct bulk probing is performed during magnetic measurements and therefore a truly representative fraction of austenite can be obtained. However, when the temperature is increased towards the Curie temperature ( $T_C$ ) the saturation magnetization decreases to almost zero, where the mutual spin coupling forces are overruled by thermal motion, so that the material becomes paramagnetic above  $T_C$  [24]. In multiphase systems, changes in the saturation magnetization can be monitored due to the different Curie temperatures of each phase, but this can also make it difficult to distinguish these phases and to obtain information about e.g. the  $A_{c1}$ -temperature. For analysing SMSS, magnetic techniques have been mainly used ex-situ [12] or in-situ at temperatures below room temperature [25].

Zhang et al. [26] used high-temperature laser scanning confocal microscopy and X-ray diffraction by synchrotron radiation for in-situ analysis of the formation of martensite during cooling of SMSS with different Ni contents. While these techniques form a promising tool for gaining in-situ information on phase formations in SMSS, they are, however, expensive and poorly accessible, and the data analysis is complex and time consuming. A combination of dilatometry, XRD and magnetic techniques can also give valuable information on the phase transformations during the heat treatments. In the present study, a thermo-magnetic technique, dilatometry, and high-temperature XRD are used for an in-situ analysis of the austenite formation and decomposition during the austenitization treatment and subsequent cooling of the 13Cr6Ni2Mo SMSS. Control of this heat treatment is important as it determines the levels of alloying elements in solution prior to subsequent tempering, in which the final microstructure is formed. Therefore, the austenite fraction is monitored during the austenitizing step and the martensite formation during cooling. The fraction of martensite as a function of temperature is described with a modified Koistinen-Marburger relation. Detailed knowledge on the martensite formation is required to control the retained austenite in this material.

## 5.2 Experimental

The chemical composition of the studied 13Cr6Ni2Mo SMSS is shown in Table 5.1. The as-received material was delivered in the double-tempered condition with a microstructure consisting of martensite, retained austenite and a very small fraction of carbides, nitrides and carbonitrides [27]. The as-received material was analysed during re-austenitization using three in-situ techniques: thermo-magnetic measurement, dilatometry and high-temperature X-ray diffraction (HT-XRD). From these experiments, a variety of characteristics on the microstructural changes during the heat treatments can be obtained. Among these, the magnetic measurements give a reliable and sensitive detection of the volume fraction of austenite and hence of martensite, when only these two phases are present at a temperature below  $T_C$  [8].

Table 5.1 Bulk composition of the tested 13Cr6Ni2Mo SMSS (in wt.%), balance Fe.

cast	C	Cr	Ni	Mo	Mn	Si	V	Ti	N
#1	0.015	12.34	5.66	2.02	0.42	0.22	0.18	0.01	0.013

### 5.2.1 Magnetic measurements

The in-situ magnetic experiments were carried out in the VSM described in section 3.2. To ensure a homogeneous heating of the sample in the VSM furnace a low heating rate of 3 K/min was applied during the heating to 950 °C. After 30 min of holding, the cooling was performed in the furnace of the magnetometer, where the temperature approximately follows an exponential relation (see equation 3.1:  $T_0 = 950$  °C,  $T_E = 29.1$  °C,  $\tau = 20$  min). The applied temperature-time profile is shown in Figure 5.1.

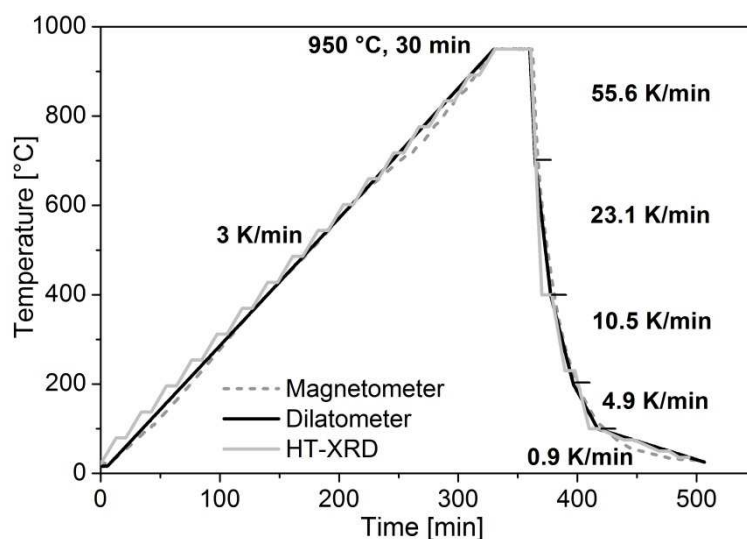


Figure 5.1 Temperature-time profiles for thermo-magnetic, dilatometer and HT-XRD experiments. The cooling rates indicated in the figure are for the dilatometer experiment.

The saturation magnetization ( $M_{sat}$ ) of the material was measured in a constant magnetic field of 1.5 T during the whole heat treatment cycle. In addition, magnetization curves at room temperature were measured by stepwise changing the applied field from 1.6 T to – 1.6 T with a step size of 0.1 T. The volume fraction of austenite,  $f_{\gamma}$ , depending on the temperature was determined using the following equation [8, 28]:

$$f_{\gamma} = 1 - \frac{M_{sat}(c)}{M_{sat}(ref)}, \quad (5.1)$$

where  $M_{sat}(c)$ , denotes the measured saturation magnetization of the sample and  $M_{sat}(ref)$  the saturation magnetization of an austenite-free reference sample of the same composition, both measured at a magnetic field of 1.5 T. As discussed in chapter 4, the fractions of carbides and nitrides are negligibly small in the material and hence the fraction of martensite is  $f_{\alpha} \approx 1 - f_{\gamma}$ .

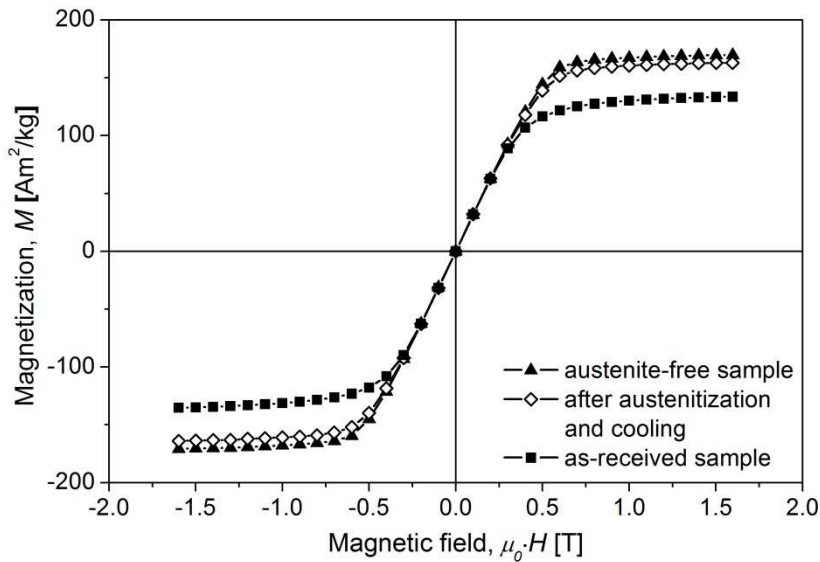


Figure 5.2 Room temperature curve of magnetization  $M$  versus the magnetic field ( $\mu_0 H$ ) for the as-received sample, the austenitized sample and the austenite-free sample.

An austenite-free reference sample was obtained by tempering an austenitized and quenched sample for 2 h at 400 °C, in order to destabilize any remaining austenite. Thus, a reference sample, which can be assumed to be fully ferromagnetic, was obtained [12]. The room temperature magnetization curve of this austenite-free sample is shown in Figure 5.2. The temperature-dependent magnetization of the austenite-free sample  $M_{ref}(T)$ , heated at 5 K/min to 950 °C in the furnace of the VSM, was described by the relation of Arrott and Heinrich [29] up to  $A_{c1}$ -temperature:

$$M_{ref}(T) = M_{sat0} \frac{(1-s)^\beta}{1 - \beta s + A s^{3/2} - C s^{7/2}}, \quad (5.2)$$

where  $M_{sat0}$  is the saturation magnetization at 0 K (-273 °C),  $\beta$ ,  $A$  and  $C$  are material dependent constants, and  $s = T/T_C$ .  $T_C$  is the Curie temperature and can be obtained from the minimum of the first derivative  $dM_{sat}/dT$  of the magnetization curve [17, 30]. Determining the magnetization of an austenite-free reference sample above  $A_{c1}$  is not straightforward. Also, extrapolation of equation (5.2) is not possible, since it does not account for the influence of the magnetic field on the magnetization above  $T_C$ . This is explained in more detail in the results section 5.3.1. Equation (5.2) is used to calculate the temperature-dependent saturation magnetization  $M_{ref}(T)$ , which is necessary for calculating the austenite fraction at any temperature. The estimated uncertainty of the calculated austenite fraction, including the influence of the instrument and the reference sample, is at room temperature  $\pm 0.5$  vol.% and at high temperatures up to  $\pm 1.5$  vol.%.

### 5.2.2 Dilatometry

The dilatometer experiments were carried out in the device described in section 3.3. To compare the results to the experiment in the magnetometer, the heating rate applied was also 3 K/min. After holding for 30 min at 950 °C the cooling rate was chosen to be as close as possible to the cooling in the VSM, to compare the results with those from the magnetometer (see Figure 5.1 for the temperature-time profile). The phase fractions were calculated using the lever-rule [7], taking the initial and the final austenite fraction of the sample, obtained from the magnetization experiment, into account. The martensite fraction,  $f_{\alpha'}$ , was then calculated by:

$$f_{\alpha'} = \frac{\Delta L_2}{\Delta L_{tot}} \cdot f_{\alpha'}^x \quad (5.3)$$

$\Delta L_2$  and  $\Delta L_{tot}$  are illustrated in Figure 3.13 in section 3.3.  $f_{\alpha'}^x$  ( $x = \text{as-received or as-quenched}$ ) is the martensite fraction before or after the austenitization obtained from the room temperature magnetization measurements. A martensite fraction of  $0.77 \pm 0.007$ , obtained as an average of 8 as-received samples, is used for calculating the martensite fraction during heating. The martensite fraction of the austenitized sample (treated in the VSM) at room temperature in the as-quenched condition is used for calculating the martensite fraction during cooling. The estimated uncertainty for the phase fractions by the lever-rule in this study is  $\pm 3$  vol.%.

The characteristic temperatures  $A_{c1}$  and  $M_s$  were determined as the temperatures at which 1 vol.% of austenite and martensite, respectively, were formed. The  $A_{c3}$ -temperature was determined as the temperature at which 99 vol.% of austenite was formed.

The Curie temperature of the material can be also obtained from the dilatometer experiment. In the heating power versus temperature curve a distinct jump occurs when the material becomes paramagnetic. Due to the combined effect of Joule heating and hysteresis heating, a ferromagnetic material is more easily heated by induction than a paramagnetic material, where only the Joule effect contributes to the heating [7, 31]. Therefore, additional energy is needed to heat the material above  $T_C$  [7, 31]. The details of this method to obtain  $T_C$  are described elsewhere [31].

The linear coefficient of thermal expansion ( $\alpha_{th}$ ) was obtained by a least-mean-square fit of the linear regions of the dilatometer curve.  $\alpha_{th}$  was obtained by [32]

$$\alpha_{th} = \frac{1}{L_0} \left( \frac{dL}{dT} \right), \quad (5.4)$$

where  $L_0$  is the initial length and  $dL/dT$  is the change in length as a function of temperature in a range where no transformation occurs. With this equation, the thermal expansion coefficients for austenite,  $\alpha_{th}(\gamma)$ , and bcc-martensite,  $\alpha_{th}(\alpha')$ , were determined.

### 5.2.3 High temperature X-ray diffraction (HT-XRD)

The in-situ X-ray diffraction measurements were carried out in the HT-XRD device described in section 3.4. The scans were measured during annealing at different constant temperatures starting with 30 °C. Between 80 and 950 °C a scan was performed every 58 °C. During the scan, the temperature was kept constant. To avoid long holding times the  $\theta$ - $2\theta$  scans were performed from 38 ° to 88 ° with a step size of 0.05 °- $2\theta$  and a counting time per step of 0.5 s. The scans comprise the three austenite peaks  $\{111\}\gamma$ ,  $\{200\}\gamma$ ,  $\{220\}\gamma$  and the three bcc-martensite peaks  $\{110\}\alpha'$ ,  $\{200\}\alpha'$  and  $\{211\}\alpha'$ . In between the measurement steps, the temperature was raised with a heating rate of 4.5 K/min, so that the average heating rate to 950 °C was 3 K/min. At 950 °C, the temperature was held for 30 min. The overall cooling rate was chosen to be as close as possible to the exponential cooling rate of the VSM, including scans at 400, 230, 100, 75, 50 and 36 °C. The temperature-time profile of the HT-XRD experiment is shown in Figure 5.1.

The volume fraction of austenite was calculated from the net integral intensities using Equation (3.7). The theoretical line intensity values,  $R_{hkl}$ , for copper radiation for the 13Cr6Ni2Mo SMSS at room temperature were calculated using the PowderCell software [33] in the Bragg Brentano configuration and an overall Debye factor of 0.9. The calculated  $R_{hkl}$  values were corrected by the change of the Lorentz Polarization factor, caused by the use of the diffracted-beam monochromator in the XRD-device for the high temperature experiments [34]. The resulting values are listed in Table 5.2. Since the  $\{111\}\gamma$  and  $\{110\}\alpha'$  peaks of the 13Cr6Ni2Mo SMSS overlap, the net integral intensities of these peaks were obtained from a pseudo Voigt approximation. The detection limit of austenite by XRD for the present study is below 2 vol.% (see section 3.4).

*Table 5.2 Theoretical line intensities (R) at room temperature for austenite and ferrite (martensite) peaks in 13Cr6Ni2Mo SMSS for copper radiation ( $\lambda_{Cu}=1.54178 \text{ \AA}$ ) and a monochromator.*

{hkl}	$\{111\}\gamma$	$\{200\}\gamma$	$\{220\}\gamma$	$\{110\}\alpha'$	$\{200\}\alpha'$	$\{211\}\alpha'$	Ref.
$R_{13Cr6Ni2Mo}$	166.6	82.6	37.5	224.3	30.5	53.9	[33, 34]

The austenite and martensite lattice parameters,  $a_\gamma$  and  $a_{\alpha'}$ , were obtained from the measured austenite and martensite peaks [35] and extrapolated against  $\cos^2\theta/\sin\theta$  for the

displacement correction [36]. The linear coefficients of thermal expansion,  $\alpha_{th}(\gamma)$  and  $\alpha_{th}(\alpha')$  were calculated using equation (5.4), where the values of the initial length and length change were replaced by the initial lattice parameter  $a_0$  and the change in the lattice parameter  $\Delta a$  [37].

## 5.3 Results

### 5.3.1 Magnetic measurements

The curve of magnetization versus temperature of the austenite-free sample is shown in Figure 5.3. It can be seen that the magnetization decreases with increasing temperature during heating, which is caused by two overlapping effects. First, the magnetization decreases with increasing temperature and approaches zero characterized by the Curie temperature  $T_C$  [24], which was found to be 670 °C by the derivative of  $dM_{sat}/dT$  during heating. The other effect is the start of austenite formation. Since austenite is paramagnetic the material gradually loses its ferromagnetism when austenite forms, starting at the  $A_{c1}$ -temperature [38]. The curve was fitted to equation (5.2) by a least-squares method between room temperature and 560 °C, which was found to be the  $A_{c1}$ -temperature for this material at a heating rate of 2 K/min [27]. The fitting parameters  $M_{sat0}$ ,  $\beta$  and  $A$  were determined to be 179.2 Am<sup>2</sup>/kg, 0.381, and 0.178 for the austenite-free reference sample. The parameter  $C$  was kept constant at 0.129, which was found by Arrott and Heinrich for pure iron whiskers [29]. The resulting value of  $M_{sat}(ref)$  at room temperature is 170.8 Am<sup>2</sup>/kg at a field of 1.5 T, which is used to calculate the austenite fraction at room temperature.

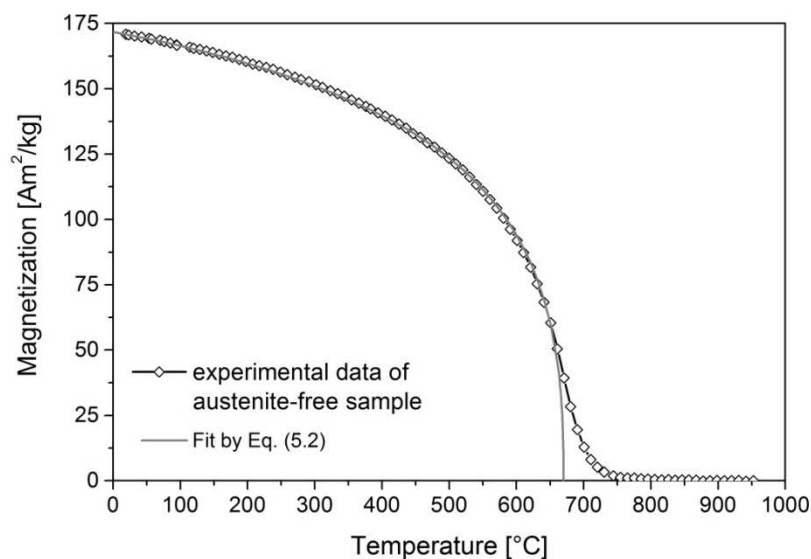


Figure 5.3 Magnetization of the austenite-free sample, measured at 1.5 T, as a function of temperature together with the fit for the reference magnetization.

The extrapolation of the fit by equation (5.2) is also given in Figure 5.3. Equation (5.2) does not account for the magnetic field effect close to the  $T_C$ -temperature. At low or zero

magnetic fields the magnetization will drop to zero according to equation (5.2), as shown in Figure 5.3, whereas at higher magnetic fields the magnetization will approach zero by forming a so called tail (visible in the experimental data of the austenite-free sample in Figure 5.3) [30, 38].

The magnetization curve of an as-received sample during heating, holding and cooling of the austenitization cycle is shown in Figure 5.4. It can be seen that the magnetization decreases with increasing temperature during heating, due to approaching  $T_C$  and the formation of austenite, as described before. At 950 °C, the material is completely austenitic. This becomes apparent during cooling when  $T_C$  is passed, where no change in magnetization due to the effect of  $T_C$  was observed. The material is paramagnetic until martensite starts to form when the magnetization sharply increases. The point where the magnetization increases correlates with the  $M_s$ -temperature, which was found by this experiment to be 230 °C. It can be also seen in Figure 5.4 that in the temperature range 340–230 °C the magnetization is already slightly increased. The underlying reason is not yet clear and needs to be studied further.

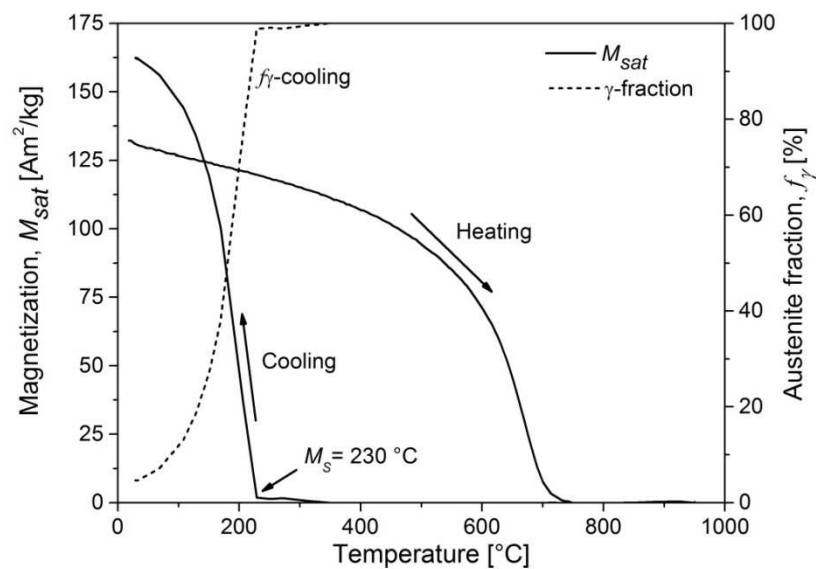


Figure 5.4 Magnetization versus temperature of the as-received sample, measured at a field of 1.5 T, together with the corresponding austenite fraction during cooling. The  $M_s$ -temperature is indicated.

The austenite fraction for temperatures below 560 °C was calculated by equation (5.1) with the reference magnetization values obtained as described above. The evolution of the austenite fraction during heating is shown in Figure 5.5 and during cooling in Figure 5.4. The corresponding martensite fraction during cooling is shown in Figure 5.6. Both the austenite fraction during heating and the martensite fraction during cooling will be compared with the fractions obtained from dilatometry and HT-XRD in the following sections.

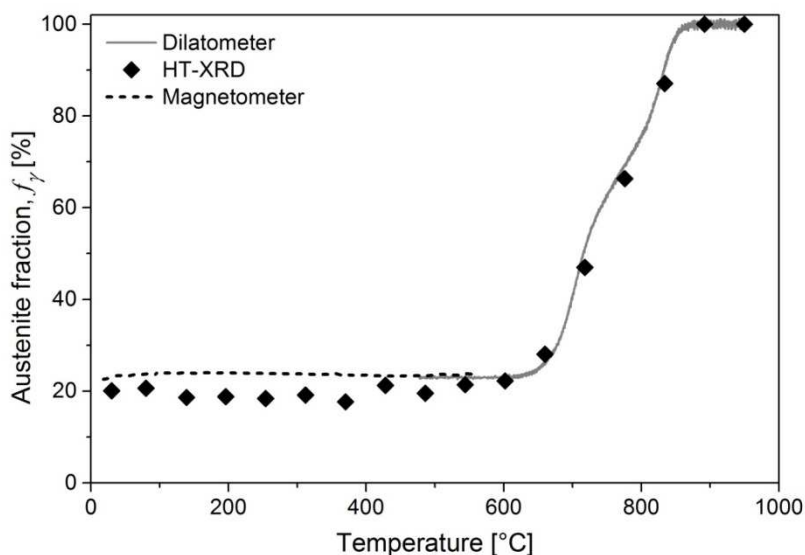


Figure 5.5 Austenite fraction,  $f_\gamma$ , of as-received 13Cr6Ni2Mo SMSS during heating obtained from thermo-magnetic measurement, dilatometry and HT-XRD experiment.

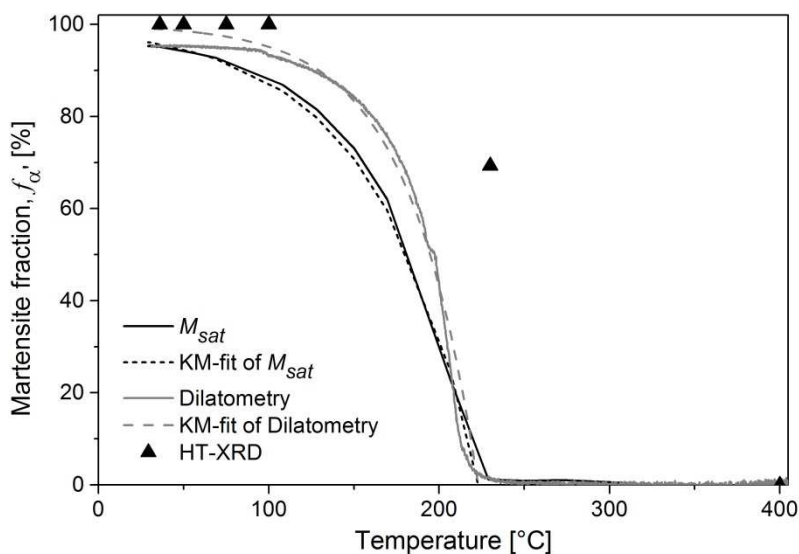


Figure 5.6 Fraction of martensite as a function of temperature during cooling from magnetic experiment ( $M_{sat}$ ), dilatometry and HT-XRD. The fractions from the magnetic and dilatometry measurements are fitted with the modified Koistinen-Marburger (KM) equation (5.9).

The room-temperature curve of the magnetization versus the magnetic field after the austenitization shows a clear increase in magnetization compared to the as-received sample (see Figure 5.2). This increase can be linked to the formation of martensite during cooling from the austenitizing temperature to a fraction that is larger than in the as-received material (see also Figure 5.4). Using the room temperature magnetization value of the austenite-free sample at 1.5 T as a reference in equation (5.1), the austenite fraction of the as-received material is determined to be 22 vol.%, whereas after the experiment the

austenite fraction is determined to be 4.7 vol.%. It was also found that immersion of the sample into liquid nitrogen ( $T = -196\text{ °C}$ ) does not lead to any changes in the magnetization. Thermodynamic calculations for this material using Thermo-Calc [39] indicate that 9 % of austenite is thermodynamically stable at room temperature (see section 4.2), which is almost twice as much as found by the magnetic measurements. This difference might partially be due to the greater inaccuracy for the austenite fraction obtained by the thermodynamic calculations, caused by inaccuracy of the values in the underlying database at such low temperatures, and partially due to local variations in the chemical composition in the steel.

### 5.3.2 Dilatometer experiment

The change in length versus temperature from the dilatometer experiment for the austenitization treatment of the as-received material is shown in Figure 5.7. During heating at 3 K/min the transformation temperatures  $A_{c1}$  and  $A_{c3}$  are determined to be 637 °C and 864 °C. A distinct change in thermal expansion can be seen between these temperatures. The  $M_s$ -temperature found from dilatometry is 233 °C, which is in good agreement with the one found from the magnetic experiment. No martensite finish-temperature could be determined from the dilatometer experiment since the slope of the curve is still changing when approaching room temperature. The Curie temperature, determined from the heating power curve (see section 5.2.2), is found to be 682 °C, which is 12 °C above the one found from the magnetic experiment.

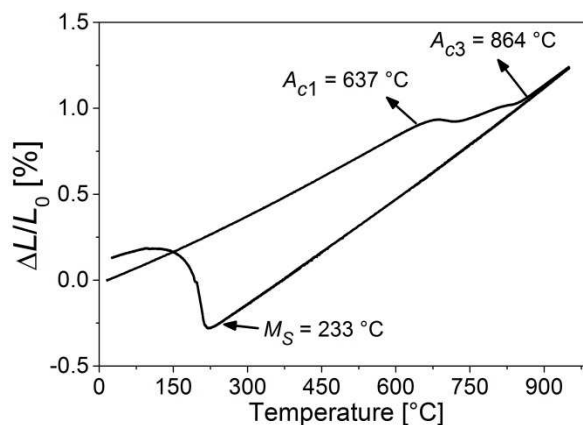


Figure 5.7 Dilatation versus temperature during heating at 3 K/min to 950 °C, holding and cooling. The  $A_{c1}$ ,  $A_{c3}$ - and  $M_s$ -temperatures are indicated.

The linear coefficient of thermal expansion of austenite,  $\alpha_{th}(\gamma)$ , is determined from the slope of the linear fit of the dilatation curve during cooling between 950 and 600 °C to be  $(2.184 \pm 0.001) \times 10^{-5} \text{ K}^{-1}$ . The linear coefficient of thermal expansion of martensite,  $\alpha_{th}(\alpha')$ , is determined from the slope of the linear fit of the dilatation curve during heating between 450 and 600 °C, where both austenite and martensite are present in the microstructure, by:

$$\alpha_{th}(\gamma+\alpha') = \alpha_{th}(\gamma)f_{\gamma,i} + \alpha_{th}(\alpha')f_{\alpha',i} \quad (5.5)$$

with the initial austenite ( $f_{\gamma,i}$ ) and martensite ( $f_{\alpha',i}$ ) fractions of the as-received sample. By this equation  $\alpha_{th}(\alpha')$  is determined to be  $(1.416 \pm 0.001) \times 10^{-5} \text{ K}^{-1}$ .

The austenite fraction during heating, calculated by equation (5.3) with  $f_{\alpha'}^x = 0.77$ , is shown in Figure 5.5. A temporary decrease in the transformation rate between  $A_{c1}$  and  $A_{c3}$  can be seen. The martensite fraction during cooling was calculated using equation (5.3) with  $f_{\alpha'}^x = 0.953$ , where a complete transformation of austenite to martensite was assumed at 50 °C for applying the lever rule. The martensite fraction obtained is shown in Figure 5.6, where it can be seen that the progress of the martensite formation is somewhat different from that found by the magnetic experiment.

### 5.3.3 High-temperature XRD experiment

Figure 5.8 shows some examples of the diffraction spectra from the in-situ HT-XRD measurements during heating at 30, 834, 892 and 950 °C and during cooling at 400, 230 and 36 °C. For better comparison, the scans are shifted along the y-axis. The martensite and austenite peaks are indexed and it can be seen that during heating small peaks of martensite are still present at 834 °C, which disappear at 892 °C. Above 892 °C no martensite peaks are observed. During cooling, martensite is first detected at 230 °C at a fraction of 69 vol.%, which means that the  $M_s$ -temperature is in the range 230–400 °C. At 36 °C no austenite peaks are observed and the material seems to be completely martensitic. On the surface of the sample a very thin oxide layer was formed during the experiment, which explains the peak of  $\text{Cr}_{1.8}\text{Fe}_{0.2}\text{O}_3$  at  $2\theta \approx 54^\circ$ .

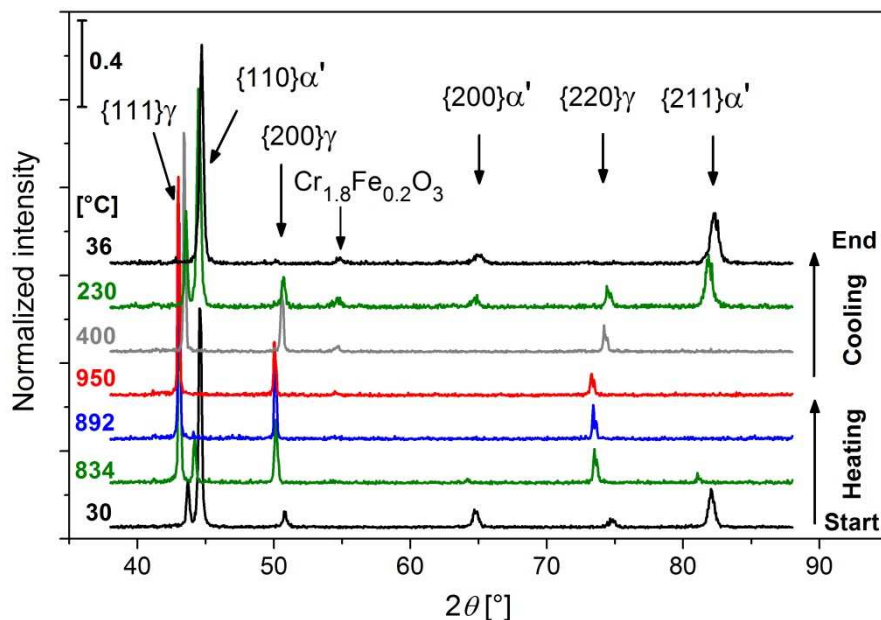


Figure 5.8 Examples of diffraction spectra during austenitization in the HT-XRD equipment, measured with  $\text{CuK}\alpha$ -radiation. The intensity was normalized by the maximum intensity of the scan. Step size:  $0.05^\circ 2\theta$ ; counting time: 0.5 s. For better comparison, the scans are shifted along the y-axis.

During heating and cooling, there is an obvious shift in the positions of the  $2\theta$  peaks, which is due to the thermal expansion of the material during heating and thermal contraction during cooling. The temperature dependence of the lattice parameters for 13Cr6Ni2Mo SMSS during heating is shown in Figure 5.9, from which the following relations were obtained by linear fitting:

$$a_{\gamma} = 3.5915 \text{ \AA} \cdot \left[ 1 + 1.90 \times 10^{-5} \text{ }^{\circ}\text{C}^{-1} (T - 30^{\circ}\text{C}) \right] \pm 0.0044 \text{ \AA} \quad (5.6)$$

$$a_{\alpha'} = 2.8809 \text{ \AA} \cdot \left[ 1 + 1.02 \times 10^{-5} \text{ }^{\circ}\text{C}^{-1} (T - 30^{\circ}\text{C}) \right] \pm 0.0018 \text{ \AA} \quad (5.7)$$

$a_{\gamma}$  and  $a_{\alpha'}$  are the lattice parameters for austenite and martensite, respectively.  $\alpha_{th}$  of austenite and martensite are  $(1.90 \pm 0.11) \times 10^{-5} \text{ K}^{-1}$  and  $(1.02 \pm 0.07) \times 10^{-5} \text{ K}^{-1}$ , respectively, which are about 13 % and 28 % lower than the ones found by dilatometry. The different  $\alpha_{th}$  of austenite and martensite explain the increase of the gap between the  $\{111\}_{\gamma}$  and  $\{110\}_{\alpha'}$  peaks during heating and the decrease during cooling.

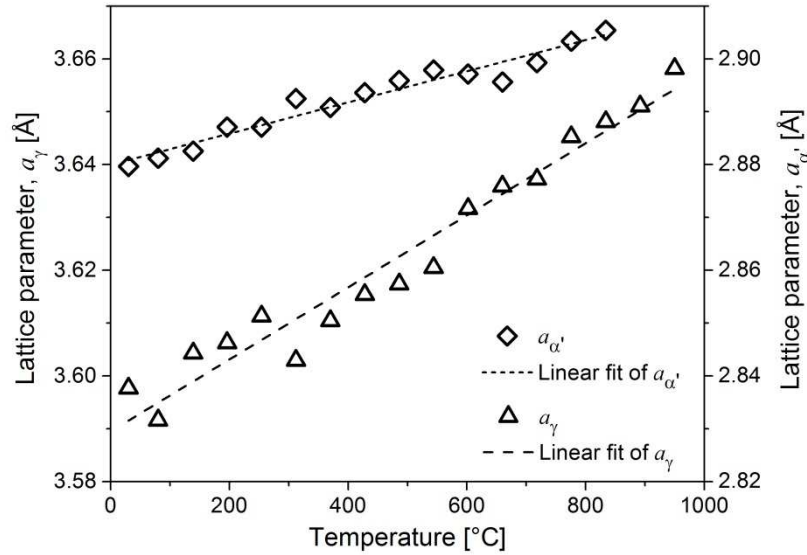


Figure 5.9 Dependence of lattice parameter of bcc-martensite,  $a_{\alpha'}$ , and fcc-austenite,  $a_{\gamma}$ , on temperature during heating to 950 °C.

The austenite and martensite lattice parameters of the as-received sample at 30 °C ( $a_{\gamma,30^{\circ}\text{C}}$ ,  $a_{\alpha',30^{\circ}\text{C}}$ ), obtained by the displacement-correction method, were  $3.5977 \pm 0.0051 \text{ \AA}$  and  $2.8796 \pm 0.0068 \text{ \AA}$ , respectively. The lattice parameter of austenite at room temperature, depending on the alloy composition, can be calculated by the relation of Dyson and Holmes [40], which is a widely used relation for high alloy steels:

$$a_{\gamma}[\text{Å}](\pm 0.0016) = 3.5780 + 0.0330x_{\text{C}} + 0.00095x_{\text{Mn}} - 0.0002x_{\text{Ni}} + 0.0006x_{\text{Cr}} + 0.0220x_{\text{N}} + 0.0031x_{\text{Mo}} + 0.0039x_{\text{Ti}} + 0.0018x_{\text{V}} \quad (5.8)$$

$x_i$  is the concentration of alloying elements  $i$  in wt.%. The factors in equation (5.8) are given for the alloying elements listed in Table 5.1 only. For the bulk composition given in Table 5.1,  $a_\gamma$  was calculated to be  $3.5921 \pm 0.0016 \text{ \AA}$ , which is lower than  $a_{\gamma,30^\circ\text{C}}$  of the as-received sample obtained by the displacement-correction method.

In Figure 5.5 the evolution of the austenite fraction during heating, calculated from the XRD-measurements, is shown. It can be seen that for  $T < 602 \text{ }^\circ\text{C}$  the austenite fraction is nearly constant at around 20 vol.% and is in good agreement with the fraction obtained from thermo-magnetic measurements. For  $T > 602 \text{ }^\circ\text{C}$  the austenite fraction is in very good agreement with the austenite fraction obtained from dilatometry. 100 vol.% austenite is reached at  $896 \text{ }^\circ\text{C}$ . The martensite fraction determined from XRD during cooling is shown in Figure 5.6. It can be seen that martensite is first detected during cooling at  $230 \text{ }^\circ\text{C}$  at a fraction of 69 vol.%, which is much more than in the results from the magnetic and dilatometer experiments. Below  $100 \text{ }^\circ\text{C}$ , no austenite was observed.

Table 5.3 Overview of the results obtained from the magnetization (VSM), dilatometer (DIL) and HT-XRD experiments.  $f_\gamma$ = austenite fraction;  $T_C$ = Curie temperature;  $\alpha_{KM}$ ,  $T_{KM}$  = Koistinen-Marburger rate parameter and theoretical martensite start temperature;  $a_{\gamma,30^\circ\text{C}}$ ,  $a_{\alpha',30^\circ\text{C}}$  = lattice parameter of austenite and martensite of the as-received sample;  $\alpha_{th}(\gamma)$ ,  $\alpha_{th}(\alpha')$  = linear coefficients of thermal expansion of austenite and martensite.

	VSM	DIL	HT-XRD	Unit
$f_\gamma$ as-received	22	-	20	%
$f_\gamma$ after austenitization	4.7	-	< 2	%
$A_{c1}$	-	637	$\geq 600$	$^\circ\text{C}$
$A_{c3}$	-	864	834...892	$^\circ\text{C}$
$M_s$	230	233	-	$^\circ\text{C}$
$T_C$	670	682	-	$^\circ\text{C}$
$a_{\gamma,30^\circ\text{C}}$ (as-rec.)	-	-	$3.5977 \pm 0.0051$	$\text{\AA}$
$a_{\alpha',30^\circ\text{C}}$ (as-rec.)	-	-	$2.8796 \pm 0.0068$	$\text{\AA}$
$\alpha_{th}(\gamma)$	-	$(2.184 \pm 0.001) \times 10^{-5}$	$(1.90 \pm 0.11) \times 10^{-5}$	$\text{K}^{-1}$
$\alpha_{th}(\alpha')$	-	$(1.416 \pm 0.001) \times 10^{-5}$	$(1.02 \pm 0.07) \times 10^{-5}$	$\text{K}^{-1}$
$\alpha_{KM}$	0.017	0.025	-	$\text{K}^{-1}$
$T_{KM}$	224	223	-	$^\circ\text{C}$

## 5.4 Discussion

In this chapter, the phase transformations of the steel 13Cr6Ni2Mo SMSS have been studied during the austenitization treatment using three in-situ experimental techniques: thermo-magnetic measurements, dilatometry and HT-XRD. The main focus was on analysing the

phase fraction evolution during the austenitization and subsequent cooling. In this section, the resulting characteristics of the phase transformations will be discussed, as well as differences between the techniques, which can lead to variations in the results. In Table 5.3 a summary of the obtained results is given.

#### **5.4.1 Austenite formation**

Since during heating the magnetization decreases when approaching the  $T_C$ -temperature, it is not feasible to quantify phase fractions from the magnetic results above the  $A_{c1}$ -temperature from this experiment only. Estimating the  $A_{c1}$ -temperature of the 13Cr6Ni2Mo SMSS using the magnetic technique during heating is difficult, since the  $A_{c1}$ - and the  $T_C$ -temperatures are rather close (see Table 5.3). In this thesis, the  $A_{c1}$ - and  $A_{c3}$ -temperatures of the as-received material were determined from dilatometry and HT-XRD only.

The in-situ HT-XRD experiment reveals that during heating martensite is still present at 834 °C, which is above the decrease in the austenite formation rate between  $A_{c1}$  and  $A_{c3}$ , found by dilatometry. The austenite fraction obtained from the HT-XRD experiment during heating is in agreement with the austenite fraction obtained by the thermo-magnetic measurements and dilatometry (Figure 5.5). It is known for the SMSS steel that Ni is crucial for stabilizing the austenite at room temperature [4, 27, 41], because austenite is enriched in Ni during heating and tempering [4, 27]. Since Ni lowers the temperature range over which austenite is stable in the 13Cr6Ni2Mo SMSS (see chapter 4), Ni-rich zones are transformed first to austenite during heating, followed by Ni-depleted zones. This implies that the austenite formation is occurring in two stages, whereby the Ni-rich regions transform to austenite first, due to their lower  $A_{c1}$ -temperature [42]. This was also assumed by Wang et al. [5] to be the reason for different slopes in the dilatation curve between the austenite start and finish temperatures during heating a low-carbon martensitic stainless steel (in wt.-%: 0.015 C, 0.41 Si, 0.44 Mn, 11.84 Cr, 4.40 Ni, 0.43 Mo) at 3 K/min. They assumed austenite-stabilizing elements to diffuse towards the formed austenite and to enrich it, causing a decrease of these elements in the austenite-surrounding areas. Due to the so obtained differences in the  $A_{c1}$ -temperature the austenite formation process is delayed [5]. Hence, the second stage of austenite formation then takes place at higher temperatures due to the lower local Ni-content. The formation of austenite in two stages is analysed in more detail in chapter 7.

The lattice parameter of austenite in the as-received material at 30 °C, obtained from the HT-XRD results ( $3.5977 \pm 0.0051 \text{ \AA}$ ), is larger than the one calculated for the bulk composition of the sample (cast #1 in Table 5.1) using the relation of Dyson and Holmes [40] ( $3.5921 \pm 0.0016 \text{ \AA}$ ). The Ni-concentration of the austenite in the as-received material of the 13Cr6Ni2Mo SMSS is expected to be increased of about 5 wt.-% compared to the bulk concentration given in Table 5.1 [27], which would decrease the lattice parameter by  $10 \times 10^{-4} \text{ \AA}$  according to equation (5.8). On the other hand, it is most likely that other elements that would increase the lattice parameter of austenite, like Cr and Mn, are enriched in the retained austenite as well [4]. According to equation (5.8) for an assumed difference in Mn-concentration of 0.6 wt.-% the austenite lattice parameter would be increased by  $5.7 \times 10^{-4} \text{ \AA}$  and by  $6 \times 10^{-4} \text{ \AA}$  for an assumed difference of 1 wt.-% in Cr. This could therefore explain the higher value of the austenite lattice parameter of the as-received

material compared to the one calculated for the bulk composition. Hence, the effects of Ni and other elements on the austenite lattice parameter, which are enriched in austenite, are overlapping.

#### 5.4.2 Martensite formation

During cooling martensite will form from austenite by a shear process. The  $M_s$ -temperature could not be determined accurately from the HT-XRD experiment because of the magnitude of the temperature steps. However, the  $M_s$ -temperature is between the temperature steps of 400 and 230 °C, since martensite was first detected at 230 °C with a fraction of 69 vol.%. This is in agreement with the  $M_s$ -temperature determined from the magnetic and dilatometer experiments (see Table 5.3). The pronounced change in length during cooling, found by the dilatometer, is due to the formation of martensite. Because of the low C-content of the material, the carbides fraction, that might form due to auto-tempering during cooling with the rate of the VSM furnace, is expected to be low since less than 2 vol.% are present in equilibrium (see chapter 4).

It can be seen from the magnetic measurements that after austenitizing the sample still contains about 5 vol.% austenite, caused by its thermodynamic stability due to the high concentrations of austenite-stabilizing elements (see chapter 4). Unlike the magnetic technique, no austenite was observed after cooling in the HT-XRD, where the detection limit of austenite is below 2 vol.% (see section 3.4). The martensite fractions obtained from the different techniques are compared in Figure 5.6. It can be seen that the martensite fraction obtained from dilatometry differs from the one obtained from the magnetic experiment. On the other hand, from the HT-XRD experiment it can be seen that as much as 69 vol.% martensite is present at 230 °C, where the martensite formation of the samples treated in the magnetometer and dilatometer just started. The XRD measurements are performed at the surface, with an effective penetration depth of only a few microns and therefore limited information of the overall martensite formation of the sample is obtained. Since the martensite formation is a displacive process, the martensite at the surface is less constrained than within the bulk of the material. This higher martensite fraction at 230 °C is therefore due to enhanced martensite formation at the sample surface, where increased stress relaxation will lead to an easier martensite formation. The measured fractions indicated an  $M_s$ -temperature at the surface that is about 40 °C higher than in the bulk material. Due to the set-up in the HT-XRD device, the actual temperature on the sample surface could be up to 10 °C lower than the measured one (see section 3.4), influencing the start of martensite formation, but not the fact of the enhanced martensite formation at the sample surface. However, both the lower temperature and the enhanced martensite formation on the sample surface could therefore explain why no austenite was measured after cooling in the HT-XRD.

The calculated martensite fraction from the thermo-magnetic and dilatometer experiments were fitted by the least-squares method with the Koistinen-Marburger equation [43] after Magee's derivation [44, 45], expressed as

$$f_{\alpha'} = 1 - \exp[-\alpha_{KM}(T_{KM} - T)], \quad (5.9)$$

where  $\alpha_{KM}$  is a rate parameter, describing the transformation progress for a certain undercooling [44, 46], and  $T_{KM}$  is the theoretical martensite start temperature, which is found to be systematically lower than  $M_s$  [45, 47]. Equation (5.9) describes the fraction of martensite formed from austenite during cooling, which is proportional to the increase in driving force for the austenite to martensite transformation for a certain undercooling [44]. In this work,  $\alpha_{KM}$  was found to be  $0.017 \text{ K}^{-1}$  and  $T_{KM} = 224 \text{ °C}$  from the fit of the martensite fraction from the data of the magnetic experiment. The fit of the martensite fraction obtained from dilatometry gives  $\alpha_{KM} = 0.025 \text{ K}^{-1}$  and  $T_{KM} = 223 \text{ °C}$ . Both values of  $\alpha_{KM}$  are different from the rate parameter  $0.011 \text{ K}^{-1}$  proposed by Koistinen-Marburger for Fe-C-steels [43], which is due to the relatively high alloy content of the 13Cr6Ni2Mo SMSS, since  $\alpha_{KM}$  is dependent on the composition [45]. The differences of  $\alpha_{KM}$  obtained from the fitting are most likely caused by the different techniques applied. Since only the length change contributes to the observation of the phase fraction rather than the total volume of the sample, the anisotropic character of the transformation can affect the results from dilatometry more than from the magnetic experiments. Furthermore, for applying the lever rule during cooling a complete transformation of austenite to martensite was assumed. The martensite fraction obtained was corrected by the austenite fraction of 4.7 vol.%, retained at room temperature after the magnetic experiment. This assumption could be responsible for the higher value of  $\alpha_{KM}$  obtained from the dilatometer data. Therefore, the results obtained from the magnetic experiment are considered to be more accurate, also because the whole sample is measured in the magnetic field. The values obtained for  $T_{KM}$  are quite similar, indicating that the start of martensite formation takes place at the same temperature.

Because of the low number of data points, the modified Koistinen-Marburger fit was not applied for the martensite formation obtained from HT-XRD.

### **5.4.3 Comparison of the in-situ techniques**

The different in-situ techniques used for studying the austenitization of the 13Cr6Ni2Mo SMSS gave a valuable analysis of the phase transformations. However, different results are obtained in terms of austenite/martensite fractions, transformation temperatures, Curie temperatures and thermal expansion coefficients.

Using the saturation magnetization from the magnetic experiment, analysing the austenite fraction at higher temperatures is problematic due to the influence of the Curie temperature. Because of this and the relatively large temperature steps in the XRD experiment, the two-stage austenite formation is only observed by dilatometry. It is shown by the HT-XRD experiment that bcc-martensite is still present until a temperature of 834 °C. A distinct austenite-start and -finish temperature is only obtained from the dilatometry experiment.

The obtained values of the  $M_s$ -temperature from the magnetic measurement and the dilatometer experiment are similar and the HT-XRD experiment only reveals a temperature range for  $M_s$ , which could be refined by adjusting the measuring temperature intervals. A value for the  $M_s$ -temperature obtained from XRD results is, however, not expected to be representative for the bulk behaviour.

The austenite fraction from HT-XRD is expected to be less accurate than obtained from the magnetic experiment [8]. The increase of thermal vibration with increasing temperature is an additional error source, since this causes a decrease of the intensities of the diffraction lines and an increase of the intensity of the background scattering between the diffraction lines [48]. However, due to the monochromator used during the measurements, the influence of the background can be neglected. Furthermore, the temperature effect, described by the Debye-Waller or temperature factor  $\exp(-2M_{DW})$  in the calculation of the theoretical line intensities  $R_{hkl}$  [34, 48], affects all the peaks in a similar way. Hence, these effects cancel. Nevertheless, the  $R$ -values used are only for the bulk composition mentioned in Table 5.1, not taking into account that the composition of the phases will change during the heat treatment. Accounting for this requires knowledge of the phase composition at each step. Another influence on the austenite fraction calculated at higher temperatures might be the formation of the very thin oxide layer containing  $\text{Cr}_{1.8}\text{Fe}_{0.2}\text{O}_3$ , which also lowers the intensities of the diffraction peaks. The influence of the texture on the calculation of the austenite fraction is negligible. The texture is also not significantly changing during the experiment, since the relative proportions of the peak intensities, which give an indication of texturing, are not changing much. This indicates also that there was no strong texture in the as-received material.

During cooling, enhanced martensite formation was detected by HT-XRD due to the increased relaxation of transformation stresses at the sample surface. This leads to a distinct difference in the measured martensite fraction compared to the martensite fraction found in the magnetic and dilatometry experiments (see Figure 5.6) and an estimated increase of the  $M_s$ -temperature of 40 °C. On the other hand, during heating the measured austenite fraction was in agreement with the austenite fraction measured by dilatometry (see Figure 5.5). The austenite formation is a diffusional phase transformation, and not, like martensite formation, a displacive process. Therefore, transformation stresses do not significantly influence the austenite formation at the sample surface and the austenite fractions obtained by HT-XRD can be compared with the austenite fractions obtained by dilatometry.

No retained austenite was detected in the material after cooling to ambient temperature in the HT-XRD device, contrary to the magnetic measurements. This could be due to the enhanced martensite formation on the sample surface, as described above or due to the detection limit of the XRD technique of about 2 vol.% austenite. Furthermore, due to the set-up in the HT-XRD device, the actual temperature on the sample surface could be up to 10 °C lower than the measured one, influencing the start of martensite formation and hence the fraction of austenite retained at room temperature.

The Curie temperatures obtained from the magnetic and dilatometer experiments differ by 12 °C (see Table 5.3). The fewer measuring points during heating in the magnetic experiment will influence the accuracy of the final value of  $T_C$ .

From the dilatometer and the HT-XRD experiments the linear coefficient of thermal expansion for austenite,  $\alpha_{th}(\gamma)$ , and martensite,  $\alpha_{th}(\alpha')$ , are determined. The value of  $\alpha_{th}(\gamma)$  obtained from dilatometry is about  $0.28 \times 10^{-5} \text{ K}^{-1}$  larger than from the HT-XRD experiment. For  $\alpha_{th}(\alpha')$ , the value obtained from dilatometry is about  $0.40 \times 10^{-5} \text{ K}^{-1}$  greater than from the HT-XRD experiment. This might be due to the different kinds of temperature measurement during both experiments.

## 5.5 Conclusions

The austenitizing step of the 13Cr6Ni2Mo SMSS was analysed in-situ using thermo-magnetic measurement, dilatometry and HT-XRD, which gave a valuable analysis of the phase transformations during the austenitization treatment and subsequent cooling.

- 1) From dilatometry the austenite formation of the 13Cr6Ni2Mo SMSS was found to take place in two stages during heating. The two-stage austenite formation is most likely caused by partitioning of Ni into the austenite. The two stages could not be observed with the magnetic measurement, because they occur above the Curie temperature.
- 2) The martensite fraction obtained from the magnetic experiment is considered to be more accurate than the one from the dilatometer. Since only the length change contributes to the observation of the phase fraction rather than the total volume of the sample, the anisotropic character of the transformation affects the results from the dilatometer more than from the magnetometer experiments. Furthermore, the austenite fraction can be calculated directly from the magnetic results.
- 3) The magnetic experiment gives an accurate determination of  $M_s$ . The martensite formation during cooling can be well fitted with the modified Koistinen-Marburger equation with  $\alpha_{KM} = 0.017 \text{ K}^{-1}$  and  $T_{KM} = 224 \text{ }^\circ\text{C}$ .
- 4) Enhanced martensite formation at the sample surface was detected by X-ray diffraction, which is assumed to be due to the increased relaxation of transformation stresses at the sample surface.
- 5) About 5 vol.% retained austenite is detected after cooling from the austenitization temperature, which is due to the thermodynamic stability of austenite at room temperature in this composition. The existence of this retained austenite may affect the subsequent heat treatment process, i.e. tempering and stress-relief treatment.

## REFERENCES

- [1] P.D. Bilmes, M. Solari and C.L. Llorente: *Mater. Charact.*, 2001, vol. 46, pp. 285-96.
- [2] Y.K. Lee, H.C. Shin, D.S. Leem, J.Y. Choi, W. Jin and C.S. Choi: *Mater. Sci. Technol.*, 2003, vol. 19, pp. 393-8.
- [3] C.A.D. Rodrigues, P.L.D. Lorenzo, A. Sokolowski, C.A. Barbosa and J.M.D.A. Rollo: *Mater. Sci. Eng. A*, 2007, vol. 460, pp. 149-52.
- [4] Y.Y. Song, D.H. Ping, F.X. Yin, X.Y. Li and Y.Y. Li: *Mater. Sci. Eng. A*, 2010, vol. 527, no.3, pp. 614-8.
- [5] P. Wang, S. Lu, D. Li, X. Kang and Y. Li: *Acta Metall. Sinica*, 2008, vol. 44, no. 6, pp. 681-5.
- [6] X.P. Ma, L.J. Wang, C.M. Liu and S.V. Subramanian: *Mater. Sci. Eng. A*, 2011, vol. 528, no. 22-23, pp. 6812-8.
- [7] T.A. Kop: *A dilatometric study of the austenite/ferrite interface mobility*, PhD Thesis, Technische Universiteit Delft, The Netherlands, 2000.
- [8] L. Zhao, N.H. van Dijk, E. Brück, J. Sietsma and S. van der Zwaag: *Mater. Sci. Eng. A*, 2001, vol. 313, no. 1-2, pp. 145-52.

- [9] C. Lemoine, A. Fnidiki, J. Teillet, M. Hédin and F. Danoix: *Scr. Mater.*, 1998, vol. 39, no. 1, pp. 61-6.
- [10] K.H. Lo, J.K.L. Lai, C.H. Shek and D.J. Li: *Mater. Sci. Eng. A*, 2007, vol. 452–453, pp. 149-60.
- [11] A.M. Beese and D. Mohr: *Exp. Mech.*, 2011, vol. 51, no. 5, pp. 667-76.
- [12] G.F. da Silva, S.S.M. Tavares, J.M. Pardal, M.R. Silva and H.F.G. Abreu: *J. Mater. Sci.*, 2011, vol. 46, no. 24, pp. 7737-44.
- [13] K. Mumtaz, S. Takahashi, J. Echigoya, Y. Kamada, L.F. Zhang, H. Kikuchi, K. Ara and M. Sato: *J. Mater. Sci.*, 2004, vol. 39, no. 6, pp. 1997-2010.
- [14] S.S.M. Tavares, J.M. Pardal, J.A. de Souza, J.M. Neto and M.R. da Silva: *J. Alloys Compd.*, 2006, vol. 416, no. 1-2, pp. 179-82.
- [15] S.S.M. Tavares, J.M. Neto and J.R. Teodosio: *J. Magn. Magn. Mater.*, 1998, vol. 182, no. 1-2, pp. 193-8.
- [16] S.S.M. Tavares, D. Fruchart and S. Miraglia: *J. Alloys Compd.*, 2000, vol. 307, pp. 311-7.
- [17] S.S.M. Tavares, R.F. de Noronha, M. R. da Silva, J.M. Neto and S. Pairis: *Mater. Res.*, 2001, vol. 4, no. 4, pp. 237-40.
- [18] N. Luzginova, L. Zhao and J. Sietsma: *Mater. Sci. Eng. A*, 2007, vol. 448, no. 1-2, pp. 104-10.
- [19] S.S.M. Tavares, S.R. Mello, A.M. Gomes, J.M. Neto, M.R. da Silva and J. M. Pardal: *J. Mater. Sci.*, 2006, vol. 41, no. 15, pp. 4732-6.
- [20] M. Amirthalingam, M.J.M. Hermans, L. Zhao and I.M. Richardson: *Metall. Mater. Trans. A*, 2010, vol. 41A, no. 2, pp. 431-9.
- [21] D. San Martin, N.H. van Dijk, E. Jiménez-Melero, E. Kampert, U. Zeitler and S. van der Zwaag: *Mater. Sci. Eng. A*, 2010, vol. 527, no. 20, pp. 5241-5.
- [22] D.C. Jiles: *Acta Mater.*, 2003, vol. 51, no. 19, pp. 5907-39.
- [23] P.E. Merinov and A.G. Mazepa: *Industrial Laboratory (Diagn. Mater.)*, 1997, vol. 63, no. 3, pp. 149-53.
- [24] W.D. Callister, Jr.: *Fundamentals of Materials Science and Engineering: An integrated approach*, 2<sup>nd</sup> ed., p. 743, John Wiley & Sons, Inc., 2005.
- [25] Y. Song, X. Li, L. Rong and Y. Li: *J. Mater. Sci. Technol.*, 2010, vol. 26, no. 9, pp. 823-6.
- [26] S. Zhang, H. Terasaki and Y.I. Komizo: *Proceedings of the Twentieth (2010) International Offshore and Polar Engineering Conference*. Beijing, China: The International Society of Offshore and Polar Engineers (ISOPE), 20-25 June 2010, p. 308–11.
- [27] Y. Wei: *Microstructural Characterization and Mechanical Properties of Super 13% Cr Steel*, PhD Thesis, The University of Sheffield, England, 2005.
- [28] J. Crangle and W. Sucksmith: *J. Iron Steel Inst.*, 1951, vol. 168, pp. 141-51.
- [29] A.S. Arrott and B. Heinrich: *J. Appl. Phys.*, 1981, vol. 52, no. 3, pp. 2113-5.
- [30] A.E. Berkowitz: Constitution of Multiphase Alloys, in: A.E. Berkowitz and E. Kneller (Eds.): *Magnetism and Metallurgy*, vol. 1, p. 344, Academic Press, Inc., New York, 1969.
- [31] A. Verma, M. Sundararaman, J.B. Singh and S.A. Nalawade: *Meas. Sci. Technol.*, 2010, vol. 21, no. 10, pp. 1-10.

- [32] R.F. Speyer: *Thermal analysis of materials*, p. 165, Marcel Dekker, Inc., New York, 1994.
- [33] PowderCell for Windows, Version 2.4 (Computer Software), Berlin, Germany: BAM; 2000.
- [34] C.F. Jaczak, J.A. Larson and S.W. Shin: *Retained austenite and its measurements by X-ray diffraction*, Society of Automotive Engineers, Inc., Warrendale, 1980.
- [35] B.D. Cullity: *Elements of X-ray diffraction*, p. 351, Addison-Wesley, Reading, MA, 1978.
- [36] B.D. Cullity: *Elements of X-ray diffraction*, p. 359-60, Addison-Wesley, Reading, MA, 1978.
- [37] H.A. McKinstry, C.Y. Huang and S.T. McKinstry: Thermal expansion by X-ray diffraction, in: R.E. Taylor (Ed.): *Thermal expansion of solids*, CINDAS Data Series on Materials Properties, pp. 193-205, ASM International, Materials Park, OH, 1998.
- [38] R.M. Bozorth, *Ferromagnetism*, pp. 715-9, John Wiley & Sons, Inc., Hoboken, NJ, 2003.
- [39] Thermo-Calc Software package, Version S, Database TCFeV6.2, Stockholm, Sweden, 2011.
- [40] D.J. Dyson and B. Holmes: *J. Iron Steel Inst.*, 1970, vol. 208, pp. 469-74.
- [41] T.G. Gooch, P. Woollin and A.G. Haynes: in *Supermartensitic Stainless Steel '99*, KCI Publishing BV, Brussels, 1999, pp. 188-95.
- [42] R. Kapoor, L. Kumar and I.S. Batra: *Materi. Sci. Eng. A*, 2003, vol. 352, no. 1-2, pp. 318-24.
- [43] D.P. Koistinen and R.E. Marburger: *Acta Metall.*, 1959, vol. 7, no. 1, pp. 59-60.
- [44] C.L. Magee: The nucleation of martensite, in: *Phase transformations*, pp. 115-56, American Society for Metals, Metals Park, Ohio, 1970.
- [45] S.M.C. van Bohemen and J. Sietsma: *Mater. Sci. Technol.* 2009, vol. 25, no. 8, pp. 1009-12.
- [46] S.M.C. van Bohemen, J. Sietsma, R. Petrov, M.J.M. Hermans and I.M. Richardson: *Mater. Trans.*, 2006, vol. 47, no. 3, pp. 607-11.
- [47] S.M.C. van Bohemen and J. Sietsma: *Metall. Mater. Trans. A*, 2009, vol. 40A, no. 5, pp. 1059-68.
- [48] B.D. Cullity: *Elements of X-ray diffraction*, p. 135-9, Addison-Wesley, Reading, MA, 1978.

# 6

## In-situ thermo-magnetic investigation of the austenitic phase during tempering of an SMSS<sup>1</sup>

The formation of austenite during tempering of the 13Cr6Ni2Mo SMSS was investigated using the thermo-magnetic technique (VSM) to establish the kinetics of the martensite to austenite transformation and the stability of austenite. The austenite fraction was obtained from in-situ magnetization measurements. It was found that during heating to the tempering temperature 1 to 2 vol.% of austenite, retained during quenching after the austenitization treatment, decomposed between 350 and 480 °C. The activation energy for martensite to austenite transformation was found by JMAK-fitting to be 233 kJ/mol. This value is similar to the activation energy for Ni and Mn diffusion in iron and supports the assumption that partitioning of Ni and Mn to austenite are mainly rate determining for the austenite formation during tempering. This also indicates that the stability of austenite during cooling after tempering depends on these elements. With increasing tempering temperature the thermal stability of austenite is decreasing due to the lower concentrations of austenite-stabilizing elements in the increased fraction of austenite. After cooling from the tempering temperature the retained austenite was further partially decomposed during holding at room temperature. This appears to be related to previous martensite formation during cooling.

Furthermore, an approach was described to calculate the magnetization and hence the austenite fraction depending on the chemical composition, which showed good agreement with the experimental results.

### 6.1 Introduction

As mentioned in chapter 2, the heat treatment of SMSS is usually carried out in three steps: austenitizing and two tempering steps. The austenitization is carried out above  $A_{c3}$ , after which air cooling might be sufficient for SMSS to obtain an almost fully martensitic microstructure [1] of highly dislocated laths [2]. Due to the low C-content the morphology of

---

<sup>1</sup> This chapter is based on: A. Bojack, L. Zhao, P.F. Morris and J. Sietsma: In Situ Thermo-magnetic Investigation of the Austenitic Phase During Tempering of a 13Cr6Ni2Mo Supermartensitic Stainless Steel, *Metall. Mater. Trans. A*, 2014, vol. 45A, p. 5956-67.

martensite is lath- or plate-like with a bcc crystal structure [3]. The subsequent first tempering step is carried out above  $A_{c1}$  to form austenite that should be stable during cooling to room temperature. If  $A_{c1}$  is exceeded by too much, fresh martensite will form during cooling, having a detrimental effect on the ductility [4, 5]. The reason for the fresh martensite formation lies in the increase of the volume fraction of austenite, having lower concentrations of austenite-stabilizing elements, which makes these areas less stable against transformation during cooling. During a second tempering step fresh martensite will be tempered and partly transformed to austenite that is stable during cooling to room temperature [4, 6-8], provided the tempering temperature is again above the  $A_{c1}$  of the fresh martensite.

The stabilization of austenite at room temperature is obtained by austenite stabilizing elements like Ni, Mn and C, that enrich austenite [4, 7-9]. Since the C-content in SMSS is very small (< 0.03 wt.%), it is mainly Ni [10, 11] and Mn [12] that are responsible for the austenite stabilization, leading to a martensite start temperature,  $M_s$ , below room temperature. However, it was also reported that the stability of austenite may have substructural origins, like an increased barrier against the shear of the martensitic transformation caused by a high dislocation density within the austenite particles [8] and the concentration of quenched-in vacancies, which is increasing with increasing tempering temperature [13].

The fraction of retained austenite in SMSS is very sensitive to the heat treatment, where small changes in the tempering temperature can have a significant effect on the mechanical properties like yield strength and hardness. In offshore applications these steels have to meet strict requirements [4] such as a high yield strength in combination with good toughness, even at sub-zero temperatures, and good stress-corrosion resistance. To meet the required properties of the material the heat treatment has to be accurately controlled.

This chapter aims to obtain an improved understanding of the mechanisms involved in the formation and stabilization of austenite in the 13Cr6Ni2Mo SMSS by means of thermo-magnetic in-situ analysis of the evolution of the phase fractions during tempering at different temperatures. Magnetic techniques, by analysing the saturation magnetization, offer a higher accuracy in estimating the austenite fraction compared to X-ray diffraction (XRD) techniques or metallography [14], since the saturation magnetization depends only on the phases present in the material and their composition, but is insensitive to other microstructural features like texture or defects [15, 16]. Moreover, a direct bulk measurement can be performed, offering a truly representative analysis of the austenite fraction. Since austenite is paramagnetic, calculating its fraction from saturation magnetization measurements needs a knowledge of the magnetization of a fully ferromagnetic sample of the same composition. A method was developed to obtain the austenite fraction from the magnetic measurements during tempering of the 13Cr6Ni2Mo SMSS. Thus, the kinetics of the martensite to austenite transformation and the stability of austenite in SMSS was established.

## **6.2 Experimental**

The chemical composition of the studied 13Cr6Ni2Mo SMSS is shown in Table 6.1. The as-received material was delivered in the double-tempered condition with a microstructure

consisting of martensite, retained austenite and a very small fraction of carbides, nitrides and carbo-nitrides [4]. The chemical composition is given in Table 6.1.

Table 6.1 Chemical composition of the tested 13Cr6Ni2Mo SMSS (in wt.%), balance Fe.

Cast	C	Cr	Ni	Mo	Mn	Si	V	Ti	N
# 2	0.020	12.27	5.62	2.01	0.42	0.21	0.18	0.01	0.016

### 6.2.1 Magnetic measurements

The in-situ thermo-magnetic experiments were carried out in the VSM described in section 3.2. The heat treatment was performed by austenitization and double tempering treatment. During the tempering treatment the magnetization of the samples was measured at a constant magnetic field of 1.5 T, where the magnetization is close to its saturation value. Prior to the tempering treatment, the samples were austenitized in an air furnace at  $T_A = 1050\text{ }^\circ\text{C}$  for  $t_A = 30.5\text{ h}$ , which was chosen to produce a higher homogeneity, and subsequently quenched in water. The first tempering step was carried out in the VSM with a heating rate of 5 K/min at different temperatures,  $T_{1t}$ , between 585 and 695 °C for  $t_{1t} = 4\text{ h}$  followed by natural cooling in the furnace. The experiments for the second tempering step were carried out at  $T_{2t} = 550\text{ }^\circ\text{C}$  for  $t_{2t} = 2\text{ h}$  with selected single tempered samples. During cooling the temperature approximately follows an exponential relation, as described by equation 3.1 ( $T_0 = T_{1t}$  or  $T_{2t}$ ,  $T_E \approx 35\text{ }^\circ\text{C}$ ,  $\tau \approx 28\text{ min}$ ). A schematic of the applied heat treatment is shown in Figure 6.1.

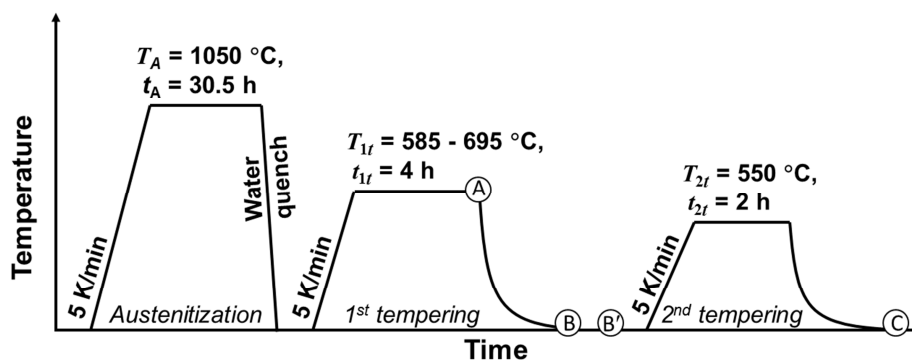


Figure 6.1 Scheme of the applied heat treatment steps.  $T_A$ ,  $t_A$ : Austenitizing temperature and time.  $T_{1t}$ ,  $t_{1t}$  and  $T_{2t}$ ,  $t_{2t}$ : Tempering temperature and time of first and second tempering, respectively. A, B, B', and C are points of time used for descriptions in the text. A: end point of the tempering step. B: end point right after cooling from first tempering at about 30 °C. B': end point of holding at room temperature after first tempering. C: end point right after cooling from second tempering at about 30 °C.

To analyse the stability of retained austenite at room temperature after the first tempering step, the magnetization of the single tempered samples was measured at 1.5 T up to 200 h (point B' in Figure 6.1).

The volume fraction of austenite,  $f_\gamma$ , was determined from the magnetization of the austenite-containing sample,  $M_{sat}(c)$ , by relating it to the magnetization of an austenite-free reference sample of the same composition,  $M_{sat}(ref)$  [14, 17], according to

$$f_\gamma = 1 - \frac{M_{sat}(c)}{M_{sat}(ref)} \cdot \quad (6.1)$$

An austenite-free reference sample was obtained by tempering an austenitized and quenched sample for 2 h at 400 °C, in order to destabilize any remaining austenite. Equation (6.1) is temperature dependent. The temperature-dependent magnetization of the austenite-free sample ( $M_{ref}(T)$ ), heated at 5 K/min to 950 °C in the furnace of the VSM, was described by the relation of Arrott and Heinrich [18] up to  $A_{c1}$ -temperature:

$$M_{ref}(T) = M_{sat0} \frac{(1-s)^\beta}{1 - \beta s + A s^{3/2} - C s^{7/2}}, \quad (6.2)$$

where  $M_{sat0}$  is the saturation magnetization at 0 K (-273 °C),  $\beta$ ,  $A$  and  $C$  are material dependent constants, and  $s = T/T_C$ , where  $T_C$  denotes the Curie temperature. As mentioned in chapter 5, determining the magnetization of an austenite-free reference sample above  $A_{c1}$  is not straightforward. Also, extrapolation of equation (6.2) is not possible, since it does not account for the influence of the magnetic field on the magnetization above  $T_C$ . This is explained in more detail in the results of section 6.3.1. In this chapter the magnetization of a fully martensitic sample was determined from the experimental results at temperatures between  $A_{c1}$  and 695 °C, the highest applied  $T_{It}$ .

The estimated uncertainty of the calculated austenite fraction at room temperature, including the influence of the instrument and the reference sample, is  $\pm 0.5$  vol.% and at high temperatures up to  $\pm 1.5$  vol.%.

## **6.2.2 Optical and scanning electron microscopy**

Microstructural analysis of the tempered samples was carried out in the optical microscope and the SEM, which is described in section 3.5 together with the sample preparation.

## **6.2.3 Thermodynamic calculations**

Thermodynamic calculations using the Thermo-Calc software [19] with the TCFE v6.2 database were performed to obtain the equilibrium fraction and composition of austenite. The phases allowed to be present during the calculations were: fcc-iron, bcc-iron,  $M_{23}C_6$ ,  $M_6C$  and liquid (see chapter 4).

## 6.3 Results

### 6.3.1 Magnetization of martensite for calculating the austenite fraction at elevated temperatures

The curve of magnetization versus temperature of the austenite-free sample is shown in Figure 6.2. The curve was fitted to equation (6.2) by a least-squares method between room temperature and 560 °C, which was found to be the  $A_{c1}$ -temperature for this material at a heating rate of 2 K/min [4].  $T_C$  was determined in chapter 5 to be 670 °C by the same magnetic technique. The fitting parameters  $M_{sat0}$ ,  $\beta$  and  $A$  were determined to be 179.2 Am<sup>2</sup>/kg, 0.381, and 0.178 for the austenite-free sample in chapter 5. The parameter  $C$  was kept the same as found by Arrott and Heinrich [18] for pure iron, 0.129. Thus, the austenite fraction for temperatures below 560 °C can be calculated by equation (6.1). For calculating the austenite fraction at temperatures above  $A_{c1}$  theoretical values for the magnetization of martensite,  $M_{sat,\alpha}$ , are necessary, which also consider the influence of the applied magnetic field, since equation (6.2) does not account for the magnetic field effect close to the  $T_C$ -temperature. At low or zero magnetic fields the magnetization will drop to zero according to equation (6.2) as shown in Figure 6.2, whereas at higher magnetic fields the magnetization will approach zero by forming a so called tail (visible in the experimental data of the austenite-free sample in Figure 6.2a) [20, 21]. To obtain the saturation magnetization of martensite above  $A_{c1}$  the results from the first tempering step were considered. As will be discussed in section 6.3.2, we know for each  $T_{It}$  if the  $M_s$ -temperature of austenite, formed during tempering, is either below or above room temperature. In order to obtain the magnetization values for martensite between  $A_{c1}$  and  $T_C$ , the following two cases, depending on the martensite formation during cooling, were considered:

- 1) No martensite is formed during cooling from  $T_{It}$  to room temperature:

The austenite fraction immediately after cooling from  $T_{It}$  was considered to be equal to that at the end of the tempering at  $T_{It}$  and hence constant during cooling to room temperature. Thus, the austenite fraction at the end of the tempering at  $T_{It}$  is known in these cases and  $M_{sat,\alpha}(T)$  at the corresponding  $T_{It}$  was obtained by equation (6.1).

- 2) Martensite is formed during cooling from  $T_{It}$  to room temperature:

The austenite fraction was calculated between  $M_s$  and room temperature by equation (6.2) with the parameters from the fit of the austenite-free sample together with equation (6.1). By this, the austenite fraction present at  $M_s$  was obtained. The austenite fraction was considered to be constant during cooling between  $T_{It}$  and  $M_s$  and was therefore known at the end of the tempering at  $T_{It}$ . Thus,  $M_{sat,\alpha}(T)$  at  $T_{It}$ , when martensite was formed during subsequent cooling to room temperature, was obtained.

$M_{sat,\alpha}(T)$  above  $A_{c1}$  was then obtained from equation (6.1) combined with  $M_{sat,\alpha}(T) = M_{sat}(f_\gamma T)/(1-f_\gamma)$ . The thus obtained  $M_{sat,\alpha}(T)$  was fitted by a polynomial equation to describe the curve between 560 and 695 °C, as shown in Figure 6.2. By this procedure the austenite fraction for the 13Cr6Ni2Mo SMSS can be calculated in the entire temperature range between room temperature and 695 °C, the highest applied  $T_{It}$ . Extrapolation to higher temperatures was not carried out in the present study.

For the austenite-free sample an  $A_{c1}$ -temperature of 580 °C was determined from the austenite fraction, defined as the temperature at which 1 % of austenite had formed. This value is 20 °C higher than the  $A_{c1}$ -temperature of 560 °C determined by Wei [4].

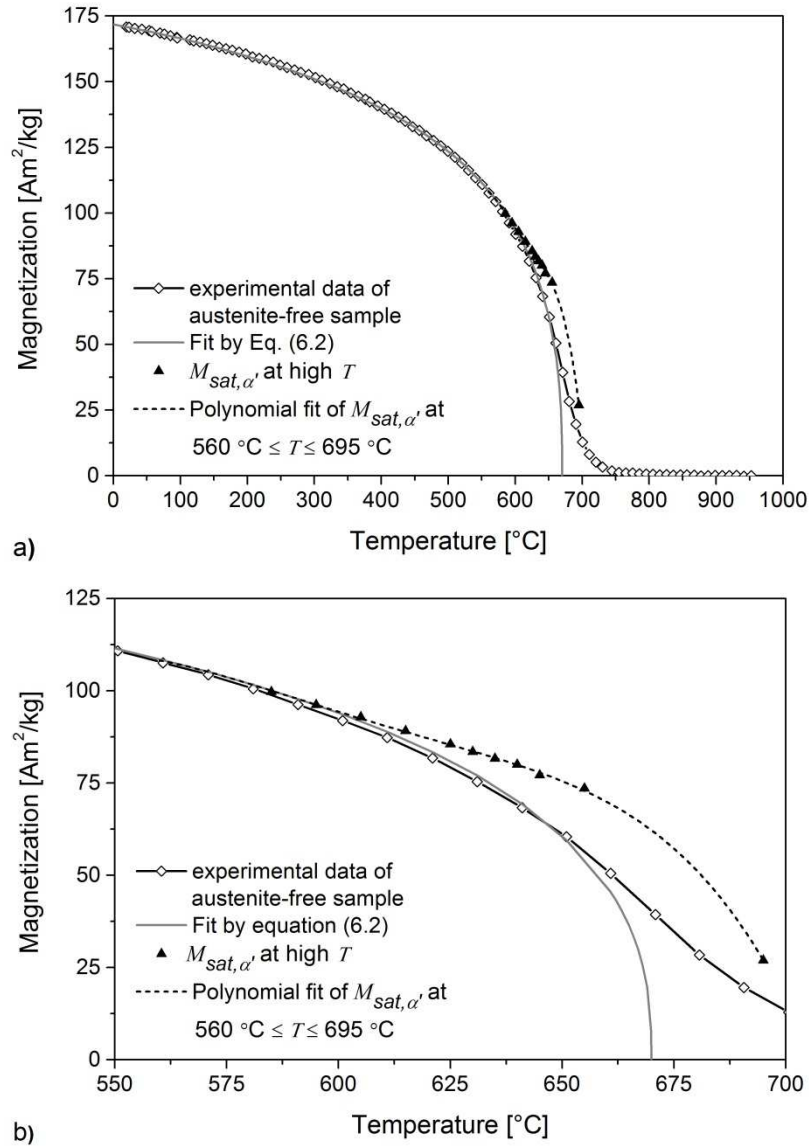


Figure 6.2 a) Magnetization of an austenite-free sample, measured at 1.5 T, as a function of temperature together with the fit for the magnetization of martensite ( $M_{sat,\alpha}$ ) for  $T \leq 560$  °C by equation (6.2) and  $M_{sat,\alpha'}$  at 1.5 T for temperatures 560 °C ≤  $T$  ≤ 695 °C. b) Enlargement of a) showing the transition between the low and high temperature fit.

The influence of carbides on the saturation magnetization was neglected, since the equilibrium fraction of carbides for the 13Cr6Ni2Mo SMSS was found to be less than 2 vol.% (see chapter 4). Since during tempering carbide formation occurs at the same time as the austenite formation and growth, it is not possible to separate these two phases by magnetization measurements. Moreover, during heating of an as-received sample to 950 °C

in chapter 5 no variations of the magnetization were detected that could be related to carbide formation.

### 6.3.2 Microstructural analysis during first tempering step

#### Evolution of magnetization

The curves of magnetization versus time for selected first tempering temperatures are shown in Figure 6.3a. In Figure 6.3b the magnetization is plotted against the temperature for the heating, holding and cooling.

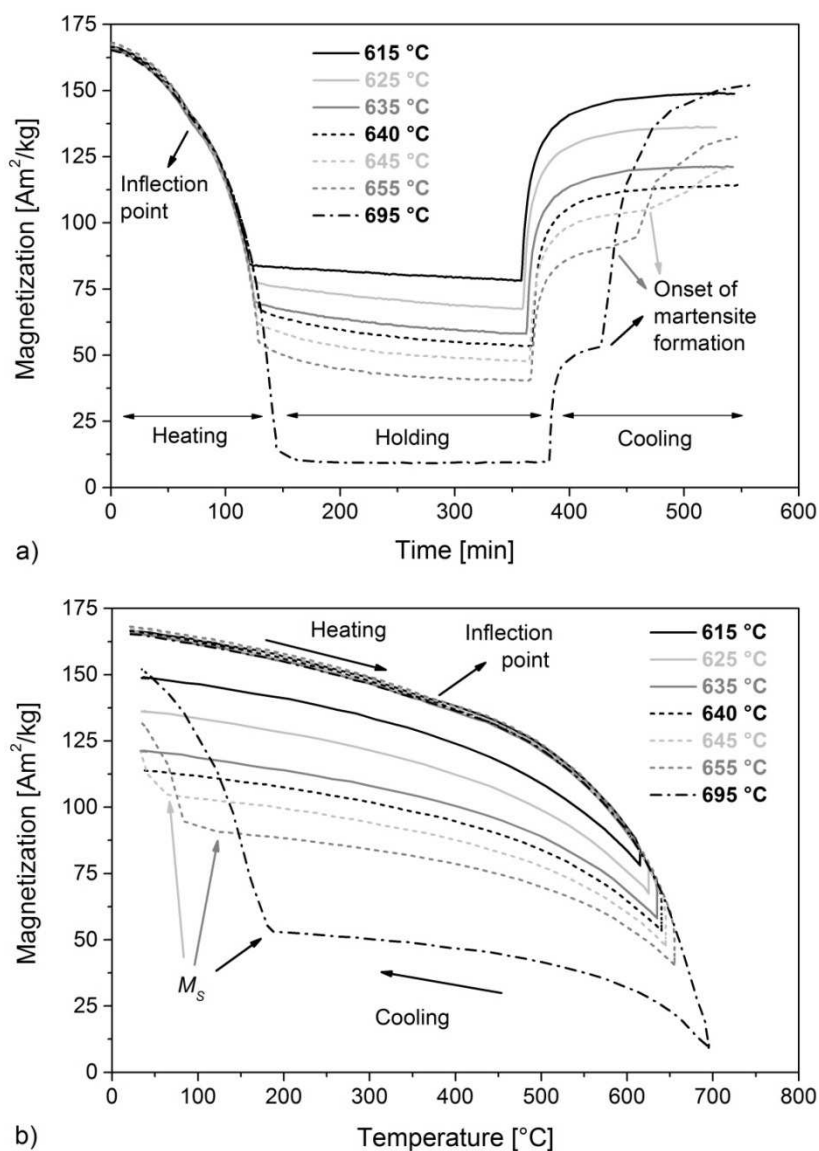


Figure 6.3 Magnetization versus a) time and versus b) temperature during the first tempering step, measured at a field of 1.5 T. The tempering temperatures  $T_{i1}$  are indicated.

During heating the magnetization is decreasing because of the temperature dependence of the magnetization [22]. Moreover, the magnetization decreases on passing through  $A_{c1}$ , at which the paramagnetic phase austenite starts to form [21]. After about 70 min heating (Figure 6.3a) at around 350 °C (Figure 6.3b) an inflection is observed, which was not observed in the curve of magnetization versus temperature of the reference sample (Figure 6.2). During holding the magnetization is decreasing. At higher  $T_{It}$  the rate of decrease is initially higher and decreases with holding time. During cooling the magnetization is increasing again and is at room temperature lower than before the tempering, indicating that more austenite was retained. During cooling from  $T_{It} \geq 645$  °C the magnetization additionally shows an abrupt increase, indicating the formation of a ferromagnetic phase during cooling, which is interpreted as martensite formation. With increasing tempering temperature the  $M_s$ -temperature is increasing.

### ***Evolution of the austenite fraction***

The austenite fraction during heating to  $T_{It}$ , derived from the data in Figure 6.3, is shown in Figure 6.4a. The initial austenite fraction is between  $2$  and  $4 \pm 0.5$  vol.%, where the scatter in the values above the uncertainty of  $\pm 0.5$  vol.% is considered to be due to differences of the austenite fraction in the initial microstructures of the samples. These initial austenite fractions indicate that the martensite transformation after quenching from the austenitization temperature was not complete. During heating, the austenite fraction starts to decrease at approximately 350 °C and reaches a minimum at approximately 480 °C. For  $T > 480$  °C it increases until the final tempering temperature.

The minimum in austenite fraction occurs around the temperature, where the inflection point in the magnetization values during heating was observed. This austenite decomposition may not be complete for all the samples, since only an amount of  $1$  to  $2 \pm 1.5$  vol.% is decomposed. Hence, the two samples that started with a volume fraction of about  $4 \pm 0.5$  vol.% did not show a complete austenite decomposition during heating. Even though the austenite fraction, decomposed during heating, lies within the estimated uncertainty of  $\pm 1.5$  vol.%, the decrease in the curves of the austenite fraction during heating is apparent at the same temperature and is considered to be due to austenite decomposition. In Figure 6.4a the equilibrium fraction of austenite is plotted as well, which is higher than the measured one during heating and shows a minimum at 400 °C, which is 80 °C below the measured minimum.

The change in austenite fraction during holding at  $585$  °C  $\leq T_{It} \leq 695$  °C is shown in Figure 6.4b. The higher  $T_{It}$ , the more austenite was already formed during heating, therefore the initial austenite fraction at  $T_{It}$  is increasing with increasing  $T_{It}$ . Moreover, the higher  $T_{It}$  the more austenite is formed during tempering, until  $T_{It} = 655$  °C. With increasing  $T_{It}$  the transformation rate at the beginning of the holding is increasing and slows down to the end of the holding at higher temperatures. During heating to 695 °C already most of the austenite was formed and less austenite was formed during holding, at which the austenite fraction becomes stable after about 50 min of holding.

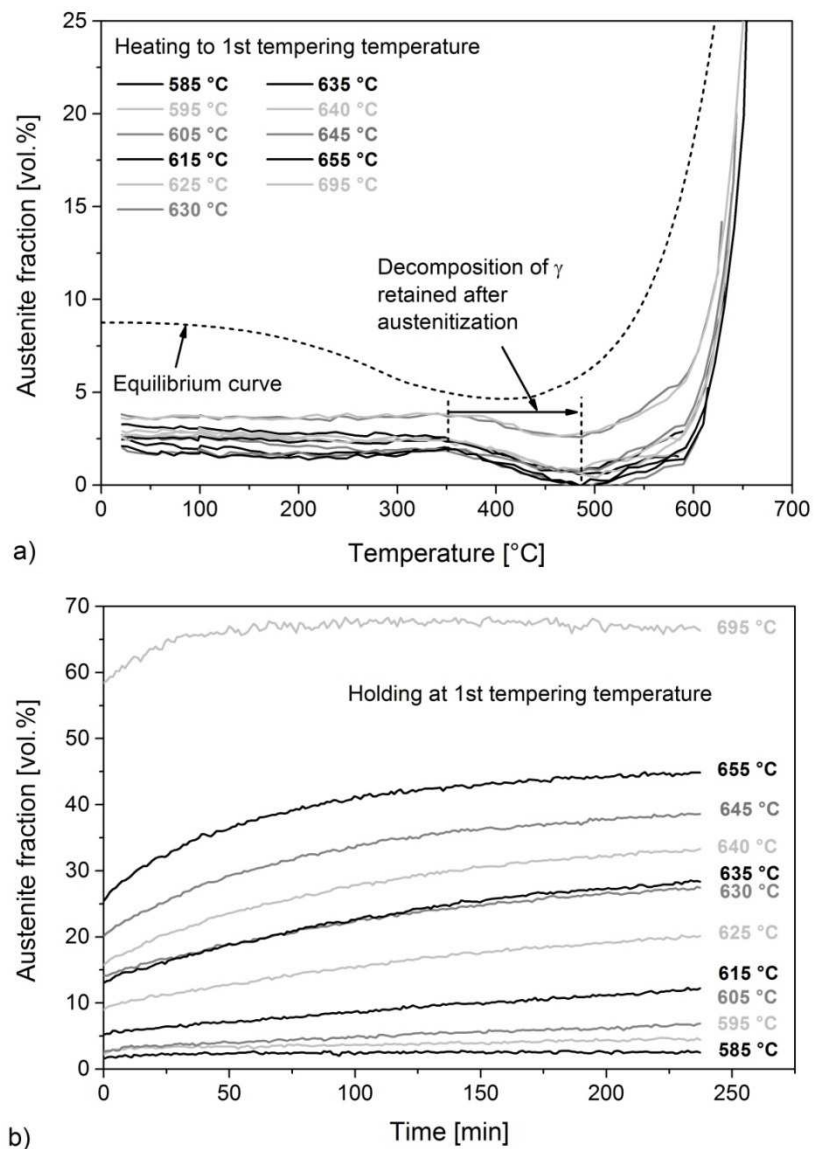


Figure 6.4 Evolution of the austenite fraction as a function of temperature during a) heating to  $T_{1t}$  and during b) holding at different  $T_{1t}$ . The tempering temperatures of the first tempering step,  $T_{1t}$ , are indicated. The equilibrium fraction of austenite is obtained from Thermo-Calc calculations [19].

An overview of the austenite fraction at the end of holding at  $T_{1t}$  (point A in Figure 6.1) and immediately after the cooling from  $T_{1t}$  (point B in Figure 6.1) is given in Figure 6.5. With increasing  $T_{1t}$  the austenite fraction at the end of the holding is increasing until around 66 vol.% at 695 °C. The austenite fraction at room temperature right after the cooling exhibits a peak at 640 °C and is decreasing for higher  $T_{1t}$  due to the formation of fresh martensite. The room temperature values of retained austenite are comparable to values found by Wei [4] for the same steel using XRD-technique after tempering treatments in a calibrated laboratory furnace. However, there are some differences in the fractions and peak position, which could be due to the different applied heat treatment techniques or analysing methods. As mentioned in the introduction, the magnetic technique offers a higher accuracy in estimating the austenite fraction compared to XRD-techniques or metallography [14],

since it probes the bulk of the material and is not sensitive to microstructural features other than the phase fractions.

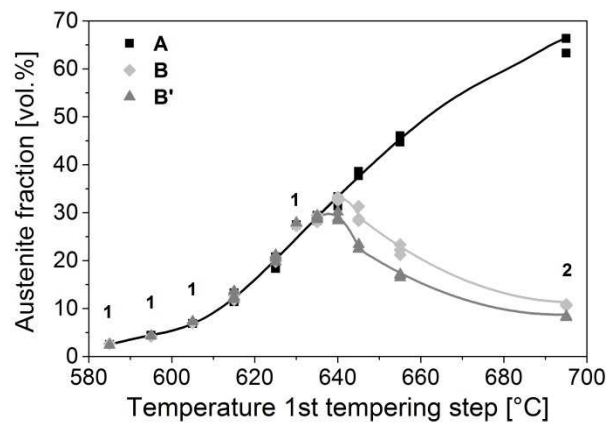


Figure 6.5 Austenite fraction versus first tempering temperature,  $T_{1t}$ . A: after 4 h at  $T_{1t}$ . B: right after cooling from  $T_{1t}$  at room temperature, B': after holding at room temperature until stable fraction of austenite was obtained (see also Figure 6.1). 1 or 2: one or two experiments were carried out at this  $T_{1t}$ ; no indication: three experiments were carried out.

To further study the stability of retained austenite, room temperature magnetization curves were measured for all tempered samples as a function of time up to 200 h after the cooling. The observed changes in the austenite fraction are shown in Figure 6.6 for selected  $T_{1t}$  and up to three experiments per  $T_{1t}$ . The first value corresponds to the value measured immediately after the cooling from the tempering step (point B in Figure 6.1). The austenite fraction is decreasing for the samples tempered at  $T_{1t} \geq 640$  °C. No austenite decomposition was observed after tempering below 640 °C, therefore the maximum fraction of retained austenite is between 635 and 640 °C, as shown in Figure 6.5. Since the  $M_s$ -temperature is above room temperature for  $T_{1t} > 640$  °C (see Figure 6.3), martensite was formed during cooling. With increasing fraction of martensite, formed during cooling from  $T_{1t}$ , the fraction of austenite that decomposes at room temperature is decreasing. The largest fraction of austenite decomposed at room temperature was found for the samples tempered at 645 °C. It seems that most of the austenite decomposition took place within the first 16 h after cooling from  $T_{1t}$ , which could be related to a further decrease in temperature, and the austenite fraction became stable after 100 h. In Table 6.2 the  $M_s$ -temperatures obtained after the tempering are presented. Given that no austenite was decomposed during holding at room temperature after tempering below 640 °C, it can be assumed that the austenite decomposition is related to the prior formation of martensite and thus the  $M_s$ -temperature. Although no distinct jump in the magnetization data was observed during cooling from  $T_{1t} = 640$  °C,  $M_s$  of austenite was assumed to be close to room temperature, since austenite decomposition at room temperature was observed for these samples.

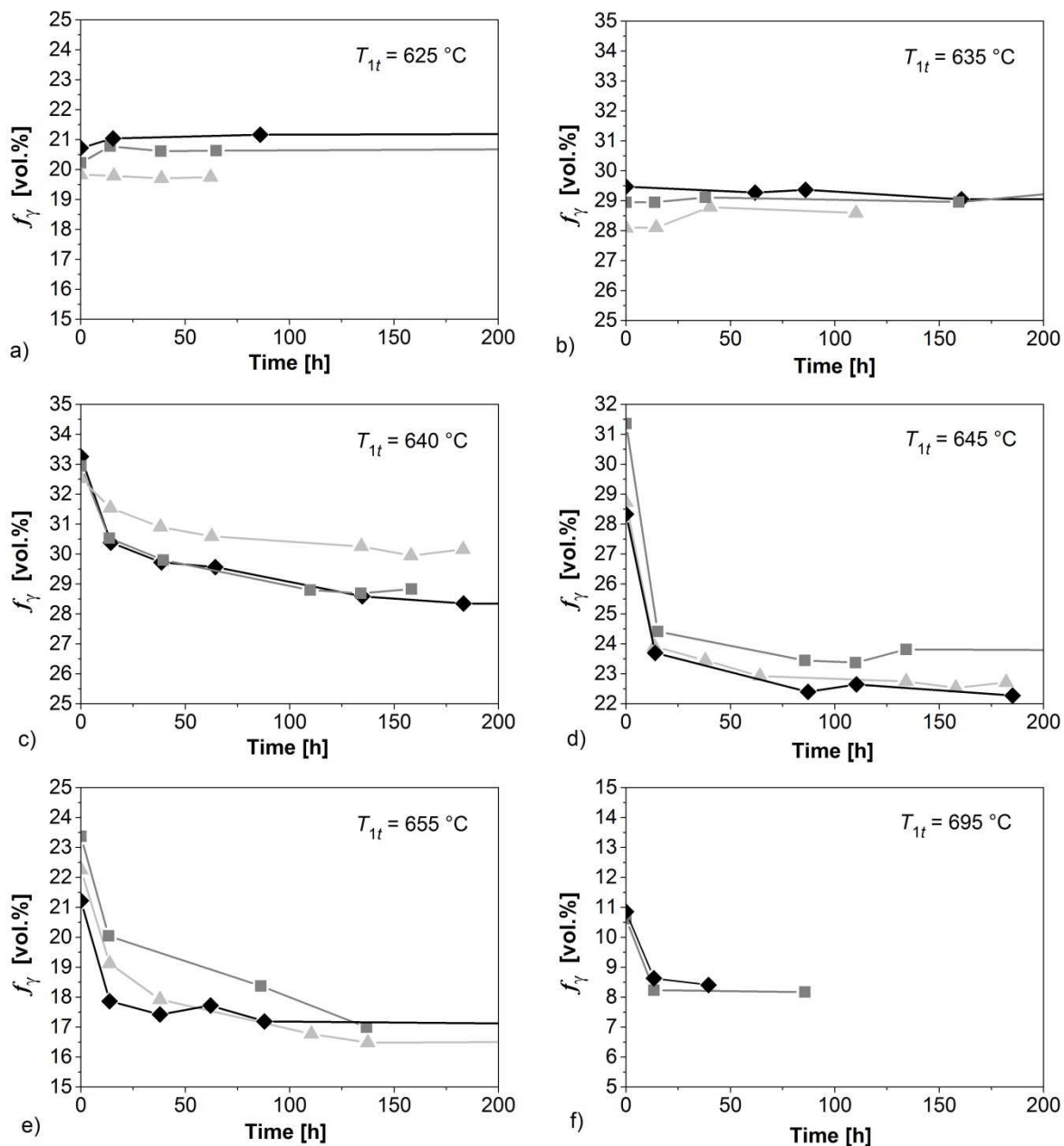


Figure 6.6 Evolution of austenite fraction during holding at room temperature after different first tempering temperatures  $T_{1t}$ : a) 625 °C, b) 635 °C, c) 640 °C, d) 645 °C, e) 655 °C and f) 695 °C. Each curve represents the behaviour of one sample annealed at  $T_{1t}$ . The first fraction value corresponds to the austenite fraction right after the cooling (see point B in Figure 6.1).

Table 6.2 Overview of the  $M_s$ -temperatures (in °C) obtained during cooling from the tempering treatment at  $T_{1t}$  (in °C). RT: room temperature.

$T_{1t}$ [°C]	≤ 635	640	645	655	695
$M_s$ [°C]	< RT	≈ RT	66	126	186

### 6.3.3 Microstructural analysis during second tempering step

#### **Evolution of magnetization**

The second tempering was carried out with samples that were held at room temperature after the first tempering step until the austenite fraction became stable. The evolution of the magnetization during the second tempering is shown in Figure 6.7. During heating, the magnetization is decreasing, starting from different magnetizations, which depend on the initial austenite fraction. During holding no significant decrease in magnetization is detected for samples first tempered at  $T_{1t} \leq 635$  °C. For  $T_{1t} > 635$  °C a decrease in the magnetization occurs during the holding of the second tempering, attributed to the formation of austenite from fresh martensite, obtained after the first tempering. This is also seen in the lower value of magnetization after the cooling to room temperature, compared to the initial value before the second tempering.

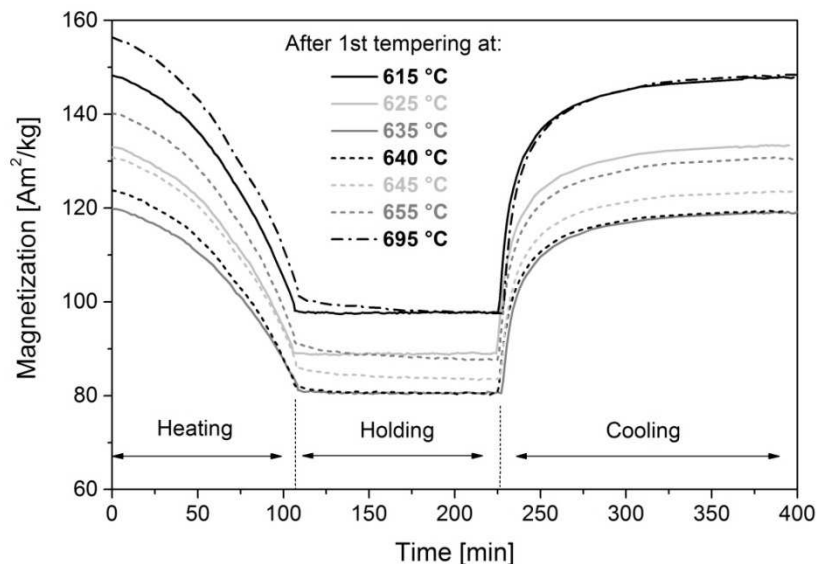


Figure 6.7 Magnetization versus tempering time during second tempering step at 550 °C at a field of 1.5 T. The indicated temperatures are the temperatures of the first tempering step.

#### **Evolution of the austenite fraction**

The evolution of the austenite fraction during heating to  $T_{2t}$  is shown in Figure 6.8a. It can be seen that the austenite fraction is decreasing by an average 2 vol.%. For the samples with  $T_{1t} \leq 635$  °C, the minimum austenite fraction is reached at  $T_{2t}$ . For the samples with  $T_{1t} > 635$  °C a minimum is reached at around 450 °C, followed by an increase during heating until  $T_{2t}$ . The evolution of the austenite fraction during the entire second tempering cycle as a function of time is shown in Figure 6.8b. During holding, the samples with  $T_{1t} \leq 635$  °C initially show a slight increase in austenite fraction, but during further holding the austenite fraction is constant. The austenite fraction of the samples with  $T_{1t} > 635$  °C is increasing during holding and the eventual fraction of austenite increases with increasing  $T_{1t}$ .

Surprisingly, during cooling the austenite fraction of most samples is increasing. Especially in the beginning of the cooling the austenite fraction shows a sudden increase. Since austenite would rather transform to martensite during cooling, it is assumed that this observed increase is due to the change in temperature control from the moment of switching from holding to cooling, influencing the measurements. Moreover, it was not observed that the second tempering of a 13Cr6Ni2Mo SMSS with similar heat treatment parameters influences the austenite fraction of the samples with  $T_{1t} \leq 635 \text{ }^\circ\text{C}$  [4] (see also Figure 2.8 in chapter 2).

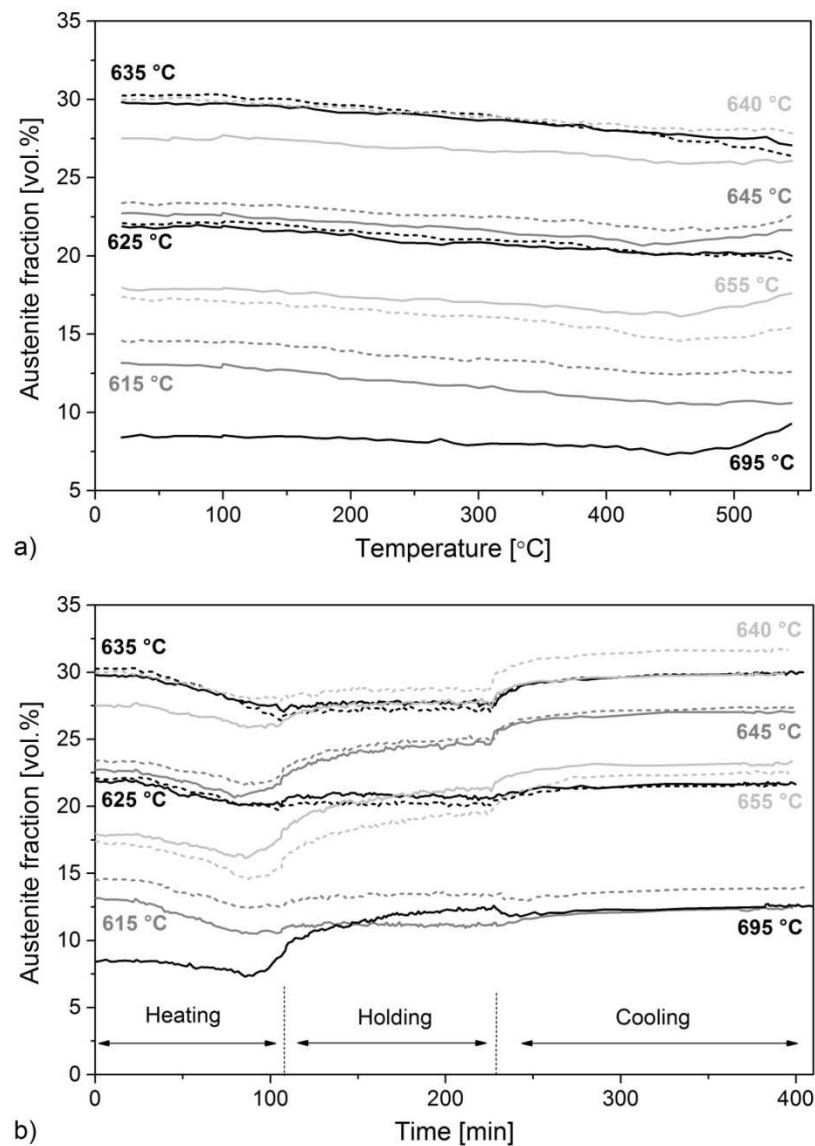


Figure 6.8 Evolution of the austenite fraction a) as a function of temperature during heating to  $T_{2t}$  and b) during the entire second tempering cycle as a function of time. The tempering temperatures of the first tempering step,  $T_{1t}$ , are indicated. A second tempering experiment was carried out for  $T_{1t} = 695 \text{ }^\circ\text{C}$  and two were carried out with the other single tempered samples.

The evolution of the austenite fraction before and after the second tempering is shown in Figure 6.9, as well as the fractions of martensite. The evolution of the austenite fractions at room temperature is similar to the ones found by Wei [4] for the same analysed 13Cr6Ni2Mo SMSS (see Figure 2.8 in chapter 2). The double tempered martensite is the martensite tempered during both the first and the second tempering step. The fresh martensite, which was formed during and after the cooling from the first tempering, becomes single tempered martensite after the second tempering. The trends in the phase fractions after the second tempering are similar to the ones after the first tempering. For the samples with  $T_{1t} > 635$  °C, the second tempering led to an increase in austenite fraction. The austenite formed during the second tempering at 550 °C is stable during cooling and no austenite decomposition was observed at room temperature after the second tempering. The initial and final austenite fraction from the second tempering step is the same for samples first tempered at  $T_{1t} \leq 635$  °C. This indicates, that the decrease in austenite fraction observed during heating might also be a result of the influence of the temperature control, especially since no austenite formation was observed for those samples during holding at  $T_{2t}$ . On the other hand, the minimum of austenite fraction during heating for the samples with  $T_{1t} > 635$  °C is obvious and could be due to the decomposition of austenite, just like observed for the as-quenched samples during heating to the temperature of the first tempering step.

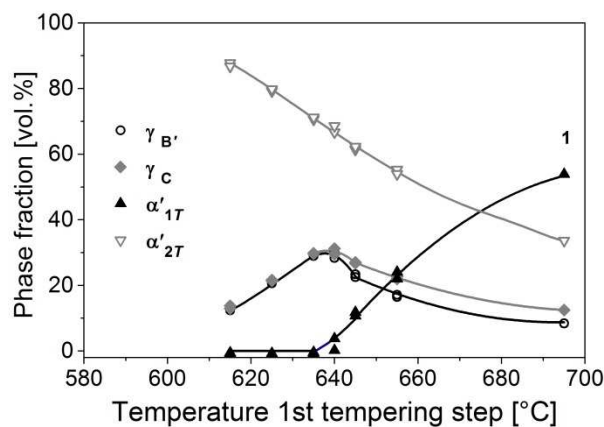


Figure 6.9 Evolution of phase fractions after the second tempering at 550 °C versus the temperature of the first tempering,  $T_{1t}$ .  $\gamma_{B'}$ : austenite before second tempering/stable after first tempering,  $\gamma_C$ : austenite after second tempering (see Figure 6.1),  $\alpha'_{1T}$ : single tempered martensite,  $\alpha'_{2T}$ : double tempered martensite.  $\alpha'_{1T} + \alpha'_{2T} + \gamma_C = 100$  vol.%. 1: one experiment was carried out at  $T_{2t}$ , no indication: two experiments were carried out at  $T_{2t}$ .

### 6.3.4 Microstructures after tempering

In Figure 6.10 to Figure 6.13 the micrographs of single and double tempered samples are shown. After single tempering (Figure 6.10 and Figure 6.12) the microstructure of samples tempered at  $T_{1t} \leq 635$  °C ( $T_{1t} \leq T_{peak}$ ) consisted of tempered martensite (OM: white areas, SEM: dark grey areas) and retained austenite (OM: dark needles, SEM: light grey areas). For the samples single tempered at  $T_{1t} > 635$  °C ( $T_{1t} > T_{peak}$ ) the microstructure consists of

tempered martensite (OM: white areas, SEM: dark grey areas) and retained austenite together with the fresh martensite formed during cooling from the first tempering temperature (OM: dark needles, SEM: light grey areas) [4]. After double tempering (Figure 6.11 and Figure 6.13) the microstructure of samples first tempered at  $T_{It} \leq 635^\circ\text{C}$  ( $T_{It} \leq T_{peak}$ ) consisted of double tempered martensite (OM: white areas, SEM: dark grey areas) and retained austenite (OM: dark needles, SEM: light grey areas). For the samples first tempered at  $T_{It} > 635^\circ\text{C}$  ( $T_{It} > T_{peak}$ ) the microstructure consists of double (OM: white areas, SEM: dark grey areas) and single tempered martensite, the latter was fresh martensite after the first tempering, and retained austenite (OM: dark needles, SEM: light grey areas). With increasing tempering temperature the microstructure seems to be more refined, due to the formation of retained austenite and martensite, as described in Figure 2.9.

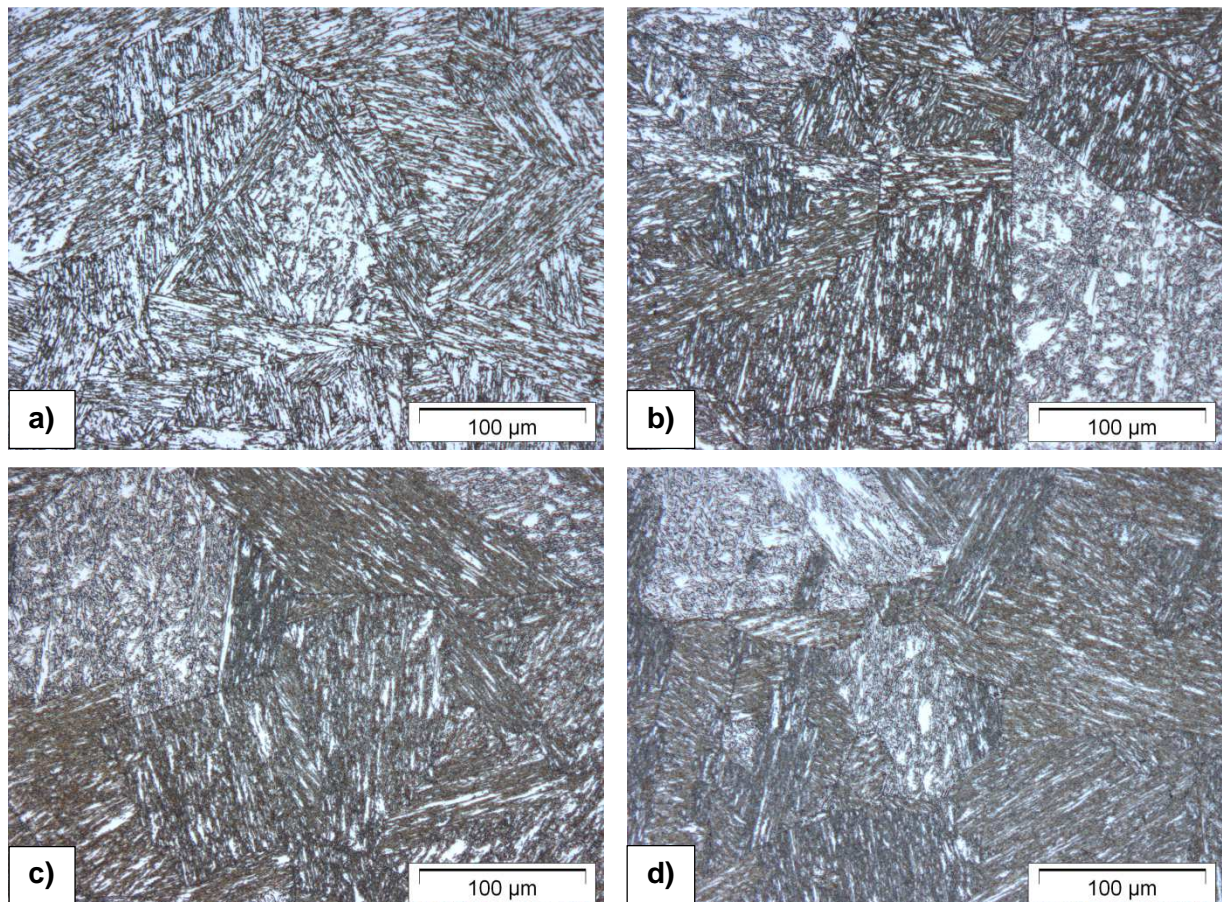
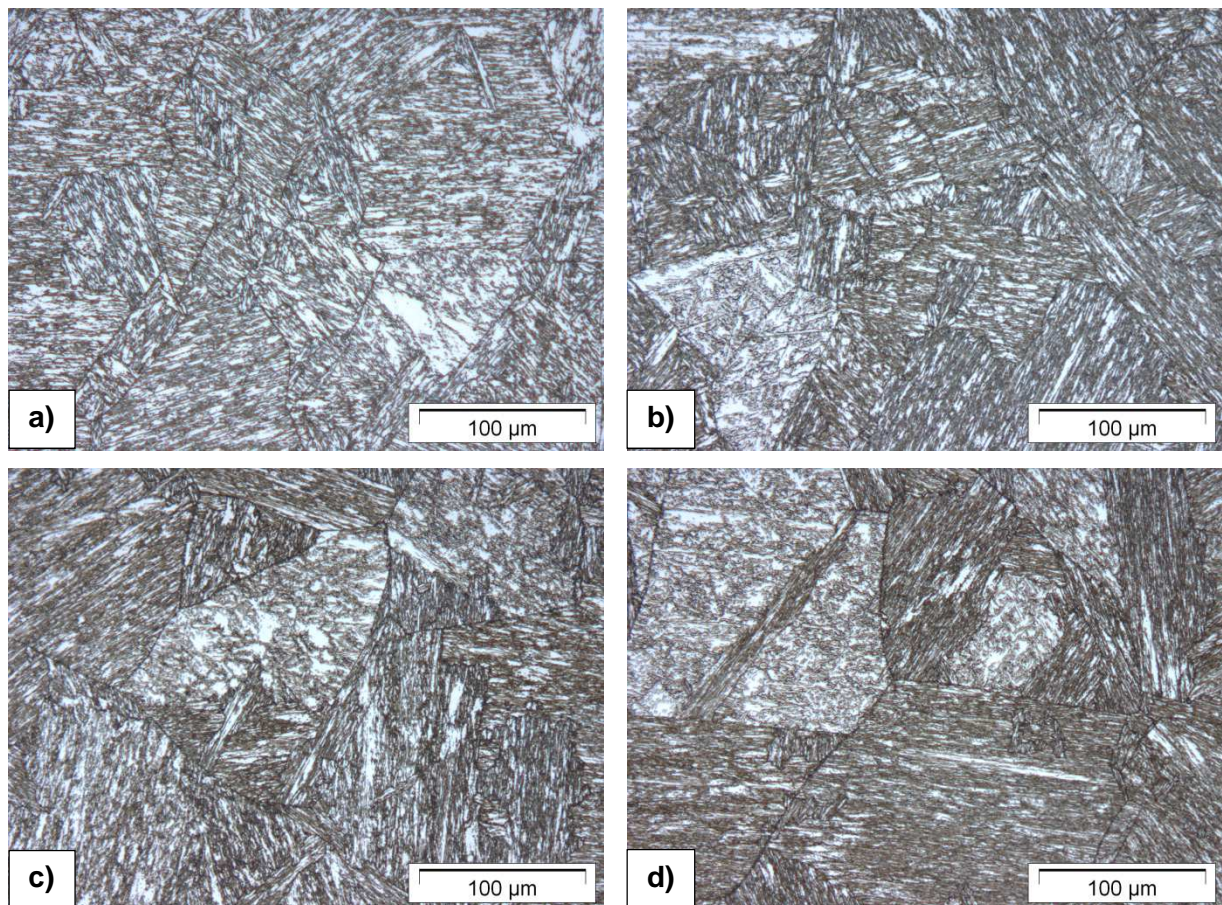


Figure 6.10 Microstructures after single tempering for 4 h at a) 615 °C, b) 635 °C, c) 645 °C and d) 655 °C. Etchant: L-B.

It can be also seen from the SEM micrographs in Figure 6.12 and Figure 6.13 that the thickness of the retained austenite needles and the retained austenite + fresh martensite needles is increasing with increasing first tempering temperature  $T_{It}$ .

There are almost no differences observed in the microstructures of the single tempered samples to the double tempered samples, even though some austenite was formed after double tempering at  $T_{It} > 635$  °C. This is probably because minor changes of the austenite fraction in the analysed samples cannot be revealed since the austenite grains are very small and finely dispersed.

From the microstructures, it can be seen that the preferred formation of the needle-shaped austenite is along the martensite lath boundaries and along the prior austenite grain boundaries. The latter is also shown in Figure 6.14 and Figure 6.15. Different orientations of the prior austenite grains can be seen by the different orientation of the austenite needles, which were growing along the martensite lath boundaries during tempering.



*Figure 6.11 Microstructures after the second tempering at 550 °C for 2 h for samples first tempered for 4 h at a) 615 °C, b) 635 °C, c) 645 °C and d) 655 °C. Etchant: L-B.*

It was observed that some prior austenite grains show a higher fraction of martensite (for instance in Figure 6.13c and Figure 6.13e) with coarser austenite grains than other areas. This is, however, not related to the tempering temperature, since it was observed in all the samples.

Small particles were found to be distributed within austenite and martensite, as shown in Figure 6.15. These could be nitrides or carbonitrides of Ti [23, 24] or V, which were found to

be present by thermodynamic calculations in chapter 4. According to these calculations, TiN is stable even above the applied austenitization temperature of 1050 °C and could therefore be still present from the as-received state of the samples.

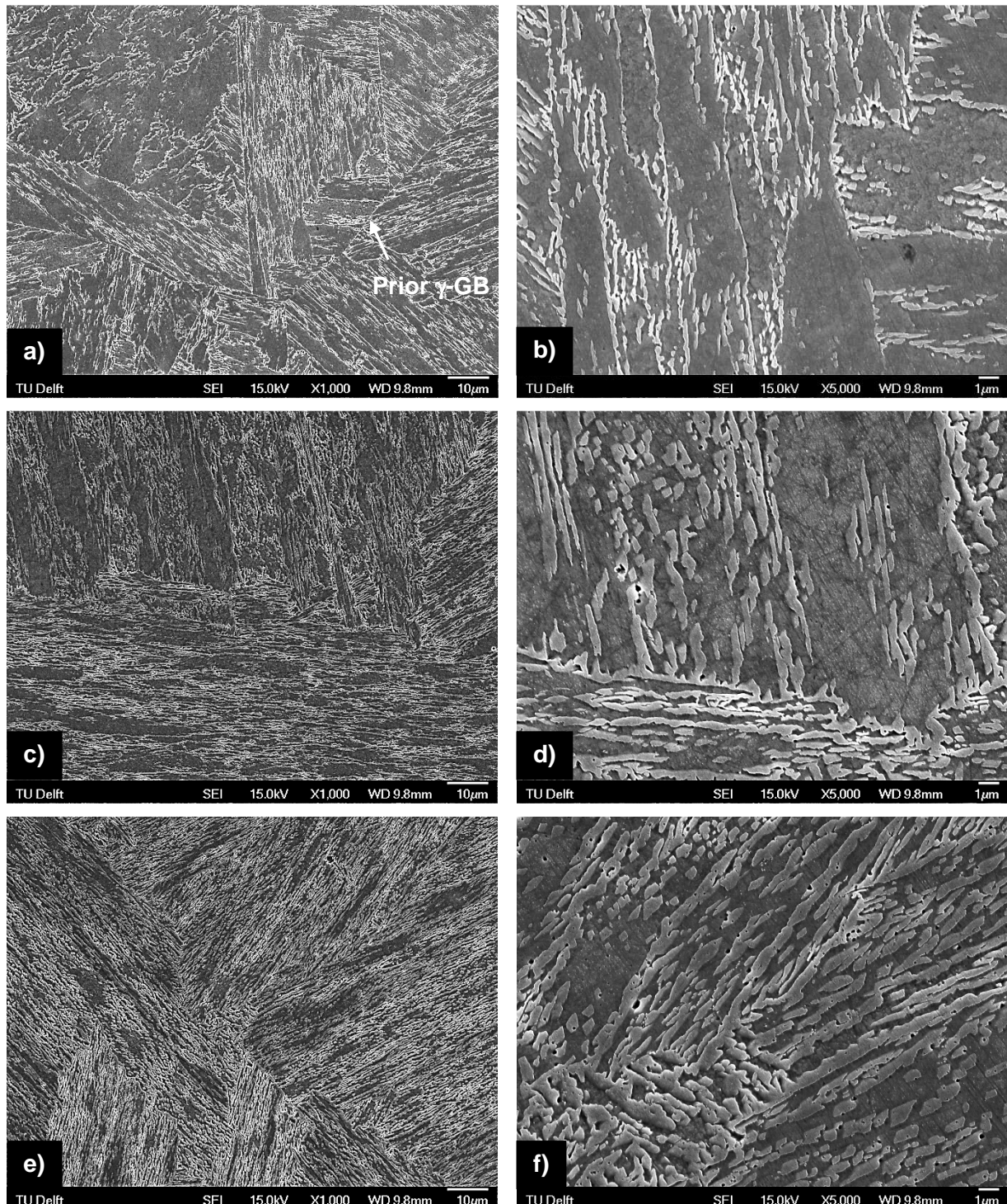


Figure 6.12 SEM micrographs after single tempering for 4 h at a),b) 615 °C, c),d) 635 °C and e),f) 655 °C. Dark grey areas: tempered martensite, light grey areas: retained austenite ( $T_t \leq T_{peak}$ ) and retained austenite + fresh martensite [4] ( $T_t > T_{peak}$ ). Prior  $\gamma$ GB: prior austenite grain boundary.

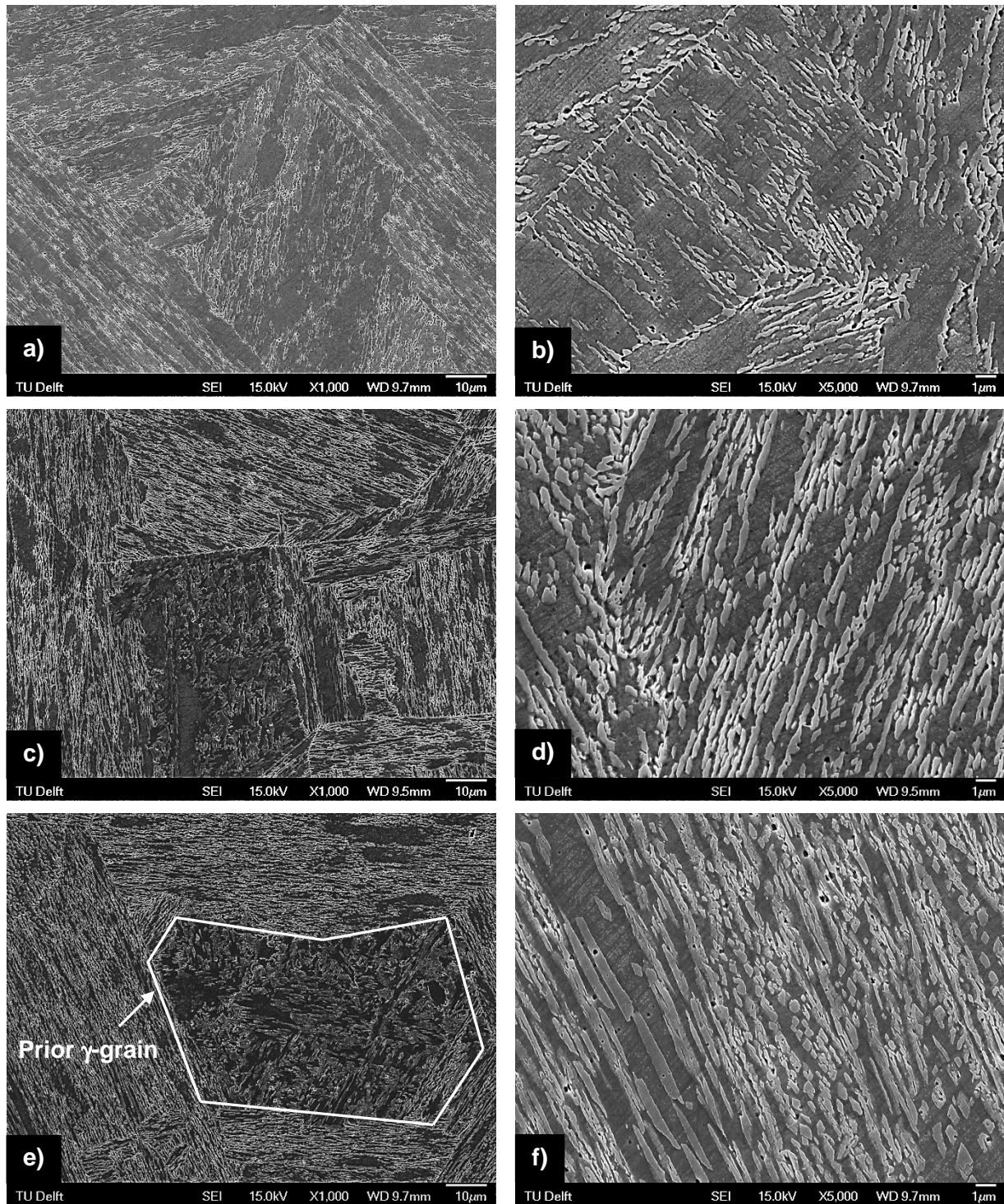


Figure 6.13 SEM micrographs after the second tempering at 550 °C for 2 h for samples first tempered for 4 h at a),b) 615 °C, c),d) 635 °C and e),f) 655 °C. Dark grey areas: double tempered martensite, light grey areas: retained austenite ( $T_{It} \leq T_{peak}$ ) and retained austenite + single tempered martensite ( $T_{It} > T_{peak}$ ) [4].

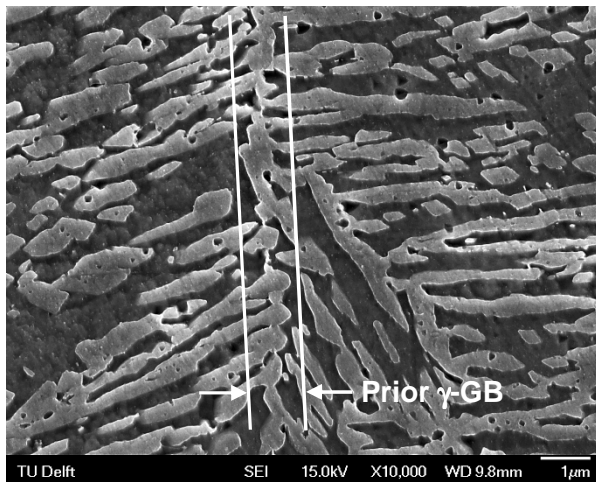


Figure 6.14 Microstructure of a sample single tempered at 655 °C for 4 h. Light grey areas: retained austenite +  $\alpha'_F$ . Dark grey areas:  $\alpha'_T$ . Prior  $\gamma$ -GB: prior austenite grain boundary.

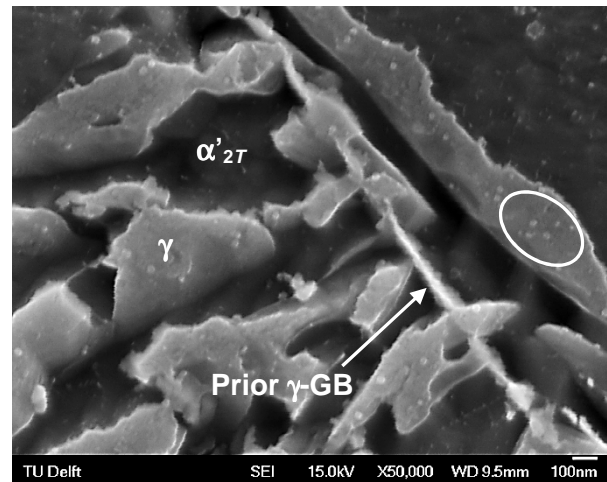


Figure 6.15 Microstructure of a sample double tempered at 625 °C for 4 h and 550 °C for 2 h.  $\alpha'_{2T}$ : double tempered martensite. Light grey areas: retained austenite. Dark grey areas:  $\alpha'_{2T}$ . Prior  $\gamma$ -GB: prior austenite grain boundary. In circled area are possibly Ti- or V-nitrides/-carbides.

## 6.4 Discussion

The in-situ analysis of the austenite fraction during the heat treatment of a 13Cr6Ni2Mo SMSS by means of the thermo-magnetic measurements gives a valuable insight into the kinetics of the austenite formation and stability.

### 6.4.1 Austenite formation and growth during first tempering step

A similar austenite fraction to be still present in the material after quenching from austenitization was found by the work in chapter 5 after austenitization at 950 °C for 0.5 h. During re-heating to  $T_{It}$ , the fraction of austenite which dissolves between 350 and 480 °C depends on heating rate, so that not all of the austenite was decomposed due to the slower kinetics at lower temperatures. Moreover, the austenite-free reference sample was obtained by tempering an austenitized sample in this temperature range, where an increase in the magnetization indicated austenite decomposition. Apparently the austenite, retained at room temperature after the austenitization, is not thermodynamically stable during re-heating. The measured austenite fraction during heating to  $T_{It}$  was found to be lower than the theoretical equilibrium fraction (Figure 6.4a), which suggests that the theoretical equilibrium fraction of austenite must be inaccurate for lower temperatures, since the measured austenite fraction is not changing towards the equilibrium curve below 480 °C.

The experimentally obtained minimum of the austenite fraction around 480 °C during heating of the as-quenched samples to  $T_{It}$  was defined to be the  $A_{c1}$ -temperature for the experiments carried out in the magnetometer furnace with a heating rate of 5 K/min. This

value is 80 °C smaller than the  $A_{c1}$  of 560 °C estimated by Wei [4] for the same material, where  $A_{c1}$  was determined to be the maximum temperature for which no austenite was formed after tempering.  $A_{c1}$  of the austenite-free sample was determined to be 580 °C, which is 100 °C above the  $A_{c1}$  of the as-quenched samples. The lower  $A_{c1}$  of the as-quenched samples could be due to the higher level of austenite-stabilizing elements in the areas that were just decomposed, being the same areas where austenite first starts to form during further heating.

During holding, austenite, which already nucleated during heating, is further growing. Additionally, more austenite might nucleate, which is also depending on  $T_{It}$ . The nucleation of austenite was reported to mainly occur on martensite laths [11, 12, 25], but also on prior austenite grain boundaries [7, 26], since they act as preferred nucleation sites. Nakada et al. [27] reported a temperature dependence of the austenite nucleation sites and the shape of retained austenite for a Fe-13Cr-6Ni-0.012C-0.012N-2.1Mo (wt.%), where at lower temperatures preferentially needle-like austenite forms at the martensite lath boundaries and at higher temperatures granular austenite forms at prior austenite grain boundaries. Nevertheless, dislocations within the martensite laths and carbides may act as nucleation sites as well [7, 11, 26, 28, 29], since they act as rapid diffusion paths for solute atoms [3] such as Ni or Mn. In Figure 6.10 to Figure 6.13 the microstructures of selected single and double tempered samples are shown, where prior austenite grain boundaries can be seen. As expected, the retained austenite is preferentially located at the former martensite laths and prior austenite grain boundaries, growing perpendicular or parallel to them [7]. Furthermore, the microstructures in Figure 6.14 and Figure 6.15 show that retained austenite grows from the prior austenite grain boundaries. Independent of the tempering temperature, regions which contain less but coarser retained austenite of a different shape were found, as can be seen for instance in Figure 6.13c and Figure 6.13e. Retained austenite in SMSS is reported to be finely dispersed and rod-shaped [4, 7, 8]. From Figure 6.13c and Figure 6.13e we can conclude that not all the retained austenite is in the form of fine rods. The areas containing coarser retained austenite also have bigger areas of martensite and are also well-defined in relation to the surroundings, i.e. they are located within one former austenite grain. Possibly, due to the orientations of the former austenite grains some areas appear to show less austenite in the microstructure, caused by a different orientation of the martensite lath. This variation in martensite occurrence could be also due to local inhomogeneities in the composition, i.e. in austenite-stabilizing elements. It has been reported [7] that narrow austenite regions are more stable than large austenite islands. Such differences in the microstructure could cause local differences in the mechanical properties, since these are strongly dependent on the fraction of retained austenite.

The evolution of the austenite fraction during holding at  $T_{It}$ , shown in Figure 6.4b, indicates that already a substantial amount of austenite has formed during heating to  $T_{It}$ , and therefore the austenite fraction at the beginning of the isothermal tempering is increasing with increasing  $T_{It}$ . The austenite fraction during holding at  $T_{It}$  can be described by the Johnson-Mehl-Avrami-Kolmogorov (JMAK) [30-34] equation, which describes the evolution of the phase fraction during isothermal conditions as a function of temperature and time [35, 36] by

$$f_{\gamma} = 1 - \exp\left[-(k \cdot t)^n\right], \quad (6.3)$$

where  $t$  denotes the holding time at  $T_{It}$ ,  $k$  the rate constant depending on the nucleation and growth rate, which is sensitive to the temperature, and  $n$  the time exponent, which is usually temperature independent [35, 36]. To describe the austenite formation during tempering with the JMAK equation only the isothermal formation process during the first tempering was considered and equation (6.3) was modified to

$$f_{\gamma} = f_{end} \cdot \left[ 1 - \exp\left(-[k \cdot (t + t_b)]^n\right) \right], \quad (6.4)$$

where  $f_{end}$  denotes the equilibrium austenite fraction at the corresponding  $T_{It}$ .  $t_b$  represents a time parameter accounting for the previous austenite formation during heating. Using equation (6.4), the parameters  $f_{end}$ ,  $k$  and  $t_b$  were obtained from fitting the austenite fraction during tempering for  $625 \text{ }^{\circ}\text{C} \leq T_{It} \leq 695 \text{ }^{\circ}\text{C}$ . In Figure 6.16 the volume fraction of austenite as a function of time is shown for the different first tempering temperatures, where experimental data from the holding at  $T_{It}$  are compared to the curves obtained by fitting with equation (6.4). The time of the experimental data was corrected by adding  $t_b$  (see equation (6.4)). In the case that more than one tempering experiment was carried out at one temperature  $T_{It}$ , the average of the fitting parameters from the different fits were taken. All curves are best described by the parameter  $n = 1$ , which refers to diffusional controlled growth of needles and plates and also to the thickening of needles [36]. This is consistent with the needle-like microstructure after tempering as shown in the micrographs in Figure 6.10 to Figure 6.13. From literature, smaller values of  $n$  for the martensite to austenite transformation were obtained for a SMSS, a ternary Fe-Cr-Ni alloy and different martensitic steels as shown in Table 6.3.

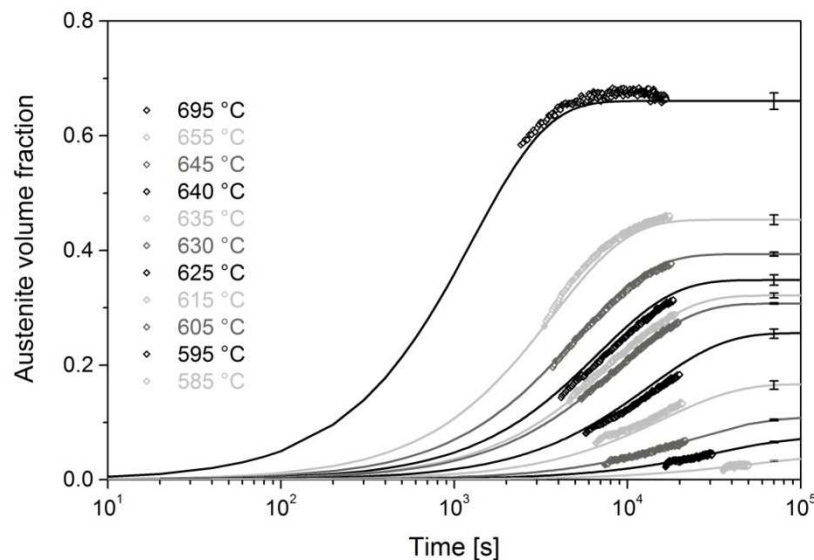


Figure 6.16 Solid lines give the volume fraction of austenite at  $T_{It}$  as a function of time obtained by equation (6.4). The symbols show the experimental data. The error bars, drawn at a time of  $7 \cdot 10^4$  s, show the standard error for the austenite fraction  $f_{\gamma}$  obtained by equation (6.4). The tempering temperatures  $T_{It}$  are indicated.

Table 6.3 Overview of the  $n$ -values and the activation energies,  $Q$ , for the martensite to austenite formation obtained from the present work compared to values from literature.

Alloy [wt.%]	$n$	$Q$ [kJ/mol]	$T$ [°C]	Ref.
13Cr6Ni2Mo-SMSS	1	233	625-695	present work
13Cr6Ni2Mo-SMSS	0.5	168	600, 625, 635	[4]
Fe-12Cr4Ni-ternary alloy	0.6	173±8	500-650	[37]
1.8Cu15.9Cr7.3Ni1.2Mo - martensitic precipitation hardening steel	0.5	240	540-580	[38]
18Ni-maraging steel	0.62-0.66	251-274	580-625	[39]
PH18-3-maraging steel	-	234±20	575-615	[29]

In the present work,  $n$  was obtained from JMAK fits for  $625\text{ °C} \leq T_{It} \leq 695\text{ °C}$ , whereas in the references of Table 6.3 the austenite formation was mostly analysed at temperatures below  $625\text{ °C}$ . A value of  $n = 2/3$  describes diffusion controlled transformation by the solute movement to dislocations for precipitation of austenite [36], which could be the diffusion controlled process dominating the austenite formation at  $T_{It} \leq 625\text{ °C}$ , whereas at  $T_{It} \geq 625\text{ °C}$  diffusional growth by thickening of the austenite needles might dominate.

The activation energy,  $Q$ , for the martensite to austenite transformation during tempering can be obtained from the temperature dependence of  $k$  by an Arrhenius type function [36]:

$$k = k_0 \cdot \exp\left(-\frac{Q}{RT}\right), \quad (6.5)$$

where  $k_0$  is a pre-exponential parameter and  $R$  denotes the gas constant. From the slope of the linear fit of the Arrhenius plot of  $\ln k$  versus  $1/T_{It}$  an activation energy of 233 kJ/mol was derived for the formation of austenite from martensite during the first tempering step. This value is in good agreement with the activation energy of the tracer impurity diffusion of Ni in  $\alpha$ -Fe between 600 and 680 °C (245.8 kJ/mol [40]) and Mn in  $\alpha$ -Fe between 700 and 760 °C (233.6 kJ/mol [40]), but not too far removed from the self-diffusion of Fe between 775 and 814 °C (250-282 kJ/mol [40]). Moreover, the activation energy found in the present work is in agreement with the one for the formation of reverted austenite reported for different martensitic steels (in the range 234-274 kJ/mol), whereas for a ternary Fe-Cr-Ni alloy a lower value was obtained as shown in Table 6.3. Wei [4] reported an activation energy of 168 kJ/mol for the formation of austenite from martensite in the 13Cr6Ni2Mo SMSS, which was interpreted as being close to the activation energy of carbon diffusion in austenite. The difference with the activation energy found in the present work could be due to applying the JMAK-fit only for relatively low tempering temperatures, i.e. 600, 625 and 635 °C [4]. The obtained activation energy for the isothermal austenite formation suggests that Ni, together

with Mn and Fe, plays a key role in the diffusional formation of austenite from martensite in 13Cr6Ni2Mo SMSS.

From the linear fit of the  $\ln k$  versus  $1/T_{It}$  plot the values of  $k$  were also determined for  $T_{It} < 625$  °C. Together with  $n = 1$ , the values of  $f_{end}$  and  $t_b$  for  $T_{It} < 625$  °C were obtained by equation (6.4) and the volume fractions of austenite are also plotted in Figure 6.16.

In Figure 6.17  $f_{end}$  from each experiment of the first tempering step is compared to the equilibrium fraction of austenite. The values obtained from the JMAK-fit for  $625$  °C  $\leq T_{It} \leq 695$  °C correlate well with the equilibrium fraction. For  $T_{It} < 625$  °C the values of  $f_{end}$  are moving away from the equilibrium line with decreasing temperature. As already suggested before with the difference between the equilibrium and measured austenite fraction shown in Figure 6.4a, the calculated equilibrium fraction of austenite are likely to be inaccurate for lower temperatures. Also,  $f_{end}$  for  $T_{It} < 625$  °C could be inaccurate since  $k$  was obtained from the linear fit of the  $\ln k$  versus  $1/T_{It}$  plot of  $625$  °C  $\leq T_{It} \leq 695$  °C. These could be reasons for the difference of the calculated equilibrium fraction to  $f_{end}$  obtained for  $T_{It} < 625$  °C.

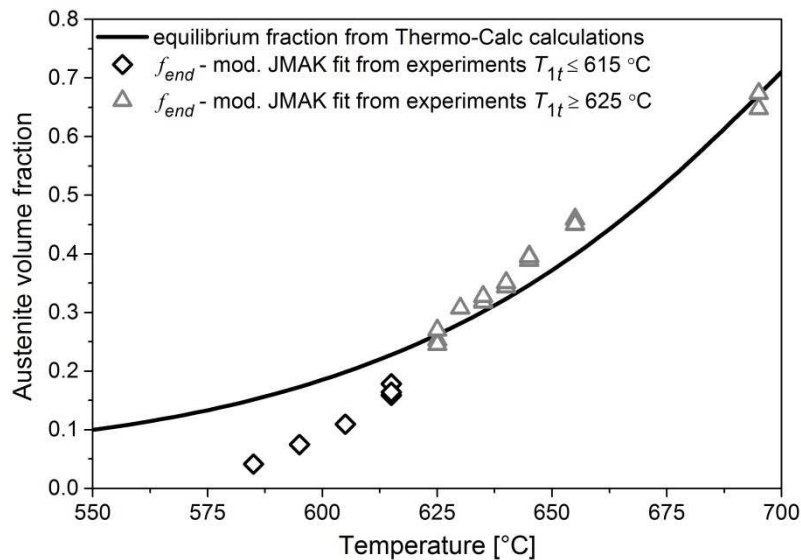


Figure 6.17 Austenite fraction vs. temperature in equilibrium condition, obtained from Thermo-Calc calculations [19], compared to the equilibrium fraction  $f_{end}$  obtained by equation (6.4) for the first tempering step. The standard error for  $f_{end}$  lies within the size of the symbols, where a maximum standard error of  $\pm 0.018$  was obtained, including the accuracy of the measurement of the austenite fraction from the magnetic experiments.

## 6.4.2 Austenite stability

### **Austenite stability during cooling to room temperature after the first tempering**

When  $T_{It}$  is above 635 °C part of the austenite formed during tempering is transformed to martensite during cooling to room temperature. It is well known that during tempering

austenite-stabilizing elements like Ni, Mn and C are enriched in austenite, making it stable against transformation during cooling by decreasing  $M_s$  [4, 7-11], whereas it is generally accepted that Ni contributes most to the stability of austenite in SMSS due to its higher concentration [2, 11, 41]. Song et al. [12] found that austenite was enriched in Mn, although to a smaller degree than Ni. This is in accordance with the activation energy obtained in this work, confirming that Ni and Mn contribute to the formation of austenite from martensite. Since the obtained activation energy is not too far removed from the self-diffusion of Fe, it also shows Fe to be involved, probably due to the substitutional diffusion of Ni and Mn. When the austenite fraction is increasing during tempering the concentration of Ni, Mn and C are decreasing in austenite [4, 9, 13]. In Figure 6.18 the equilibrium concentration of Ni, Mn, Mo and Cr in fcc-austenite is shown as a function of temperature. It shows that the Ni and Mn-content in austenite is increasing with decreasing temperature, while Cr and Mo show almost no change. Since the equilibrium austenite fraction is decreasing with decreasing temperature, as shown in Figure 6.4a, Figure 6.18 shows the importance of Ni on the austenite stability in SMSS. The effect of C on the austenite stability is considered to be rather small, since it is preferably bound in carbides, as found by Thermo-Calc [19] analysis in chapter 4. However, the formation of carbides could indirectly influence the austenite stability by removing C from austenite, as reported by Kulmburg et al. [42] for precipitation within austenite.

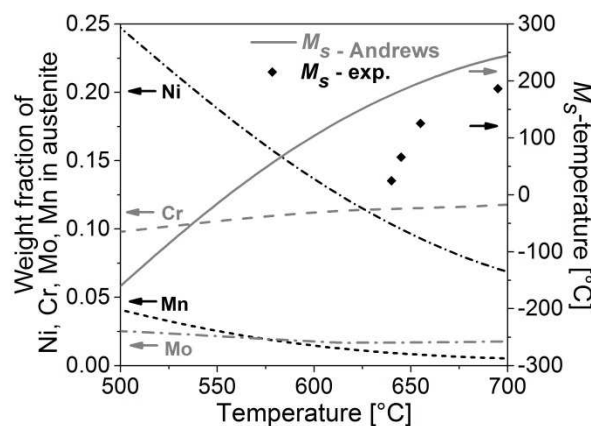


Figure 6.18 Content of Ni, Mn, Cr and Mo in austenite obtained from thermodynamic calculations [19] together with the  $M_s$ -temperature obtained by Andrews equation (see equation (6.6)) [43] using the composition changes obtained by Thermo-Calc [19] and from the first tempering step experiments (exp.).

As discussed above, the stability of austenite after tempering can be described in terms of the  $M_s$ -temperature [4, 7, 8, 41]. The  $M_s$ -temperature for the 13Cr6Ni2Mo SMSS was calculated by Andrews equation [43]:

$$M_s [^{\circ}\text{C}] = 539 - 423x_C - 30.4x_{Mn} - 17.7x_{Ni} - 12.1x_{Cr} - 7.5x_{Mo} . \quad (6.6)$$

$x_i$  is the concentration of the alloying elements  $i$  in wt.%. The thus obtained  $M_s$  of the bulk composition, 255 °C, is in good agreement with the one measured by the VSM (230 °C) and dilatometry (233 °C) in chapter 5, although equation (6.6) was used outside the composition limits set in [43]. Equation (6.6) shows that  $M_s$  decreases more strongly by an increase in

austenite stabilizing elements C, Mn and Ni than for Cr and Mo, where the influence of Mn and C is much stronger than that of Ni. In Figure 6.18  $M_s$ , calculated by equation (6.6) depending on the equilibrium composition of austenite, is plotted together with the  $M_s$ -temperatures obtained from the first tempering step experiments (see Table 6.2). Both  $M_s$ -temperatures are increasing with increasing temperature, showing the strong influence of Ni and Mn on the austenite stability in the 13Cr6Ni2Mo SMSS. The discrepancy between the calculated and experimental values is due to the non-equilibrium state of the material. The increase in  $M_s$  with  $T_{It}$  (Figure 6.3b) implies the decrease in the concentration of austenite-stabilizing elements in austenite and hence an increased fraction of austenite is transformed to fresh martensite during cooling (see Figure 6.5) [7].

The austenite fraction,  $f_{RT}^\gamma$ , obtained after holding at room temperature ( $T_{RT}$ ) after the first tempering until the austenite fraction stabilized (point B' in Figure 6.1), can be obtained as a function of the  $M_s$ -temperature (see Table 6.2) derived from a modified Koistinen-Marburger [44] equation for tempering at  $T_{It} \geq 640$  °C for 4 h:

$$f_{RT}^\gamma = f_{ini} \cdot \exp[-\alpha_{KM} \cdot (M_s - T_{RT})], \quad (6.7)$$

where  $f_{ini}$  is 0.29, which is the maximum fraction of austenite stable at room temperature after cooling from tempering at  $T_{It} = 640$  °C.  $\alpha_{KM}$  is the rate parameter, which was found to be  $0.00647 \text{ K}^{-1}$  for tempering for 4 h at  $T_{It} \geq 640$  °C. From cooling from an austenitization treatment in the VSM at 950 °C for 0.5 h,  $\alpha_{KM}$  was found to be  $0.017 \text{ K}^{-1}$  for the 13Cr6Ni2Mo SMSS in chapter 5, which is much higher than the one found after the tempering. It is known that  $\alpha_{KM}$  is dependent from the composition [45, 46]. However, the much smaller value found after the tempering is not only caused by the differences in the composition, since the enrichment would not cause a change of that magnitude [45]. Most likely, the refined microstructure after tempering, influencing the nucleation and growth of martensite [47], and a lower driving free energy for the austenite to martensite formation could cause the lower value of  $\alpha_{KM}$ .

It is worth mentioning that also the holding time during tempering can have an influence on the austenite stability [4, 5, 27], regardless of the tempering temperature, so that variations in the holding times can shift the peak temperature for the austenite fraction shown in Figure 6.5. Although it is believed by the authors that the main reason for the austenite stability is the contribution of the austenite-stabilizing elements, other reasons being involved in the austenite stability have been discussed in the literature. Bilmes et al. [8] suggested that the presence of a high dislocation density within the austenite particles may act as barriers against the shear process of the martensite formation, which also influences the stability of austenite during cooling. However, a high dislocation density within the austenite, as found by Bilmes et al. [8], would result from the formation of austenite by a shear process, as reported for high Ni-carbon steels [48]. On the other hand, the obtained activation energy suggests the diffusion of Ni, Mn and Fe to be the main driving force for the austenite formation from martensite. Moreover, with the low heating rates applied in the present work the austenite formation during heating would rather be due to diffusional transformation than to a shear transformation [13]. It has been suggested for martensitic stainless steels that the stability of retained austenite could be also related to the concentration of quenched-in vacancies [2, 13]. The concentration of vacancies in the material is increasing with increasing temperature, so that on cooling more quenched-in

vacancies lead to an increase of  $M_s$  caused by a decrease in the driving force for the martensite formation [49]. However, this is also influenced by the cooling rate, i.e. during slow cooling  $M_s$  is lowered, since the quenched-in vacancies have more time to migrate and disappear than during high cooling rates [49]. Since in the present work the cooling rate was very low, the contribution of quenched-in vacancies to increase the  $M_s$  of austenite would be rather small compared to the effect of the chemical stabilization of austenite.

### ***Room temperature austenite stability after the first tempering step***

A significant fraction of austenite decomposed at room temperature after cooling when  $T_{It} \geq 640$  °C, which seems to be related to prior martensite formation during cooling. In the cases where the  $M_s$ -temperature was below room temperature, no austenite was decomposed during room temperature holding. Such austenite decomposition at room temperature was also observed in TRIP-steels [50] after cooling from the austenitization temperature, which was thought to possibly be due to stored energy from transformation stresses or due to hydrogen diffusion. A decrease of the retained austenite fraction related to hydrogen absorption was reported by Hojo et al. [51] for ultra high-strength low alloy TRIP-aided steels. Zhao et al. [52] reported a time-dependent increase in strain in TRIP-steels under different constant stresses at room temperature, which was interpreted to be due to the martensite formation from austenite.

In the present work it was found that the room temperature transformation of austenite might depend on the presence of fresh martensite. However, a small fraction of austenite was decomposed during holding at room temperature for the samples single tempered at 640 °C, where no martensite formation was detected during cooling (see Figure 6.6). For this  $T_{It}$ , the  $M_s$ -temperature is assumed to be close to room temperature, which could allow for a small fraction of martensite to be present in the microstructure. It is also possible that some of the austenite decomposition at room temperature is due to variations in the room temperature itself, especially within the first 16 h after cooling from  $T_{It}$ .

No decomposition of austenite in different martensitic steels was reported by several authors after cooling down to -196 °C [8, 12, 42, 53]. During slow cooling of a 0.20C-1.52Mn-0.25Si-0.96Al (wt.%) TRIP steel from 27 to -268 °C, however, austenite continuously transforms to martensite until -118 °C [54]. On the other hand, quenching of different TRIP steels in liquid nitrogen also showed martensite formation of about 2 % [55]. To clarify this effect, a sample, single tempered at 635 °C for 4 h, where no martensite was formed during cooling and also no martensite formation is expected at room temperature according to our results, was put into liquid nitrogen (-196 °C) for 20 h subsequent to cooling to room temperature after the first tempering step. The magnetization was subsequently measured at room temperature and no change in the saturation magnetization was detected. This implies that neither martensite was formed nor austenite was decomposed. This result supports the assumption that the austenite is stable at room temperature after tempering if no martensite was formed during cooling subsequent to the tempering treatment. Moreover, it is suggested that the austenite decomposition is a time-dependent process. Since the room temperature austenite decomposition was related to the holding time at room temperature and only occurred after the formation of fresh martensite during cooling,

the austenite decomposition might be due to stored energy from transformation stresses [50, 52].

### 6.4.3 Austenite formation during the second tempering step

It has been reported that a second tempering can lead to a substantial increase in the retained austenite fraction and also to a refinement of the microstructure [6-8]. The austenite, formed during the second tempering, was formed from the fresh martensite obtained from the first tempering. This is shown in the overview of the phase fractions in Figure 6.9, where for the samples first tempered at  $T_{1t} > 635$  °C ( $T_{1t} > T_{peak}$ ) an increase in retained austenite fraction was obtained. The fresh martensite which transformed into austenite during the second tempering was enriched in austenite stabilizing elements, compared to the single tempered martensite, and therefore the  $A_{c1}$ -temperature was below the tempering temperature of 550 °C. Moreover, the fresh martensite offers an increased interphase area to the retained austenite, which act as additional nucleation sites and therefore a substantial increase in the austenite fraction can be obtained [6, 7]. It was reported by Wei [4] for the 13Cr6Ni2Mo SMSS that the fresh martensite, formed during cooling from the first tempering temperature, was formed within or attached to the retained austenite. Therefore it is very difficult to distinguish fresh martensite from retained austenite, even when using scanning electron microscopy, as can be seen from Figure 6.12 and Figure 6.14.

It was observed that the austenite fraction during heating to  $T_{2t}$  is decreasing for  $T_{1t} \leq 635$  °C until  $T_{2t}$  is reached. For  $T_{1t} > 635$  °C the austenite fraction is decreasing during heating to a minimum at around 450 °C (see Figure 6.8). Furthermore, a sudden increase in austenite fraction was observed in the beginning of the cooling after the holding at  $T_{2t}$  and the austenite fraction for some samples is slightly increasing during cooling to room temperature. These de- and increasing austenite fractions are on average 2 vol.%, which are within the estimated accuracy of  $\pm 1.5$  vol%, obtained by the magnetization measurements in this work. As shown during heating of the as-quenched samples (see Figure 6.4a), retained austenite might decompose during heating. For samples first tempered at  $T_{1t} \leq 635$  °C, no austenite formation during holding is observed, which is in agreement with the results of Wei [4], where no increase in austenite fraction for samples first tempered at  $T_{1t} \leq 635$  °C was observed. Also in the present work, when comparing the room temperature phase fractions shown in Figure 6.9, no austenite formation was obtained for samples first tempered at  $T_{1t} \leq 635$  °C. It is assumed that changes in the temperature control during the second tempering step might have influenced the measured magnetization and this could have caused the variations in the austenite fraction obtained during heating and cooling. However, the decrease in austenite fraction during heating and the unexpected discrepancy between the austenite fraction at the end of holding and at the end of cooling cannot be explained now and should be investigated further.

### 6.4.4 Austenite fraction from calculations of phase composition

It was mentioned in chapter 2 that the saturation magnetization is dependent on the chemical composition of the ferromagnetic phases [15, 16]. The partitioning of the elements

which takes place during tempering will lead to a change in the eventual composition of martensite. Moreover, tempered ( $\alpha'_T$ ) and fresh ( $\alpha'_F$ ) martensite also have a different composition, since the fresh martensite forms from the austenite that was formed during tempering, which is enriched in austenite stabilizing elements. This might influence the accuracy of the austenite fraction obtained from the magnetization measurements, since the calculations are based on the reference value of magnetization, obtained from heating an almost fully martensitic sample of the 13Cr6Ni2Mo SMSS. In the following, an attempt is made to calculate the magnetization of the samples at room temperature after the first tempering step, depending on the chemical composition of the phases  $\gamma$ ,  $\alpha'_T$  and  $\alpha'_F$ .

As explained in section 2.2.3 (see equation (2.6)), the magnetization of the sample at room temperature can be obtained by

$$M_{sat} = f_{\alpha'_T} M_{\alpha'_T} + f_{\alpha'_F} M_{\alpha'_F} + f_{\gamma} M_{\gamma}, \quad (6.8)$$

where  $f_{\gamma} M_{\gamma} = 0$ , since austenite is paramagnetic. The magnetization of  $\alpha'_T$  and  $\alpha'_F$  at room temperature, depending on the chemical composition, was calculated using equation (2.8.) The composition of  $\alpha'_T$  and  $\alpha'_F$  was obtained by Thermo-Calc [19]. Since  $\alpha'_F$  forms from the austenite during cooling, the composition of  $\alpha'_F$  is assumed to be equal to the equilibrium composition of fcc-austenite at the respective tempering temperature. The composition of  $\alpha'_T$  was assumed to be equal to the equilibrium composition of bcc-ferrite.

In Figure 6.19 the magnetization of  $\alpha'_T$  and  $\alpha'_F$ , both depending on the composition obtained by the thermodynamic calculations as described above, are given for temperatures between 580 and 700 °C. It is shown that both the magnetizations are between 164 and 173 Am<sup>2</sup>/kg. The magnetization of  $\alpha'_T$  is decreasing with increasing temperature, whereas the magnetization of  $\alpha'_F$  is increasing. Using the magnetization values from Figure 6.19 and the room temperature fractions of  $\alpha'_T$  and  $\alpha'_F$  obtained from the experiments after the first tempering step, when the austenite fraction was stable, the magnetization of the samples was calculated and compared to the measured ones. This is shown in Figure 6.20. It can be seen that the calculated and measured magnetization values are correlating very well. Hence, it can be assumed that the room temperature magnetization of  $\alpha'_T$  and  $\alpha'_F$  are close to the ones shown in Figure 6.19. Moreover, almost no differences between the magnetization obtained from tempering above and below  $T_{peak}$  (= 635 °C) between the calculated and the measured values are obtained. This indicates that the composition of fresh martensite is indeed similar to the one of fcc-austenite, calculated by Thermo-Calc [19]. Nevertheless, when calculating the austenite fraction from the calculated magnetization values using equation (6.1) the austenite fractions obtained are on average 1.2 vol.% smaller than the ones from the experiments, as shown in Figure 6.21. This difference is caused by the different reference values used for the calculation, where the reference magnetization  $M_{sat(ref)}$  for the calculated magnetization was obtained for the bulk composition by equation (2.8).

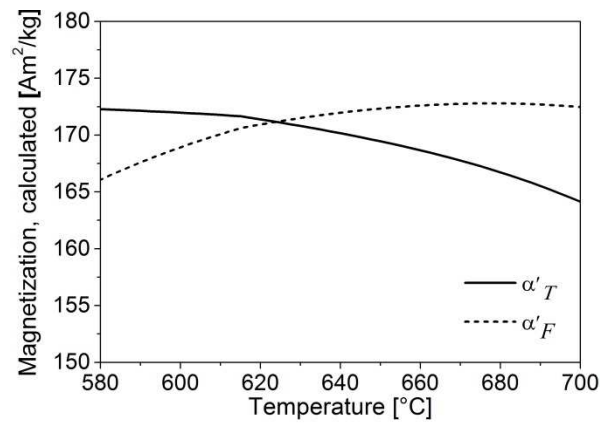


Figure 6.19 Magnetization, calculated by equation (2.8), as a function of first tempering temperature for tempered martensite  $\alpha'_T$  (from composition of bcc-iron obtained from thermodynamic calculation using Thermo-Calc [19]) and fresh martensite  $\alpha'_F$  (from composition of fcc-austenite). The accuracy for each point is  $\pm 3 \text{ Am}^2/\text{kg}$ .

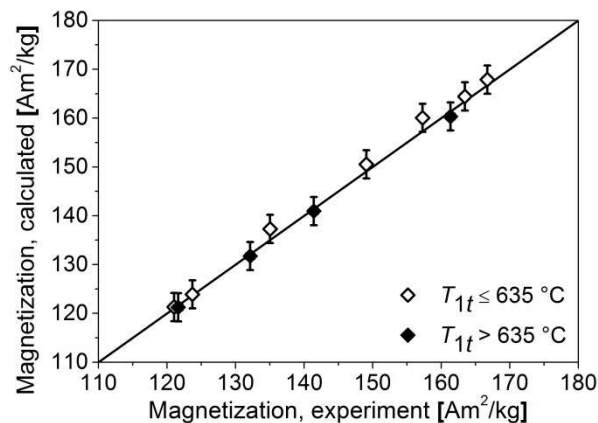


Figure 6.20 Calculated (equation (2.8)) versus measured magnetization after cooling from the first tempering temperature and holding at room temperature until the values became stable.

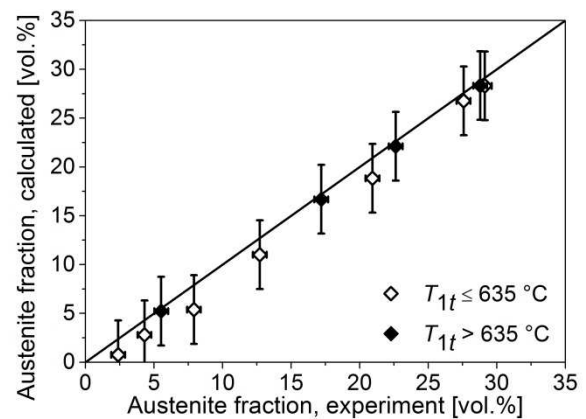


Figure 6.21 Calculated austenite fraction (see Figure 6.20) versus the austenite fraction obtained after cooling from the first tempering temperature and holding at room temperature until the values became stable.

## 6.5 Conclusions and recommendations

### 6.5.1 Conclusions

The formation of austenite during tempering of a 13Cr6Ni2Mo SMSS was analysed using a thermo-magnetic technique and the transformation kinetics of the martensite to austenite transformation were discussed. The main conclusions and findings are:

1. During heating to the first tempering temperature about 1 to 2 vol.% of austenite, retained from quenching after the austenitization, is decomposed between 350 and

480 °C. At 480 °C austenite starts to form, therefore this temperature was defined to be the  $A_{c1}$ -temperature of the as-quenched material for the heating rate of 5 K/min.

2. The activation energy for the isothermal martensite to austenite transformation during the first tempering was found to be 233 kJ/mol, which is similar to the activation energy of Ni and Mn diffusion in Fe. This supports the assumption that partitioning of Ni and Mn to austenite are mainly responsible for the austenite formation during tempering and hence its stabilization during subsequent cooling.
3. With increasing first tempering temperature the  $M_s$ -temperature of austenite is increasing, due to the lower concentration of austenite-stabilizing elements in the increased fraction of austenite obtained at the tempering temperature.
4. Austenite decomposition was observed during holding at room temperature after cooling from the first tempering step at 640 °C and above. It was argued that this might be related to stored energy, caused by the formation of martensite during cooling. The underlying mechanism is not yet understood and further study is needed.
5. During the second tempering at 550 °C austenite was formed if fresh martensite was formed during cooling from the first tempering temperature.
6. The retained austenite, mostly rod-shaped, is finely dispersed in the martensitic matrix, where some former austenite grains show a higher fraction of martensite with coarser austenite grains than other areas. This might be caused by different orientations of the grains or due to local inhomogeneities in austenite-stabilizing elements. Such differences in the microstructure could cause local differences in the mechanical properties, since these are strongly dependent on the fraction of retained austenite.
7. An approach was described to calculate the magnetization and hence the austenite fraction depending on the chemical composition, which showed good agreement with the results from the first tempering step.

### **6.5.2 Recommendations for future work**

Based on the findings in this chapter, the following suggestions are recommended for future work:

1. For distinguishing fresh martensite from austenite, an electron backscattered diffraction (EBSD) analysis is recommended to be performed on differently tempered samples. This can help to distinguish single and double tempered martensite after the second tempering treatment.
2. A thorough EBSD analysis is recommended to study the influence of the orientation of the prior austenite grains on the austenite nucleation and growth during tempering.
3. For further investigation of the time-dependent room temperature austenite decomposition synchrotron analysis is recommended to study the underlying kinetics and mechanisms. This can help to optimize the tempering parameters.

## REFERENCES

- [1] P. Toussaint and J.J. Dufrane: in *Supermartensitic Stainless Steel 2002*, KCI Publishing BV, Brussels, 2002, pp. 23-8.
- [2] X.P. Ma, L.J. Wang, C.M. Liu and S.V. Subramanian: *Mater. Sci. Eng. A*, 2011, vol. 528, no. 22-23, pp. 6812-8.
- [3] R.W.K. Honeycombe and H.K.D.H. Bhadeshia: *Steels: Microstructure and Properties*, 3rd ed., pp. 95-128, Elsevier Ltd., Amsterdam, 2006.
- [4] Y. Wei: *Microstructural Characterization and Mechanical Properties of Super 13% Cr Steel*, PhD Thesis, The University of Sheffield, England, 2005.
- [5] D.N. Zou, Y. Han, W. Zhang and X.D. Fang: *J. Iron Steel Res. Int.*, 2010, vol. 17, no. 8, pp. 50-4.
- [6] C. Gesnouin, A. Hazarabedian, P. Bruzzoni, J. Ovejero-García, P. Bilmes and C. Llorente: *Corros. Sci.*, 2004, vol. 46, no. 7, pp. 1633-47.
- [7] J. Hubackova, V. Cihal and K. Mazanec: *Z. Werkstofftech.*, 1984, vol. 15, pp. 411-5.
- [8] P.D. Bilmes, M. Solari and C.L. Llorente: *Mater. Charact.*, 2001, vol. 46, no. 4, pp. 285-96.
- [9] T.G. Gooch, P. Woollin and A.G. Haynes: in *Supermartensitic Stainless Steel '99*, KCI Publishing BV, Brussels, 1999, pp. 188-95.
- [10] Y. Song, X. Li, L. Rong and Y. Li: *Mater. Sci. Eng. A*, 2011, vol. 528, no. 12, pp. 4075-9.
- [11] Y.Y. Song, X.Y. Li, L.J. Rong, D.H. Ping, F.X. Yin and Y.Y. Li: *Mater. Lett.*, 2010, vol. 64, no. 13, pp. 1411-4.
- [12] Y.Y. Song, D.H. Ping, F.X. Yin, X.Y. Li and Y.Y. Li: *Mater. Sci. Eng. A*, 2010, vol. 527, no. 3, pp. 614-8.
- [13] Y.K. Lee, H.C. Shin, D.S. Leem, J.Y. Choi, W. Jin and C.S. Choi: *Mater. Sci. Technol.*, 2003, vol. 19, no. 3, pp. 393-8.
- [14] L. Zhao, N.H. van Dijk, E. Brück, J. Sietsma and S. van der Zwaag: *Mater. Sci. Eng. A*, 2001, vol. 313, no. 1-2, pp. 145-52.
- [15] D.C. Jiles: *Acta Mater.*, 2003, vol. 51, pp. 5907-39.
- [16] P.E. Merinov and A.G. Mazepa: *Industrial Laboratory (Diagn. Mater.)*, 1997, vol. 63, no. 3, pp. 149-53.
- [17] J. Crangle and W. Sucksmith: *J. Iron Steel Inst.*, 1951, vol. 168, pp. 141-51.
- [18] A.S. Arrott and B. Heinrich: *J. Appl. Phys.*, 1981, vol. 52, no. 3, pp. 2113-5.
- [19] Thermo-Calc Software package, Version S, Database TCFE6.2, Stockholm, Sweden, 2011.
- [20] A.E. Berkowitz: Constitution of Multiphase Alloys, in: A.E. Berkowitz and E. Kneller (Eds.): *Magnetism and Metallurgy*, vol. 1, p. 335, Academic Press, Inc., New York, 1969.
- [21] R.M. Bozorth: *Ferromagnetism*, pp. 715-9, John Wiley & Sons, Inc., Hoboken, NJ, 2003.
- [22] W.D. Callister Jr: *Fundamentals of Materials Science and Engineering: An integrated approach*, 2nd ed., p. 743, John Wiley & Sons, Inc., 2005.
- [23] C.A.D. Rodrigues, P.L.D. Lorenzo, A. Sokolowski, C.A. Barbosa and J.M.D.A. Rollo: *Mater. Sci. Eng. A*, 2007, vol. 460, pp. 149-52.

- [24] G.F. da Silva, S.S.M. Tavares, J.M. Pardal, M.R. Silva and H.F.G. Abreu: *J. Mater. Sci.*, 2011, vol. 46, no. 24, pp. 7737-44.
- [25] X.P. Ma, L.J. Wang, C.M. Liu and S.V. Subramanian: *Mater. Sci. Eng. A*, 2012, vol. 539, pp. 271-9.
- [26] Y.R. Liu, D. Ye, Q.L. Yong, J. Su, K.Y. Zhao and W. Jiang: *J. Iron Steel Res. Int.*, 2011, vol. 18, no. 11, pp. 60-6.
- [27] N. Nakada, T. Tsuchiyama, S. Takaki and N. Miyano, *ISIJ Int.*, 2011, vol. 51, no. 2, pp. 299-304.
- [28] Y. He, K. Yang and W. Sha: *Metall. Mater. Trans. A*, 2005, vol. 36A, no. 9, pp. 2273-87.
- [29] R. Schnitzer, R. Radis, M. Nöhrer, M. Schober, R. Hochfellner, S. Zinner, E. Povoden-Karadeniz, E. Kozeschnik and H. Leitner: *Mater. Chem. Phys.*, 2010, vol. 122, no. 1, pp. 138-45.
- [30] M. Avrami: *J. Chem. Phys.*, 1939, vol. 7, no. 12, pp. 1103-12.
- [31] M. Avrami: *J. Chem. Phys.*, 1940, vol. 8, no. 2, pp. 212-24.
- [32] M. Avrami: *J. Chem. Phys.*, 1941, vol. 9, no. 2, pp. 177-84.
- [33] W. Johnson and R. Mehl: *Trans. Am. Inst. Min. (Metall.) Eng.*, 1939, vol. 135, pp. 416.
- [34] A.N. Kolmogorov: *Izv. Akad. Nauk. SSSR, Ser Mat.*, 1937, vol. 3, pp. 355.
- [35] D.A. Porter, K.E. Easterling and M.Y. Sherif: *Phase Transformations in Metals and Alloys*, 3rd ed., pp. 285-8, CRC Press, Boca Raton, 2009.
- [36] J.W. Christian: *The Theory of Transformations in Metals and Alloys*, Part 1, 3<sup>rd</sup> ed., pp. 83, pp. 538-46, Pergamon, Amsterdam, 2002.
- [37] I. Varga, E. Kuzmann and A. Vértes: *Hyperfine Interact.*, 1998, vol. 112, no. 1-4, pp. 169-73.
- [38] H. Nakagawa, T. Miyazaki and H. Yokota: *J. Mater. Sci.*, 2000, vol. 35, no. 9, pp. 2245-53.
- [39] P.P. Sinha, D. Sivakumar, N.S. Babu, K.T. Tharlan and A. Natarajan: *Steel Res.*, 1995, vol. 66, no. 11, pp. 490-4.
- [40] *Smithells Metals Reference Book*, W.F. Gale and T.C. Totemeier (Eds.), 8 ed., chapter 13, Elsevier Butterworth-Heinemann, Amsterdam, 2004.
- [41] P. Wang, S. Lu, D. Li, X. Kang and Y. Li: *Acta Metall. Sinica*, 2008, vol. 44, no. 6, pp. 681-5.
- [42] A. Kulmburg, F. Korntheuer, M. Koren, O. Gründler and K. Hutterer: *BHM*, 1981, vol. 126, pp. 104-8.
- [43] K.W. Andrews: *J. Iron Steel Inst.*, 1965, vol. 203, pp. 721-7.
- [44] D.P. Koistinen and R.E. Marburger: *Acta Metall.*, 1959, vol. 7, no. 1 pp. 59-60.
- [45] S.M.C. van Bohemen and J. Sietsma: *Mater. Sci. Technol.*, 2009, vol. 25, no. 8, pp. 1009-12.
- [46] C.L. Magee: The nucleation of martensite, in: *Phase transformations*, pp. 115-56, American Society for Metals, Metals Park, Ohio, 1970.
- [47] E. Jimenez-Melero, N.H. van Dijk, L. Zhao, J. Sietsma, S.E. Offerman, J.P. Wright and S. van der Zwaag: *Scripta Mater.*, 2007, vol. 56, no. 5, pp. 421-4.

- 
- [48] G. Krauss: *Steels: Heat Treatment and Processing Principles*, p. 187, ASM International, Materials Park, Ohio, 1990.
- [49] Z. Nishiyama: *Martensitic Transformation*, M.F. Fine, M. Meshii and C.M. Wayman (Eds.), pp. 280-1, p. 322, Academic Press, Inc., New York, 1978.
- [50] M. Amirthalingam: *Microstructural Development during Welding of TRIP Steels*, PhD Thesis, Technische Universiteit Delft, The Netherlands, 2010.
- [51] T. Hojo, K.I. Sugimoto, Y. Mukai and S. Ikeda: *ISIJ Int.*, 2008, vol. 48, no. 6, pp. 824-9.
- [52] L. Zhao, B. Mainfroy, M. Janssen, A. Bakker and J. Sietsma: *Scripta Mater.*, 2006, vol. 55, no. 4, pp. 287-90.
- [53] H.-J. Niederau: *Stahl und Eisen*, 1978, vol. 98, no. 8, pp. 385-92.
- [54] S. Van Der Zwaag, L. Zhao, S.O. Kruijver and J. Sietsma: *ISIJ Int.*, 2002, vol. 42, no. 12, pp. 1565-70.
- [55] P.J. Jacques, S. Allain, O. Bouaziz, A. De, A.F. Gourgues, B.M. Hance, Y. Houbaert, J. Huang, A. Iza-Mendia, S.E. Kruger, M. Radu, L. Samek, J. Speer, L. Zhao and S. van der Zwaag: *Mater. Sci. Technol.*, 2009, vol. 25, no. 5, pp. 567-74.



# 7

## Influence of austenitization treatment on the austenite fraction during subsequent heat treatment of an SMSS<sup>1</sup>

The formation of austenite from martensite in two stages, observed during heating in chapter 5, is further investigated for the 13Cr6Ni2Mo SMSS. The influence of different austenitization treatment parameters on austenite formation during reheating and on the fraction of austenite retained after tempering treatment is measured and analysed. The two-stage formation of austenite is probably due to inhomogeneous distribution of the austenite-stabilizing elements Ni and Mn, resulting from their slow diffusion from martensite into austenite and carbide and nitride dissolution during the second, higher temperature, stage. A better homogenization of the material causes an increase in the transformation temperatures for the martensite to austenite transformation and a lower retained austenite fraction with less variability after tempering. Furthermore, the martensite to austenite transformation was found to be incomplete at the target temperature of 950 °C, which is influenced by the previous austenitization treatment and the heating rate. The activation energy for martensite to austenite transformation was determined by a modified Kissinger equation to be approximately 400 kJ/mol and 500 kJ/mol for the first and the second stages of transformation, respectively. Both values are much higher than the activation energy found during isothermal treatment in chapter 6 and are believed to be effective activation energies comprising the activation energies of both mechanisms involved, i.e. nucleation and growth.

### 7.1 Introduction

It was found from the austenitization experiments in chapter 5 that the formation of austenite from martensite in the 13Cr6Ni2Mo SMSS takes place in two stages during heating to 950 °C. However, these experiments have been carried out with as-received, double tempered material, containing about 22 vol.% retained austenite. It was argued that the

---

<sup>1</sup> This chapter is based on: A. Bojack, L. Zhao, P.F. Morris and J. Sietsma: Austenite Formation from Martensite in a 13Cr6Ni2Mo Supermartensitic Stainless Steel, *Metall. Mater. Trans. A*, 2016, vol. 47A, pp. 1996-2009.

reason for the two-stage transformation could be the partitioning of Ni to austenite, where the martensite with a lower Ni-concentration has a higher  $A_{c1}$ -temperature and therefore transforms to austenite at a higher temperature. These two stages were found by dilatometry to be distinct, even though most of the austenite-stabilizing elements that would have caused this effect are already dissolved in austenite. As a consequence, the differences in Ni-concentration were considered to be the most likely cause of the two-stage austenite formation. Since for SMSS the heat treatment is crucial for obtaining the desired properties of high strength and good toughness, control of the austenitization step is important, as it determines the levels of alloy in solution and their distribution prior to subsequent tempering.

The austenitization treatment of low carbon martensitic stainless steels and SMSS is carried out above the  $A_{c3}$ -temperature, usually between 950 and 1100 °C [1-9]. This is to obtain an almost fully martensitic microstructure after cooling to ambient temperature by avoiding formation of delta-ferrite, which can have detrimental effects on the properties. It was observed for different SMSS grades that the prior austenite grain size, together with the width of the martensite laths, was increasing with increasing austenitization temperature [10-12], whereas the hardness was decreasing [11, 12]. Liu et al. [10] found for an SMSS (in wt.%, 0.02C-12Cr-5Ni-2Mo-0.4Mn-0.2Si) the grain size of the original austenite increases with increasing austenitization temperature from 900 to 1100 °C. Moreover, they observed that the tensile strength after tempering decreases with increasing previous austenitization temperature and that the elongation increases for austenitization up to 1050 °C.

So far, only a limited number of studies giving a direct comparison of the influence of the austenitization treatment of SMSS on the austenite formation during reheating and on the austenite fraction obtained after tempering have been carried out. This chapter focuses on the austenite formation in the 13Cr6Ni2Mo SMSS, previously austenitized at different temperatures and times, during reheating at different rates and measured using dilatometry. Furthermore, the influence of the austenitization treatment on the retained austenite fraction after tempering between 615 and 655 °C was analysed using the VSM. The influence of heating rate on the austenite transformation temperatures and the formation of austenite in two stages was measured using dilatometry and analysed by applying a modified Kissinger-method to obtain the activation energy for the formation of austenite from martensite.

## **7.2 Experimental**

### **7.2.1 Material**

Samples from the as-received material of the 13Cr6Ni2Mo SMSS studied were taken from two casts with minor differences in composition (see Table 7.1). The as-received material was supplied in the solution treated and double-tempered condition with a microstructure consisting of martensite, retained austenite and a very small fraction of carbides, nitrides and carbonitrides [13].

Table 7.1 Chemical composition of the 13Cr6Ni2Mo SMSS (in wt.%), balance Fe.

Cast	C	Cr	Ni	Mo	Mn	Si	V	Ti	N
# 1	0.015	12.34	5.66	2.02	0.42	0.22	0.18	0.01	0.013
# 2	0.020	12.27	5.62	2.01	0.42	0.21	0.18	0.01	0.016

### 7.2.2 Heat treatments

An overview of the heat treatments performed in this work is given in Figure 7.1. Two different austenitization treatments (heat treatment A) were chosen: A conventional austenitization treatment at low temperature with short-term soak and one at high-temperature with long-term soak. The latter provides an increased homogenization of the material. After the austenitization treatment the samples were either reheated to 950 °C (heat treatment B) or tempered (heat treatment C). The heat treatment steps are described in the following sections.

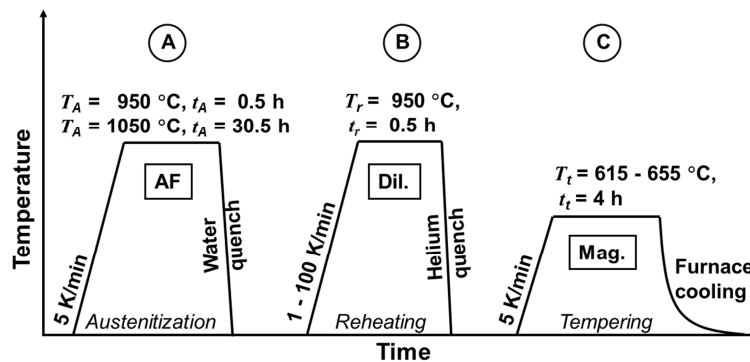


Figure 7.1 Scheme of the applied heat treatment steps A, B and C.  $T$  and  $t$  denote temperature and time. Subscripts 'A' denote austenitization, 'r' reheating and 't' tempering. 'AF' denotes treatment in air furnace, 'Dil.' in dilatometer and 'Mag.' in magnetometer.

#### Austenitization treatments

The as-received material was subsequently austenitized in an air furnace at 950 °C for 0.5 h and at 1050 °C for 30.5 h, for the two treatments, followed by quenching in water (see Figure 7.1). The microstructure of the material after quenching is martensitic with 2–4 vol.% of retained austenite. The term 'austenitization' in this chapter is used to refer to these subsequent austenitization treatments. The symbols  $T_A$  and  $t_A$  denote the austenitization temperature and time.

#### Reheating experiments

The reheating experiments were carried out in the dilatometer device described in section 3.3. The materials used are from cast #2 for both previously austenitized samples. The differently austenitized samples were heated to 950 °C with heating rates between 1

and 100 K/min, held there for 0.5 h and subsequently quenched to room temperature using helium gas (see heat treatment B in Figure 7.1). Three experiments per heating rate were carried out. In Figure 7.2 examples of dilatation curves are given for an as-received sample, containing about 23 vol.% austenite, heated at 3 K/min, and a sample austenitized at 950 °C for 0.5 h, heated at 1 K/min. The austenite formation from martensite is taking place in two stages and the temperatures  $A_{s1}$  and  $A_{f1}$  denote the start and finish of the austenite formation in the first stage.  $A_{s2}$  denotes the start of the austenite formation in the second stage. A temperature corresponding to the finish of the second stage of martensite to austenite transformation was not obtained from the present experiments, as will be described later in section 7.3.1. The transformation temperature range was defined as the temperature range at which 1 and 99 vol.% of the product phase were formed. The precision is  $\pm 5$  °C.

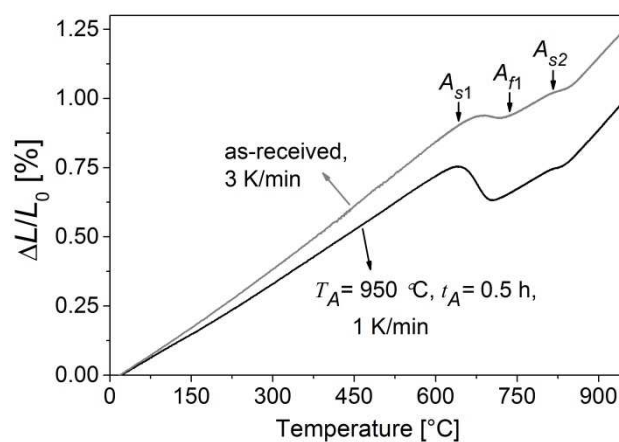


*Figure 7.2 Dilatation versus temperature of an as-received sample, heated at 3 K/min, and a sample previously austenitized at 950 °C for 0.5 h, heated at 1 K/min.  $A_{s1}$  and  $A_{f1}$  denote the start and finish temperatures of the first stage of austenite formation and  $A_{s2}$  the start of the second stage.*

The austenite fraction,  $f_\gamma$ , was obtained by the lever-rule using equation (3.6). The estimated uncertainty of the austenite fraction obtained by the lever-rule in this work is  $\pm 3$  vol.%. However, lever-rule analysis relies on the assumption that lattice spacing for martensite and austenite depends on temperature only. The redistribution of alloying elements during heat treatment could increase the uncertainty of the austenite fraction in this study to approximately  $\pm 6$  vol.%.

### **Tempering treatments**

Magnetic measurements were carried out to analyse the influence of austenitization treatment on the austenite fraction that is retained at room temperature after the tempering treatment (see heat treatment C in Figure 7.1). The materials used are from cast #1 for the samples previously austenitized at 950 °C for 0.5 h and from cast #2 for the samples previously austenitized at 1050 °C for 30.5 h.

Tempering treatments of the previously austenitized samples were carried out in the VSM described in section 3.2. The heating was performed at a nominal rate of 5 K/min, followed

by tempering for 4 h at temperatures between 615 and 655 °C. The cooling was carried out in the VSM-furnace. In-situ thermo-magnetic analysis of the formation of austenite during tempering treatments has been carried out in chapter 6 and further details about the experiments can be found there.

Immediately after cooling from tempering, the magnetization of the samples was measured at 1.5 T, a value close to its saturation (see section 3.2). The corresponding austenite fraction,  $f_\gamma$ , was obtained using equation 3.2. The estimated uncertainty of the calculated austenite fraction from the measured magnetization at room temperature is  $\pm 0.5$  vol.%, which includes the uncertainty from the measurement and the reference sample.

### 7.2.3 Microscopy

Microstructural analysis of the tempered samples was carried out in the optical microscope and the SEM, which is described in section 3.5 together with the sample preparation.

## 7.3 Results

### 7.3.1 Influence of previous austenitization treatment and the heating rate on austenite formation upon reheating

#### *Reheating to 950 °C*

Dilatation curves during reheating between 600 and 950 °C of the different previously austenitized samples are shown in Figure 7.3 for all heating rates. All curves show a distinct first contraction between 650 and 750 °C, marked by the temperatures  $A_{s1}$  and  $A_{f1}$ . Another change in length with a smaller expansion coefficient between 800 and 900 °C is observed in some curves, where the beginning is marked by  $A_{s2}$ . This is attributed to the formation of austenite from martensite in two stages, as will be described later. With increasing heating rate the second stage becomes less pronounced and is also less pronounced for the samples austenitized at 1050 °C. The separation of the austenite formation in two stages is much more pronounced for the as-received sample, shown in Figure 7.2, than for the samples which have been given the austenitization treatment. This is seen by the different relative length changes between the two stages.

The influence of heating rate on the transformation temperatures  $A_{s1}$ ,  $A_{f1}$  and  $A_{s2}$  is shown in the continuous-heating-transformation (CHT) diagram in Figure 7.4. The transformation temperatures increase with increasing heating rate, whereas the temperatures for the samples austenitized at 950 °C for 0.5 h are lower than for the samples austenitized at 1050 °C for 30.5 h. This difference is about 10 °C for the first stage and about 30 °C for the start of the second stage of austenite formation. Since with increasing heating rate the second stage becomes less pronounced, it was not possible to define the start of the second stage clearly for higher heating rates, as can be seen in Figure 7.4. However, this does not necessarily mean that the second stage of transformation does not take place at high

heating rates, but it might start later. The finish of the second stage of austenite formation could not be determined, as will be described in the following section.

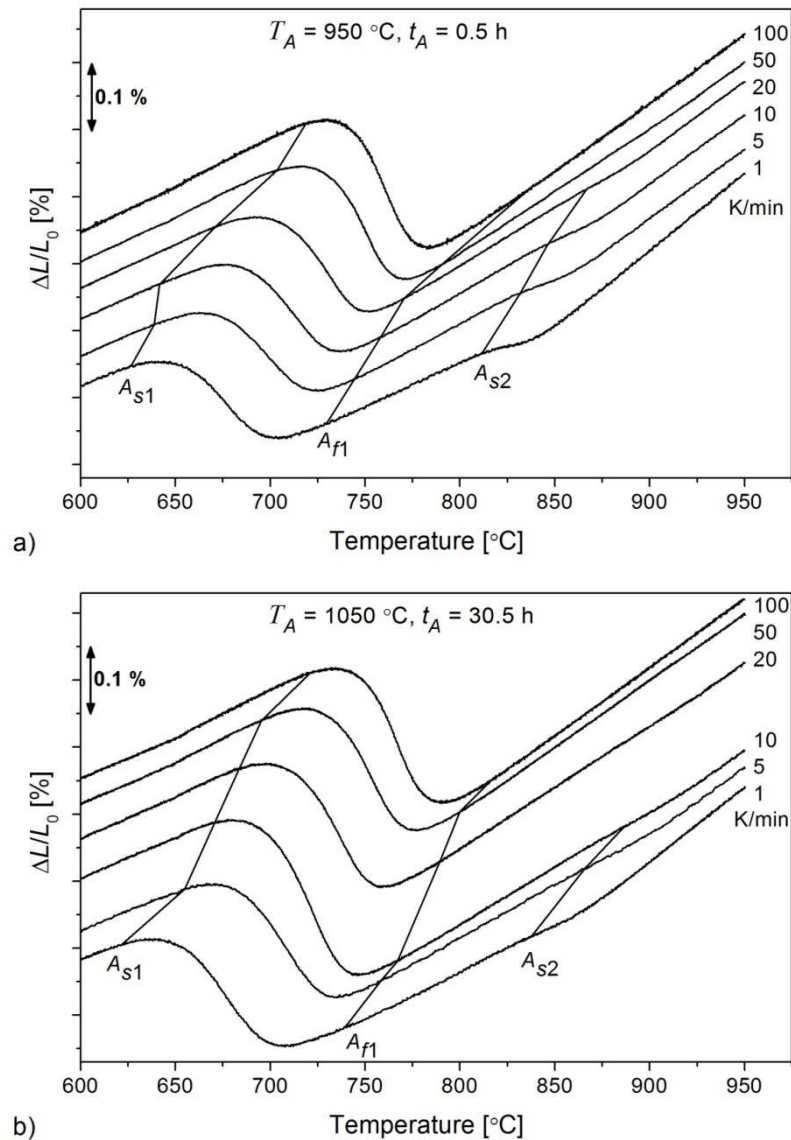


Figure 7.3 Dilatation versus temperature during rehaeting at different heating rates of samples austenitized at a) 950 °C for 0.5 h and b) 1050 °C for 30.5 h. For better visualization, the curves are shifted on the y-axis by 0.05 %.

In Figure 7.5, the change in the transformation temperatures as a function of heating rate is presented. It can be seen that the influence of heating rate is strongest up to 20 K/min. The transformation temperatures were fitted with

$$A_{s,f} = A_0 + m \left[ 1 - \exp\left(-\frac{\phi}{r}\right) \right], \quad (7.1)$$

where  $A_{s,f}$  denotes the start and finish transformation temperatures, respectively,  $A_0$  the extrapolated transformation temperatures to a zero heating rate,  $m$  and  $r$  constants, and  $\phi$  the heating rate. The fitting parameters  $A_0$ ,  $m$  and  $r$  are listed in Table 7.2 together with the standard deviations obtained from fitting statistics.  $(A_0 + m)$  equals the temperatures at infinitely high heating rate. The samples austenitized at 1050 °C show lower  $m$ -values compared to the samples austenitized at 950 °C. This indicates a more homogeneous distribution of alloying elements in the samples austenitized at 1050 °C for 30.5 h.

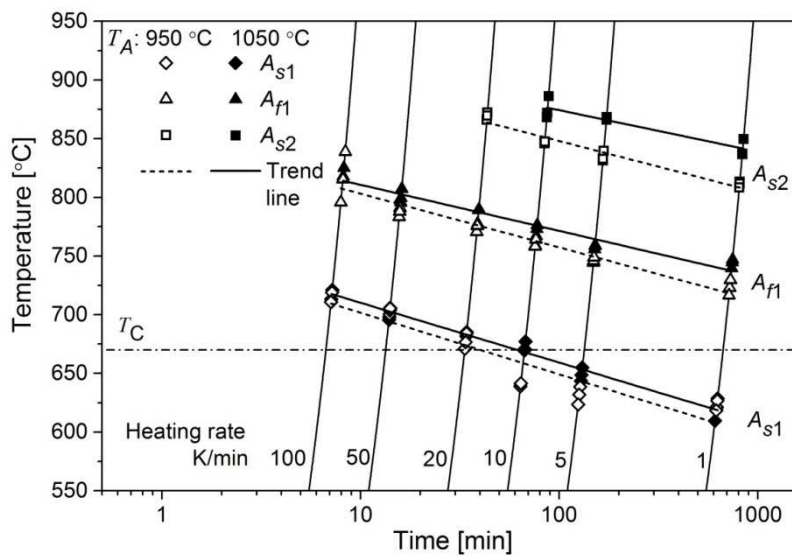


Figure 7.4 Continuous-heating-transformation (CHT) diagram for reheating of the different previously austenitized samples.  $T_C$  is the Curie temperature of the bulk material (see chapter 5).

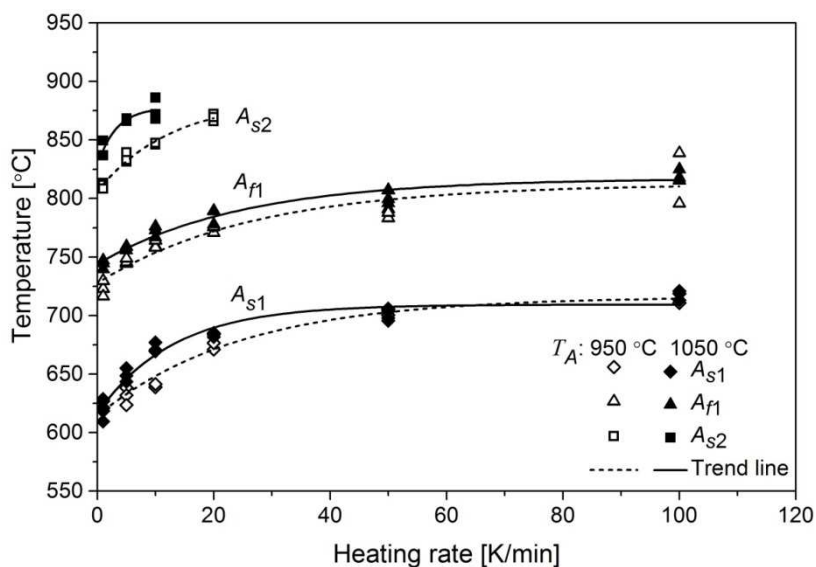


Figure 7.5 Variation of  $A_{s1}$ ,  $A_{f1}$  and  $A_{s2}$  with heating rate for reheating of the different previously austenitized samples.

By equation (7.1) the equilibrium transformation temperatures at zero heating rate are obtained.  $A_0$  is in the following denoted as  $A_0^{s1}$ ,  $A_0^{f1}$  and  $A_0^{s2}$ , indicating that it belongs to the respective transformation temperatures. This extrapolation helps to compare the experimentally obtained transformation temperatures with equilibrium values. The most important equilibrium transformation temperatures and phase stability ranges for the 13Cr6Ni2Mo SMSS are discussed in chapter 4 and are listed in Table 4.3. From Table 7.2 and Table 4.3, it can be seen that the  $A_{e3}$ -temperature is within the range of the  $A_0^{f1}$ -temperatures. Moreover, the dissolution of  $M_{23}C_6$ , VN and  $\chi$ -phase occurs within the range of the second stage of the martensite to austenite transformation.

Table 7.2 Overview of the fitting parameters  $A_0$ ,  $m$  and  $r$  from the fit of transformation temperatures in Figure 7.5 using equation (7.1).

	$T_A = 950 \text{ }^\circ\text{C}$			$T_A = 1050 \text{ }^\circ\text{C}$		
	$A_0$	$m$	$r$	$A_0$	$m$	$r$
	$^\circ\text{C}$	$^\circ\text{C}$	K/min	$^\circ\text{C}$	$^\circ\text{C}$	K/min
$A_{s1}$	$614 \pm 4$	$102 \pm 5$	$25 \pm 3$	$616 \pm 5$	$93 \pm 6$	$13 \pm 2$
$A_{f1}$	$728 \pm 6$	$85 \pm 8$	$27 \pm 8$	$744 \pm 3$	$73 \pm 4$	$25 \pm 4$
$A_{s2}$	$806 \pm 3$	$76 \pm 7$	$13 \pm 3$	$828 \pm 10$	$50 \pm 8$	$3 \pm 2$

### **Holding at 950 °C**

In Figure 7.6, the length changes during holding at 950 °C of the different previously austenitized samples are shown for the different heating rates. The curves show that the length is still changing during holding at 950 °C. In general, the change in relative length during holding is greater for higher heating rates. Almost no change was detected for the samples heated at a rate of 1 K/min. When the samples were heated at a rate of 5 K/min the decrease in length saturates after approximately 15 min of holding. The samples austenitized at 950 °C for 0.5 h show, for heating rates up to 20 K/min, a larger decrease in relative length compared to the samples austenitized at 1050 °C for 30.5 h. For comparison, the change in relative length during holding at 950 °C of an as-received sample, heated at a rate of 3 K/min, is added in Figure 7.6a. Its decrease in length is greater than for the sample austenitized at 950 °C for 0.5 h and heated at a rate of 1 K/min, and is similar to the length change of the sample austenitized at 1050 °C for 30.5 h and heated at a rate of 5 K/min.

The decreases in length during holding at 950 °C indicate that the austenite formation of the second stage is not completed after heating to 950 °C. Therefore, temperatures defining the finish of the second stage of austenite formation could not be determined from the measured dilatation curves in the present study. A similar high value of the austenite finish temperature was recently found by Ravi Kumar et al. [14] by high-temperature X-ray diffraction for a Fe-0.023C-11.3Cr-7.6Ni-1.3Mn-0.62Si (wt.%) steel. There, the martensite to austenite formation was found to be complete at 950 °C. Christien et al. [15] also recently observed an  $A_{e3}$ -temperature of 950 °C for a 17-4PH martensitic stainless steel using neutron

diffraction measurements, where 5 % of martensite was still present at 930 °C. Bénéteau et al. [16] reported for a high-nitrogen martensitic stainless steel that 70 % of the ferrite was transformed between 845 and 890 °C, whereas in the temperature range between 890 and 1025 °C the austenite formation slowly ends.

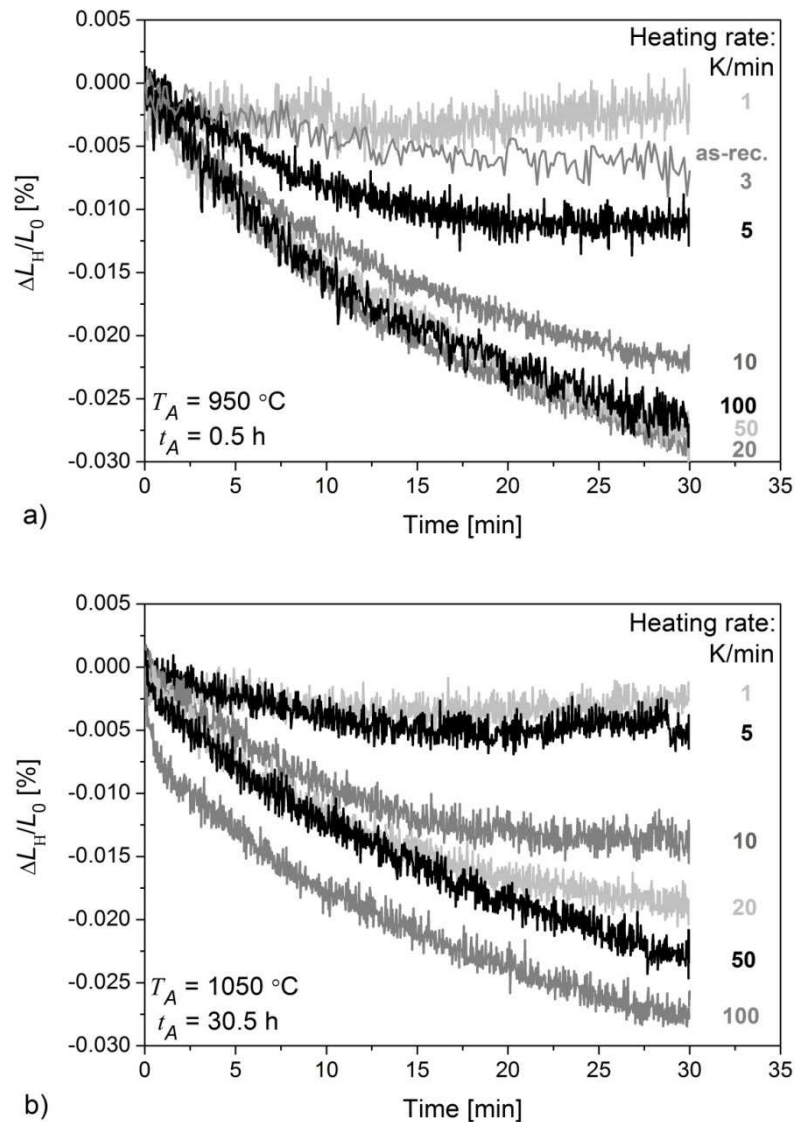


Figure 7.6 Comparison of the relative length changes during holding,  $\Delta L_H/L_0$ , at 950 °C after heating with different rates for samples previously austenitized at a) 950 °C for 0.5 h and b) 1050 °C for 30.5 h. The curve of an as-received (as-rec.) sample is also shown in a).

### Calculation of the austenite fraction

For the analysis of the results, the fractions transformed during holding at 950 °C need to be calculated first. For this reason, the relative length change during holding at 950 °C (Figure 7.6),  $\Delta L_H/L_0 = (\Delta L - \Delta L_{H,ini})/L_0$  with  $\Delta L_{H,ini}/L_0$  the initial value of relative length change during holding, was fitted by an exponential decay equation of the type:

$$\frac{\Delta L_H}{L_0} = \frac{\Delta L_A}{L_0} \exp\left(-\frac{t}{\tau_A}\right) + \frac{\Delta L_B}{L_0} \exp\left(-\frac{t}{\tau_B}\right) + \frac{\Delta L_{inf}}{L_0}, \quad (7.2)$$

where  $\Delta L_A$  and  $\Delta L_B$  are fitting parameters,  $\Delta L_{inf}$  denotes the value of the length change after infinite holding at which the transformation would be complete,  $\Delta L_0$  the initial sample length at experiment start,  $t$  the holding time, and  $\tau_A$  and  $\tau_B$  the mean rate parameters.

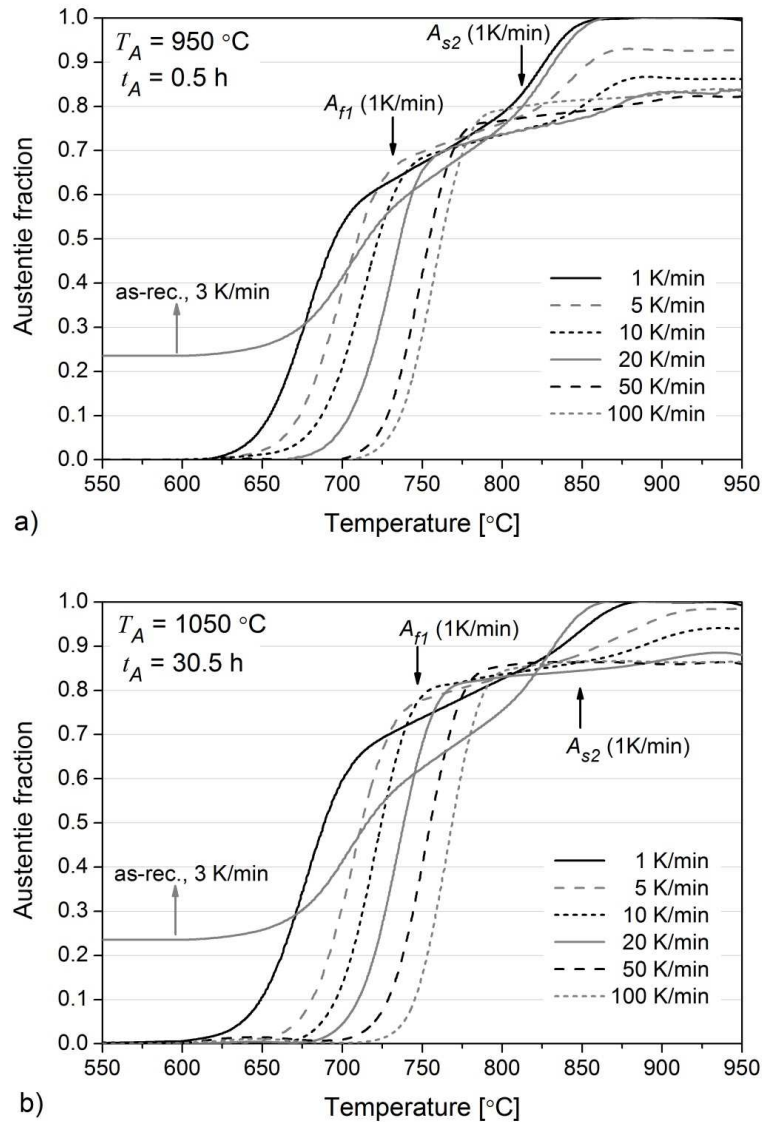


*Figure 7.7 Austenite fraction versus temperature for different heating rates with samples previously austenitized at a) 950 °C for 0.5 h and b) 1050 °C for 30.5 h. The austenite fraction of an as-received sample (as-rec.) with an initial austenite fraction of about 0.23 is also presented.*

The austenite fraction during heating, which was obtained by the lever-rule, was corrected for the fraction of austenite at infinite time of holding at 950 °C, when the transformation is assumed to be finished. The austenite fractions, obtained during heating, are shown in

Figure 7.7. The two stages of austenite formation can be clearly seen for the lower heating rates. However, the increase of the austenite fraction between the two stages indicates that austenite also forms in that temperature range, but at a lower rate. The formation rate of austenite between the two stages is decreasing with increasing heating rate. The fraction of austenite formed during the second stage up to 950 °C is also decreasing with increasing heating rate, whereas the fraction of austenite formed during the first stage appears to be slightly increasing. The samples austenitized at 950 °C show an approximately 10 % lower fraction of austenite formed during the first stage than those austenitized at 1050 °C for the same heating rate. For the second stage the difference is about 5 %. The austenite fraction of an as-received sample, heated at 3 K/min, is also included in Figure 7.7, showing a lower transformation rate in the first stage and an increased transformation rate in the second stage. This sample shows similar behaviour to the sample previously austenitized at 950 °C and heated with a rate of 1 K/min.

The austenite fractions, formed during holding at 950 °C for the different samples, based on the calculations with equation (7.2) and the lever-rule, are shown in Figure 7.8. For both previous austenitization treatments the austenite fraction formed during holding at 950 °C for 0.5 h is increasing with the heating rates up to 10 K/min. Thereafter, the austenite fraction is almost constant at approximately 13 % for the samples austenitized at 950 °C and at approximately 9 % for the samples austenitized at 1050 °C. The samples heated at a rate higher than 10 K/min would continue to form austenite during infinite holding at 950 °C.

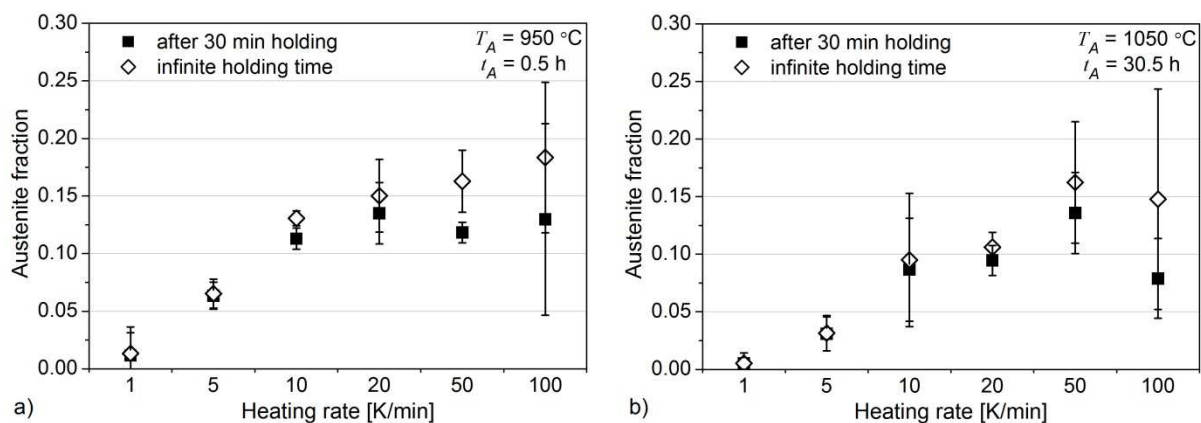


Figure 7.8 Austenite fraction formed during holding at 950 °C for 30 min and for infinite holding time, calculated by equation (7.2) and the lever-rule, versus heating rate for the samples previously austenitized at a) 950 °C for 0.5 h and b) 1050 °C for 30.5 h.

### Determination of activation energy of austenite formation during heating

The activation energy governing the transformation during continuous heating can be obtained by a Kissinger-like method, valid also for non-isothermal annealing, which is described by Mittemeijer et al. [17-19]. The state variable  $\beta$  (dimensionless), which determines the fraction transformed, can be obtained for non-isothermal annealing by

$$\beta = \int_0^t k dt', \quad (7.3)$$

where the rate constant  $k$  ( $s^{-1}$ ) is described by an Arrhenius-type equation:

$$k = k_0 \exp(-E/RT). \quad (7.4)$$

$t$  denotes the duration of the process considered and  $T$  (K) the temperature, where  $T$  and  $k$  depend on  $t$  for non-isothermal annealing.  $E$  (J/mol) denotes the effective activation energy of the overall transformation process,  $R$  (8.31441 J/(mol K)) the universal gas constant and  $k_0$  ( $s^{-1}$ ) the pre-exponential factor. [17-19]

For constant heating rates  $\phi$  (K/s),  $\beta$  can be obtained by

$$\beta = \frac{T^2}{\phi} \frac{R}{E} k \left\{ 1 - 2 \frac{RT_f}{E} + \dots \right\} \cong \frac{T^2}{\phi} \frac{R}{E} k, \quad (7.5)$$

since  $RT_f/E \ll 1$  for solid-state transformations [17-19]. Taking the temperature for a fixed fraction transformed for various heating rates,  $T_f$  (K), into account [17-19], the activation energy can be obtained by

$$\ln \left( \alpha \frac{T_f^2}{\phi} \right) = \frac{E}{RT_f} + \ln \left( \alpha \frac{E}{Rk_0} \right) + \ln \beta_f. \quad (7.6)$$

$\beta_f$  determines the fraction transformed at  $T_f$ .  $\alpha = 1/(Ks)$  is introduced to make the argument of the logarithm dimensionless.  $\alpha$  is necessary for consistency. The only alternative solution is to use the exponential equation:

$$\frac{T_f^2}{\phi} = \frac{E\beta_f}{Rk_0} \exp \left( \frac{E}{RT_f} \right). \quad (7.7)$$

Applying the Kissinger-like method requires the following conditions. The original Kissinger method was developed for homogeneous reactions, but was found to be applicable for heterogeneous reactions as well [18], since  $T_f$  depends systematically on the heating rate [18, 20]. Heterogeneous transformations are characterized by a maximum transformation rate, where the corresponding temperature  $T_i$  occurs at approximately the same transformed fraction  $f$ . Moreover, in heterogeneous transformations more than one mechanism govern the transformation, e.g. nucleation and growth. If these temperature-dependent sub-steps are thermally activated according to the Arrhenius-type relationship, the assumption of the Arrhenius-type temperature dependence of  $k$  holds and the Kissinger-like method can be applied for heterogeneous solid-state transformations [18, 20]. Hence,  $T_f$  can be replaced by the temperature where the transformation rate is maximum,  $T_i$ , which corresponds to the point of inflection of the austenite fraction,  $f_\gamma$ , versus  $T$  curve [17, 18, 20]. The activation energy for the austenite formation can then be obtained from the slope of a Kissinger-plot of  $\ln(\alpha T_i^2/\phi)$  versus  $1/T_i$  according to equation (7.6) [17, 18, 20].

The kinetic analysis in the present study was performed on the values of the austenite fraction. It was stated in [19] that the kinetic analysis by non-isothermal dilatometry requires the reference length for the calculation of the degree of transformation. However, since the austenite fraction was obtained directly from the length change by the lever-rule,  $T_i$  can also be determined from the austenite fraction as in the present study. The first derivative of the austenite fractions shown in Figure 7.7 with respect to temperature is plotted in Figure 7.9 for all the heating rates. For both previous austenitization treatments two peaks are obtained, related to the two stages of austenite formation.  $T_i$ -values were obtained by applying a peak position analysis. The peak, and hence the transformation rate, corresponding to the first transformation is higher than the second peak. With increasing heating rate the peaks are shifted to higher temperatures  $T_i$ , which correlates with the increase in the transformation temperatures. Moreover, the second peak is decreasing with increasing heating rate. The peak positions corresponding to the first and second stages are at higher values of  $T_i$  for the samples austenitized at 1050 °C for 30.5 h. This corresponds to the differences in the transformation temperatures as shown in Figure 7.4. Between both stages the transformation rate is nearly constant and is larger than zero, since the austenite formation did not stop between both stages. However, this rate is very low with maximum of about 0.0025 °C<sup>-1</sup>.

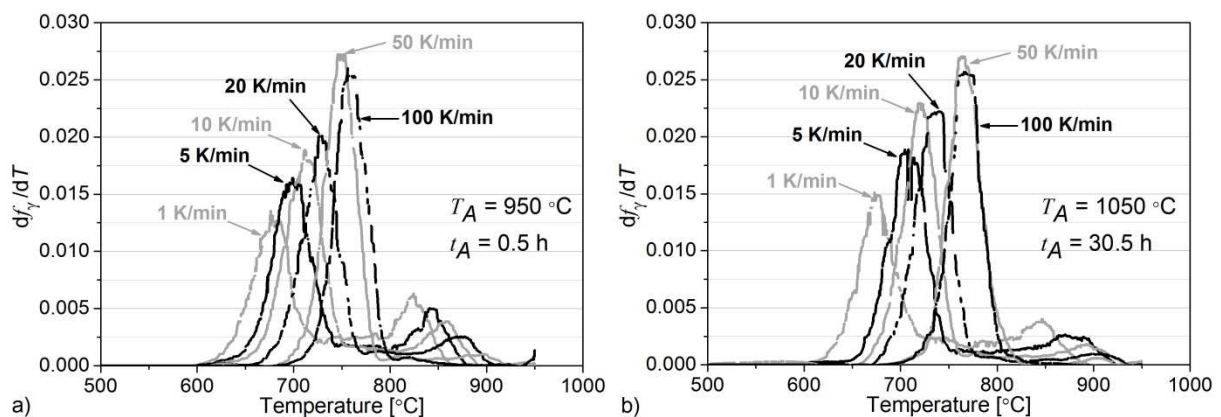


Figure 7.9 Transformation rate  $df_i/dT$  versus temperature for different heating rates of samples previously austenitized at a) 950 °C for 0.5 h and b) 1050 °C for 30.5 h.

As discussed above, to apply the Kissinger-like method  $T_i$  must occur at about the same transformed fraction  $f_i$ . Therefore, the austenite fractions at  $T_i$  are plotted for all heating experiments in Figure 7.10, including the average values and standard deviations obtained from the austenite fractions at all heating rates at each stage.  $f_i$  of the first stage corresponding to a heating rate of 1 K/min is noticeably lower than the standard deviation from the average and was therefore excluded from the estimation of the activation energy.

According to equation (7.6), the  $\ln(\alpha T_i^2/\phi)$  versus  $1/T_i$  plots for both previous austenitization treatments and transformation stages are shown in Figure 7.11. The activation energies obtained from the slope of the linear regressions are given in Table 7.3. The activation

energies calculated were similar for both prior austenitization treatments. The activation energies of the second stage are about 100 kJ/mol higher than of the first stage. Moreover, the activation energies for both stages are almost twice as high as the activation energy of 233 kJ/mol, obtained in chapter 6, for austenite formation during tempering at temperatures between 585 and 695 °C for 4 h of samples previously austenitized at 1050 °C for 30.5 h.

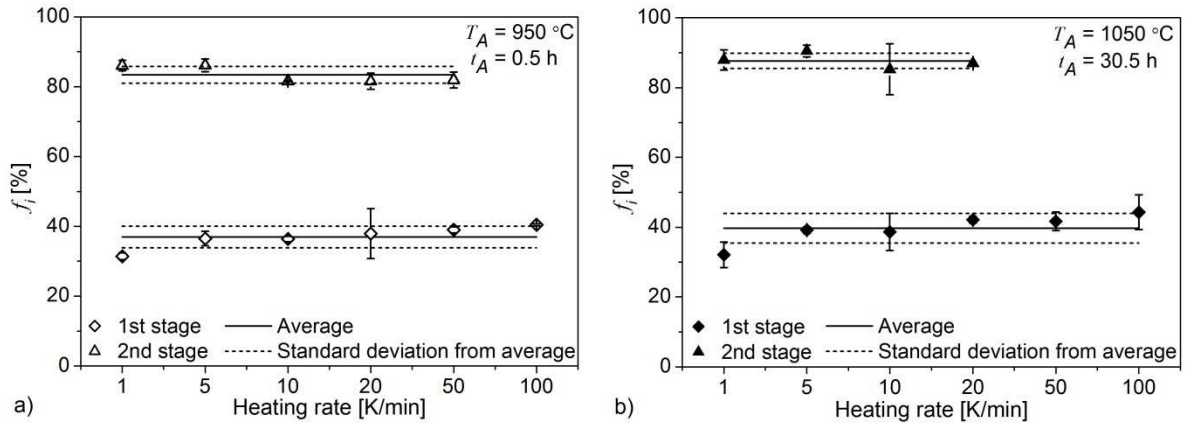


Figure 7.10 Overview of the austenite fractions  $f_i$  obtained at different peak temperatures  $T_i$ . The average values correspond to the average of all austenite fractions at each stage, including the standard deviation.

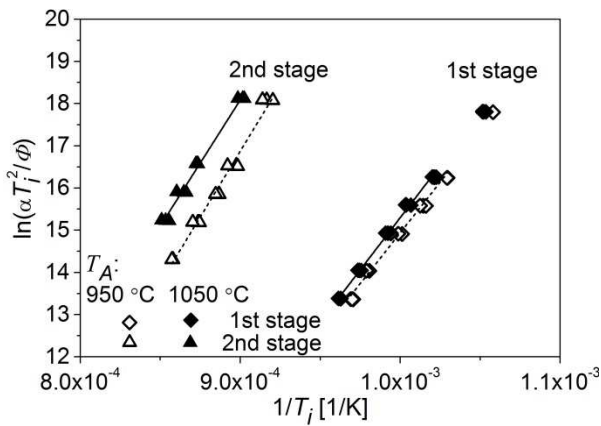


Figure 7.11 Kissinger-plot of  $\ln(\alpha T_i^2/\phi)$  versus  $1/T_i$ . The values obtained for the first stage for the heating rate of 1 K/min were excluded for the estimation of the activation energy.

Table 7.3 Activation energies for the formation of austenite from martensite during heating for the previous austenitization treatments.

$T_A$	$t_A$	1st stage	2nd stage
°C	h	kJ/mol	kJ/mol
950	0.5	400 ±14	519 ±19
1050	30.5	411 ±8	497±17

### 7.3.2 Influence of previous austenitization treatment on retained austenite fraction after tempering

The fractions of austenite, retained after quenching from the austenitization temperature, were  $3.0 \pm 0.4$  vol.% and  $2.2 \pm 0.5$  vol.% for the samples previously austenitized at  $950\text{ }^{\circ}\text{C}$  for 0.5 h and at  $1050\text{ }^{\circ}\text{C}$  for 30.5 h, respectively. The fractions of retained austenite at room temperature, measured immediately after cooling from tempering between  $615$  to  $655\text{ }^{\circ}\text{C}$  for 4 h (point B in Figure 6.1) are shown for both previous austenitization treatments in Figure 7.12. The data obtained in chapter 6 of samples previously austenitized at  $1050\text{ }^{\circ}\text{C}$  for 30.5 h are shown for comparison. With increasing tempering temperature the austenite fractions are increasing until a tempering temperature of  $640\text{ }^{\circ}\text{C}$ . As discussed in chapter 6, due to the lower concentration of austenite-stabilizing elements in the increased fraction of austenite on tempering, fresh martensite forms during cooling for tempering temperatures exceeding  $640\text{ }^{\circ}\text{C}$ , leading to a decrease in retained austenite fraction. The samples previously austenitized at  $950\text{ }^{\circ}\text{C}$  for 0.5 h show a scatter in the austenite fraction of up to 12 vol.%. On the other hand, an austenitization treatment at  $1050\text{ }^{\circ}\text{C}$  for 30.5 h leads to results showing a greater reproducibility and also a clear peak of the austenite fraction on tempering at  $640\text{ }^{\circ}\text{C}$ . Moreover, the average austenite fractions of the samples austenitized at  $1050\text{ }^{\circ}\text{C}$  for 30.5 h are lower than those of the samples austenitized at  $950\text{ }^{\circ}\text{C}$  for 0.5 h. This difference can be up to 12 vol.%.

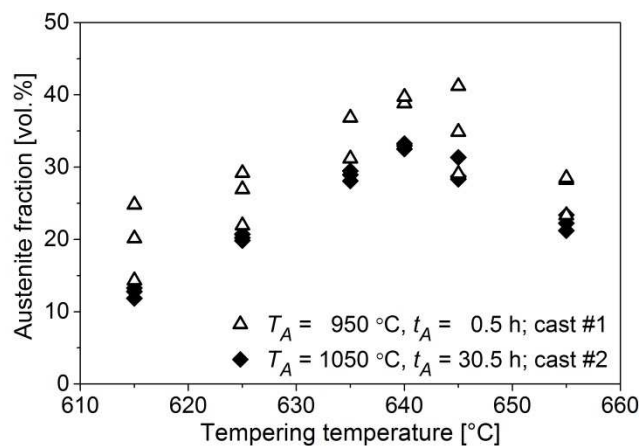


Figure 7.12 Evolution of the austenite fraction obtained at room temperature immediately after cooling from tempering for 4 h for the two series of previously austenitized samples. Estimated uncertainty in austenite fraction:  $\pm 0.5$  vol.%.

### 7.3.3 Microstructures after tempering

Microstructures of samples tempered at  $655\text{ }^{\circ}\text{C}$  for 4 h are shown in Figure 7.13 and Figure 7.14 for both previous austenitization treatments. From the optical micrographs in Figure 7.13, a greater prior austenite grain size and thus martensite lath size of the samples previously austenitized  $1050\text{ }^{\circ}\text{C}$  for 30.5 h can be derived, which in general shows a coarser microstructure than the sample austenitized at  $950\text{ }^{\circ}\text{C}$  for 0.5 h. Figure 7.14 shows that the retained austenite (needle-shaped) is finely dispersed in the martensitic matrix. It was

reported by Wei [13] that the fresh martensite is attached to the retained austenite, making it difficult to distinguish it with SEM.

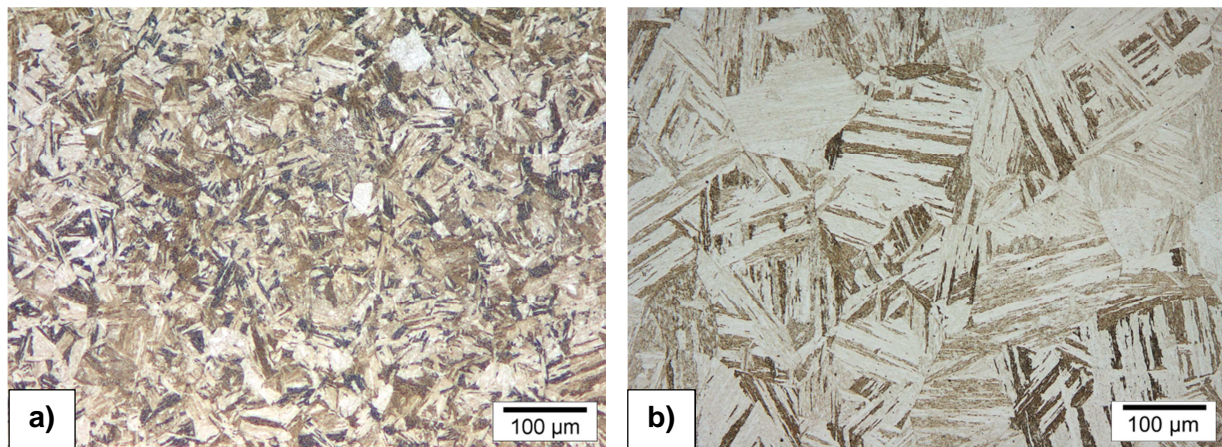


Figure 7.13 Microstructure of samples tempered at 655 °C for 4 h, previously austenitized at a) 950 °C for 0.5 h and b) 1050 °C for 30.5 h.

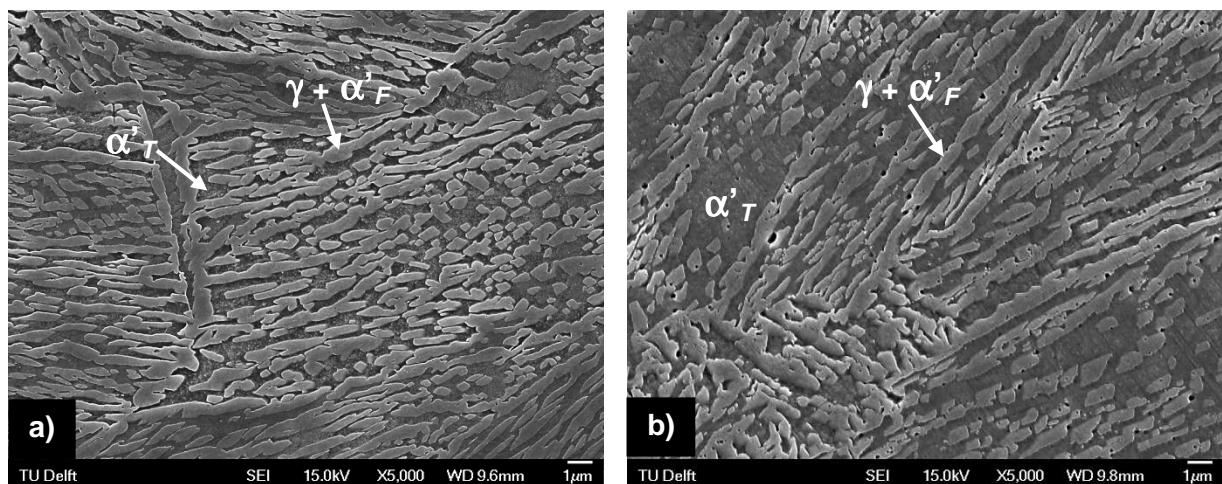


Figure 7.14 Microstructure of samples tempered at 655 °C for 4 h, previously austenitized at a) 950 °C for 0.5 h and b) 1050 °C for 30.5 h. Light grey areas: retained austenite ( $\gamma$ ) + fresh martensite ( $\alpha'_F$ ) [13]. Dark grey areas: tempered martensite ( $\alpha'_T$ ).

## 7.4 Discussion

### 7.4.1 Austenite formation in two stages

It was discussed in chapter 5 that the austenite formation from martensite during continuous heating at 3 K/min of an as-received sample occurs in two stages and that martensite is still present at 834 °C. This was found by dilatometry and confirmed by high-temperature X-ray diffraction analysis. From the continuous heating experiments in the present study it was found that the austenite formation in two stages depends on the heating rate. First, the transformation temperatures are shifted to higher temperatures with

increasing heating rate, which is a well-known effect due to the thermally activated character of the transformation [3, 21-24]. Phase transformations can take place by either a diffusional or a shear mechanism [25, 26]. Diffusional transformation of martensite to austenite is in general heating-rate dependent, whereas a shear transformation is independent of the heating rate [3, 22, 27]. Thus, the martensite to austenite transformation in the present study can be assumed to be diffusional.

For the austenite formation from martensite activation energies of about 400 kJ/mol for the first stage and about 500 kJ/mol for the second stage were obtained (see Table 7.3). The activation energies for the first stage are around 170 kJ/mol higher than the activation energy of 233 kJ/mol, determined for austenite formation from martensite during isothermal treatment of the 13Cr6Ni2Mo SMSS in chapter 6. A different value of the activation energy implies that a different mechanism is governing the transformation rate. From the tempering experiments presented in chapter 6, it is assumed that the growth of austenite in the 13Cr6Ni2Mo SMSS is governed by the diffusion of substitutional austenite-stabilizing elements. The influence of nucleation on the overall activation energy is more complex. Several authors have described the influence of the activation energies of nucleation and growth on the effective activation energy and described numerical solutions for obtaining the individual activation energies from the overall activation energy [18, 28-30]. The higher values for the activation energy found in this work are thus believed to be an effective activation energy comprising the energies of both the mechanisms involved, i.e. nucleation and growth. Furthermore, the activation energies obtained for the two stages are similar to those found by Kapoor et al. [22] for the precipitation hardening steel PH 13-8Mo, where the martensite to austenite transformation occurs through a diffusional mechanism in two stages.

The difference of 100 kJ/mol between the two stages could imply a change in the transformation mechanism. A much higher activation energy for the martensite to austenite transformation occurring by shear compared to diffusional mechanism was reported for an M350 and an 17-4 PH steel at higher heating rates [22]. Possibly, the increased activation energy for the second stage of martensite to austenite transformation in the 13Cr6Ni2Mo SMSS is due to a competing diffusionless mechanism. However, the peak value of  $df/dT$  used for determining  $T_i$  in the second stage is not as pronounced as in the first stage (see Figure 7.9), which could influence the precision in  $T_i$  determination. Furthermore, since the austenite formation was not finished at 950 °C, this could also influence the position determined for  $T_i$  of the second stage and therefore the value of activation energy obtained.

It is assumed that the two-stage formation is promoted by the diffusion of austenite stabilizing elements such as Ni and Mn, leaving a reduced concentration in the regions surrounding austenite and hence an increase of the start temperature of austenite formation in those regions [9]. It was observed in other steels, that the formation of Ni-precipitates caused Ni-rich and Ni-depleted regions in the matrix, leading to a two-stage formation of austenite [22, 23, 27]. However, the only precipitates found in the 13Cr6Ni2Mo SMSS were carbo-nitrides and  $M_{23}C_6$  and  $M_6C$  carbides [13], which are rich in Cr and Mo. Furthermore, the maximum equilibrium fraction of carbides and nitrides in the current steel is below 2 vol.%, as found in chapter 4. This fraction seems to be too low to cause the formation or growth of austenite of about 30 % during the second stage due to their dissolution, e.g. at a heating rate of 1 K/min for the samples austenitized at 950 °C for 0.5 h

(see Figure 7.7). However, carbide dissolution during heating could promote the formation of austenite in two stages, where the release of C lowers the  $A_{c1}$ -temperature. Since martensite was still present in the second stage (see chapter 5), the possibility that the second stage is due to carbide and/or nitride dissolution only can be excluded. The  $A_{e3}$ -temperature of the 13Cr6Ni2Mo SMSS is found to be similar to the  $A_0^{f1}$ -temperature of the first stage (see Table 7.2 and Table 4.3) and the dissolution of  $\chi$ -phase (if present in the material),  $M_{23}C_6$  and VN are in equilibrium within the range of the second stage (see Table 4.3). This shows that the second stage of austenite formation might indeed be influenced by carbides/nitrides dissolution.  $\chi$ -phase in the 13Cr6Ni2Mo SMSS has an approximate equilibrium composition of  $Fe_{33}Cr_{12}Mo_6Ni$  (see chapter 4), which would provide little Ni to cause all the martensite in the second stage to transform. However, in case of  $\chi$ -phase formation, the release of Fe and the ferrite stabilizers Cr and Mo, would further increase the formation temperature for austenite, promoting the two stage formation.

Gooch et al. [31] give an approximation for the  $A_{c1}$ -temperature of 13%Cr steels with less than 0.05 wt.% C, expressed as

$$A_{c1} [^{\circ}C] = 850 - 1500(x_C + x_N) - 50x_{Ni} - 25x_{Mn} + 25x_{Si} + 25x_{Mo} + 20(x_{Cr} - 10), \quad (7.8)$$

where  $x_i$  is the concentration of the alloying elements  $i$  in wt.%. Accordingly, a concentration of 0.03 wt.%C in 30 % of untransformed martensite in the second stage is expected to lower the  $A_{c1}$ -temperature by 45 °C. Hence, the formation of the above mentioned carbides and nitrides would on the one hand lower the concentration of C and N in the surrounding matrix, which would increase the  $A_{c1}$ -temperature for the first stage. On the other hand, the concentration of Cr and Mo would also decrease in the surrounding matrix, which would lower the  $A_{c1}$ -temperature. Owing to a much higher diffusivity of interstitials in iron, the influence of the diffusion of carbide and nitride forming substitutional elements is assumed to be localized to the regions around the carbides/nitrides, which offer additional nucleation sites for austenite. Furthermore, the Ni concentration was found to be increased in austenite after tempering treatments of the 13Cr6Ni2Mo SMSS, while the Cr-concentration was similar in austenite and martensite [13].

The fraction of austenite formed during the first stage is increased with increasing heating rate, while the amount of austenite formed during the second stage decreases. Furthermore, the tendency of the austenite formation to split up in two stages seems to be reduced at higher heating rates and more austenite was formed during holding at the target temperature of 950 °C (see Figure 7.6 and Figure 7.7). These observations again imply the process being diffusional. Heating an as-received sample also showed the austenite formation in two stages, where the extent of the second stage was similar to the samples heated at 1 K/min (see Figure 7.2, Figure 7.7). This shows that the diffusion of austenite stabilizing elements to austenite and the carbides/nitrides formation influence the two-stage austenite formation. Since the as-received sample was double-tempered, it provides much greater local differences in Ni and Mn content together with a higher fraction of carbides compared to the previously austenitized samples.

In summary, the first stage of austenite formation is assumed to be mainly due to partitioning of Ni and Mn, leaving martensite partially untransformed. Untransformed

martensite, due to Ni- and Mn-depleted regions, might transform due to the dissolution of carbides and nitrides and an increased diffusivity of Ni and Mn in the second stage. To support this theory, further research on the distribution of alloying elements during heat treatment is necessary, e.g. by using transmission electron microscopy or atom probe tomography. If the reason for the two-stage austenite formation is mainly the partitioning of Ni, it can be assumed that, depending on the local concentration of Ni, a completely austenitic microstructure might not be obtained during austenitization. This can be deduced from the pseudo-binary phase diagram of the 13Cr6Ni2Mo SMSS, shown in Figure 4.5, where below a Ni-concentration of 2.8 wt.% bcc-phase is present at all temperatures and TiN is stable within the temperature range analysed.

#### 7.4.2 Influence of previous austenitization treatment on the austenite formation

The experiments performed showed that an increased previous austenitization temperature and time leads to an increase in the transformation temperatures, especially in the second stage (see Figure 7.4), and to a lower fraction of austenite formed during holding at 950 °C (see Figure 7.8). Furthermore, a significant influence of austenitization treatment on the retained austenite fraction, obtained after tempering between 615 and 655 °C for 4 h, was observed (see Figure 7.12). Smaller values of austenite fraction with smaller variations were obtained when austenitized at 1050 °C for 30.5 h. Thermodynamic analysis of the equilibrium phase fractions and transformation temperatures in chapter 4 showed only minor differences between both casts of the 13Cr6Ni2Mo SMSS used. Furthermore, according to equation (7.8) the  $A_{c1}$ -temperature of the bulk material of cast #1 is 617 °C and of cast #2 is 605 °C. Accordingly, for the samples previously austenitized at 950 °C for 0.5 h (cast #1) a lower fraction of retained austenite would have been expected compared to the samples previously austenitized at 1050 °C for 30.5 h. Hence, an influence of the two different casts used for the tempering experiments on the differences in the austenite fraction can be neglected. The differences rather suggest that during the austenitization at 1050 °C for 30.5 h the material is more homogeneous in the distribution of alloying elements than that austenitized at 950 °C for 0.5 h. This is also supported by the austenite fraction obtained from the reheating experiments, showing a higher fraction of austenite formed in the first stage. It is worth to mention here again that the as-received material was supplied in the double-tempered condition, hence local differences in alloying elements such as Ni and Mn together with carbides/nitrides were present in the as-received material. The homogenization is thus related to these initial differences.

An increased homogenization would lead to an increased  $A_{c1}$ -temperature. Since partitioning of Ni and Mn is mainly rate determining for the austenite formation during tempering and its stabilization during cooling (see chapter 6), a locally increased Ni or Mn concentration could decrease the total  $A_{c1}$ -temperature as assumed for the previous austenitization at 950 °C for 0.5 h. According to equation (7.8) a variation of 25 °C of the  $A_{c1}$ -temperature can, for example, be obtained when the Ni-concentration varies by only 0.5 wt.%. The observed variation in the austenite fraction of the tempered samples (Figure 7.12), austenitized at 950 °C for 0.5 h, are significant and suggest local inhomogeneity of austenite stabilizing elements depending on the previous austenite formation. This is also supported by the higher transformation rate between the two stages for the samples austenitized at 950 °C

for 0.5 h, since an inhomogeneous Ni and Mn distribution provides some areas with a lower temperature for the austenite start formation than the  $A_{s2}$ -temperature. These differences in the transformation rate could also be influenced by the dissolution of carbides and nitrides.

Figure 7.15 shows the influence of the austenitization temperature on the diffusion distances,  $d$ , of Ni and Mn in fcc-austenite, where the diffusion distance was obtained by  $d = \sqrt{Dt}$  with  $D = D_0 \exp(-Q/(RT))$ .  $D$  denotes the diffusion coefficient,  $D_0$  the pre-exponential factor and  $Q$  the activation energy, taken from [32]. It can be seen that after 0.5 h at 950 °C Ni and Mn diffuse only 0.4 μm and 0.5 μm, respectively, compared to 1.1 μm and 1.3 μm at 1050 °C. This is of course dependent on the alloy composition, but indicates that austenitization at 950 °C for 0.5 h is not enough to obtain sufficient homogenization of the material. However, further research on the homogenization of the material, e.g. by using transmission electron microscopy or atom probe tomography, is necessary to prove this assumption.

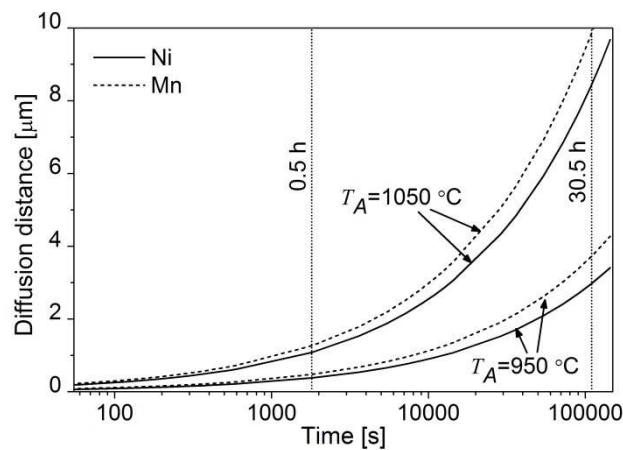


Figure 7.15 Diffusion distance of Ni and Mn in fcc-iron at 950 °C and 1050 °C. Vertical lines indicate austenitization times.

Furthermore, the prior austenite grain size can influence austenite formation. It was reported that with increasing austenitization temperature the grain size of the prior austenite increases [10-12], as can be deduced from the microstructures shown in Figure 7.13, and hence the size of the lath martensite increases [10-12]. Since the prior austenite grain boundaries and the boundaries of lath martensite act as nucleation sites for the austenite formation in SMSS [1, 7, 8, 10, 33], an increased grain and lath size would provide a lower density of nucleation sites, since the total density of grain boundaries is lower. It can be seen from Figure 7.14 that the retained austenite grains together with the fresh martensite grains are slightly bigger for the samples previously austenitized at 1050 °C for 30.5 h. This could also be responsible for the lower austenite fraction of the samples previously austenitized at 1050 °C for 30.5 h, since a lower density of nucleation sites would slow down the formation of austenite.

Likewise, austenite that is retained after quenching from austenitization treatment can influence the austenite formation during reheating and tempering such that existing austenite is growing faster, since it does not require nucleation [34]. However, the fraction

of austenite retained after quenching from austenitization was about 1 vol.% lower for the samples previously austenitized at 1050 °C for 30.5 h and is not considered to have a significant contribution to the much larger difference in austenite fraction obtained after the tempering experiments.

## 7.5 Conclusions and recommendations

### 7.5.1 Conclusions

The formation of austenite from martensite during continuous heating of a 13Cr6Ni2Mo SMSS was analysed using dilatometry and magnetic techniques. The influence of austenitization treatment on austenite formation on reheating and the retained austenite fraction after tempering was analysed. The main conclusions and findings are as follows:

1. The obtained results suggest a two-stage formation of austenite during heating of the 13Cr6Ni2Mo SMSS, probably caused by local inhomogeneities of Ni and Mn due to their limited diffusion at lower temperatures. The first stage of austenite formation is mainly due to partitioning of Ni and Mn, leaving martensite partially untransformed. The second stage of austenite formation is probably governed by an increased diffusivity of Ni and Mn at higher temperatures together with the decomposition of carbides and nitrides.
2. The transformation temperatures were shifted to higher temperatures with increasing heating rate, indicating diffusional transformation. An austenitization treatment at 950 °C for 0.5 h leads to the start and finish temperatures for the formation of austenite in the first stage being 10 °C lower than the temperatures after austenitization at 1050 °C for 30.5 h. The second stage was shifted to higher temperatures by about 30 °C.
3. With increasing heating rate more austenite was formed during the first stage. The second stage of austenite formation became less pronounced and even disappeared at the highest heating rates. It was argued that the transformation is not finished at the target temperature of 950 °C since, during holding at 950 °C, the relative length is still decreasing, indicating further austenite formation caused by both diffusion of Ni and Mn and decomposition of carbides and nitrides.
4. The activation energy for austenite formation from martensite during continuous heating, obtained by a modified Kissinger method, was approximately 400 kJ/mol for the first stage and 500 kJ/mol for the second stage. These values are believed to be an effective activation energy comprising the energies of both the mechanisms involved, i.e. nucleation and growth.
5. An austenitization treatment at 1050 °C for 30.5 h produced a lower retained austenite fraction after different tempering treatments, but with less scatter than the one previously austenitized at 950 °C for 0.5 h. This is assumed to be due to the increased homogenization of the material with respect to the austenite stabilizing elements, especially Ni, but also Mn, since local inhomogeneity can lead to variations in the austenite fraction at the same tempering temperature. Furthermore, the smaller prior austenite grain size of the samples previously austenitized at 950 °C for 0.5 h led to more nucleation sites compared to samples previously austenitized at 1050 °C for 30.5 h, which could also influence the fraction of retained austenite.

### **7.5.2 Recommendations for future work**

For further investigation of the influence of the austenitization treatment on the homogenization of the material and the fraction of retained austenite after tempering treatment, the following suggestions are recommended for future work:

1. In this thesis solely as-received SMSS materials, delivered in the solution treated and double tempered condition, were analysed. The effect of the austenitization treatment on the retained austenite fraction after tempering of material, which has not been given the double tempering treatment (green material), is recommended to be studied by the in-situ thermo-magnetic technique. With this, the influence of the re-treatment on the retained austenite fraction can be further analysed.
2. To further study the influence of the austenitization treatment on the austenite fraction and hence the mechanical properties after tempering treatment a thorough analysis of the chemical concentrations using TEM and energy dispersive X-ray spectrometry are recommended. The influence of the prior austenitization treatment on mechanical properties after tempering treatment is suggested to be analysed by (micro-)tensile tests.

### **REFERENCES**

- [1] J. Hubackova, V. Cihal and K. Mazanec: *Z. Werkstofftech.*, 1984, vol. 15, pp. 411-5.
- [2] K. Kondo, M. Ueda, K. Ogawa, H. Amaya, H. Hirata, H. Takabe and Y. Miyazaki: in *Supermartensitic Stainless Steel '99*, KCI Publishing BV, Brussels, 1999, pp. 11-8.
- [3] Y.K. Lee, H.C. Shin, D.S. Leem, J.Y. Choi, W. Jin and C.S. Choi: *Mater. Sci. Technol.*, 2003, vol. 19, no. 3, pp. 393-8.
- [4] C. Gesnouin, A. Hazarabedian, P. Bruzzoni, J. Ovejero-García, P. Bilmes and C. Llorente: *Corros. Sci.*, 2004, vol. 46, no. 7, pp. 1633-47.
- [5] G. Rožnovská et al.: *The Effect of Heat Treatment on Microstructure and Properties of a 13Cr6Ni2.5Mo Supermartensitic Steel*, Sborník vědeckých Vysoké školy báňské – TU Ostrava, číslo 1, rok 2005, ročník XLVIII, řada hutnická článek č. 1241, pp. 225-31; from: <http://www.fmmi.vsb.cz/shared/uploadedfiles/fmmi/35Roz41-225.pdf>
- [6] C.A.D. Rodrigues, P.L.D. Lorenzo, A. Sokolowski, C.A. Barbosa and J.M.D.A. Rollo: *Mater. Sci. Eng. A*, 2007, vol. 460, pp. 149-52.
- [7] Y.Y. Song, D.H. Ping, F.X. Yin, X.Y. Li and Y.Y. Li: *Mater. Sci. Eng. A*, 2010, vol. 527, no. 3, pp. 614-8.
- [8] X.P. Ma, L.J. Wang, C.M. Liu and S.V. Subramanian: *Mater. Sci. Eng. A*, 2012, vol. 539, pp. 271-9.
- [9] P. Wang, S. Lu, D. Li, X. Kang and Y. Li: *Acta Metall. Sinica*, 2008, vol. 44, no. 6, pp. 681-5.
- [10] Y.R. Liu, D. Ye, Q.L. Yong, J. Su, K.Y. Zhao and W. Jiang: *J. Iron Steel Res. Int.*, 2011, vol. 18, no. 11, pp. 60-6.
- [11] X. Liu, K. Zhao, Y. Zhou, D. Ye, W. Jiang, Q. Yong and J. Su: *Adv. Mater. Res.*, 2012, vols. 393-395, pp. 440-3.

- [12] Y. Zhou, K. Zhao, X. Liu, D. Ye, W. Jiang, Q. Yong and J. Su: *Adv. Mater. Res.*, 2012, vols. 399-401, pp. 211-5.
- [13] Y. Wei: *Microstructural Characterization and Mechanical Properties of Super 13% Cr Steel*, PhD Thesis, The University of Sheffield, England, 2005.
- [14] B. Ravi Kumar, S. Sharma, P. Munda and R.K. Minz: *Mater. Des.*, 2013, vol. 50, pp. 392-8.
- [15] F. Christien, M.T.F. Telling and K.S. Knight: *Mater. Charact.*, 2013, vol. 82, pp. 50-7.
- [16] A. Bénéteau, P. Weisbecker, G. Geandier, E. Aeby-Gautier and B. Appolaire: *Mater. Sci. Eng. A*, 2005, vol. 393, no. 1-2, pp. 63-70.
- [17] E.J. Mittemeijer, L. Cheng, P.J. van der Schaaf, C.M. Brakman and B.M. Korevaar: *Metall. Trans. A*, 1988, vol. 19A, no. 4, pp. 925-32.
- [18] E.J. Mittemeijer: *J. Mater. Sci.*, 1992, vol. 27, no. 15, pp. 3977-87.
- [19] E.J. Mittemeijer, A. van Gent and P.J. van der Schaaf: *Metall. Trans. A*, 1986, vol. 17A, no. 8, pp. 1441-5.
- [20] W. Baumann, A. Leineweber and E. Mittemeijer: *J. Mater. Sci.*, 2010, vol. 45, no. 22, pp. 6075-82.
- [21] C. Garcia, L.F. Alvarez and M. Carsi: *Weld. Int.*, 1992, vol. 6, no. 8, pp. 612-21.
- [22] R. Kapoor and I.S. Batra: *Mater. Sci. Eng. A*, 2004, vol. 371, no. 1-2, pp. 324-34.
- [23] A. Goldberg and D.G. O'Connor: *Nature*, 1967, vol. 213, no. 5072, pp. 170-1.
- [24] Y.Y. Meshkov and E.V. Pereloma: The effect of heating rate on reverse transformations in steels and Fe-Ni based alloys, in: E. Pereloma, D.V. Edmonds (Eds.): *Phase transformations in steels*, Vol. 1, pp. 581-618, Woodhead Publishing, Oxford, 2012.
- [25] R.W.K. Honeycombe and H.K.D.H. Bhadeshia: *Steels: Microstructure and Properties*, 3rd ed., pp. 7-8, Elsevier Ltd., Amsterdam, 2006.
- [26] R.D. Doherty: Diffusive phase transformations in the solid state, in: R.W. Cahn, P. Haasen (Eds.): *Physical Metallurgy*, 4th ed., vol. 2, pp. 1363-505, Elsevier Science B.V., Amsterdam, 1996.
- [27] R. Kapoor, L. Kumar and I.S. Batra: *Mater. Sci. Eng. A*, 2003, vol. 352, no. 1-2, pp. 318-24.
- [28] F. Liu, F. Sommer, C. Bos and E.J. Mittemeijer: *Int. Mater. Rev.*, 2007, vol. 52, no. 4, pp. 193-212.
- [29] Y.H. Jiang, F. Liu and S.J. Song: *Acta Mater.*, 2012, vol. 60, no. 9, pp. 3815-29.
- [30] F. Liu, S.J. Song, F. Sommer and E.J. Mittemeijer: *Acta Mater.*, 2009, vol. 57, no. 20, pp. 6176-90.
- [31] T.G. Gooch, P. Woollin and A.G. Haynes: in *Supermartensitic Stainless Steel '99*, KCI Publishing BV, Brussels, 1999, pp. 188-95.
- [32] *Smithells Metals Reference Book*, W.F. Gale and T.C. Totemeier (Eds.), 8 ed., chapter 13, Elsevier Butterworth-Heinemann, Amsterdam, 2004.
- [33] Y.Y. Song, X.Y. Li, L.J. Rong, D.H. Ping, F.X. Yin and Y.Y. Li: *Mater. Lett.*, 2010, vol. 64, no. 13, pp. 1411-4.
- [34] M. de Sanctis, G. Lovicu, R. Valentini, A. Dimatteo, R. Ishak, U. Migliaccio, R. Montanari and E. Pietrangeli: *Metall. Mater. Trans. A*, 2015, vol. 46A, no. 5, pp. 1878-87.



# 8

## In-situ thermo-magnetic and dilatometry investigation of phase transformations in multi-phase steels

The phase transformations of two multi-phase Fe-C-Mn-Si steels are investigated in-situ in this chapter by a thermo-magnetic technique and dilatometry with the aim to monitor the austenite fraction from saturation magnetization measurements. Additionally, X-ray diffraction and microscopy are used for further interpretation of the results. An approach to calculate the austenite fraction from saturation magnetization at elevated temperatures is applied, reflecting the different phase transformations during heating and cooling. The experiments show that valuable information about phase transformations in multi-phase steels can be obtained from in-situ analysis of the saturation magnetization. This has special benefit for analysing microstructure developments in multi-phase steels, e.g. during the quenching and partitioning treatment, which would give further valuable insight to the phase transformations during the partitioning step.

### 8.1 Introduction

Measurements of the saturation magnetization at room temperature are often used to determine the austenite fraction in steels [1-7]. By analysing the saturation magnetization, the austenite fraction can be determined more accurately than by XRD or metallography [1], since the saturation magnetization depends on the temperature, the chemical composition and the phases present only, but is insensitive to texture or defects [8-10]. Furthermore, a truly representative fraction of austenite can be obtained due to the direct bulk probing. Due to the paramagnetic nature of austenite, its fraction can be derived by relating the saturation magnetization of the austenite-containing sample to a fully ferromagnetic reference sample of the same composition [1, 9]. Analysis of the evolution of the saturation magnetization has often been used to study in-situ phase transformations [10-12], especially the evolution of austenite fraction [4, 5]. Moreover, it was shown in chapters 5 and 6 that the thermo-magnetic technique can be applied for in-situ investigation of the austenite formation and transformation in a steel consisting of mainly one ferromagnetic and one paramagnetic phase.

This chapter aims to analyse the phase transformations of multi-phase Fe-C-Mn-Si steels during austenitization treatment from in-situ thermo-magnetic measurements, together with dilatometry, X-ray diffraction and microscopy. An approach to obtain the austenite fraction from in-situ saturation magnetization measurements is presented. This work provides a basis to further develop the analysis of austenite retention and carbides formation of multi-phase steels using thermo-magnetic techniques. Small variations in the austenite fraction can be monitored, which for instance offers interesting insight into the stabilization of austenite.

## 8.2 Experimental

### 8.2.1 Material

Two multi-phase Fe-C-Mn-Si steels were investigated and their chemical compositions are listed in Table 8.1. The main difference between both steels is the carbon content. The steel with the lower carbon content is micro-alloyed with Mo, which retards the bainite transformation kinetics [13]. Mn, an austenite-stabilizing element, is added to retard the formation of bainite and ferrite during cooling from austenitization treatment and Si and Al inhibit the formation of carbides [14].

*Table 8.1 Chemical composition (in wt.%) of the analysed multi-phase steels, balance Fe.*

Steel name	C	Mn	Si	Mo	Al	P
0.6C <sup>1</sup>	0.57	3.54	1.480	-	0.030	-
0.2C <sup>2</sup>	0.20	3.51	1.523	0.247	0.040	0.005

The as-received materials were produced using a laboratory vacuum induction furnace and were hot rolled after casting to a final thickness of 4.5 mm [15]. Cylindrical samples with the axis parallel to the rolling direction were cut from the as-received material using electro-discharge machine (EDM). The sample dimensions are  $\varnothing$  4 mm x 10 mm for the dilatometer experiments and  $\varnothing$  2 mm x 2 mm for the magnetic experiments.

### 8.2.2 Equilibrium phase analysis

Equilibrium phase fractions and equilibrium transformation temperatures were calculated using the Thermo-Calc software package [16] with the TCFE v6.2 database. The following phases were allowed to be present during the calculations: liquid, fcc, bcc, and cementite, but also  $M_5C_2$ ,  $M_7C_3$ , and  $M_6C$  are allowed to be present to show which carbides appear in equilibrium.

---

<sup>1</sup> Internal code: QPI

<sup>2</sup> Internal code: QPF

### 8.2.3 Heat treatment experiments in the magnetometer

#### *Magnetic measurements*

In-situ thermo-magnetic experiments were carried out in a Vibrating Sample Magnetometer (VSM), which is described in section 3.2.2. The magnetization of the samples was measured in-situ at a constant field of 1.5 T, where the magnetization is close to its saturation value.

Austenitization treatments were carried out with a nominal heating rate of 5 K/min to a temperature above the  $A_{c3}$ -temperature. The material was then held there for 5 or 6 min and cooled in the furnace of the magnetometer by natural cooling, approximately following an exponential relation (see equation 3.1). An overview of the parameters for the heat treatments carried out in the VSM are given in Table 8.2. The temperature-time profiles for heating and cooling in the furnace of the VSM and the dilatometer are shown in Figure 8.1. Two different cooling rates were applied, where the cooling in the dilatometer experiment was faster. Further details about the dilatometer experiments are given in section 8.2.4. The experiments are designated in this chapter by  $T_h$  (in °C)/ $t_h$  (in min)/cooling (see Table 8.2), where  $T_h$  and  $t_h$  denote the temperature and time of isothermal holding, respectively. The cooling is either described by the time constant  $\tau$  (in min) or by water quenching (wq) and helium gas quenching (hq).

The Curie temperature,  $T_C$ , is obtained by the minimum of the first derivative,  $dM_{sat}/dT$ , of the magnetization curve [17, 18].

*Table 8.2 Overview of the parameters for the heat treatments carried out in the VSM.  $T_h$ ,  $t_h$  denote temperature and time of the isothermal holding.  $\tau$  and  $T_E$  are the time constant for cooling and temperature after cooling according to equation 3.1.*

Steel	Experiment ( $T_h/t_h/\tau$ )	Heat rate [K/min]	$T_h$ [°C]	$t_h$ [min]	Cooling	
					$\tau$ [min]	$T_E$ [°C]
0.6C	855/5/ $\tau_{41}$	5	855	5	41	28
0.2C	906/6/ $\tau_{38}$	5	906	6	38	27

Magnetization curves were measured at room temperature before and after the heat treatment by stepwise changing of the applied magnetic field from 1.6 T to -1.6 T with a step size of 0.1 T. Examples for the room temperature magnetization curves are shown in Figure 8.2 for as-received samples of both steels.

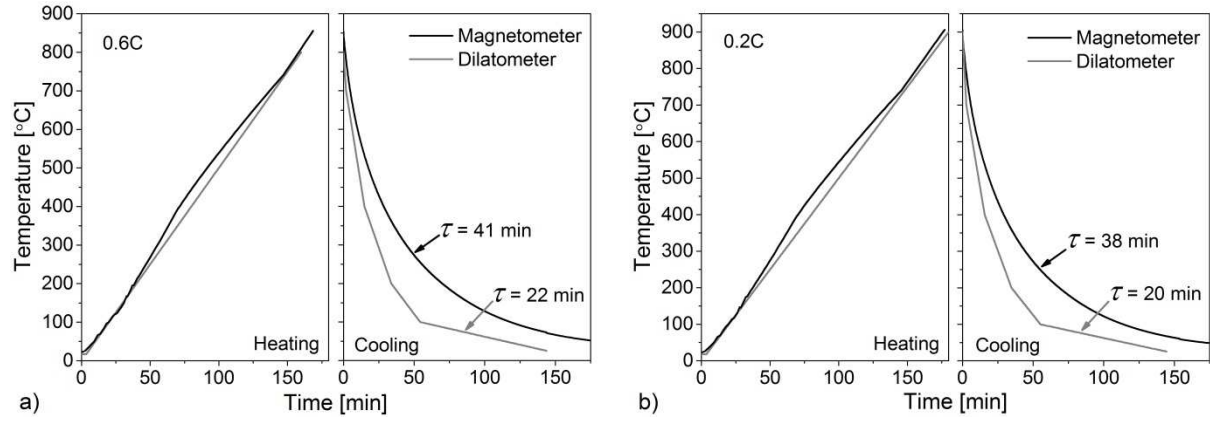


Figure 8.1 Temperature-time profiles for thermo-magnetic and dilatometer experiments during heating and cooling of a) 0.6C-steel and b) 0.2C-steel. The time constants  $\tau$  for the different cooling rates are indicated.

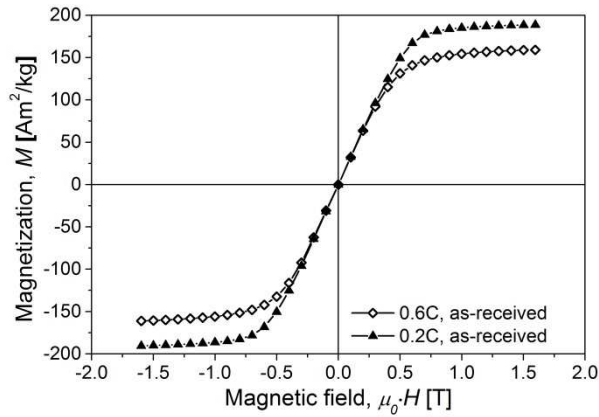


Figure 8.2 Room temperature magnetization curves of as-received steels.

**Determination of the austenite fraction from magnetization measurements at room temperature**

Since austenite is paramagnetic, the volume fraction of austenite,  $f_\gamma$ , measured by magnetization techniques, can be obtained by the relation of the saturation magnetization of an austenite-containing sample,  $M_{sat}(c)$ , compared to the saturation magnetization of an austenite-free, entirely ferromagnetic, reference sample,  $M_{sat}(ref)$ , of the same composition by [1, 10]

$$f_\gamma = 1 - \frac{M_{sat}(c)}{M_{sat}(ref)} \tag{8.1}$$

However, this equation is only valid if all ferromagnetic phases in the analysed material have the same magnetization.

Due to the carbon content of the analysed multi-phase Fe-C-Mn-Si steels, the fraction of carbides might have a significant influence on the saturation magnetization compared to the 13Cr6Ni2Mo supermartensitic stainless steel, analysed in the previous chapters. The overall

saturation magnetization,  $M_{sat}$ , of a multiphase steel can be described by the linear relation [10, 18]

$$M_{sat} = \sum f_i M_{sat,i}, \quad (8.2)$$

where  $f_i$  denotes the fraction of the individual phases  $i$  and  $M_{sat,i}$  the saturation magnetization of the individual phases.

Since several phases, such as austenite, ferrite, bainite, pearlite and different carbides, can be present in the Fe-C-Mn-Si steels during the experiments, the following assumptions were made to calculate the austenite fraction from the magnetization measurements:

- Cementite is the only carbide that is considered for the calculations, although transitional carbides and other carbides might form in the material, as found for the equilibrium condition discussed in section 8.3.2.
- The ferromagnetic ferrite and martensite are considered to have the same magnetization and this is designated as the magnetization of ferrite,  $M_{sat,\alpha}$ . This also counts for ferritic bainite and ferrite in pearlite.

When assuming ferrite ( $\alpha$ ), cementite ( $\theta$ ), and austenite ( $\gamma$ ), to be present in the sample, it follows from equation (8.2) with  $M_{sat} = M_{sat}(c)$  that

$$f_{\gamma} = 1 - \frac{M_{sat}(c)}{M_{sat,\alpha}} - \omega, \quad (8.3)$$

where  $\omega$  takes into account the volume fraction and magnetization of cementite at room temperature and is obtained by

$$\omega = f_{\theta} \left( 1 - \frac{M_{sat,\theta}}{M_{sat,\alpha}} \right). \quad (8.4)$$

For the calculations  $M_{sat,\theta} = 128 \text{ Am}^2/\text{kg}$  (at 15 °C [19]) is used.  $M_{sat,\alpha}$  is obtained by

$$M_{sat,\alpha} = x_{Fe} M_{sat,Fe} \quad (8.5)$$

where  $x_{Fe}$  is the atomic fraction of Fe on the substitutional lattice of the steel.  $M_{sat,Fe}$  is the saturation magnetization of pure iron at room temperature, which was determined for an iron sample of 99.99% purity in a field of 1.5 T to be  $215.75 \text{ Am}^2/\text{kg}$ . The thus obtained room temperature values of  $M_{sat,\alpha}$  for both steels are listed in Table 8.3. Equation (8.5) is a good approximation to obtain  $M_{sat,\alpha}$  given the low alloying grade of the steels analysed in this chapter.

For the determination of the austenite fraction saturation magnetization values measured at 1.5 T were used.

Table 8.3 Room temperature values of  $M_{sat,Fe}$  obtained from equation (8.5).

Steel	$x_{Fe}$ [at.%]	$M_{sat,Fe}$ [ $\text{Am}^2/\text{kg}$ ]
0.6C	93.5	201.7
0.2C	93.3	201.3

### **Determination of the austenite fraction from magnetization measurements during heat treatment**

Since the saturation magnetization is temperature dependent and decreases to almost zero when the temperature approaches the Curie temperature,  $T_C$ , the saturation magnetizations in equations (8.1) to (8.5) are dependent on temperature. This is due to the thermal energy annihilating the magnetic order of ferromagnetic materials when approaching  $T_C$  [20]. To calculate the austenite fraction during the heat treatment, an austenite-free reference sample of the same composition is necessary. This was obtained for the 0.6C-steel by austenitizing an as-received sample in an air furnace at 850 °C for 30 min followed by water quenching. The sample was subsequently tempered at 500 °C for 60 min followed by water quenching (experiment code: 850/30/wq+500/60/wq) to transform any retained austenite. For the 0.2C-steel an as-received sample was austenitized at 900 °C for 30 min followed by water quenching (experiment code: 900/30/wq). To prevent oxidation, the samples treated in the air furnace were put in a stainless steel bag filled with nitrogen.

The reference samples were heated in the magnetometer with the same parameters as given in Table 8.2 for the respective materials. The magnetization curves of the reference samples were fitted by the relation of Arrott and Heinrich [21]:

$$M(T)_{ref} = M_{sat0} \frac{(1-s)^\beta}{1 - \beta s + A s^{3/2} - C s^{7/2}}, \quad (8.6)$$

where  $M_{sat0}$  is the saturation magnetization at 0 K,  $\beta$ ,  $A$  and  $C$  are material dependent constants, and  $s = T/T_C$ . The fit was performed up to 600 °C, which is well below the  $A_{c1}$ -temperature of the material, to avoid the formation of austenite influencing the fit. With the thus obtained magnetization of the reference sample the austenite fraction during heating and cooling was calculated by equation (8.1), neglecting the effect of cementite. This is a good approximation since cementite is already included in the overall magnetization of the reference sample and hence is accounted for in the calculation of the austenite fraction. The influence of the actual fraction of cementite will be discussed later in this chapter.

The accuracy of the obtained austenite fraction by this approach is  $\pm 2$  vol.%, which comprises the influence of the magnetization of the reference sample.

#### **8.2.4 Heat treatment experiments in the dilatometer**

The heat treatment experiments were carried out in the dilatometer described in section 3.3. An overview of the dilatometer experiments is given in Table 8.4. The heat treatments were carried out on the as-received materials.

For the austenitization treatments the samples were heated at a rate of 5 K/min to a temperature above the  $A_{c3}$ -temperature and held there for 5 min. The subsequent slow cooling was performed to follow a cooling similar to the cooling in the magnetometer

furnace<sup>3</sup>. The temperature-time profiles for heating and cooling in the furnace of the VSM and the dilatometer are shown in Figure 8.1, showing that the cooling in the furnace of the VSM was slower than in the dilatometer ( $\tau_{\text{VSM}}$  was about 40 min and  $\tau_{\text{DIL}}$  was about 21 min).

Additional quenching experiments from the austenitization temperatures were carried out to compare the effect of the different cooling rates on the microstructure evolution. To identify phase transformations during heating, quenching experiments were carried out from temperatures before and after a distinct change in length observed during heating. The quenching was by helium gas quenching with an average cooling rate of 45 K/s.

The transformation temperatures were determined from the dilatation curves by the lever rule. The transformation temperatures were defined as the temperatures at which 1 and 99 vol.% of the product phase was formed.

Table 8.4 Overview of the heat treatments carried out in the dilatometer.  $T_h$ ,  $t_h$  denote temperature and time of the isothermal treatment.  $\tau$  is the time constant for cooling and  $T_E$  is the temperature after cooling according to equation 3.1. hq denotes helium gas quenching.

Steel	Experiment ( $T_h/t_h$ /cooling)	Heat rate [K/min]	Cooling			
			$T_h$ [°C]	$t_h$ [min]	$\tau$ [min]	$T_E$ [°C]
0.6C	800/5/ $\tau_{22}$	5	800	5	22	25
	800/5/hq		800	5	hq	
	400/0/hq		400	0	hq	
	500/0/hq		500	0	hq	
0.2C	900/5/ $\tau_{20}$	5	900	5	20	25
	900/5/hq		900	5	hq	
	350/0/hq		350	0	hq	
	510/0/hq		510	0	hq	

### 8.2.5 X-ray diffraction

The X-ray diffraction (XRD) measurements were carried out at room temperature with the equipment described in section 3.4. The surface of the samples perpendicular to the rolling direction was metallographically prepared with a final polishing step using 1  $\mu\text{m}$  diamond paste. The measurements were carried out at room temperature on as-received materials and on samples treated in the dilatometer.

<sup>3</sup> Differences in the cooling rates of the dilatometer and thermo-magnetic experiments are greater than originally planned. Both experiments were not carried out in the same period. Meanwhile, a new oven was installed to the VSM, having a much lower natural cooling rate. However, this does not influence the validity of the results.

The  $\theta$ - $2\theta$  scans were measured from  $30^\circ$  to  $130^\circ$  with a step size of  $0.062^\circ$ - $2\theta$  and a counting time per step of 8 s. The scans comprise the austenite peaks  $\{111\}\gamma$ ,  $\{200\}\gamma$ ,  $\{220\}\gamma$ ,  $\{311\}\gamma$ ,  $\{222\}\gamma$  and the ferrite/martensite peaks  $\{110\}\alpha$ ,  $\{200\}\alpha$ ,  $\{211\}\alpha$ ,  $\{220\}\alpha$ . The scans of the as-received steels are shown in Figure 8.3, where less austenite is present in the 0.2C steel.

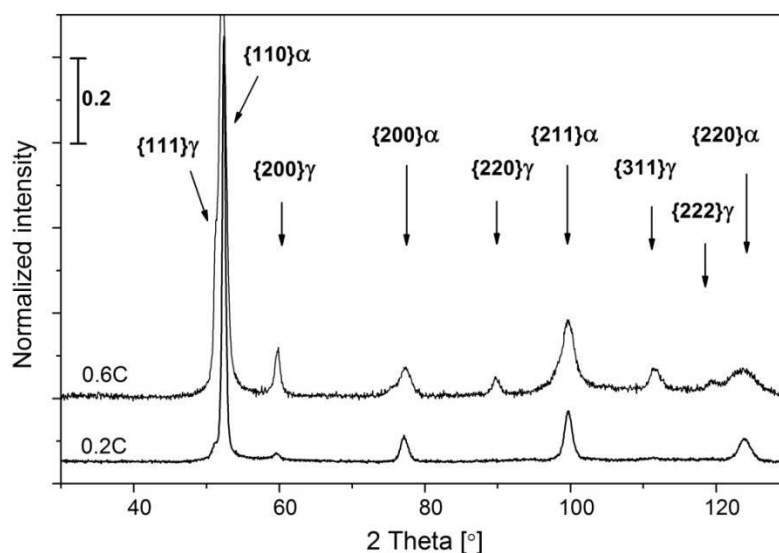


Figure 8.3 Background subtracted diffraction spectra of the as-received steels measured with  $\text{CoK}\alpha$ -radiation. The intensity was normalized by the maximum intensity of the scan. Step size:  $0.062^\circ$ - $2\theta$ ; counting time: 8 s. The spectra are shifted along the y-axis.

Table 8.5 Theoretical line intensity ( $R_{hkl}$ ) at room temperature for austenite and ferrite peaks in steel for Co radiation ( $\lambda_{\text{Co}}=1.79021 \text{ \AA}$ ) [22].

{hkl}	$\{200\}\gamma$	$\{220\}\gamma$	$\{311\}\gamma$	$\{200\}\alpha$	$\{211\}\alpha$	$\{220\}\alpha$
$R_{hkl}$	37.0	20.4	30.1	14.8	32.4	15.4

The volume fraction of austenite was calculated from the net integral intensities using equation (3.7). The theoretical line intensity values,  $R_{hkl}$ , for cobalt radiation for steels are listed in Table 8.5 for the peaks used in the calculations of the austenite fraction. Due to the overlapping of the  $\{111\}\gamma$  and  $\{110\}\alpha$  peaks, both peaks are excluded from the calculations and the following were used:  $\{200\}\gamma$ ,  $\{220\}\gamma$ ,  $\{311\}\gamma$  and  $\{200\}\alpha$ ,  $\{211\}\alpha$ ,  $\{220\}\alpha$ . The accuracy of the XRD measurements is influenced by the sample conditions such as stress at the sample surface, texture and grain size as well as influences of the instrument and the analysis method [1]. The accuracy of the austenite fraction calculated in the present work was on average  $\pm 2 \text{ vol\%}$ , accounting for errors caused by the crystallographic texture.

### 8.2.6 Optical and scanning electron microscopy

Microstructural analysis of the samples was carried out using optical microscopy (OM) and scanning electron microscopy (SEM) as described in section 3.5 together with the sample preparation.

### 8.3 Results

#### 8.3.1 Microstructure of as-received materials

The microstructures of the as-received materials are shown in Figure 3.2 (OM) and in Figure 8.4 (SEM). Both as-received materials consist of a mixture of austenite, martensite, (ferritic) bainite and carbides. In the SEM microstructures of steel 0.2C carbides can be found in ferritic bainite, showing a structure of lower bainite. Since carbon is rejected to austenite, the elongated thin films within the (ferritic) bainite are possibly retained austenite. The austenite fraction, determined by XRD, is 18 % in steel 0.6C and 4 % in steel 0.2C (see Figure 8.3).

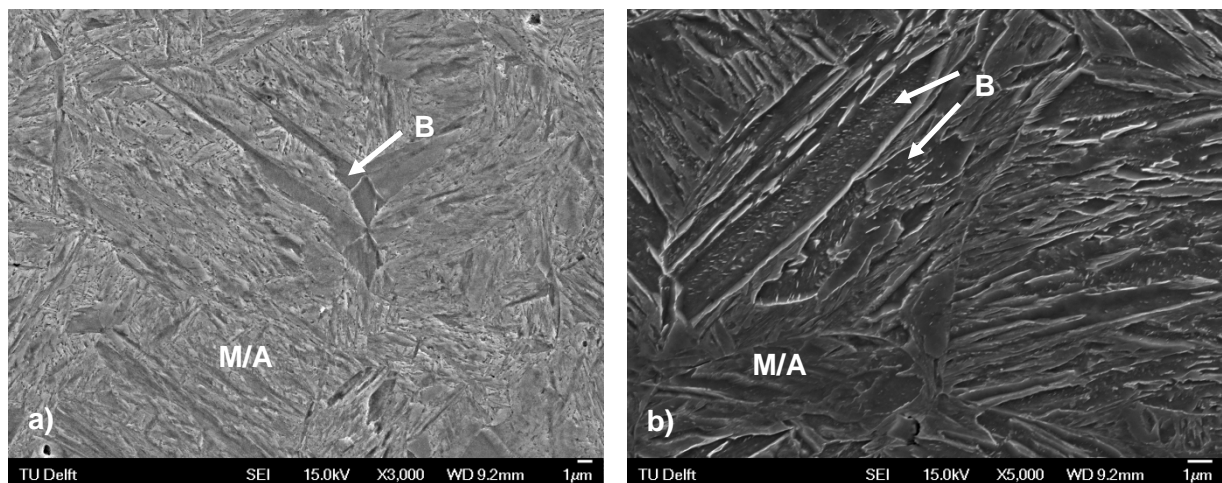


Figure 8.4 Microstructures of the as-received steels. a) 0.6C-steel b) 0.2C-steel. M denotes martensite, A austenite and B bainite.

#### 8.3.2 Equilibrium phase analysis

In Figure 8.5 the evolution of the equilibrium phase fractions of steel 0.6C, as calculated by Thermo-Calc, is shown. In Figure 8.5a cementite ( $M_3C$ ) is the only carbide allowed to be present for the calculations and in Figure 8.5b also  $M_5C_2$  and  $M_7C_3$  are allowed to be present. M stands for Fe and Mn. It shows that if cementite is the only carbide, it is present with an almost constant fraction. However, during tempering of martensite, several transition carbides like  $\epsilon$ - and  $\eta$ -carbides might form [23-25], which can influence the magnetization of the material. If  $M_5C_2$  and  $M_7C_3$  are taken into account in the equilibrium diagrams, both carbides are thermodynamically more favourable at lower temperatures than cementite (Figure 8.5b). Below 200 °C an  $Mn_5C_{14}$ -bcc phase is stable.

In Figure 8.6 the evolution of the equilibrium phase fractions of steel 0.2C is shown. In Figure 8.6a cementite and  $M_6C$  (M = Mo, Fe) are the only carbides allowed to be present for the calculations and in Figure 8.6b also  $M_5C_2$  and  $M_7C_3$  are allowed to be present. M in  $M_3C$ ,  $M_5C_2$  and  $M_7C_3$  stands for Fe and Mn. If cementite and  $M_6C$  are the only carbides allowed, they are present with an almost constant fraction. However,  $M_5C_2$  and  $M_7C_3$  are thermodynamically more favourable than cementite between 150 and 600 °C.

The equilibrium transformation temperatures,  $A_{e1}$  and  $A_{e3}$ , and the upper stability limit of cementite,  $A_{\theta}$ , are not influenced by the carbides present. They are listed in Table 8.6.

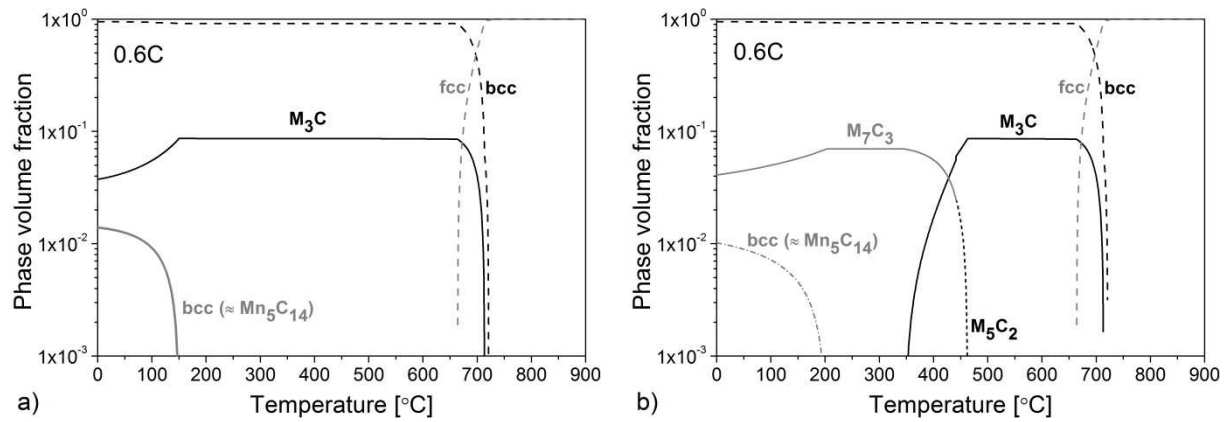


Figure 8.5 Equilibrium phase fractions obtained by Thermo-Calc [16] for steel 0.6C. a) Cementite was the only carbide allowed to be present. b) Several carbides were allowed to be present. M stands for Mn and Fe.

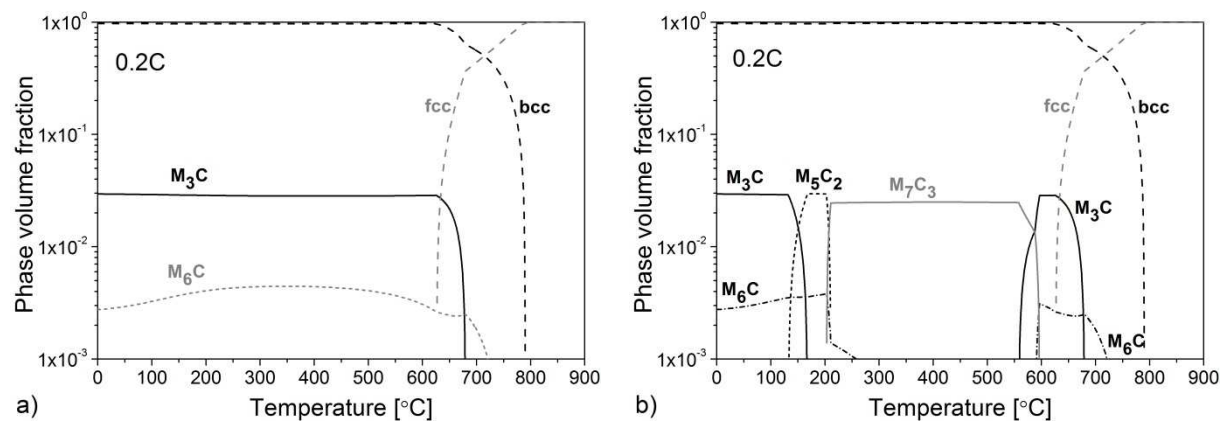


Figure 8.6 Equilibrium phase fractions obtained by Thermo-Calc [16] for steel 0.2C. a) Only carbides present for calculations: cementite and  $M_6C$ . b) Several carbides allowed to be present for calculations.  $M = Fe$  and  $Mn$  in  $M_3C$ ,  $M_5C_2$ ,  $M_7C_3$ , and  $M = Mo$  and  $Fe$  in  $M_6C$ .

Table 8.6 Overview of the equilibrium transformation temperatures,  $A_{e1}$  and  $A_{e3}$ , and maximum equilibrium fraction of cementite,  $f_{\theta,max}$  (in vol.%), obtained by Thermo-Calc [16].  $A_{\theta}$  denotes the upper stability limit of cementite. The Curie temperature,  $T_C$ , is obtained from the thermo-magnetic experiments.

Steel	$A_{e1}$ [°C]	$A_{e3}$ [°C]	$A_{\theta}$ [°C]	$T_C$ [°C]
0.6C	664	721	713	731
0.2C	626	790	680	721

### 8.3.3 Magnetization and dilatometry measurements

In this section, the results of the magnetization and dilatometry measurements during heating and cooling are presented for the different analysed steels.

#### 0.6C-steel

##### a) Analysis of phase transformations during heating

The magnetization ( $855/5/\tau_{41}$ ) and dilatation ( $800/5/\tau_{22}$ ) versus temperature curves of as-received 0.6C-steel samples are shown in Figure 8.7 during the heating and cooling. During heating, the magnetization is generally decreasing due to approaching the  $T_C$ -temperature [20] and the formation of the paramagnetic austenite above the austenite start temperature,  $A_{c1}$  [19].  $T_C$  was determined from the minimum of the  $dM/dT$  curve, which is shown in Figure 8.8, to be 731 °C.  $T_C$  is greater than  $A_{c3}$  of the material (see Table 8.6), which suggests that metastable ferrite is present or indicates inaccuracies in both the Thermo-Calc database or the results from the thermo-magnetic measurements.

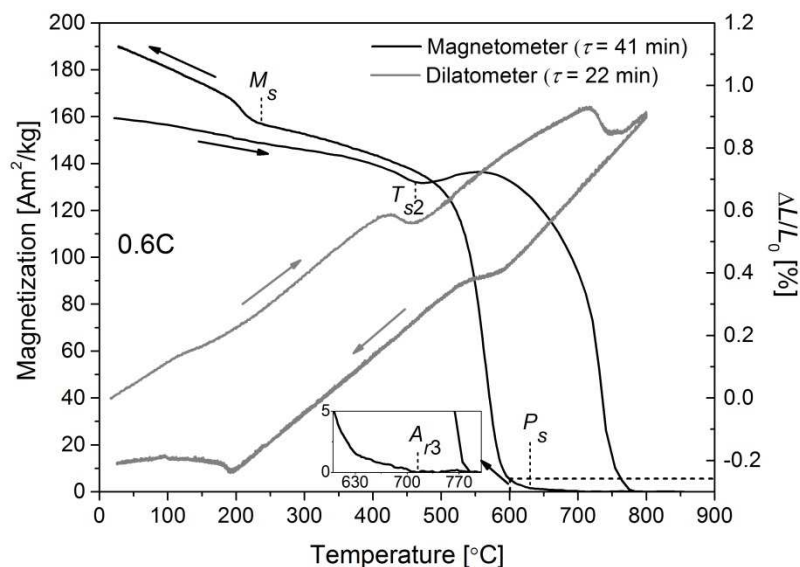


Figure 8.7 Magnetization, measured at a field of 1.5 T, and relative length change,  $\Delta L/L_0$ , versus temperature of as-received samples of 0.6C-steel. The inset shows an enlargement of the magnetization curve at high temperatures. The time constants  $\tau$  for the different cooling rates and transformation temperatures from magnetic experiments are indicated.

An inflection can be noticed in the magnetization curve during heating at around 200 °C, which causes a minimum in the  $dM/dT$  curve (see Figure 8.8), while a small reduction in the relative length change occurs between 109 and 219 °C ( $T_{s1}$  and  $T_{f1}$  in Figure 8.9). This can be attributed to the formation of transitional carbides due to tempering of martensite, resulting in a contraction of the sample [23]. In the temperature range between 475 and 550 °C the magnetization is increasing by about 5 %, which gives a distinct change in the  $dM/dT$  curve (see Figure 8.8), while a strong length reduction is observed between 386 and 501 °C ( $T_{s2}$  and  $T_{f2}$  in Figure 8.9). The quenching experiments 400/0/hq and 500/0/hq, reveal an



During further heating in the dilatometer the material expands with varying slopes, first until around 580 °C and then until the start of austenite formation at  $A_{c1}$ . The austenite formation is taking place in two stages until the  $A_{c3}$ -temperature is reached.  $A_{c1}$  and  $A_{c3}$  are listed in Table 8.7. The first stage of austenite formation is due to the coincidental transformation of ferrite and cementite to austenite and the second stage is due to the ferrite decomposition (see also Figure 8.5). Above 800 °C the magnetization is zero, indicating the completely paramagnetic state of the material. Furthermore,  $T_C$  is below  $A_{c3}$ , which is contrary to the equilibrium temperatures listed in Table 8.6, but which indicates that ferrite is present above  $T_C$ .

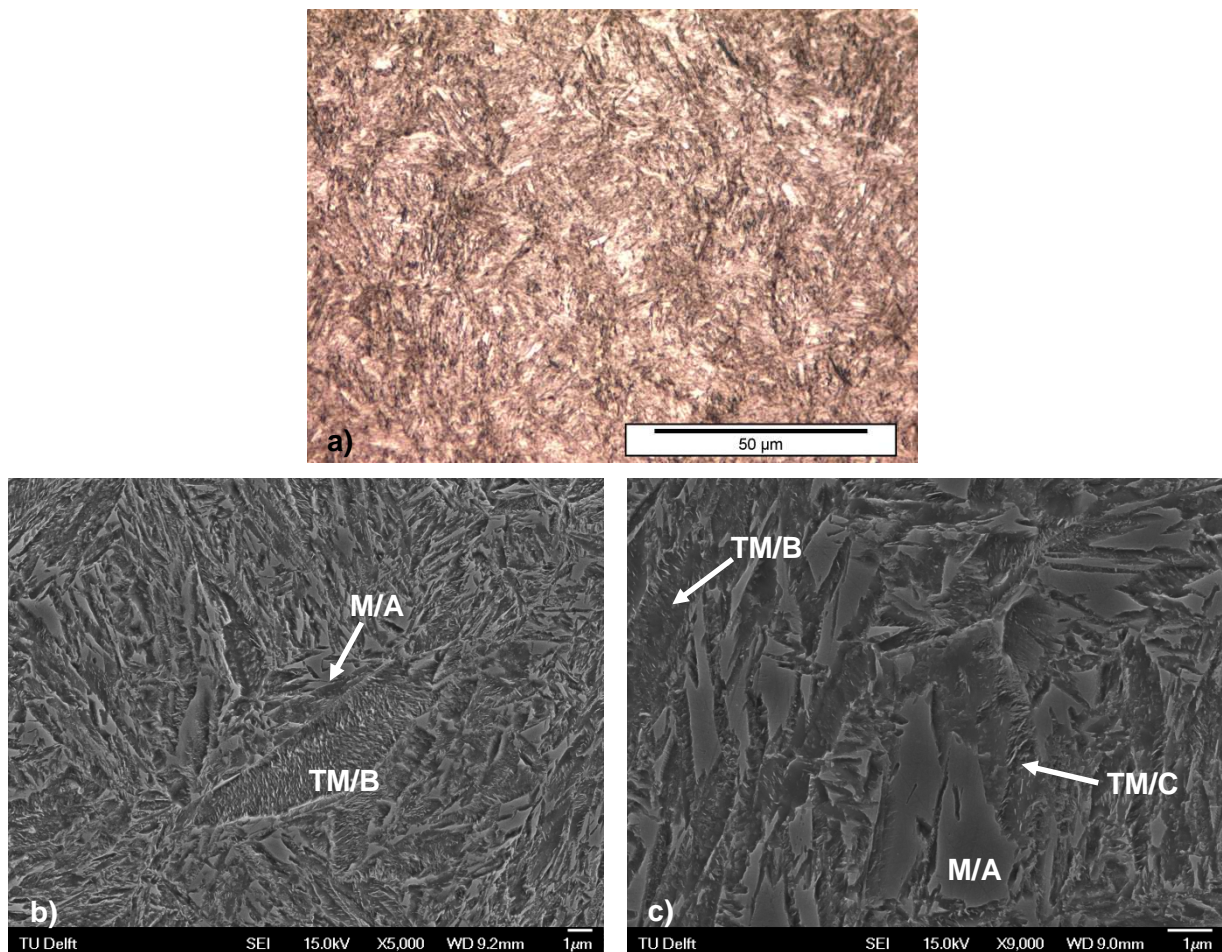


Figure 8.10 Microstructures of steel 0.6C quenched from 400 °C. a) OM and b)-c) SEM. M denotes martensite, TM tempered martensite, A austenite, B bainite and C carbides.

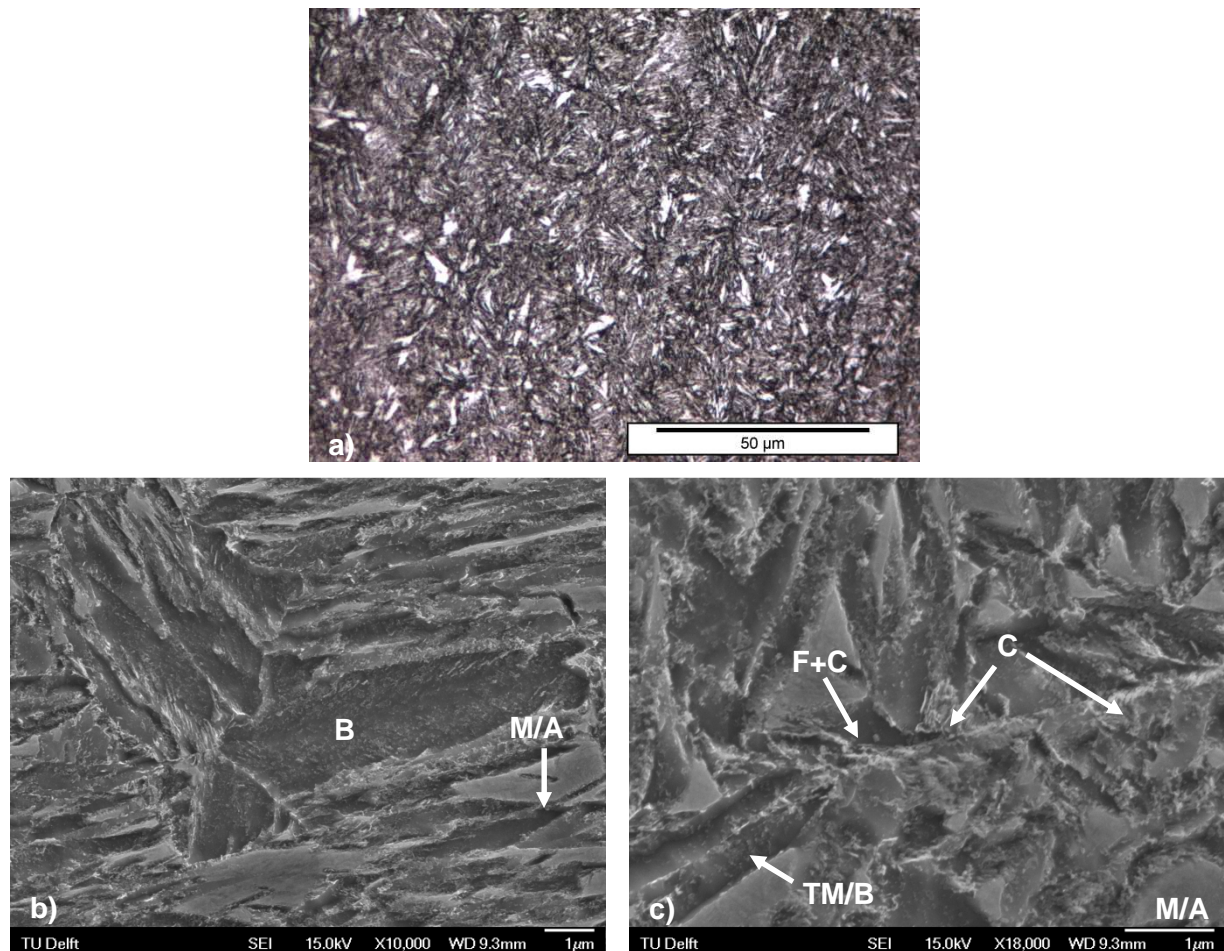


Figure 8.11 Microstructures of steel 0.6C quenched from 500 °C. a) OM and b)-c) SEM. M denotes martensite, TM tempered martensite, A austenite, B bainite and C carbides.

#### b) Analysis of phase transformations during cooling

During cooling of steel 0.6C (see Figure 8.7) the magnetization is slowly increasing from a temperature around 715 °C (point  $A_{r1}$  in Figure 8.7 and Table 8.7), indicating the presence or formation of a small fraction of a ferromagnetic phase. This is shown more clearly in the enlargement of the magnetization curve in Figure 8.7. Possibly, the ferrite to austenite transformation was not complete at 855 °C and a small fraction of ferrite is still present in the material, causing an increase in magnetization when approaching and passing the  $T_c$ -temperature of the material (731 °C). However, the beginning of the increase in magnetization is close to the  $A_{e3}$ -temperature of 721 °C, determined from Thermo-Calc (see Table 8.6), and hence the slow increase in magnetization can be also due to the formation of a small fraction of ferrite from austenite. No corresponding change in length was observed during cooling in the dilatometer experiment, which implies a lower sensitivity of the dilatometer. Furthermore, no or less ferrite might be formed during cooling in the dilatometer, where the cooling rate was higher than in the VSM (see Figure 8.1).

At temperatures below 630 °C the magnetization increases more strongly, while an expansion of the sample was observed between 618 and 503 °C ( $P_s$  and  $P_f$  in Figure 8.9 and

Table 8.7, P denotes pearlite). This is due to the formation of pearlite, which is shown in the optical micrographs in Figure 8.12. The light matrix in the optical micrographs (Figure 8.12a) and c)) is martensite and retained austenite and not ferrite, as can be seen in the SEM micrographs (Figure 8.12b) and d)). Due to the lower cooling rate in the VSM, a higher fraction of pearlite is found in the sample austenitized in the VSM compared to the sample treated in the dilatometer (Figure 8.12a) and c)). The fraction of retained austenite of the dilatometer sample, obtained by XRD, is 9 %. A small fraction of ferrite grains can be seen in the microstructures, which are adjacent to the pearlite.

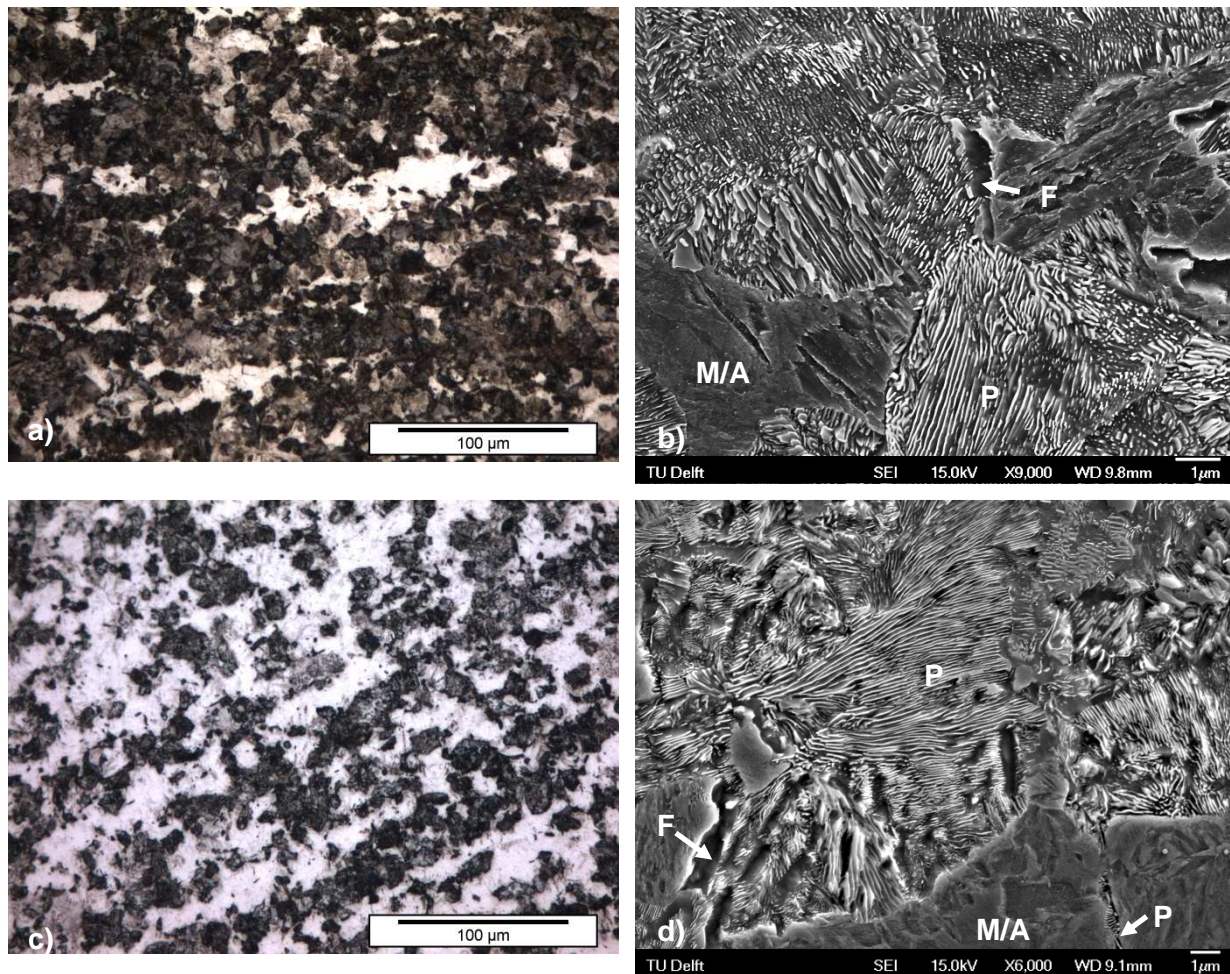


Figure 8.12 Microstructure of steel 0.6C. a)-b) treated in VSM with cooling from 855 °C,  $\tau = 41$  min. c)-d) treated in dilatometer with cooling from 800 °C,  $\tau = 22$  min. M denotes martensite, A austenite, F ferrite and P pearlite.

When approaching room temperature the magnetization is continuously increasing with a smaller slope until around 240 °C. From 240 °C the magnetization is increasing more rapidly, indicating the formation of martensite and the pearlite formation comes to a halt. The  $M_s$ -temperature from the dilatometer experiment is determined to be 203 °C. A small discontinuity in the dilatation at 100 °C is due to a change in cooling rate as can be seen in Figure 8.1a. The lower  $M_s$ -temperature obtained from the dilatometer experiment

compared to the thermo-magnetic experiment is likely to be due to the faster cooling in the dilatometer and the hence smaller fraction of pearlite obtained, leaving more carbon stabilizing the austenite.

Quenching from 800 °C did not show the intermediate expansion and the  $M_s$ -temperature was determined to be 219 °C (see Table 8.7). The microstructure did not show any pearlite and a retained austenite fraction of 16 % was determined by XRD.

**0.2C-steel**

a) Analysis of phase transformations during heating

The magnetization ( $906/6/\tau_{38}$ ) and dilatation ( $900/5/\tau_{20}$ ) versus temperature curves of as-received samples of steel 0.2C are shown in Figure 8.13 during the heating and cooling.  $T_C$  was determined from the minimum of the  $dM/dT$  curve, which is given in Figure 8.14, to be 721 °C (see Table 8.6).

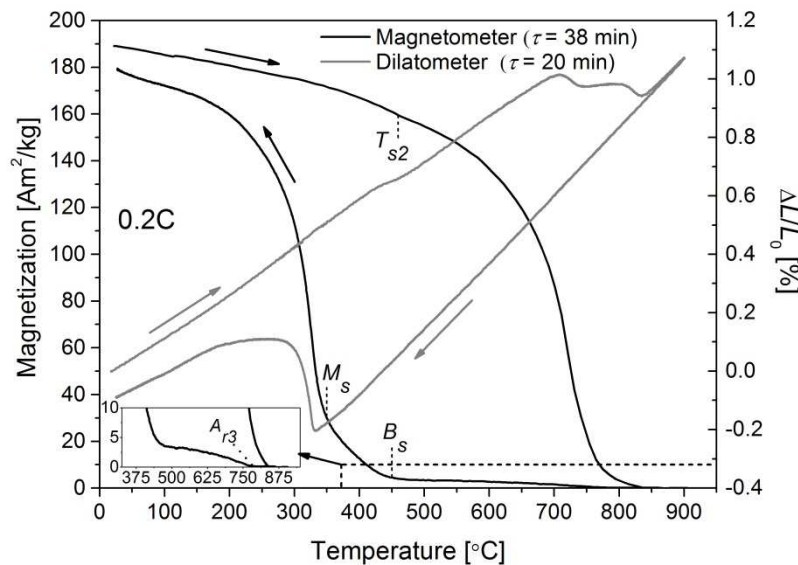


Figure 8.13 Magnetization, measured at a field of 1.5 T, and relative length change,  $\Delta L/L_0$ , versus temperature of as-received samples of 0.2C-steel. The inset shows an enlargement of the magnetization curve at high temperatures. The time constants  $\tau$  for the different cooling rates and transformation temperatures from magnetic experiments are indicated.

During heating of the as-received steel 0.2C an inflection can be noticed in the magnetization curve at around 460 °C. This causes an increase in the  $dM/dT$  curve (see Figure 8.14), which is smaller than observed for the steel 0.6C. A contraction in the relative length change is noticed between 403 and 502 °C ( $T_{s2}$  and  $T_{f2}$  in Figure 8.15). Unlike observed for steel 0.6C, no contraction is observed at lower temperatures, which could be due to a smaller fraction of transitional carbides formed. The quenching experiments 350/0/hq and 510/0/hq reveal an austenite fraction, obtained by XRD, of 5 % and 3 %, respectively.

respectively. As for the 0.6C-steel, this indicates that the contraction is related to the decomposition of austenite. The transformation temperatures of steel 0.2C, determined from the dilatometer and magnetometer experiments, are listed in Table 8.8.

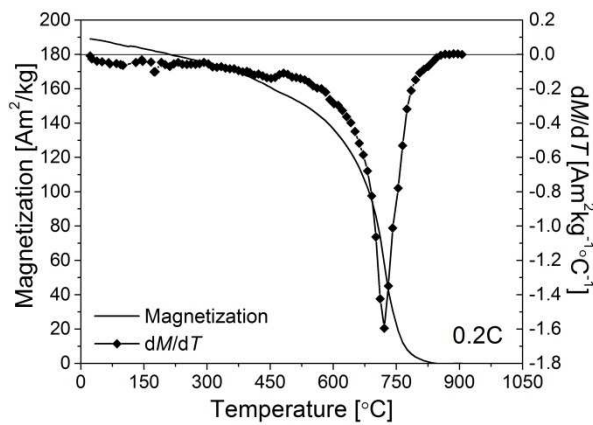


Figure 8.14 Magnetization and  $dM/dT$  versus temperature during heating of steel 0.2C.

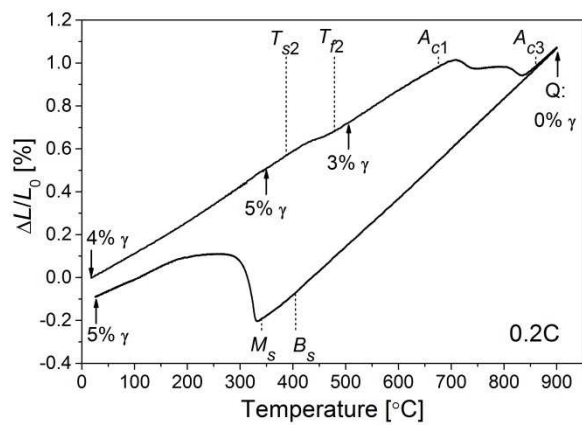


Figure 8.15 Relative change in length versus temperature during heating and cooling of steel 0.2C. Transformation temperatures and austenite fractions from XRD are indicated. Q: after quenching.

Table 8.8 Overview of the transformation temperatures and Curie temperature (in °C) determined from experiments in the dilatometer (DIL) and magnetometer (VSM). The transformation temperatures are indicated in Figure 8.15.

Steel	Experiment	$T_{s1}$	$T_{f1}$	$T_{s2}$	$T_{f2}$	$A_{c1}$	$A_{c3}$	$A_{r3}$	$B_s$	$M_s$	$T_C$
0.2C	DIL: 900/5/ $\tau_{20}$	-	-	403	502	678	842	-	383	332	-
	DIL: 900/5/hq	-	-	373	504	695	848	-	-	402	-
	VSM: 906/6/ $\tau_{38}$	-	-	460	-	-	-	785	450	350	721

The microstructure of the sample quenched from 350 °C is shown in Figure 8.16, which is similar to the as-received one and possibly comprises a small fraction of tempered martensite. The decomposition of retained austenite into ferrite and carbides can be seen in the sample quenched from 510 °C, shown in Figure 8.17. There, just like in the 0.6C-steel, an irregular pattern at the grain boundaries (light spots in Figure 8.17b) consists of carbides. Hence, the inflection observed in the magnetization curve at around 460 °C (see Figure 8.13) can be attributed to the decomposition of retained austenite. During further heating in the dilatometer the material expands with varying slopes, first until around 580 °C and then until the start of austenite formation at  $A_{c1}$ . As described for the 0.6C-steel, the austenite formation is taking place in two stages until  $A_{c3}$  is reached. The transformation temperatures, determined from the dilatometer and magnetometer experiments, are given in Table 8.8. Above 850 °C the magnetization is zero, indicating the completely paramagnetic state of the material.

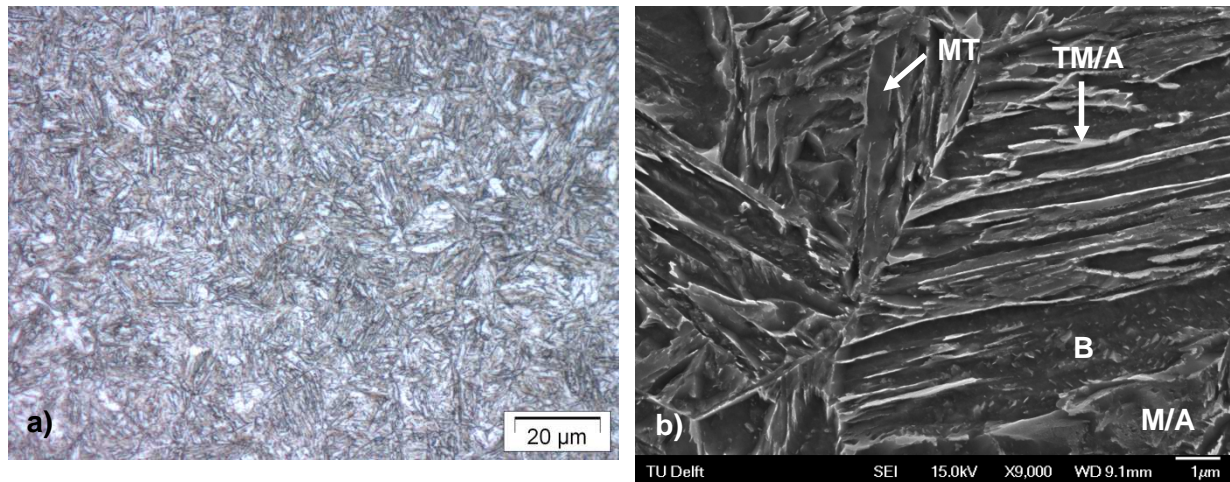


Figure 8.16 Microstructures of steel 0.2C quenched from 350 °C. a) OM and b) SEM. M denotes martensite, TM tempered martensite, A austenite and B bainite.

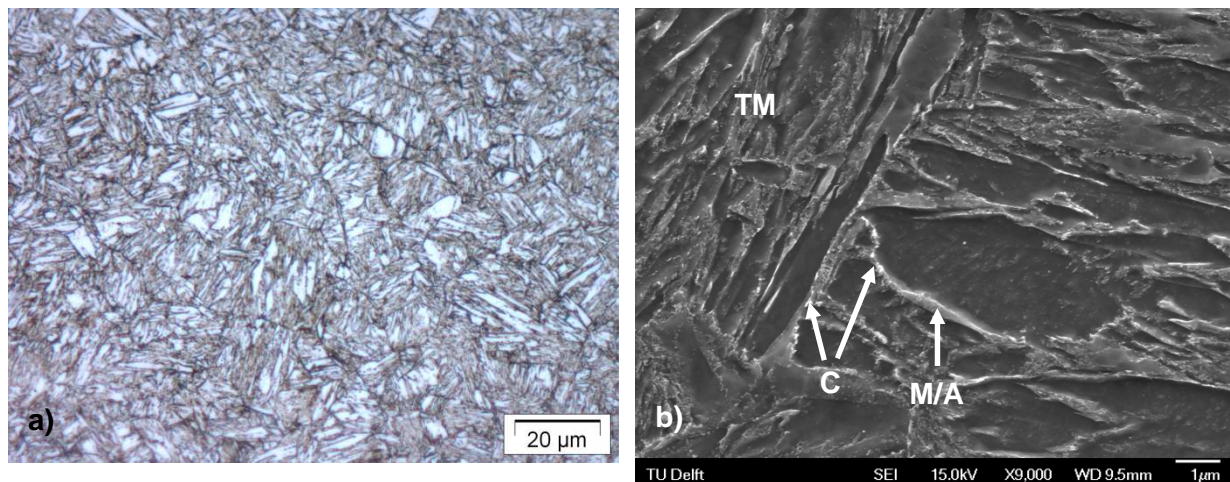


Figure 8.17 Microstructures of steel 0.2C quenched from 510 °C. a) OM and b) SEM. M denotes martensite, TM tempered martensite, A austenite and C carbides.

#### b) Analysis of phase transformations during cooling

As observed during cooling of steel 0.6C, the magnetization during cooling of steel 0.2C is initially increasing at a low rate. This is observed for the 0.2C-steel from a temperature around 785 °C (point  $A_{r3}$  in Figure 8.13 and Table 8.8) until 450 °C, which is shown more clearly in the enlargement of the magnetization curve in Figure 8.13. As discussed before, this increase is likely to be due to either the presence or the formation of ferrite. The beginning of this increase in magnetization is close to the  $A_{e3}$ -temperature of 790 °C, determined by Thermo-Calc (see Table 8.6). Since the  $T_c$ -temperature of the material (721 °C) is much lower than the temperature at which the magnetization slowly starts to increase, this effect is attributed to the formation of a small fraction of ferrite. No corresponding change in length was observed during cooling in the dilatometer experiment,

which is either due to the higher cooling rate (see Figure 8.1) and the thus lower fraction of ferrite formed or due to a lower sensitivity of the dilatometer experiment.

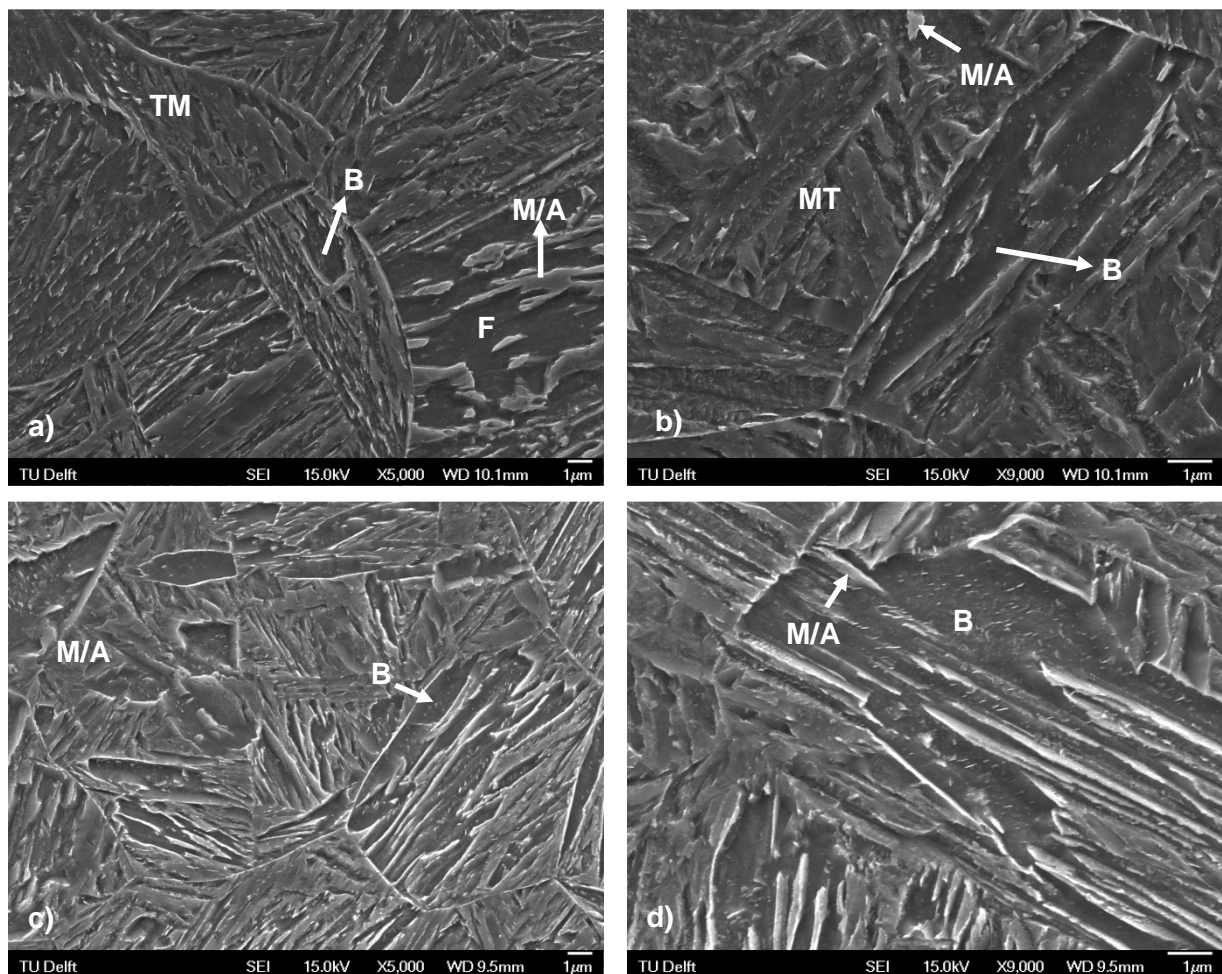


Figure 8.18 Microstructure of steel 0.2C. a)-b) Experiment in VSM with cooling from 906 °C,  $\tau = 38$  min. c)-d) Experiment in dilatometer with cooling from 900 °C,  $\tau = 20$  min. M denotes martensite, TM tempered martensite, A austenite, F ferrite and B bainite.

At temperatures below around 450 °C the magnetization increases more rapidly. This is likely due to the formation of bainite. The bainite start temperature,  $B_s$ , calculated after van Bohemen [26], is 421 °C, which matches well with the increase in magnetization. During cooling in the dilatometer experiment a slight change in length is detected at 383 °C (point  $B_s$  in Figure 8.15 and Table 8.8), which indicates the start formation of bainite, considering the higher cooling rate in the magnetometer (see Figure 8.1).

A clear change in length is observed at 332 °C, the beginning of the martensite formation. The start of martensite formation is determined to be at 350 °C from the magnetization measurements, noticed by a distinct change in slope of the curve. Subsequently, the magnetization is increasing strongly and is continuously increasing at a lower rate when approaching room temperature.

The lower  $M_s$ -temperature obtained in the dilatometer experiment can be due to a higher concentration of carbon in austenite, caused by the formation of lower bainite. This is supported by the microstructure of the samples shown in Figure 8.18. The sample austenitized in the magnetometer (Figure 8.18a-b)) shows ferrite, bainite, austenite and untempered martensite. Tempered martensite, from auto-tempering, can be also seen. In the microstructure of the sample austenitized in the dilatometer (Figure 8.18c-d)) bainite, martensite and austenite can be identified. The retained austenite fraction of the dilatometer sample, obtained by XRD, is 5 %. The  $M_s$ -temperature of a sample quenched from the austenitization temperature in the dilatometer is 402 °C (see Table 8.8), which is 50-70 °C larger than obtained from the treatments in the VSM and dilatometer. The lower  $M_s$ -temperatures are due to an increased concentration of austenite stabilizing elements, especially carbon, in the remaining austenite. This is likely a result of the previous formation of ferrite or bainite, rejecting carbon to austenite. No austenite was detected by XRD in the quenched sample.

### **8.3.4 Determination of the austenite fraction from saturation magnetization**

#### ***0.6C-steel***

##### **a) Austenite fraction at room temperature**

The austenite fraction from saturation magnetization measured at room temperature was calculated by equations (8.3) to (8.5) for an as-received sample, the sample treated in the VSM (855/5/ $\tau_{41}$ ), a sample quenched from 850 °C (850/30/wq) and the austenite-free reference sample (850/30/wq+500/60/wq). As discussed in section 8.2.3, only cementite is considered for the calculations, although other carbides might be present. Since the fraction of cementite is not known, the austenite fraction was calculated for varying cementite fractions up to the equilibrium cementite fraction. The austenite fraction as a function of the assumed cementite fraction is shown in Figure 8.19. For comparison, the austenite fraction obtained by XRD-measurements on an as-received sample, the samples from the dilatometer experiments and the reference sample are presented in Figure 8.20. Depending on the cementite fraction present in the as-received material, the austenite fraction, obtained from magnetization measurements, is between 18 and 21 vol.%, which is in accordance with the value obtained by XRD of 18 vol.%. For 18 vol.% austenite, the maximum of 8.3 vol.% cementite would be present in the as-received material according to Figure 8.19. For the sample 850/30/wq (AF) the austenite fraction is 16 vol.%, since the sample was quenched and therefore no cementite is expected to be present. This is in accordance with the fraction of 16 vol.%, obtained by XRD for the sample 800/5/hq (DIL).

The reference sample (850/30/wq+500/60/wq) shows a high density of carbides, as is shown in the microstructure in Figure 8.21, where spheroidized and acicular carbides at grain and lath boundaries appear in light grey. These are most likely cementite, since it is the only carbide present in equilibrium at 500 °C (see Figure 8.5), but also transitional carbides such as  $\epsilon$  can be still present. No austenite is detected by XRD, indicating that all austenite is decomposed. According to the magnetic measurements, as shown in Figure 8.19, 2 vol.% of austenite would be still present in the reference sample, for the maximum fraction of

cementite. However, the detection limit for austenite by XRD is 2 vol% (see chapter 3.4). Thus, both results are in accordance.

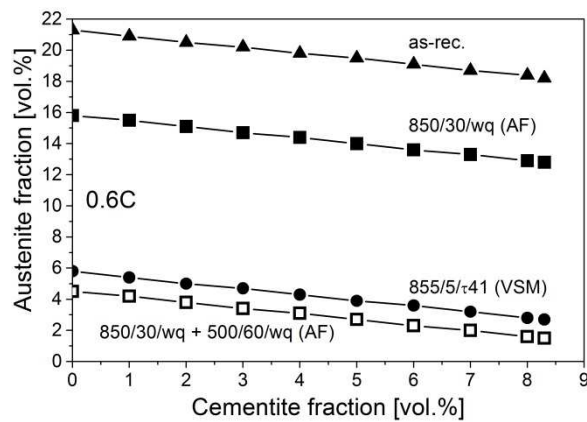


Figure 8.19 Austenite fraction, obtained from magnetic measurements at room temperature, versus assumed cementite fraction for steel 0.6C. VSM and AF denote the heat treatment carried out in the magnetometer and in the air furnace, respectively.

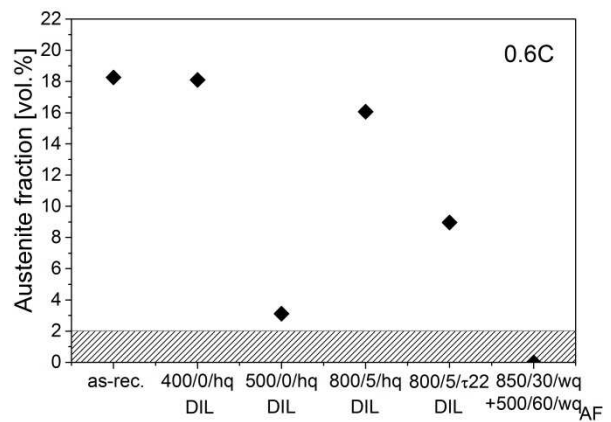


Figure 8.20 Austenite fractions obtained by XRD measurements at room temperature for samples of steel 0.6C. DIL denotes the heat treatment carried out in the dilatometer and AF in the air furnace. Accuracy is  $\pm 2$  vol.%. Hashed area indicates detection limit by XRD (see chapter 3.4).

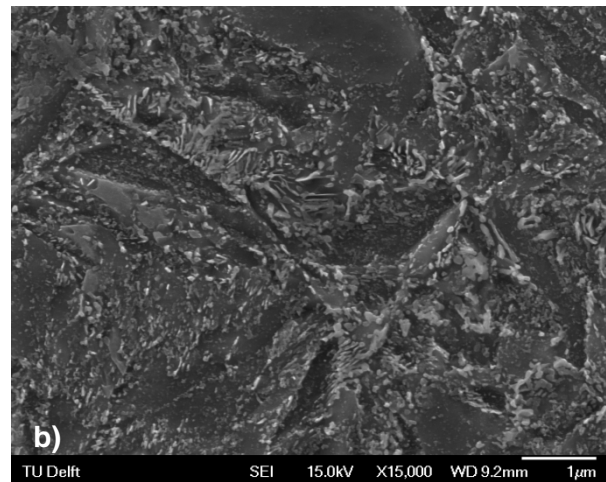
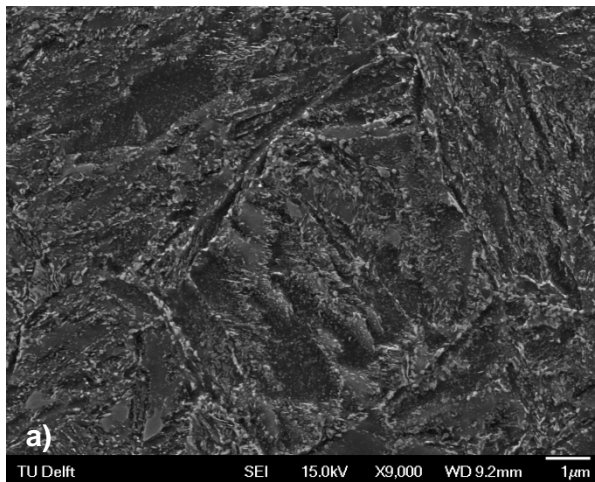


Figure 8.21 Microstructure of the reference sample 850/30/wq+500/60/wq of steel 0.6C.

The sample austenitized in the VSM ( $855/5/\tau_{41}$ ) showed an austenite fraction between 3 and 6 vol.%, depending on the assumed cementite fraction. This is about half the value measured by XRD for the sample austenitized in the dilatometer with the higher cooling rate ( $800/5/\tau_{22}$ ). This difference can arise from the lower fraction of pearlite formed during the faster cooling in the dilatometer experiment (see Figure 8.12), compared to the lower cooling rate in the VSM, leaving more C in austenite, which lowers the  $M_s$ -temperature (see Table 8.7).

b) Temperature dependent austenite fraction

In order to determine the temperature dependent austenite fraction, the reference sample 850/30/wq+500/60/wq was heated in the VSM at a rate of 5 K/min and the corresponding temperature-dependent magnetization curve during heating is presented in Figure 8.22. For comparison, the magnetization curve of the as-received sample is shown as well. The magnetization of the reference sample starts at a higher value due to the absence or a lower fraction of austenite. Both curves follow a similar magnetization above 610 °C. No change in magnetization, apart from the influence of the  $T_C$ -temperature, is observed in the curve of the reference sample, indicating a stable fraction of cementite until 600 °C. However, an appreciably high fraction of cementite is expected to cause a decrease in the magnetization at around 212 °C,  $T_C$  of cementite [18]. Cementite fractions or that of other carbides can only be distinguished from ferrite by their Curie temperatures, since the saturation magnetization is a linear superposition of the saturation magnetization of the single phases [10, 18] (see Figure 2.19). Since no change in magnetization was detected, the detection limit of cementite, measured by the saturation magnetization during heating, is assumed to be at least 8 vol.%. According to the room temperature calculations (see Figure 8.19), this is the cementite fraction in the austenite-free reference sample, if 2 vol.% austenite is retained.

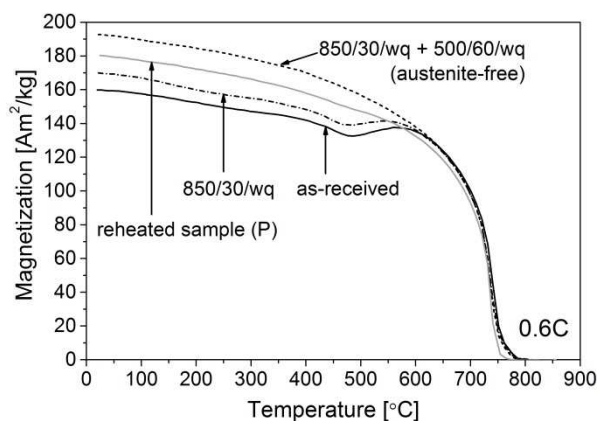


Figure 8.22 Magnetization versus temperature curves during heating, measured at 1.5 T for the as-received and prior treated samples of steel 0.6C. P indicates that pearlite is in the microstructure.

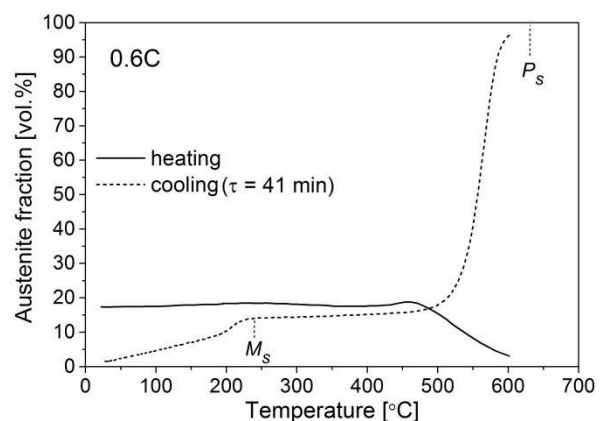


Figure 8.23 Austenite fraction versus temperature during heating and cooling of the as-received steel 0.6C. The transformation temperatures  $P_s$  and  $M_s$  are indicated.

The curve of the reference sample was fitted by equation (8.6) and the fitting parameters are listed in Table 8.9. The parameter  $C$  was given the same value as found by Arrott and Heinrich [21] for pure iron, 0.129.  $\beta$  and  $A$  are close to the values found by Arrott and Heinrich [21] for pure iron, 0.368 and 0.11, respectively. With the thus obtained magnetization of the reference sample the austenite fraction of the as-received sample during heating and cooling was calculated by equation (8.1), as described in section 8.2.3. The thus obtained austenite fraction during heating and cooling between room temperature and 600 °C is shown in Figure 8.23. During heating until 460 °C the austenite fraction is

varying between 17 and 19 vol.%. These variations are likely to be due to the formation and transformation of transition carbides in the as-received sample, introducing variations to the obtained austenite fraction. The fraction, however, is in accordance with the values found for the as-received sample determined from the room temperature magnetization measurements (see Figure 8.19) and by XRD (see Figure 8.20). From 460 °C the decomposition of austenite is taking place until a value of 3 vol.% at 600 °C, which is in accordance with the austenite fraction determined by XRD of a sample quenched from 500 °C (500/0/hq) in the dilatometer (see Figure 8.20).

Table 8.9 Fitting parameters for fit of reference samples by equation (8.6).

Steel	$M_0$ [Am <sup>2</sup> /kg]	$\beta$	A	C
0.6C	198.8	0.366	0.106	0.129
0.2C	206.0	0.366	0.115	0.129

Table 8.10 Overview of phase fractions (in %) during cooling of steel 0.6C in VSM.

Phase	600 °C	500 °C	240 °C	RT
$\gamma$	96	18	14	2
$\alpha + P$	4	82	86	86
$\alpha'$	-	-	-	12

During cooling the fraction of austenite is 96 vol.% at 600 °C, indicating the formation of 4 vol.% ferrite above 600 °C. However, pearlite formation already starts at 630 °C, as found from the magnetization curve (see Figure 8.7). Hence, the 4 vol.% ferrite at 600 °C is partly ferrite, initially formed before the formation of pearlite, and partly ferrite formed during pearlite formation. On further cooling, the austenite fraction decreases strongly until 500 °C to a fraction of 18 vol.% and with a lower slope until 240 °C to a fraction of 14 vol.%. An overview of the corresponding phase fractions is given in Table 8.10. From 240 °C the austenite fraction is decreasing at a higher rate until room temperature due to the formation of martensite. At room temperature the fraction of austenite is 2 vol.%, whereas from the room-temperature calculations a fraction between 3 and 6 vol.%, depending on the cementite fraction, is determined (see Figure 8.19). According to equilibrium, a maximum fraction of 8.3 vol.% cementite in the material corresponds to a ferrite fraction in pearlite of 61 vol.%, thus 69 vol.% pearlite would be present at maximum. Since martensite was formed during cooling, a lower fraction of pearlite and thus cementite must be present. This means that either more ferrite is present in the material or more martensite was formed and thus the determined in-situ austenite fraction during cooling is incorrect. Therefore, the reference values for calculating the in-situ austenite fraction are considered to be not valid during cooling. This is possibly due to the influence of compositional variations in the sample during cooling caused by the phase transformations.

Since the start of martensite formation coincides with  $T_C$  of cementite (212 °C [18]), the corresponding increase of the magnetization due to passing  $T_C$  of cementite could be undetected. Therefore, a sample, previously austenitized in the magnetometer (855/5/ $\tau_{41}$ ), was heated again and the corresponding magnetization curve is shown in Figure 8.22, denoted as 'reheated sample (P)'. Although a considerable fraction of pearlite was formed during cooling in the VSM, no change of the magnetization is detected when passing  $T_C$  of cementite. Hence, the increase in magnetization during cooling in the magnetometer indeed corresponds to the start of the martensite formation. This means that the saturation magnetization measurements show a low sensitivity for the detection of cementite. However, the sample 850/30/wq, with 16 vol.% retained austenite and no cementite, since it was quenched (see Figure 8.19), shows during heating a similar progress of the magnetization curve like the as-received sample. This can be seen in Figure 8.22. This sample shows a more pronounced decrease in magnetization at around 220 °C, related to the tempering of martensite and hence the formation of transitional carbides.

### **0.2C-steel**

#### a) Austenite fraction at room temperature

As for steel 0.6C, the austenite fraction from saturation magnetization measured at room temperature was determined for the 0.2C steel samples by equations (8.3) to (8.5) for varying cementite fractions up to the equilibrium cementite fraction. In Figure 8.24 the austenite fraction as a function of the assumed cementite fraction is shown for an as-received sample, the austenite-free reference sample, which was quenched from 900 °C (900/30/wq), and the sample treated in the VSM (906/6/ $\tau_{38}$ ). For comparison, the austenite fractions obtained by XRD-measurements of an as-received sample, the samples from dilatometer experiments and the reference sample are presented in Figure 8.25. Depending on the cementite fraction present in the as-received material, the austenite fraction, obtained from magnetization measurements, is between 5 and 6 vol.%, which is in accordance with the value obtained by XRD of 4 vol.%. However, for 4 vol.% austenite more than 3 vol.% cementite, thus the maximum equilibrium fraction of cementite, would be present in the as-received material. Thus, the value measured by XRD is expected to be larger within the uncertainty of  $\pm 2$  vol.% for the XRD experiments in this chapter. From the magnetic measurements, a fraction of 1 vol.% retained austenite was obtained for the reference sample 900/30/wq, since no cementite is expected to be present after quenching. This is, within the uncertainty of the measurements, in agreement with the XRD measurement of the sample 900/5/hq, treated in the dilatometer, where no austenite was detected. The martensitic microstructure of the 900/30/wq reference sample is shown in Figure 8.26.

The sample austenitized in the VSM (906/6/ $\tau_{38}$ ) shows an austenite fraction between 10 and 11 vol.%, depending on the cementite fraction. This is almost twice as much as measured by XRD for the sample austenitized in the dilatometer with the higher cooling rate (900/5/ $\tau_{20}$ ). As discussed for the 0.6C-steel, this difference could arise from the different cooling rates applied for the two experiments.

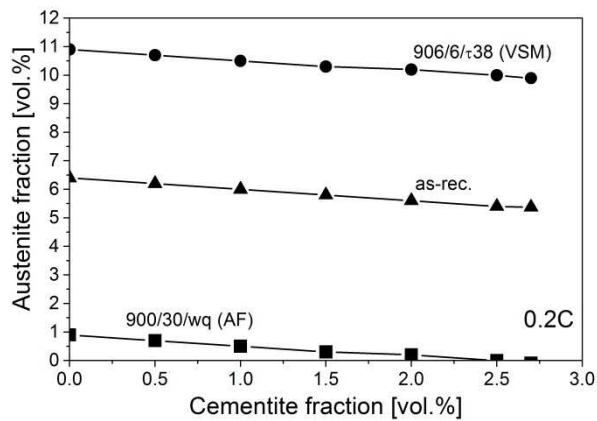


Figure 8.24 Austenite fraction, obtained from magnetic measurements at room temperature, versus assumed cementite fraction for steel 0.2C. VSM and AF denote the heat treatment carried out in the magnetometer and in the air furnace, respectively.

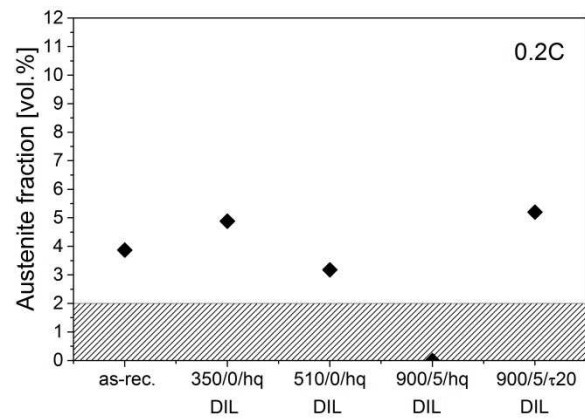


Figure 8.25 Austenite fractions obtained by XRD measurements at room temperature for samples of steel 0.2C. DIL denotes the heat treatment carried out in the dilatometer. Accuracy is  $\pm 2$  vol.%. Hashed area indicates detection limit by XRD (see section 3.4).

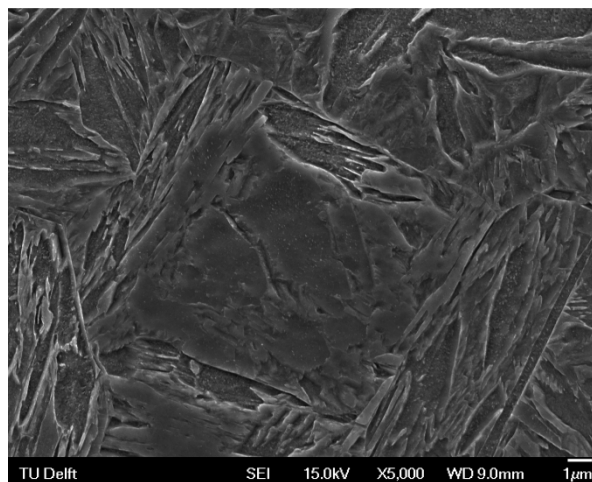


Figure 8.26 Microstructure of the reference sample 900/30/wq of steel 0.2C.

#### b) Temperature dependent austenite fraction

In order to determine the temperature dependent austenite fraction, the reference sample 900/30/wq, with a maximum fraction of 1 vol.% retained austenite (see Figure 8.24), was heated in the VSM at a rate of 5 K/min. The corresponding temperature-dependent magnetization curve during heating is shown in Figure 8.27 together with the one of the as-received sample. Since less austenite is present in the reference sample, the initial magnetization is higher and the two curves show a similar magnetization for temperatures above 600 °C. For calculating the temperature dependent austenite fraction, the curve of the reference sample 900/30/wq was fitted by equation (8.6) and the thus obtained fitting parameters are listed in Table 8.9. As discussed for the 0.6C-steel, the parameter  $C$  was given the value as found by Arrott and Heinrich [21] for pure iron, 0.129.  $\beta$  and  $A$  are close to

the values found by Arrott and Heinrich [21] for pure iron, 0.368 and 0.11, respectively.  $\beta$  is found to be the same as for steel 0.6C. Both  $A$  and  $M_0$  are smaller for steel 0.6C than for steel 0.2C, indicating that the compositional differences in C and Mo of both steels have an influence on the parameters  $A$  and  $M_0$ . With the thus obtained magnetization of the reference sample the austenite fraction during heating and cooling was calculated by equation (8.1), as described in section 8.2.3.

The corresponding austenite fraction of the as-received sample during heating and cooling between room temperature and 600 °C is shown in Figure 8.28. The austenite fraction during heating is about 5 vol.% until around 250 °C and decreases until 460 °C to about 4 vol.%. This decrease could be due to the formation of transition carbides or cementite due to tempering of martensite, which influences the calculated austenite fraction. The fraction, however, is in accordance with the values found for the as-received sample determined from the room temperature magnetization measurements (see Figure 8.24) and by XRD (see Figure 8.25). The decomposition of austenite starts at 460 °C and a fraction of about 3 vol.% is present at 510 °C, which is in accordance with the austenite fraction determined by XRD of the sample quenched from 510 °C (510/0/hq) in the dilatometer (see Figure 8.25). About 1 vol.% austenite is present at 600 °C.

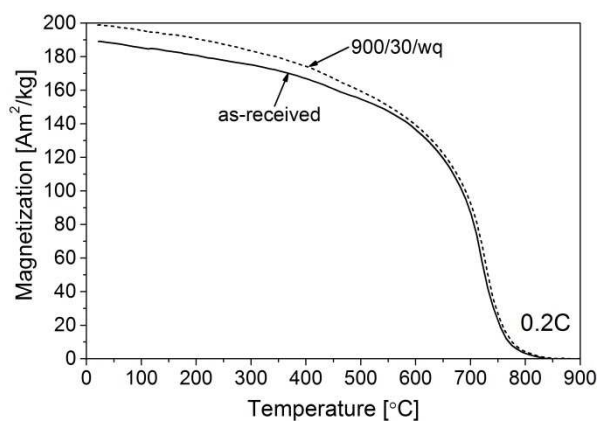


Figure 8.27 Magnetization versus temperature curves during heating, measured at 1.5 T for the as-received and the austenite-free reference sample of steel 0.2C.

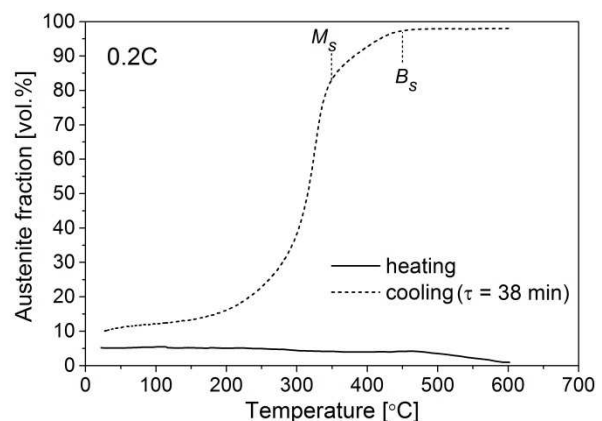


Figure 8.28 Austenite fraction, obtained from magnetization measurements, versus temperature during heating and cooling of the as-received steel 0.2C.

During cooling the fraction of austenite is 98 vol.% at 600 °C, indicating the formation of 2 vol.% ferrite until 600 °C. The phase fractions are listed in Table 8.11. At the start of bainite formation at 450 °C, 3 vol.% ferrite is present and until the formation start of martensite 14 vol.% bainite/bainitic ferrite has formed, according to the curve of the austenite fraction. Due to the martensite formation, starting at 350 °C, the austenite fraction decreases further until room temperature to a fraction of 10 vol.%. This matches well with the calculations of the room temperature austenite fraction as shown in Figure 8.24. Accordingly, about 2 vol.% cementite is present in the material.

Table 8.11 Overview of phase fractions (in %) during cooling of 0.2C.

Phase	600 °C	450 °C	350 °C	RT
$\gamma$	98	97	83	10
$\alpha$	2	3	3	3
B/ $\alpha$	-	-	14	14
$\alpha'$	-	-	-	73

## 8.4 Discussion

Two multi-phase steels were in-situ investigated by thermo-magnetic and dilatometry technique during heating to temperatures above  $A_{c3}$  and during subsequent cooling to monitor the phase transformations, which are discussed in the following, also in the view of the information that can be obtained by thermo-magnetic techniques.

### 8.4.1 Phase transformations during heating

Generally, during tempering of iron-carbon martensite above room temperature a sequence of processes occurs, which are described as segregation and clustering of carbon atoms, precipitation of transition carbides like  $\epsilon$ - and  $\eta$ -carbides, decomposition of austenite into ferrite and cementite and conversion of transition carbides into cementite, which on further tempering coarsen and spheroidize [23-25]. These carbides exhibit different  $T_C$ -values such as 212 °C ( $\theta$ ) [18], 245 °C ( $\text{Fe}_2\text{C}$ ) [27], 265 °C ( $\text{Fe}_{2-3}\text{C}$ ) [18] and 320 °C ( $\epsilon$ ) [18] and hence information about their formation and decomposition could be obtained by magnetic analysis.

Phase transformation analysis in the present work has been performed on as-received multi-phase microstructures. During heating of steel 0.6C in the dilatometer a first contraction occurred between 109 and 219 °C, where also a slight decrease in magnetization was noticed. This can be attributed to the formation of transition carbides ( $\epsilon/\eta$ ) during tempering of martensite, which is accompanied by a volume decrease [23]. The formation of  $\epsilon$ -carbides has been described by a decrease in magnetization in this temperature range [28, 29], although  $T_C$  of  $\epsilon$  is reported to be at a higher temperature [18]. Possibly, there is a range of the  $T_C$ -temperature for this carbide, due to variations in the composition. When heating an as-quenched sample of steel 0.6C (850/30/wq) the decrease in magnetization is more pronounced as shown in Figure 8.22, indicating that the as-received sample already contains transition carbides, like  $\epsilon$ , or  $\theta$  and thus the martensite present is tempered martensite.

An increase in magnetization due to the decomposition of austenite [10, 28, 29] is observed in both steels, starting at 460 °C and resulting in a decrease in austenite fraction, while austenite decomposition was observed by a length reduction starting at around 400 °C. This difference in temperature between both in-situ techniques is likely to be due to a higher heating rate in this temperature range during the treatment in the magnetometer compared to the dilatometer as shown in Figure 8.1. While austenite decomposition to ferrite and  $\theta$  is

usually accompanied by a length increase [23], a reduction in length has been found possible for high carbon concentrations in austenite [30]. This can be approximately described by the influence of the carbon concentration in austenite on the atomic volumes of austenite, cementite and ferrite [30]. For isotropic expansion/contraction the relative length change  $\Delta L/L_0$  is related to the volume change of the sample, expressed by [31]:

$$\frac{\Delta L}{L_0} = \frac{1}{3} \frac{\Delta V}{V_0}, \quad (8.7)$$

with  $\Delta V$  and  $V_0$  the average atomic volume change and the initial average atomic volume, respectively. The decomposition of austenite to cementite and ferrite at a given temperature can be described by the volume fractions of the unit cells and the volume phase fractions by [30]:

$$\frac{\Delta L}{L_0} = \frac{1}{3} \left( \frac{\left( 2f_\alpha a_\alpha^3 + \frac{1}{3} f_\theta a_\theta b_\theta c_\theta \right) - f_\gamma a_\gamma^3}{f_\gamma a_\gamma^3} \right), \quad (8.8)$$

with  $f_i$  the volume fraction of phase  $i$  and  $a_\gamma$ ,  $a_\alpha$ ,  $a_\theta$ ,  $b_\theta$  and  $c_\theta$  the lattice parameters of austenite, ferrite and cementite, respectively. The lattice parameters as a function of temperature and atomic fraction of carbon, used for the calculations in this study, are given in reference [31]. Figure 8.29 shows the relative length change as a function of carbon concentration in austenite for the decomposition of retained austenite to ferrite and cementite during isothermal holding at 400 °C. This was calculated by equation (8.8) under the assumption that all carbon of austenite partitions to cementite during the decomposition.

Figure 8.29 shows that for carbon concentrations higher than 3.3 at.% (0.73 wt.%) the decomposition of retained austenite is indeed accompanied by a reduction in relative length. Thus, a high carbon concentration in austenite causes a net contraction during the decomposition to ferrite and cementite [30]. Furthermore, the process of  $\epsilon/\eta$ -carbide-to- $\theta$  transformation, which is known to cause a reduction in length [23], can occur simultaneously with the austenite decomposition, contributing to the length reduction. However, still about 3 vol.% austenite was found to be present in both steels after this pronounced length reduction by quenching from around 500 °C, where the material was already expanding again. For both steels, an expansion with a higher slope was observed at around 580 °C. Possibly, the remaining austenite decomposes to  $\theta$  and ferrite, noticeable by an expansion. Such small changes in magnetization, due to the decomposition of a remaining small fraction of austenite, were not detected by the magnetization measurements due to the decrease in magnetization when approaching  $T_C$  of the material.

Independent of the measuring method, both steels show the decomposition of austenite at around the same temperatures during heating (460 °C) despite having different concentrations in C and Mo. This indicates that the two elements have an opposing effect of equal magnitude on the kinetics of the austenite decomposition, since C stabilizes austenite and Mo stabilizes ferrite. This is in agreement with the effect of Si and Mn on the retardation of formation and growth of  $\epsilon$ - and  $\theta$ -carbides [28, 32].

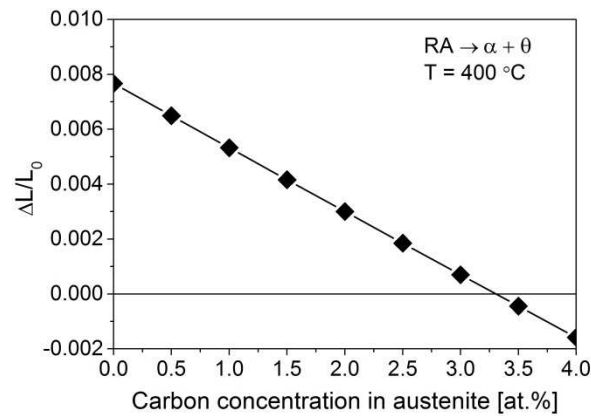


Figure 8.29 Relative length change versus carbon concentration in austenite at 400 °C. RA denotes retained austenite.

#### 8.4.2 Phase transformations during cooling

Due to the different carbon contents of the two analysed steels, different phase transformations were observed by thermo-magnetic technique and dilatometry during the slow cooling applied. The different cooling rates applied during the in-situ thermo-magnetic ( $\tau \approx 40$  min) and dilatometer experiments ( $\tau \approx 20$  min) (see Figure 8.1) resulted in different transformation temperatures and transformed phase fractions for the same steel. However, valuable information was found by both techniques, which complement one another.

A small fraction of about 2 vol.% ferrite was detected by magnetization measurements for both steels starting to form at 715 °C (0.6C-steel) and 785 °C (0.2C-steel), which are close to the individual  $A_{e3}$ -temperatures. This small fraction was not detected by dilatometry, possibly due to the texture sensitivity of the dilatometer technique, but was observed in the microstructures of both steels. Due to the higher cooling rate in the dilatometer a smaller fraction is formed during cooling and hence no distinct change in length was observed.

Due to the low cooling rates and the high C-content, pearlite formation was detected in steel 0.6C. The effect of the different cooling rates in the magnetometer and dilatometer on the temperature range for the pearlite formation, the pearlite fraction, the carbon concentration in austenite at the start of martensite formation and its effect on the  $M_s$ -temperature and the fraction of retained austenite are summarized in Table 8.12. From the microstructures (Figure 8.12) it can be seen that a higher fraction of pearlite was formed during cooling with  $\tau = 41$  min in the magnetometer compared to the faster cooling with  $\tau = 22$  min in the dilatometer. A greater fraction of pearlite leaves less carbon in austenite until the start of martensite formation due to the greater fraction of cementite. Therefore, a higher  $M_s$ -temperature was measured during cooling with the lower rate in the magnetometer and a smaller fraction of austenite was obtained. Table 8.12 shows that this is in accordance with the austenite fraction calculated from room temperature magnetic measurements for the sample treated in the magnetometer and the austenite fraction obtained by XRD for the sample treated in the dilatometer.

Table 8.12 Effect of different cooling rates on selected transformation temperatures and phase fractions during cooling of steel 0.6C in the magnetometer (VSM) and dilatometer (DIL). P denotes pearlite,  $x_c$  carbon concentration and RT room temperature.

	VSM ( $\tau = 41$ min)		DIL ( $\tau = 22$ min)	
T-range P [°C]	630 - 240		618 - 503	
$f_p$	high	>	low	
$x_c$ in $\gamma$ at $M_s$	low	<	high	
$M_s$ [°C]	240		> 203	
$f_\gamma$ at RT [vol.%]	3 - 6 (RT-calculations)		<	9 (XRD)

Table 8.13 Effect of different cooling rates on selected transformation temperatures and phase fractions during cooling of steel 0.2C in the magnetometer (VSM) and dilatometer (DIL). B denotes bainite,  $x_c$  carbon concentration and RT room temperature. ? = unknown.

	VSM ( $\tau = 38$ min)		DIL ( $\tau = 20$ min)	
$B_s$ [°C]	450		> 383	
$f_B$	14	(>)	?	
$x_c$ in $\gamma$ at $M_s$	low	<	high	
$M_s$ [°C]	350		> 332	
$f_\gamma$ at RT [vol.%]	10 - 11 (RT- calculations)		>	5 (XRD)

Bainite was found in the microstructures after both dilatometer and magnetometer experiments with steel 0.2C. An overview of the bainite start temperature and the effect of the bainite fraction on the carbon concentration in austenite at the start of martensite formation and its effect on the  $M_s$ -temperature and the fraction of retained austenite is given in Table 8.13. A lower  $M_s$ -temperature was observed in the sample cooled with  $\tau = 20$  min in the dilatometer compared to the sample cooled with  $\tau = 38$  min. The observed temperature differences between both techniques applied are due to the different fractions of bainite formed during cooling, caused by the different cooling rates. According to Andrews equation [33] for the  $M_s$ -temperature:

$$M_s [^\circ\text{C}] = 539 - 423x_c - 30.4x_{Mn} - 7.5x_{Mo}, \quad (8.9)$$

where  $x_i$  is the concentration of the alloying elements in wt.%, 14 % of bainite and 3 % of ferrite, found by the magnetization measurements, give an  $M_s$ -temperature of 397 °C if 2 % of cementite is present and only C is assumed to diffuse. A lower fraction of bainite together with a lower fraction of cementite, obtained when cooling with  $\tau = 20$  min in the dilatometer, gives a lower  $M_s$ -temperature, e.g. 367 °C for 8 % bainite and 1 % cementite.

Hence, a greater fraction of bainite with cementite would leave less C in austenite, which is the reason for the higher  $M_s$ -temperature, measured when cooled in the magnetometer with  $\tau = 38$  min (see Table 8.13). However, the fraction of retained austenite obtained from the magnetic measurements after cooling in the magnetometer is greater than the one obtained by XRD for the sample treated in the dilatometer. The reason is not fully understood yet and needs to be studied further.

From the curve of the austenite fraction obtained during cooling in the magnetometer the martensite fraction was deduced and fitted by the least-squares method with the Koistinen-Marburger (KM) equation [34] after Magee's derivation [35, 36] and multiplied by the final fraction of martensite,  $f_{\alpha'f}$ :

$$f_{\alpha'} = \left(1 - \exp[-\alpha_{KM}(T_{KM} - T)]\right) f_{\alpha'f}, \quad (8.10)$$

with  $\alpha_{KM}$  the rate parameter and  $T_{KM}$  the theoretical martensite start temperature.  $\alpha_{KM}$  and  $T_{KM}$  were found to be  $0.013 \text{ K}^{-1}$  and  $221 \text{ }^\circ\text{C}$  for steel 0.6C and  $0.017 \text{ K}^{-1}$  and  $350 \text{ }^\circ\text{C}$  for steel 0.2C. It can be seen in Figure 8.30 that the KM-fit does not match well with the martensite fraction of steel 0.6C. Possibly, the overlaying effect of cementite or transitional carbides formation, affecting the magnetization increase below  $240 \text{ }^\circ\text{C}$ , influences the calculated fraction of austenite and hence that of martensite. However,  $T_{KM}$  is found to be systematically lower than  $M_s$  [36, 37]. While this is true for steel 0.6C,  $T_{KM}$  of steel 0.2C is equal to the measured  $M_s$ -temperature. These discrepancies can also be due to inaccuracies in the determination of the austenite fraction from the in-situ magnetization measurements and need to be studied further.

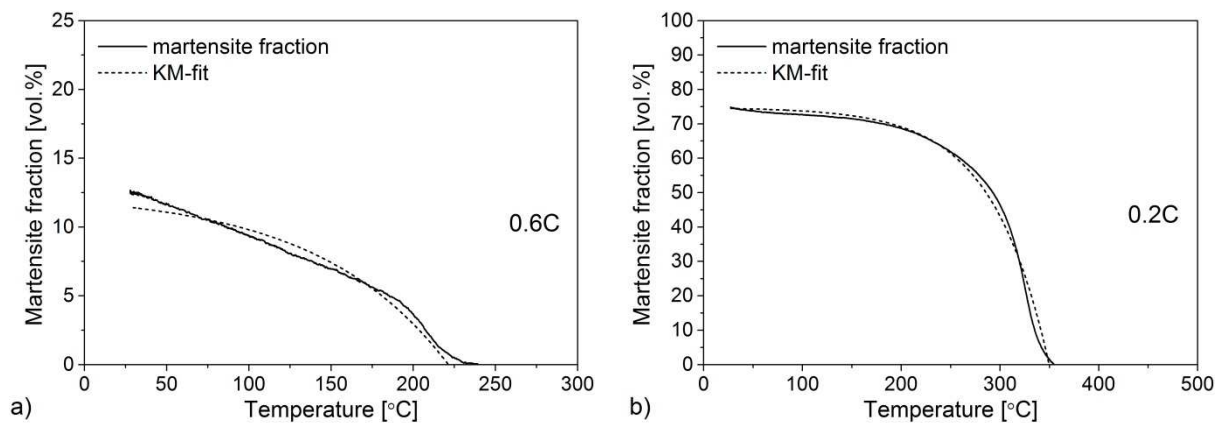


Figure 8.30 Fraction of martensite as a function of temperature during cooling from magnetic experiments fitted with Koistinen-Marburger (KM) equation for a) 0.6C-steel and b) 0.2C-steel.

While during cooling a clear increase in magnetization due to passing  $T_C$  of cementite was reported for several high carbon steels [10, 28, 38], no such effect due to the cementite was observed in the present study. Due to the lower carbon content and thus low fraction of carbides (max. about 3 vol.% in equilibrium, see Figure 8.6) in steel 0.2C, no effect of carbides on the magnetization was observed. Although a rather high fraction of pearlite was formed during cooling of steel 0.6C in the magnetometer, where an appreciably high fraction

of cementite should be present, no effect on the magnetization was observed during reheating of the sample in the magnetometer. Moreover, when heating the austenite-free reference sample 850/30/wq+500/60/wq of steel 0.6C no effect on the magnetization during heating due to the cementite was observed, although cementite could be present at a maximum fraction of 8.3 vol.%, according to the calculations of the austenite fraction (see Figure 8.19) and the equilibrium calculations (see Figure 8.5). This is especially remarkable as sample 850/30/wq, and also the as-received sample, shows formation of transition carbides during heating in the magnetometer, seen by distinct changes in the magnetization until 350 °C (see Figure 8.22). Apparently, the fraction of transition carbides is greater than that of cementite, the observation of which by saturation magnetization measurements seems more sensitive. Moreover, due to possible variations in the composition of cementite, the Curie temperature can exhibit a temperature range, making it more difficult to observe cementite by saturation magnetization measurements.

#### **8.4.3 Application of in-situ thermo-magnetic analysis to quenching and partitioning treatment**

This section discusses possible applications of in-situ saturation magnetization measurements for the phase transformation analysis during quenching and partitioning (QP) treatment, based on the findings in this chapter.

The QP-treatment is applied to advanced steels, belonging to the third generation of advanced high strength steels (AHSS), which are currently under development to offer high strength with reasonable ductility and cost effectiveness [13]. The QP-treatment comprises a complete or partial austenitization treatment followed by quenching between the start temperature for martensite formation and room temperature to obtain a controlled fraction of martensite, which is supersaturated in carbon. Subsequently, an isothermal partitioning step follows at the same or higher temperature, where the carbon partitions from martensite to austenite to stabilize the austenite against martensitic transformation during cooling to room temperature. The final microstructure is aimed to consist of tempered martensite and retained austenite, and also ferrite in the case of partial austenitization [7, 13].

Studies of the phase evolution during the QP-treatment are mostly carried out using dilatometry together with X-ray diffraction and microscopy [6, 7]. By analysing the evolution of the saturation magnetization, the evolution of phase fractions during the QP-treatment can be determined. This offers additional possibilities for in-situ analysing phase transformations and optimizing the QP-treatment parameters.

The saturation magnetization is sensitive to small fractions of the ferromagnetic ferrite during cooling from the austenitization temperature, as found in this study. This can be helpful for choosing the austenitization temperature in the QP-treatment, since for complete austenitization the lowest possible temperature should be chosen to obtain a small grain size. This, however, bears the risk that small fractions of ferrite are still present in the material, which can be monitored with in-situ thermo-magnetic measurements during cooling.

From the saturation magnetization measurements during cooling the quenching temperature can be determined on the basis of the rate of the austenite-to-martensite transformation. This enables the determination of the temperature at which the austenite is less sensitive to changes in the temperature adjustments.

Since austenite is paramagnetic it is possible to distinguish austenite and bainite during the partitioning step. This enables to determine the partitioning temperature where bainite formation can be avoided. The stabilization of austenite can be monitored and the partitioning temperature, from which fresh martensite formation is expected during subsequent cooling to room temperature can be determined.

Since the decomposition of retained austenite to ferrite and cementite is accompanied by an increase in magnetization, the influence of carbon concentration in retained austenite on the stabilization of austenite during partitioning treatment can be studied. By this an accurate temperature range for partitioning treatment can be determined by the magnetic technique.

The experiments have shown that saturation magnetization is sensitive to the formation of transition carbides during tempering of martensite at temperatures below 300 °C. Hence, the in-situ thermo-magnetic technique can be applied in studying the effect of the decomposition of transition carbides on the austenite stability during the partitioning step.

## 8.5 Conclusions and recommendations

### 8.5.1 Conclusions

The austenitization step with different cooling rates was analysed for two different multi-phase Fe-C-Mn-Si steels using in-situ thermo-magnetic and dilatometry techniques as well as XRD and microscopy. Both in-situ techniques give valuable information of the phase transformations during the heating and cooling. The austenite fraction was calculated from in-situ measurements of the saturation magnetization between room temperature and 600 °C, reflecting the different phase transformations during heating and cooling.

- 1) During heating of the as-received materials, austenite decomposition of both steels was detected by magnetic measurements starting at 460 °C. Due to the different bulk concentrations of C and Mo in the analysed materials, it is assumed that the two elements have an opposing effect of equal magnitude on the austenite decomposition.
- 2) The austenite decomposition during heating is found to accompany a volume contraction, which is assumed to be caused by a high carbon concentration in austenite. The process of  $\epsilon/\eta$ -carbide-to- $\theta$  transformation, occurring simultaneously with the austenite decomposition, could also contribute to the observed length reduction.
- 3) The formation of the ferromagnetic phases ferrite, pearlite, bainite and martensite from austenite can be monitored from magnetization measurements during cooling due to their different formation temperatures.
- 4) A small ferrite fraction of around 2 vol.% was found by magnetic measurements to form during cooling close to the  $A_{e3}$ -temperature of the analysed materials. No respective changes in length were detected by dilatometry, showing the sensitivity of the magnetic

technique to changes of 2 vol.% of the paramagnetic austenite phase at elevated temperatures.

- 5) Cementite formation was not detected directly by saturation magnetization measurements, indicating a detection limit of at least 8 vol.%. It is argued that variations in the composition of carbides might influence their Curie temperature, resulting in a range of Curie temperatures for e.g. cementite, which furthermore influences the detection limit of cementite by saturation magnetization measurements.

### **8.5.2 Recommendations for future work**

Based on the findings in this chapter, the following suggestions are recommended for future work:

1. To further investigate the decomposition of retained austenite during heating, samples with different initial retained austenite fractions are suggested to be analysed in-situ with the thermo-magnetic technique. This can be combined with analysing the stability of retained austenite of samples which have been given the quenching and partitioning treatment.
2. For improving the applicability of the thermo-magnetic technique on analysing carbide formation, further thermo-magnetic experiments with steels of different cementite fractions are suggested.
3. In-situ thermo-magnetic analysis of the entire quenching and partitioning treatment cycle is suggested to be performed with an improved cooling capability to provide required quenching rates.

### **REFERENCES**

- [1] L. Zhao, N.H. van Dijk, E. Brück, J. Sietsma and S. van der Zwaag: *Mater. Sci. Eng. A*, 2001, vol. 313, no. 1-2, pp. 145-52.
- [2] K. Mumtaz, S. Takahashi, J. Echigoya, Y. Kamada, L.F. Zhang, H. Kikuchi, K. Ara and M. Sato: *J. Mater. Sci.*, 2004, vol. 39, no. 6, pp. 1997-2010.
- [3] S.S.M. Tavares, J.M. Pardal, J.A. de Souza, J.M. Neto and M.R. da Silva: *J. Alloys Compd.*, 2006, vol. 416, no. 1-2, pp. 179-82.
- [4] M. Amirthalingam, M.J.M. Hermans, L. Zhao and I.M. Richardson: *Metall. Mater. Trans. A*, 2010, vol. 41A, no. 2, pp. 431-9.
- [5] N. Luzginova, L. Zhao and J. Sietsma: *Mater. Sci. Eng. A*, 2007, vol. 448, no. 1-2, pp. 104-10.
- [6] M.J. Santofimia, L. Zhao, R. Petrov and J. Sietsma: *Mater. Charact.*, 2008, vol. 59, no. 12, pp. 1758-64.
- [7] M. J. Santofimia, L. Zhao and J. Sietsma: *Metall. Mater. Trans. A*, 2009, vol. 40, no. 1, pp. 46-57.
- [8] D.C. Jiles: *Acta Mater.*, 2003, vol. 51, no. 19, pp. 5907-39.

- [9] P.E. Merinov and A.G. Mazepa: *Industrial Laboratory (Diagn. Mater.)*, 1997, vol. 63, no. 3, pp. 149-53.
- [10] J. Crangle and W. Sucksmith: *J. Iron Steel Inst.*, 1951, vol. 168, pp. 141-51.
- [11] D. San Martin, N.H. van Dijk, E. Brück and S. van der Zwaag: *Mater. Sci. and Eng. A*, 2008, vol. 481-482, pp. 757-61.
- [12] N.H. Van Dijk, S.E. Offerman, J.C.P. Klaasse, J. Sietsma and S. van der Zwaag: *J. Magn. Magn. Mater.*, 2004, vol. 268, no. 1-2, pp. 40-8.
- [13] D. K. Matlock, J.G. Speer, E. de Moor and P.J. Gibbs: *JESTECH*, 2012, vol. 15, no. 1, pp. 1-12.
- [14] M.J. Santofimia, L. Zhao and J. Sietsma: *Metall. Mater. Trans. A*, 2011, vol. 42, no. 12, pp. 3620-6.
- [15] M.J. Santofimia, T. Nguyen-Minh, L. Zhao, R. Petrov, I. Sabirov and J. Sietsma: *Mater. Sci. and Eng. A*, 2010, vol. 527, no. 23, pp. 6429-39.
- [16] Thermo-Calc Software package, Version S, Database TCFeV6.2, Stockholm, Sweden, 2011.
- [17] S.S.M. Tavares, R.F. de Noronha, M. R. da Silva, J.M. Neto and S. Pairis: *Mater. Res.*, 2001, vol. 4, no. 4, pp. 237-40.
- [18] A.E. Berkowitz and E. Kneller (Eds.): *Magnetism and Metallurgy*, vol. 1, pp. 331-47, p. 415, Academic Press, Inc., New York, 1969.
- [19] R. M. Bozorth: *Ferromagnetism*, pp. 367, pp. 716-9, John Wiley & Sons, Inc., Hoboken, NJ, 2003.
- [20] W.D. Callister, Jr.: *Fundamentals of Materials Science and Engineering: An integrated approach*, 2<sup>nd</sup> ed., pp. 730-64, John Wiley & Sons, Inc., 2005.
- [21] A.S. Arrott and B. Heinrich: *J. Appl. Phys.*, 1981, vol. 52, no. 3, pp. 2113-5.
- [22] C.F. Jatczak, J.A. Larson and S.W. Shin: *Retained austenite and its measurements by X-ray diffraction*, Society of Automotive Engineers, Inc., Warrendale, 1980.
- [23] L. Cheng, C.M. Brakman, B.M. Korevaar and E.J. Mittemeijer: *Metall. Trans. A*, 1988, vol. 19 A, no. 10, pp. 2415-26.
- [24] R.W.K. Honeycombe and H.K.D.H. Bhadeshia: *Steels: Microstructure and Properties*, 3rd ed., pp. 184-9, Elsevier Ltd.,
- [25] G. Krauss: *Steels: Heat Treatment and Processing Principles*, pp. 218-29, ASM International, Materials Park, Ohio, 1990.
- [26] S.M.C. van Bohemen: *Mater. Sci. Technol.*, 2012, vol. 28, no. 4, pp. 487-95.
- [27] E.M. Cohn and L.J.E. Hofer: *J. Am. Chem. Soc.*, 1950, vol. 72, pp. 4662-4.
- [28] W.S. Owen: *Trans. Am. Soc. Metals*, 1954, vol. 46, pp. 812-29.
- [29] Y. Ivanisenko, R.K. Wunderlich, R.Z. Valiev and H.J. Fecht: *Scripta Mater.*, 2003, vol. 49, no. 10, pp. 947-52.
- [30] F.G. Caballero, C. García-Mateo and C. García de Andrés: *Mater. Trans.*, 2005, vol. 46, no. 3, pp. 581-6.
- [31] T.A. Kop: *A dilatometric study of the austenite/ferrite interface mobility*, PhD Thesis, Technische Universiteit Delft, The Netherlands, 2000.

- [32] G. Miyamoto, J.C. Oh, K. Hono, T. Furuhashi and T. Maki: *Acta Mater.*, 2007, vol. 55, no. 15, pp. 5027-38.
- [33] K.W. Andrews: *J. Iron Steel Inst.*, 1965, vol. 203, pp. 721-7.
- [34] D.P. Koistinen and R.E. Marburger: *Acta Metall.*, 1959, vol. 7, no. 1, pp. 59-60.
- [35] C.L. Magee: The nucleation of martensite, in: *Phase transformations*, pp. 115-56, American Society for Metals, Metals Park, Ohio, 1970.
- [36] S.M.C. van Bohemen and J. Sietsma: *Mater. Sci. Technol.* 2009, vol. 25, no. 8, pp. 1009-12.
- [37] S.M.C. van Bohemen and J. Sietsma: *Metall. Mater. Trans. A*, 2009, vol. 40A, no. 5, pp. 1059-68.
- [38] O. Zmeskal and M. Cohen: *Rev. Scientific Instruments*, 1942, vol. 13, no. 8, pp. 346-8.

# Summary

Controlling the retention of austenite during thermal processing of advanced multiphase steels has become a major issue in their production. Magnetic techniques are of increasing interest in the steel industry for monitoring the development of austenite on the basis of different magnetic properties of the phases in the steel. In this project, *in-situ* and *ex-situ* magnetic investigations using the Vibrating Sample Magnetometer as a primary experimental technique for measuring the saturation magnetization are performed on two types of advanced steels: a supermartensitic stainless steel (SMSS), on which the main focus of the thesis is, and multi-phase Fe-C-Mn-Si steels. The saturation magnetization is a unique magnetic property, which is only dependent on temperature, the phases present in the material and the composition. Additionally, X-ray diffraction, dilatometry, microscopy and thermodynamic calculations are applied. For SMSS, the retained austenite fraction plays an essential role in controlling mechanical properties that often have a narrow tolerance window. This project leads to an improved understanding of the influence of the composition and temperature on the austenite stability in different tempering cycles. For the multi-phase Fe-C-Mn-Si steels, this project contributes to the development of these advanced steels and a more accurate control over the microstructure development in order to have a better predictive capability. The scientific aim of the project is thus twofold: (i) to study the microstructural evolution involved in thermal processing of advanced steels based on optimising retained austenite and (ii) to optimise and extend the application of magnetic methods for these steels.

The thesis comprises eight chapters, where chapter 1 gives a general introduction to the thesis.

Chapter 2 introduces supermartensitic stainless steels, whose analysis is the main focus of this thesis. An account is given on fundamentals of magnetism, relevant for this work, and its application in metallurgy, especially for the detection of austenite by saturation magnetization measurements. Based on literature information, an improved equation to calculate the theoretical saturation magnetization of SMSS is proposed.

The materials and experimental techniques used in this thesis are introduced in chapter 3 and the determination of austenite from the different *in-situ* techniques is briefly described.

Chapter 4 studies the influence of alloying elements on the equilibrium fraction of austenite of a 13Cr6Ni2Mo SMSS, the austenite transformation temperatures and the presence of different phases using the Thermo-Calc software package. The results have shown that, within the composition range considered, the  $A_{e3}$ -temperature is more sensitive to changes in concentration of Cr, Ni and Mo than to C, which is present in low concentrations.

Furthermore, with increasing Ni- and Mn-concentration the austenite fraction at lower temperatures increases. Hence, a higher content of Ni and Mn in austenite at room temperature would increase its stability. Chi- and Laves-phases are shown to be thermodynamically more favourable than  $M_6C$ . This implies that deviations from the original heat treatment (higher tempering temperature and/or time) could lead to Chi- and/or Laves-phase formation. A comparison of pseudo-binary Fe-Ni phase diagrams for 13Cr6Ni2Mo SMSS, allowing the presence of different phases in equilibrium, has shown that the presence of Chi- and Laves-phases also depends on the Ni-content of the material.

In chapter 5 the austenite fraction during austenitization treatment of 13Cr6Ni2Mo SMSS is determined by three *in-situ* techniques: thermo-magnetic technique, dilatometry and high-temperature X-ray diffraction. An approach for in-situ determination of the austenite fraction from thermo-magnetic measurements below the  $A_{c1}$ -temperature is presented. The thermo-magnetic technique shows the highest accuracy in the determination of the austenite fraction. The start of martensite formation is accurately determined due to the different magnetic behaviour of the two phases present in the material, i.e. martensite and austenite. However, the influence of the Curie temperature leads to less detailed information at temperatures close to the Curie temperature. The measurements could therefore not confirm the observations by dilatometry that the martensite-to-austenite transformation takes place in two stages. The presence of bcc-martensite up to a temperature of 834 °C was confirmed by high-temperature X-ray diffraction. Enhanced martensite formation at the sample surface was detected by X-ray diffraction, which is assumed to be due to the increased relaxation of transformation stresses at the sample surface. About 5 vol.% retained austenite is detected after cooling from the austenitization temperature, which is consistent with the thermodynamic stability of austenite at room temperature in this composition. The existence of this retained austenite may affect the subsequent heat treatment process, i.e. tempering and stress-relief treatment.

Chapter 6 studies *in-situ* the formation of austenite during double tempering treatment of 13Cr6Ni2Mo SMSS samples by the thermo-magnetic technique. A new approach is proposed for determining the austenite fraction in 13Cr6Ni2Mo SMSS from in-situ thermo-magnetic measurements based on the theoretical magnetization of martensite. By this approach the austenite fraction was determined as a function of temperature up to 695 °C, the highest applied tempering temperature in the present work. The austenite fraction was monitored during the tempering treatment and the activation energy of the austenite formation from martensite during the first tempering step was found by a modified JMAK-equation to be 233 kJ/mol, which is similar to the activation energy for Ni and Mn diffusion in Fe and for Fe self-diffusion. This supports the assumption that partitioning of Ni and Mn to austenite plays a role in the austenite formation during tempering and hence its stabilization during subsequent cooling. During heating to the first tempering temperature about 1 to 2 vol.% of austenite, retained from quenching after the austenitization, is decomposed between 350 and 480 °C. At 480 °C austenite starts to form, therefore this temperature is indicated as the  $A_{c1}$ -temperature of the as-quenched material for the heating rate of 5 K/min. With

increasing first tempering temperature the  $M_s$ -temperature of austenite is increasing, due to the lower concentration of austenite-stabilizing elements in the increased fraction of austenite obtained at the tempering temperature. At room temperature austenite decomposition is observed after cooling from the first tempering at temperatures higher than 640 °C, which only occurs if martensite formation takes place during cooling from the first tempering temperature. The austenite decomposition is related to the holding time at room temperature. The underlying mechanisms are not yet understood and further studies are needed. During the second tempering at 550 °C austenite is only formed in samples in which martensite is formed during cooling from the first tempering temperature. The retained austenite fraction after tempering is increasing with first tempering temperature, exhibits a peak at 635 °C and decreases with further increase in first tempering temperature. An approach is described to calculate the magnetization and hence the austenite fraction depending on the chemical composition. The results show good agreement with the results of the first tempering step.

In Chapter 7 the influence of austenitization treatment of the 13Cr6Ni2Mo SMSS on austenite formation during reheating and on the fraction of austenite retained after tempering treatment is measured and analysed. Two different austenitization temperatures and times are analysed: 950 °C for 0.5 h and 1050 °C for 30.5 h. The latter yields a better homogenization of the material, which causes an increase in the transformation temperatures for the martensite-to-austenite transformation and a lower retained austenite fraction with less variability after tempering. Furthermore, the smaller prior austenite grain size of the samples previously austenitized at 950 °C for 0.5 h is proposed to lead to a higher density of nucleation sites compared to samples previously austenitized at 1050 °C for 30.5 h, which can influence the fraction of retained austenite. As found in *chapter 5*, the austenite formation takes place in two stages during heating to 950 °C, which is probably caused by local inhomogeneities of Ni and Mn due to their limited diffusion at lower temperatures. The first stage of austenite formation is mainly related to partitioning of Ni and Mn into the austenite, leaving martensite partially untransformed. The second stage of austenite formation is probably governed by an increased diffusivity of Ni and Mn at higher temperature, together with the decomposition of carbides and nitrides. The transformation temperatures shift to higher temperatures with increasing heating rate, indicating a diffusional transformation mechanism. The activation energy for austenite formation from martensite during continuous heating, obtained by a modified Kissinger method, is approximately 400 kJ/mol for the first stage and 500 kJ/mol for the second stage. These values are believed to be an effective activation energy comprising the energies of both the mechanisms involved, i.e. nucleation and growth.

Chapter 8 studies *in-situ* the phase transformations during austenitization of two multi-phase Fe-C-Mn-Si steels with different carbon contents by thermo-magnetic and dilatometry techniques. Additionally, X-ray diffraction and microscopy are used for further interpretation of the results. This chapter provides a basis to further develop the analysis of austenite

formation of multi-phase steels using thermo-magnetic techniques. The austenite fraction is determined from in-situ measurements of the saturation magnetization between room temperature and 600 °C, reflecting the different phase transformations during heating and cooling. Decomposition of the paramagnetic austenite in both steels is detected during heating of the as-received materials, which is accompanied by an increase in magnetization and a volume contraction. The latter is assumed to be caused by a high carbon concentration in austenite. The process of  $\epsilon$ -carbide-to-cementite transformation, occurring simultaneously with the austenite decomposition, could also contribute to the observed volume contraction. Furthermore, the formation of the ferromagnetic phases ferrite, pearlite, bainite and martensite from austenite is monitored from magnetization measurements during cooling due to their different formation temperatures. Cementite formation could not be detected directly by saturation magnetization measurements, indicating a detection limit of at least 8 vol.%. It is argued that variations in the composition of carbides might influence their Curie temperature, resulting in a Curie temperature range for e.g. cementite, which furthermore influences the detection limit of cementite by saturation magnetization measurements.

# Samenvatting

Een belangrijk onderwerp in de productie van geavanceerd multi-fase staal is het beheersen van de retentie van austeniet gedurende de thermische verwerking. Magnetische technieken zijn in toenemende mate interessant voor de staalindustrie om de ontwikkeling van austeniet te monitoren, gebaseerd op de verschillende magnetische eigenschappen van de fasen in het staal. In dit project zijn *in-situ* en *ex-situ* magnetische onderzoeken uitgevoerd met de Vibrating Sample Magnetometer als de voornaamste experimentele techniek om de verzadigingsmagnetisatie van twee soorten geavanceerd staal te meten: een supermartensitisch roestvast staal (SMSS), waar de nadruk van dit proefschrift op ligt, en multi-fase Fe-C-Mn-Si staalsoorten. De verzadigingsmagnetisatie is een unieke magnetische eigenschap die alleen van de temperatuur, de aanwezige fasen in het materiaal en de chemische samenstelling afhangt. Bovendien worden röntgendiffractie, dilatometrie, microscopie en thermodynamische berekeningen toegepast. Het restausteniet speelt voor de SMSS een belangrijke rol in het beheersen van de mechanische eigenschappen die vaak een nauwe tolerantie hebben. Dit project leidt tot een verbeterd begrip van de invloed van de chemische samenstelling en temperatuur op de austenietstabiliteit in verschillende tempercycli. Voor de multi-fase Fe-C-Mn-Si staalsoorten draagt dit project bij aan de ontwikkeling van dit geavanceerde staal en aan een nauwkeurige beheersing van de microstructuurontwikkeling met betrekking tot beter voorspelbare mogelijkheden. De wetenschappelijke doestellingen van dit project zijn: (i) bestuderen van de microstructurele processen die plaatsvinden bij de productie van geavanceerd staal, gebaseerd op de optimalisering van restausteniet en (ii) het gebruik van magnetische methoden voor deze staalsoorten optimaliseren en uitbreiden.

Dit proefschrift bevat acht hoofdstukken, waar hoofdstuk 1 een algemene inleiding over dit proefschrift geeft.

Hoofdstuk 2 steelt de supermartensitische roestvast staal voor, waar de nadruk van dit proefschrift op ligt. De relevante achtergrond van het magnetisme en zijn toepassing in de materiaalkunde worden beschreven, met name het detecteren van austeniet door verzadigingsmagnetisatie. Gebaseerd op informatie uit de literatuur wordt een verbeterde vergelijking ter berekening van de theoretische verzadigingsmagnetisatie van SMSS voorgesteld.

Hoofdstuk 3 beschrijft de materialen en experimentele technieken die toegepast zijn in dit proefschrift. De bepaling van austeniet met de verschillende *in-situ* technieken wordt kort beschreven.

Hoofdstuk 4 bestudeert de invloed van legeringselementen op de fractie austeniet in evenwicht, de austeniettransformatietemperaturen en de verschillende fasen die voor een 13Cr6Ni2Mo SMSS in evenwicht aanwezig zijn met behulp van Thermo-Calc software. De resultaten wijzen uit dat, binnen de geanalyseerde chemische samenstelling, de  $A_{e3}$ -temperatuur gevoeliger is voor veranderingen in concentratie Cr, Ni, en Mo dan in C, dat in lage concentraties aanwezig is. Bovendien neemt de fractie austeniet bij lage temperaturen toe met toename van Ni en Mn concentratie. Dit betekent dat een grotere concentratie Ni en Mn in austeniet de austenietstabiliteit bij kamertemperatuur verhoogt. Chi- en Laves-fasen zijn thermodynamisch gunstiger dan  $M_6C$ . Dit betekent dat afwijkingen van de oorspronkelijke warmtebehandeling (hogere temperatuur en/of -tijd) tot de vorming van Chi- en Laves-fasen kan leiden. Een vergelijking van pseudo-binaire Fe-Ni fasediagrammen voor de 13Cr6Ni2Mo SMSS met verschillende fasen, die in evenwicht aanwezig zijn, wijst uit dat de aanwezigheid van Chi- en Laves-fasen ook van de Ni-concentratie afhangt.

In hoofdstuk 5 wordt de fractie austeniet gedurende de austeniteerbehandeling van 13Cr6Ni2Mo SMSS bepaald met drie *in-situ* technieken: thermo-magnetische techniek, dilatometrie en röntgendiffractie. Een benadering om de fractie austeniet *in-situ* te bepalen middels thermo-magnetische metingen onder de  $A_{c1}$ -temperatuur wordt gepresenteerd. De thermo-magnetische techniek geeft de hoogste nauwkeurigheid in de bepaling van de fractie austeniet. Het begin van de martensietvorming is nauwkeurig bepaald op grond van het verschillende magnetische gedrag van martensiet en austeniet, de twee fasen die in het materiaal aanwezig zijn. De invloed van de Curietemperatuur heeft echter tot gevolg dat er minder gedetailleerde informatie nabij de Curietemperatuur te verkrijgen is. Vandaar dat deze metingen de dilatometrische observaties, namelijk dat de martensiet-naar-austeniettransformatie in twee stappen gebeurt, niet konden bevestigen. Met hogetemperatuur-röntgendiffractie is de aanwezigheid van bcc-martensiet tot een temperatuur van 834 °C bevestigd. Een verhoogde martensietvorming op het proefstukoppervlak is gedetecteerd met röntgendiffractie. Deze martensietvorming is mogelijk het gevolg van verhoogde relaxatie van transformatiespanningen op het proefstukoppervlak. Circa 5 vol.% restausteniet is gemeten na de afkoeling vanaf de austeniteertemperatuur. Dit is in overeenstemming met de thermodynamische stabiliteit van austeniet bij kamertemperatuur voor deze chemische samenstelling. Het bestaan van dit restausteniet kan de daaropvolgende warmtebehandeling, de temper- en spanningsverlagende behandeling, beïnvloeden.

Hoofdstuk 6 bestudeert *in-situ* de vorming van austeniet gedurende de dubbele temper-behandeling van 13Cr6Ni2Mo SMSS proefstukken met hulp van de thermo-magnetische techniek. Een nieuwe benadering wordt voorgesteld om de fractie austeniet in 13Cr6Ni2Mo SMSS te bepalen middels *in-situ* thermo-magnetische metingen gebaseerd op de theoretische verzadigingsmagnetisatie van martensiet. Met deze benadering is de fractie austeniet bepaald als functie van temperatuur tot 695 °C, de hoogste temperatuur die in dit proefschrift toegepast is. De fractie austeniet is gemonitord gedurende de

temperbehandeling. De activeringsenergie voor de martensiet-naar-austenietvorming gedurende de eerste temperfase is gevonden door een gemodificeerde JMAK-vergelijking toe te passen en bedraagt 233 kJ/mol. Deze is vergelijkbaar met de activeringsenergie van Ni- en Mn-diffusie en voor Fe-zelfdiffusie. Dit steunt de aanname dat de diffusie van Ni en Mn naar austeniet een rol speelt bij de austenietvorming gedurende temperen en dus diens stabilisatie gedurende daaropvolgende afkoeling. Circa 1 tot 2 vol.% restausteniet, behouden na de austeniteerbehandeling, transformeert tussen 350 and 480 °C gedurende het verwarmen tot de eerste temperfase. De austenietvorming begint bij 480 °C. Deze temperatuur wordt dus aangegeven als de  $A_{c1}$ -temperatuur voor het afgeschrikte materiaal met een opwarmingsnelheid van 5 K/min. Bij toename van de temperatuur voor de eerste temperfase, neemt de  $M_s$ -temperatuur toe vanwege de lagere concentratie van austenietstabiliserende elementen in de toenemende austenietfractie bij de tempertemperatuur. Austenietdecompositie bij kamertemperatuur is waargenomen na afkoeling van de eerste temperfase bij temperaturen hoger dan 640 °C. Deze decompositie gebeurt alleen als martensiet gedurende afkoeling werd gevormd. De decompositie van austeniet is gerelateerd aan de duur die de proefstukken bij kamertemperatuur worden gehouden. De onderliggende mechanismen zijn nog niet begrepen en verdere studies zijn nodig. Gedurende de tweede temperfase bij 550 °C wordt austeniet alleen gevormd als martensiet is gevormd gedurende afkoeling vanaf de eerste tempertemperatuur. De fractie restausteniet na de temperbehandeling neemt met de eerste tempertemperatuur toe, vertoont een piek bij 635 °C en neemt af met verdere toename van de eerste tempertemperatuur. Een methode is beschreven om de verzadigingsmagnetisatie, en dus ook de austenietfractie, afhankelijk van de chemische samenstelling, te berekenen. De resultaten geven een goede overeenkomst met de resultaten van de eerste temperfase.

De invloed van de austeniteerbehandeling van het 13Cr6Ni2Mo SMSS op de austenietvorming gedurende herverwarmen en op de fractie restausteniet na de temperbehandeling is gemeten en geanalyseerd in hoofdstuk 7. Twee verschillende austeniteertemperaturen en -tijden worden geanalyseerd: 950 °C gedurende 0.5 h en 1050 °C gedurende 30.5 h. Deze laatste temperatuur en tijd leiden tot een betere homogenisatie van het materiaal. Dit leidt tot een toename van de transformatietemperaturen voor de martensiet-naar-austeniettransformatie en tot een lagere fractie restausteniet met minder variabiliteit na de temperbehandeling. Bovendien wordt voorgesteld dat de kleinere korrelgrootte van de voormalige austenietkorrels na de austeniteerbehandeling bij 950 °C gedurende 0.5 h tot een hogere dichtheid van nucleatieplekken leidt, vergeleken met de proefstukken die bij 1050 °C gedurende 30.5 h worden geaustenitiseerd. Dit verschil kan de fractie restausteniet beïnvloeden. Zoals beschreven in *hoofdstuk 5*, gebeurt de austenietvorming in twee stappen gedurende het verwarmen tot 950 °C. Dit is waarschijnlijk veroorzaakt door lokale inhomogeniteiten van Ni en Mn vanwege hun beperkte diffusie bij lage temperaturen. De eerste stap van de austenietvorming is hoofdzakelijk gerelateerd aan de herverdeling van Ni en Mn naar austeniet, waar martensiet gedeeltelijk ongetransformeerd overblijft. De tweede stap van de

austenietvorming wordt waarschijnlijk gedomineerd door een diffusiviteitstoename van Ni en Mn bij hogere temperaturen, samen met de decompositie van carbiden en nitriden. De transformatietemperaturen verschuiven naar hogere temperaturen met toenemende opwarmingsnelheid, hetgeen op een diffusieel transformatiemechanisme wijst. De activeringsenergie voor de martensiet-naar-austenietvorming gedurende continue verwarming, berekend door middel van een modificeerde Kissinger methode, is circa 400 kJ/mol voor de eerste stap en 500 kJ/mol voor de tweede stap. Deze waarden worden geïnterpreteerd als een effectieve activeringsenergie, die zowel nucleatie als groei omvat.

Hoofdstuk 8 bestudeert *in-situ* de faseformaties gedurende de austeniteerbehandeling van twee multi-fase Fe-C-Si-Mn stalen met verschillende koolstofconcentraties door middel van thermo-magnetische en dilatometrische technieken. Bovendien worden röntgendiffractie en microscopie voor verdere interpretatie van de resultaten toegepast. Dit hoofdstuk vormt een basis om de analyse van de austenietvorming in multi-fase stalen middels thermo-magnetische technieken verder te ontwikkelen. De fractie austeniet is bepaald door *in-situ* metingen van de verzadigingsmagnetisatie tussen kamertemperatuur en 600 °C, die de verschillende faseformaties gedurende opwarming en afkoeling representeren. Gedurende opwarming van de aangeleverde materialen is decompositie van het paramagnetische austeniet in beide stalen gedetecteerd, tezamen met een toename van de magnetisatie en een afname in volume. Dit laatste is mogelijk het gevolg van een hoge koolstofconcentratie in austeniet. Het proces transformatie van de  $\epsilon$ -carbide naar cementiet, die tegelijk met de austenietdecompositie plaatsvindt, kan ook bijdragen tot de volumenafname. Bovendien is de formatie van de ferritische fasen ferriet, perliet, bainiet en martensiet uit austeniet gedurende afkoeling gemonitord door de magnetische metingen vanwege hun verschillende formatietemperaturen. Cementietformatie is niet direct gedetecteerd met de metingen van de verzadigingsmagnetisatie, hetgeen op een detectielimiet van tenminste 8 vol.% wijst. Het wordt beargumenteerd dat afwijkingen in de chemische samenstelling van de carbiden mogelijk hun Curietemperatuur beïnvloeden. Dit zou tot een Curietemperatuur-marge voor bijvoorbeeld cementiet leiden, die bovendien de detectielimiet van cementiet door metingen van de verzadigingsmagnetisatie beïnvloedt.

# Acknowledgements

This research was carried out under the project number M41.5.10392 in the framework of the Research Program of the Materials innovation institute (M2i) in The Netherlands ([www.m2i.nl](http://www.m2i.nl)). This thesis would not have been possible to realize without the help and support of many people, to whom I wish to express my sincere gratitude:

- I would like to thank M2i for funding this research and for making it possible to extend my work from an application engineer to a PhD thesis. Special thanks goes to Dr. ir. Viktoria Savran, Ir. Heiko Sportel, Monica Reulink, Oscar Ruigrok, Irina Bruckner and Brigitte van Uden. Monica, thank you for all your support and help over the years.
- Prof. dr. ir. Jilt Sietsma, my promotor, and Dr. Lie Zhao, my daily supervisor, thank you for making this work possible, all your critical advice, valuable discussions, support and patience. Without your guidance my dissertation would not have been possible and would not have come to a successful end. Thanks for not giving up on me!
- Dr. Peter F. Morris, Cathy Bell and Matthew Green, my industrial supervisors from Tata Steel Speciality Steels, now Liberty Speciality Steels, thank you for your interest in my work, for valuable discussions on the supermartensitics and your support. Peter, your feedback and attention to details is highly appreciated!
- Dr. Dave Hanlon and Dr. Stefan van Bohemen, from Tata Steel Research, Development and Technology, thank you for useful discussions on chapter 8.
- Prof. dr. Maria Santofimia Navarro, thank you for your help and valuable discussions about the QP-steels and chapter 8.
- Dr. Murugaiyan Amirthalingam, thank you for all your help with ThermoCalc and any other software, and for useful discussions about my work.
- Dr. Niels van Dijk, thank you for helpful discussions on magnetics.
- Nico Geerlofs and Hans Hofmann, thank you for all your help with the magnetometer, dilatometer and heat treatment experiments.
- Erik Peekstok<sup>†</sup> and Sander van Asperen, thank you for your help with sample preparations, microscopy and useful discussions.
- Niek van der Pers and Ruud Hendrikx, thank you for performing the XRD measurements, for all your help and explanations on their analysis and for calculating the R-values for chapter 5.

- Kees Kwakernaak, thank you for the training and help with the SEM.
- Tjerk Koopmans, thank you for performing magnetometer experiments for chapter 8.
- Richard Huizenga, thank you for your help with ThermoCalc.
- Frans Bosman and Ton Riemslag, laboratory staff, thank you for your help.
- Bert Bakker from DEMO workshop, thank you for manufacturing my samples.
- Hans Dorp from 3mE workshop, thank you for helping me with my sample holders.
- Lambert Schipperheijn from Tetraëder FME, thank you for manufacturing my sample holders and for your ideas.
- Special thanks go to my (former) colleagues at the Material Science department at TU Delft. Especially to Farideh and Yulia, with whom I shared the office. Thank you for all the discussions and for your help. Thanks to Patricia and Sepideh for their support. Thanks to Janneke for correcting my Samenvatting.
- Olga Wens van Swol and Prisca Koelman, Secretaries, thank you for taking care of all the non-scientific stuff.
- Finally, I would like to thank my friends for their support. Special thanks go to my family, especially my parents, for their love and support.
- Last but not least, I would like to thank my husband, Torsten, for his love, endless encouragement, support and friendship. This thesis would certainly not have been possible nor finished without you on my side.

# List of publications

## Journal papers:

A. Bojack, L. Zhao and J. Sietsma: Thermodynamic Analysis of the Effect of Compositional Inhomogeneity on Phase Transformations in 13Cr6Ni2Mo Supermartensitic Stainless Steel, Solid State Phenomena, 2011, vols. 172-174, pp. 899-904.

A. Bojack, L. Zhao, P.F. Morris and J. Sietsma: In-Situ Determination of Austenite and Martensite Formation in 13Cr6Ni2Mo Supermartensitic Stainless Steel, Materials Characterization, 2012, vol. 71, pp.77-86.

A. Bojack, L. Zhao, P.F. Morris and J. Sietsma: In Situ Thermo-Magnetic Investigation of the Austenitic Phase During Tempering of a 13Cr6Ni2Mo Supermartensitic Stainless Steel, Metallurgical and Materials Transactions A, 2014, vol. 45A, pp. 5956-67.

A. Bojack, L. Zhao, P.F. Morris and J. Sietsma: Austenite Formation from Martensite in a 13Cr6Ni2Mo Supermartensitic Stainless Steel, Metallurgical and Materials Transactions A, 2016, vol. 47A, pp. 1996-2009.

## Conference poster and presentation:

A. Bojack, L. Zhao and J. Sietsma: Thermodynamic Analysis of the Effect of Compositional Inhomogeneity on Phase Transformations in a 13Cr6Ni2Mo Supermartensitic Stainless Steel, International Conference on Solid-Solid Phase Transformations in Inorganic Materials (PTM2010), 6-11 June 2010, Avignon, France.

S. Ramos Pascual, F. HajyAkbar, A. Bojack, M.J. Santofimia and J. Sietsma: Effect of Microstructure on the Mechanical Properties of a Quenched and Partitioned Medium-Carbon, High-Silicon Steel, National Student Conference in Metallic Materials, 17-18 June 2013, Brunel University, Uxbridge, United Kingdom.



# About the author

Andrea Bojack was born in April 1981 in Freiberg/Germany. She studied Materials Science and Engineering with a specialisation in Materials Engineering at the faculty of Materials Science and Materials Technology at Technische Universität Bergakademie Freiberg in Freiberg/Germany, where she obtained her degree 'Diplom-Ingenieurin' (M.Sc.) in 2005. Between 2004 and 2005 she was an exchange student at the Norwegian University of Science and Technology (NTNU) in Trondheim/Norway, where she also performed her diploma thesis on the subject 'Thermal stability of selected aluminium alloys'. Between 2006 and 2009 she worked as a test engineer at Hoerbiger Antriebstechnik GmbH in Schongau/Germany. She joined the Materials innovation institute (M2i) in 2009, where she worked as an application engineer at Delft University of Technology in Delft/The Netherlands, on the project 'Thermo-magnetic determination of retained austenite fraction in supermartensitic stainless steel'. In 2010 her project was extended to a Ph.D. research project at M2i and Delft University of Technology in Delft/The Netherlands.